

The Assembly and Modification of Screen-Printed Platforms for Electroanalytical Applications



**Manchester
Metropolitan
University**

Christopher William Foster

The Assembly and Modification of Screen-Printed Platforms for Electroanalytical applications

Christopher William Foster

*Submitted in partial fulfilment of the
requirements of Manchester Metropolitan
University for the degree of Doctor of
Philosophy*

2015

*School of Science and the Environment
Division of Chemistry and Environmental
Science
Manchester Metropolitan University*

Abstract

This thesis reports upon the novel assembly and modification of screen-printed electrode systems. These key electrochemical proof-of-concepts have been benchmarked utilising voltammetric techniques, supporting the design of next-generation electrochemical sensing platforms, this thesis allows for proven laboratory-based approaches to be potentially up-scaled and commercially applied.

Chapter 3 introduces the potential influence mechanical contortion upon the electrochemical performance of graphite based electroanalytical screen-printed platforms upon graphic paper, tracing paper and an ultraflexible polyester-based substrate are used. These sensors are electrochemically benchmarked against well-known redox probes hexammineruthenium (III) chloride, potassium ferrocyanide and nicotinamide adenine dinucleotide (NADH). It was found that these ultraflexible based polyester-based electrodes are superior since they can withstand extensive mechanical contortion, yet still give rise to useful electrochemical performances. Most importantly the ultraflexible polyester electrodes do not suffer from capillary action as observed in the case of paper-based sensors causing the solution to wick-up the electrode towards the electrical connections. A new configuration is also explored using these electrode substrate supports where the working carbon electrode contains the electrocatalyst, cobalt (II) phthalocyanine (CoPC), and is benchmarked towards the electroanalytical sensing of the model analytes citric acid and hydrazine.

Chapter 4 for the first time critically compares CoPC modified electrodes prepared by drop-casting CoPC nanoparticles (nano-CoPC) onto a range of carbon based electrode substrates with that of CoPC bulk modified screen-printed electrodes, towards the sensing of the model analytes L-ascorbic acid, oxygen and hydrazine. It is found that no “electrocatalysis” is observed towards L-ascorbic acid using either of these CoPC modified electrode configurations and that the bare underlying carbon electrode is the origin of the obtained voltammetric signal, which gives rise to useful electroanalytical signatures, providing new insights into literature reports where “electrocatalysis” has been reported with no clear control experiments undertaken.

Chapter 5 presents a concise study upon the effect of *in-situ* bismuth, antimony, tin modified electrodes and combinations thereof towards the electrochemical

detection of model analytes cadmium (II) and lead (II). It is found that the electrochemical response using the available range of metallic modifications is only ever observed when the underlying electrode substrate exhibits relatively slow electron transfer properties; in the case of fast electron transfer properties, no significant advantages are evident. It is demonstrated that a simple change of pH can allow the detection of the target analytes (cadmium (II) and lead (II)) at levels below that set by the World Health Organisation (WHO) using bare graphite screen-printed electrodes.

Chapter 6 introduces the electroanalytical sensing of lead (II) ions utilising square-wave anodic stripping voltammetry where an increase in the electroanalytical sensitivity is observed by a factor of 5 with the screen-printed back-to-back microband configuration. Upon application of this configuration towards the quantification of lead (II) ions, within drinking water corresponds to a concentration of 2.8 (± 0.3) $\mu\text{g/L}$. Independent validation was performed using ICP-OES with the levels of lead (II) ions found to correspond to 2.5 (± 0.1) $\mu\text{g/L}$; the excellent agreement between the two methods validates the electroanalytical procedure for the quantification of lead (II) ions in drinking water.

Finally, Chapter 7 examines for the first time, characterisation of the number of drawn pencil layers and the grade of pencil; these parameters are commonly overlooked when utilising PDEs. It is demonstrated that a PDE drawn ten times with a 6B pencil presented the most advantageous electrochemical platform, in terms of electrochemical reversibility and peak height/analytical signal. These PDEs have demonstrated beneficial electroanalytical capabilities towards *p*-benzoquinone and the simultaneous detection of heavy metals, namely, lead (II) and cadmium (II) all of which are explored for the first time utilising PDEs. Initially, the detection limits of this system were lower than desired for an electroanalytical platforms, however implementation of PDEs in a back-to-back configuration (as shown within Chapter 6), the detection limits for lead (II) and cadmium (II) correspond to 10 $\mu\text{g/L}^{-1}$ and 98 $\mu\text{g/L}^{-1}$ respectively within model aqueous (0.1 M HCl) solutions.

Aims and Objectives

The aims and objectives at the start of this PhD were as follows:

1) *Academic Aim*: To extend the horizons of screen-printed electrochemical sensors

2) *Objectives*:

2.1) Design and fabricate screen-printed electrode configurations upon new substrates.

2.2) Develop modified screen-printed sensors to provide potential improvements within the electron transfer.

2.3) Explore and design these potentially improved screen-printed sensors for electroanalytical applications

2.4) Establish the development of the fundamental understanding of screen-printed electrochemical sensors to PhD level.

Acknowledgements

Throughout this PhD 'journey' I have encountered many tough and challenging times, therefore I would like to take some time to mention a selection of people, whose influence and guidance have been paramount to the completion of this doctorate.

I would first like to thank Prof. Craig Banks whose support and dedication towards research has enabled my doctorate to be one of my most enjoyable adventures to date. I further extend this gratitude to Dr Dale Brownson and Dr Jonathan Metters, whose extensive knowledge of electrochemistry and the art of screen-printing have been a key asset throughout this project. In addition, I would like to extend my thanks to everyone who has been a part of the Banks Research Group, as if it was not for the camaraderie within the group on a day-to-day basis, I would have not achieved the research outputs that I attained over the years within the group.

Finally, I would like to extend my undying gratitude to the whole of my family (grandparents, aunties, uncles and cousins), however I would like to specifically thank my mother and father (Debbie and Ian Foster), and my girlfriend Kerry-Ann whose support through every aspect of this journey has been key to the completion of this PhD.

Contents

Abstract	i
Aims and Objectives	iii
Acknowledgements	iv
Contents	v
List of Tables	ix
List of Figures.....	x
Chapter 1 - <i>Concepts of Electrochemistry</i>	1
1.1 Introduction to Electrochemistry	1
1.1.1 Faradaic and Non-Faradaic Processes	2
1.1.2 Effect of Mass Transport within Electrochemistry	4
1.1.3 Effect of Electron-Transfer within Electrochemistry	7
1.2 Electrochemical Techniques/Methods.....	8
1.2.1 Cyclic Voltammetry	8
1.2.2 Stripping Voltammetry	14
1.2.3 Chronoamperometry	16
1.2.4 Square-Wave Voltammetry	17
1.2.5 Benchmarking Electroanalysis	18
1.2.6 Selection of redox probes	20
1.2.7 Changing the electrode geometry: macro to micro	22
1.3 Common Electrode Materials.....	24
1.3.1 Carbon Materials	25
Chapter 2 - <i>Introduction and Current Applications of Screen-Printed Electrochemical Architectures</i>	28
2.1 History of Screen-Printed Electrodes	28
2.1.1 Screen-Printed Design	33

2.1.2	Printing Media	37
2.1.3	Substrate.....	40
2.2	Screen-Printing Process.....	42
2.3	Selection of Screen-Printing Equipment	44
2.3.1	The Screen	44
2.3.2	The Squeegee.....	46
2.3.3	The Flood Bar/Distributor	47
2.3.4	Printing Medium	48
2.3.5	Curing of the Ink	50
2.4	Fabrication of the screen-printed electrodes within this Thesis	51
2.4.1	Connection of the fabricated screen-printed electrochemical platforms....	54
2.4.2	Quantifying the composition of the screen-printed reference electrode....	57
Chapter 3 - <i>Flexibility and Robustness of Screen-Printed Electrodes</i>		59
3.1	Ultra-Flexible Paper based Electrochemical Sensors: Effect of Mechanical Contortion upon Electrochemical Performance	59
3.1.1	Introduction	59
3.1.2	Experimental Section.....	60
3.1.3	Results and Discussion.....	61
3.1.4	Conclusions	76
3.2	Ultra-Flexible Screen-Printed Graphitic Electroanalytical Sensing Platforms..	77
3.2.1	Introduction	77
3.2.2	Results and Discussion.....	78
3.2.3	Conclusions	91
Chapter 4 - <i>CoPC Modified Screen-Printed Electrodes</i>		92
4.1	Cobalt Phthalocyanine Modified Electrodes Utilised in Electroanalysis: Nano-Structured Modified Electrodes vs. Bulk Modified Screen-Printed Electrodes	92

4.1.1	Introduction	92
4.1.2	Experimental Section	95
4.1.3	Results and Discussion	96
4.2.4	Conclusions	108
Chapter 5 - <i>In-situ Modified Screen-Printed Electrode Systems</i>		110
5.1	Metallic Modified (bismuth, antimony, tin and combinations thereof) Film Electrodes	110
5.1.1	Introduction	110
5.1.2	Experimental Section	114
5.1.3	Results and Discussion	115
5.1.4	Conclusions	140
Chapter 6 - <i>Screen-Printed Designs to improve Electroanalytical Responses</i>		141
6.1	Screen-Printed Back-to-Back Electroanalytical Sensors	141
6.1.1	Introduction	141
6.1.2	Experimental Section	143
6.1.3	Results and Discussion	145
6.1.4	Conclusions	160
Chapter 7 - <i>Simplistic Electrode Fabrication Methods</i>		161
7.1	Pencil It In: Pencil Drawn Electrochemical Sensing Platforms	161
7.1.1	Introduction	161
7.1.2	Experimental Section	164
7.1.3	Results and Discussion	165
7.1.4	Conclusions	178
Chapter 8 - <i>Conclusions and Future Work</i>		179
8.1	Overall Conclusions	179
8.2	Suggestions for Future Work	181

Publications arising from this Thesis	182
References	184
Appendices	196

List of Tables

Table 1.1: Variation of ΔE_p with ψ at 298 K. Reproduced with permission from Ref. ¹⁰	12
Table 1.2: A table indicating the Matsuda and Ayabe ranges for reversible, quasi-reversible and irreversible electrode kinetics at 298 K assuming α is 0.5.....	13
Table 2.1: Product codes, substrate type, value of the heterogeneous rate constant k^0 (cm s^{-1}) and their respective denotation of the screen-printed electrodes used throughout.	53
Table 7.1: De-convoluted data from XPS spectra for the bulk 6B pencil lead (prior to fabricating PDEs) and assignments based on binding energies (BE).	174
Table 7.2: Anodic stripping voltammetry of lead (II) and cadmium (II) utilising a 6B PDE as a function of different times drawn. Deposition time and potential of 120 seconds and -1.5 V (vs. SCE) respectively; N = 3.	176

List of Figures

Figure 1.1: A) A typical three electrode system utilising an edge pyrolytic plane working electrode (WE), saturated calomel reference electrode (RE) and a platinum counter electrode (CE). B) A screen-printed electrode with a carbon composite working and counter electrode and an Ag/AgCl reference electrode within an electrolyte solution. .	2
Figure 1.2: Schematic of the Nernst Diffusion Layer	6
Figure 1.3: The triangular potential waveform used within cyclic voltammetry and linear sweep voltammetry.	8
Figure 1.4: A typical cyclic voltammogram within 1 mM hexaammineruthenium (III) chloride/ 0.1 M KCl utilising a standard-SPE. Scan rate: 100 mV s ⁻¹ . Additionally showing are the peak heights (<i>i</i> _{pa} and <i>i</i> _{pc}) and positions (<i>E</i> _{pa} and <i>E</i> _{pc}) for the (anodic) reduction and (cathodic) oxidation respectively.	9
Figure 1.5: Cyclic voltammograms representing a reversible (solid line), quasi-reversible (dashed line) and irreversible (dotted line).	10
Figure 1.6: A typical anodic stripping voltammogram in the absence (dotted line) and presence of lead (II) (solid line) within 0.1 M acetate buffer solution, utilising a screen-printed electrode. Deposition potential and time: -1.2 V and 120 seconds respectively.	14
Figure 1.7: A typical chronoamperometric potential waveform (A) and a current-time response for increasing additions of an analyte (B).	16
Figure 1.8: Square-wave voltammetric waveform (A) and the resulting voltammetric profile of current versus staircase potential.	17
Figure 1.9: Classification of redox systems according to their kinetic sensitivity to particular surface modifications on carbon electrodes. Adapted from Ref ¹⁶	21
Figure 1.10: The unique differences between the cyclic voltammetric signatures observed at a macroelectrode (A) compared to a microelectrode (B).	22
Figure 1.11: Graphite and diamond structures derived from their respective hybridised orbitals of the carbon atoms.	25
Figure 1.12: a) Image of a commercially available slab of HOPG. b) Schematic of a side-on view of a HOPG surface, highlighting its basal plane and edge plane like- sites/defects. c) A representation of a HOPG surface showing the discrete basal plane and edge plane	

islands. d) A typical STM image of a HOPG surface with the corresponding fragment of the graphene structure superimposed. Reproduced with permission from Ref ¹⁵26

Figure 2.1: Example of a typical drop-cast fabrication upon screen-printed systems and the corresponding electrochemical measurement of a target analyte. Reproduced from Ref ³⁸30

Figure 2.2: Schematic illustration of the screen-printed configuration, the procedures used in the process of MWCNTs-doped SPE fabrication. Reproduced from Ref ³⁹31

Figure 2.3: Optical image (A) and schematic diagram (B) of a screen-printed solar cell and fuel cell respectively. Adapted from Ref ^{54, 55}32

Figure 2.4: (A) A schematic of a layer-by-layer structure of the screen-printed ultra-microelectrode assembly. (B) Cross-sectional diagram the electrode system with a built-in three-electrode configuration. Reproduced with permission from Ref ⁶⁸34

Figure 2.5: Optical and SEM imaging of a 2 cm (length) x 100 μM (width) screen-printed band electrode.35

Figure 2.6: Optical image of a microarray screen-printed electrode and schematic of an immunoassay created upon this system.36

Figure 2.7: Cyclic voltammetric profiles (A) obtained in 1 mM potassium ferrocyanide / 1 M KCl using a copper plated standard SPE (solid line) with that of a bespoke electrochemical platform (dashed line). Scans recorded at 100 mV s⁻¹ vs. SCE. SEM images of the copper plated standard (B) and bespoke (C) screen-printed electrochemical platforms. Reproduced from ref ⁷⁹ with permission from Elsevier.38

Figure 2.8: Optical images of the electrochemical tattoo upon the substrate and skin. Reproduced from Ref ⁸⁷40

Figure 2.9: Schematic of the Screen-Print Process. A) Placement of the printing media (i.e. ink, emulsion or paste) upon the mesh screen, where it is visible that the screen is not in contact with the substrate. B) The printing medium is passed through the openings in the screen mesh in a controlled manner. C) The print is finished and the stencil design has been transferred onto the substrate.....43

Figure 2.10: Optical image of a stainless steel screen-mesh, for a working electrode (left image) and counter electrode (right image).Magnification x50.....45

Figure 2.11: Schematic of a mesh opening.45

Figure 2.12: Angles of the squeegee and their effect upon the screen-print.	47
Figure 2.13: Optical images of fineness of grind gauge. Reproduced from Ref ⁸⁹	49
Figure 2.14: Representation of curing of the printing medium upon the conductive layers.	50
Figure 2.15: Image of a sheet of F-SPE (A) highlighting the ultra-flexible nature of the plastic substrate and fabricated electrode it gives rise to. Image B shows a single F-SPE which has an on-board counter and reference electrode which is used as a single sensor.	51
Figure 2.16: Typical cyclic voltammograms using both an edge connector (A) and a crocodile clip setup (B) recorded in hexaammineruthenium (III) chloride/ 0.1 M KCl. Also shown are plots of peak height versus square root of scan rate (C) for the edge connector and crocodile clip setup (squares and circles respectively).....	55
Figure 2.17: Images showing the correct (A) and incorrect (B) way to connect the screen-printed electrodes/sensors to the potentiostat/electrodes utilising crocodile clips, with their corresponding cyclic voltammograms (C & D respectively) recorded in 1 mM hexaammineruthenium (III) chloride/ 0.1 M KCl.	56
Figure 3.1: Photographs of: (A) The standard polymer-based screen-printed electrode (standard-SPE) (left), the Sellotape™ coated paper-based screen-printed sensor (ps-SPE) (middle) and the clear nail varnish coated paper-based screen-printed sensor (pv-SPE) (right). The contortion angles of 45 and 90° utilised throughout this investigation are shown in (B) and (C) respectively.	62
Figure 3.2: Cyclic voltammetric responses obtained at standard-SPE contorted at angles of (A): 45 and (B): 90°, recorded in 1 mM potassium ferrocyanide (II) / 0.1 M KCl. Contortion times of 60 (dashed line), 10 (dash-dotted line), 5 (dotted line) and 0 minutes (solid line) were utilised for each of the standard-SPEs. Scan rate: 100 mV s ⁻¹ . Also shown is the effect of contortion time for the two angles upon voltammetric peak-to-peak separation (ΔE_p): 45° (squares) and 90° (circles). N = 3.	63
Figure 3.3: Cyclic voltammetric responses for ps-SPE contorted at angles of (A): 45 and (B): 90°, recorded in 1 mM potassium ferrocyanide (II) / 0.1 M KCl. Contortion times of 60 (dashed line), 10 (dash-dotted line), 5 (dotted line) and 0 minutes (solid line) were utilised for each of the standard-SPEs. Scan rate: 100 mV s ⁻¹ . Also shown is the effect of	

contortion time for the two angles upon peak-to-peak separation (ΔE_p): 45° (squares) and 90° (circles). N = 3.64

Figure 3.4: Cyclic voltammetric responses for pv-SPE contorted at angles of (A): 45 and (B): 90°, recorded in 1 mM potassium ferrocyanide (II) / 0.1 M KCl. Contortion times of 60 (dashed line), 10 (dash-dotted line), 5 (dotted line) and 0 minutes (solid line) were utilised for each of the standard-SPEs. Scan rate: 100 mV s⁻¹. Also shown is the effect of contortion time for the two angles upon peak-to-peak separation (ΔE_p); 45° (squares) and 90° (circles). N = 3.66

Figure 3.5: Cyclic voltammetric responses for standard-SPE contorted at angles of (A): 45 and (B): 90°, recorded in 100 μM NADH in pH 7 phosphate buffer. Contortion times of 60 (dashed line), 10 (dash-dotted line), 5 (dotted line) and 0 minutes (solid line) were utilised for each of the standard-SPEs. Scan rate: 100 mV s⁻¹. Also shown is the effect of contortion time for the two angles upon the voltammetric peak potential (E_p): 45 (squares) and 90° (circles). N = 3.69

Figure 3.6: Cyclic voltammetric responses for ps-SPE contorted at angles of (A): 45 and (B): 90°, recorded in 100 μM NADH in pH 7 phosphate buffer. Contortion times of 60 (dashed line), 10 (dash-dotted line), 5 (dotted line) and 0 minutes (solid line) were utilised for each of the standard-SPEs. Scan rate: 100 mV s⁻¹. Also shown in (C) is the effect of contortion time for the two angles upon the voltammetric peak potential (E_p): 45 (squares) and 90° (circles). N = 3..... 70

Figure 3.7: Cyclic voltammetric responses for pv-SPE contorted at angles of (A): 45 and (B): 90°, recorded in 100 μM NADH in pH 7 phosphate buffer. Contortion times of 60 (dashed line), 10 (dash-dotted line), 5 (dotted line) and 0 minutes (solid line) were utilised for each of the standard-SPEs. Scan rate: 100 mV s⁻¹. Also shown in (C) is the effect of contortion time for the two angles upon the voltammetric peak potential (E_p): 45 (squares) and 90° (circles). N = 3..... 71

Figure 3.8: SEM images of the conductive track of a carbon screen-printed electrodes on polyester-substrates (A and B) and a paper-based substrate (C and D, prior to coating with nail varnish and Sellotape™ respectively), following 60 minutes contorted at an angle of 45° at magnifications of x 25 (A & C) and x 85 (B & D). 73

Figure 3.9: The effect of numerous and consecutive contortions to an angle of 45° on voltammetric peak current (I_p), in a solution of 1 mM potassium ferrocyanide (II) / 0.1 M KCl when utilising the standard-SPE (squares), ps-SPE (circles) and pv-SPE (triangles). Scan rate: 100 mV s⁻¹. N = 3. 74

Figure 3.10: The effect of numerous and consecutive contortions to an angle of 45° on voltammetric peak current (I_p), in a solution of 100 μM NADH in a pH 7 phosphate buffer solution when utilising the standard-SPE (squares), ps-SPE (circles) and pv-SPE (triangles). Scan rate: 100 mV s⁻¹. N = 3. 75

Figure 3.11: Typical cyclic voltammograms and a plot of peak height vs. square root of scan rate for increasing scan rates (5 mV s⁻¹ to 500 mV s⁻¹) using a F-SPE (A & B respectively) recorded in 1 mM potassium ferrocyanide (II) / 0.1 M KCl and 1 mM hexaammineruthenium (III) chloride / 0.1 M KCl (C & D)..... 78

Figure 3.12: Calibration plots resulting from the additions of NADH (10 to 100 μM) into pH 7.5 PBS using new P-SPEs (squares), standard-SPEs (circles) and F-SPEs (triangle) after each addition. Scan rate: 100 mV s⁻¹ using cyclic voltammetry. N = 3. 80

Figure 3.13: Cyclic voltammograms depicting the effect of mechanical contortion upon the voltammetric response when contorted at an angle of 45 ° over a range of 0 (solid line), 10 (dashed line), 20 (dotted line), 100 contortions (dash-dotted line) towards the P-SPE (A), standard-SPE (B), F-SPE (C) recorded in a solution of 100 μM NADH in a pH 7.5 PBS. Also shown is a plot showing peak height ($I_p/\mu A$) vs. number of contortions (D) for P-SPE (squares), standard-SPE (circles), F-SPE (triangles). Scan rate: 100 mV s⁻¹. N = 3. 81

Figure 3.14: Cyclic voltammograms show the response of the CoPC-P-SPE (solid line), CoPC-T-SPE (dotted line) and CoPC-F-SPE (dashed line) recorded in a pH 7.5 PBS containing 10 mM citric acid. Scan rate: 100 mV s⁻¹. Also shown is the response of the blank (standard SPE, no CoPC) showing that the electrochemical response is due to the CoPC contained within the working electrode. 83

Figure 3.15: Calibration plots resulting from the additions of citric acid (1 to 10 mM) / pH 7.5 PBS using a different CoPC-P-SPE (A), CoPC-T-SPE (B) and CoPC-F-SPE (C) following every addition. Scan rate: 100 mV s⁻¹. N = 3. 86

Figure 3.16: Cyclic voltammograms (A) showing a blank solution of pH 7.5 PBS (solid line) and in the presence of 1mM hydrazine / pH 7.5 PBS using CoPC-F-SPE (dashed line). B is

a calibration plot showing the consequent additions of hydrazine (10 to 100 μM) into pH 7.5 PBS using a different CoPC-F-SPE following each addition of hydrazine. Scan rate: 100 mV s^{-1} . N = 3.87

Figure 3.17: Cyclic voltammograms (A) performed over the range 5 to 500 mV s^{-1} recorded in a solution of 1mM hydrazine in pH 7.5 PBS using a different CoPC-F-SPE at each scan rate. Parts (B) and (C) show plots of the square root of the scan rate vs. peak height and logarithm of the peak height vs. logarithm of scan rate respectively. N = 388

Figure 3.18: Cyclic voltammograms showing both the first (solid line) and second (dashed line) voltammetric scans upon the CoPC-F-SPEs utilising the model analytes (A) 10 mM citric acid in PBS pH 7.5 and (B) 1 mM hydrazine in PBS pH 7.5. Scan rate: 100 mV s^{-1}90

Figure 4.1: Typical SEM images of a bare standard-SPE (A), CoPC-SPE (B) and a standard-SPE modified with 20 μg and 70 μg nano-CoTAPC (C & D respectively).....97

Figure 4.2: Cyclic voltammograms (A) in the presence (dashed line) and absence (solid line) of 1 mM L- Ascorbic acid in pH 7.4 PBS utilising a standard-SPE modified with 20 μg nano-CoPC. (B) shows the corresponding plots of peak height (using peak at $\sim + 0.30 \text{ V}$ vs. SCE) utilising a varied amount (mass) of nano-CoPC. Scan rate: 100 mV s^{-1} . N = 3. .99

Figure 4.3: Typical cyclic voltammograms utilising a standard-SPE (solid line), GCE (dashed line) and BDDE (dotted line) in a blank pH 7.4 PBS and in the presence of 1 mM L-Ascorbic acid. Scan rate: 100 mV s^{-1}100

Figure 4.4: Calibration plots with error bars for L-Ascorbic acid over the concentration range 100 to 1000 μM within a pH 7.4 PBS using a nano-CoPC SPEs (circles), CoPC-SPEs (squares) after each scan and a standard-SPE (triangles), a utilising the voltammetric peak obtained at + 0.30 V vs. SCE. Scan rate: 100 mV s^{-1} using cyclic voltammetry, N = 3.101

Figure 4.5: Cyclic voltammograms (A) in a nitrogen degassed (solid line) and an oxygen saturated 0.1 M H_2SO_4 solution utilising a standard-SPE (short dashed line), CoPC SPE (dotted line) and a standard-SPE modified with 20 μg nano-CoPC (dotted-dashed line). Corresponding plots of coverage of nano-CoPC mass vs. peak height (B) and peak potential (C). Scan rate: 100 mV s^{-1}103

Figure 4.6: Cyclic voltammograms comparing the electrochemical oxidation of hydrazine utilising a standard SPE (solid line) and 20 μg nano-CoPC SPEs in the presence and absence (dashed line and dotted line) of 500 μM hydrazine in a pH 7.4 PBS. Scan rate: 100 mV s^{-1}104

Figure 4.7: Cyclic voltammograms (A) in the presence (dashed line) and absence (solid line) of 500 μM hydrazine in pH 7.4 PBS utilising a standard-SPE modified with 20 μg nano-CoPC. Corresponding plots of nano-CoPC mass vs. peak height (B). Scan rate: 100 mV s^{-1} . N = 3.105

Figure 4.8: Cyclic voltammograms (A) and plots of diluted nano-CoPC mass vs. peak height (B) in the presence of 500 μM hydrazine in pH 7.4 PBS utilising a standard-SPE as the underlying electrode surface. Scan rate: 100 mV s^{-1} . N = 3.106

Figure 4.9: Calibration plots showing nano-CoTAPC SPE (squares) and CoPC-SPE (circles) towards subsequent additions of (10 μM to 100 μM) hydrazine into pH 7.4 PBS, utilising a new electrode after each addition. Scan rate: 100 mV s^{-1} . N = 3107

Figure 5.1: Linear sweep voltammograms resulting from additions of 5 mgL^{-1} antimony (III) (at 0.0 V) into a pH 4.3 acetate buffer solution containing 1.03 mgL^{-1} lead (II) (at - 0.34 V) and 0.56 mgL^{-1} cadmium (II) (at - 0.60 V) in a using both SPE (A) and BDDE (B). Dotted line equates to the optimum concentration of antimony (III). Deposition potential and time: - 1.2 V (vs. SCE) and 120 seconds respectively. Inset: Corresponding plots of voltammetric peak height versus antimony (III) concentration (cadmium (II) – triangles; lead (II) – circles) N = 3.117

Figure 5.2: Linear sweep voltammograms resulting from additions of 20 mgL^{-1} tin (II) (at - 0.34 V) into a pH 4.3 acetate buffer solution containing 1.03 mgL^{-1} lead (II) (at - 0.34 V) and 0.56 mgL^{-1} cadmium (II) (at - 0.60 V) using both SPE (A) and BDDE (B). Dotted line equates to optimum concentration of tin (II). Deposition potential and time: - 1.2 V (vs. SCE) and 120 seconds respectively. Inset: Corresponding plots of voltammetric peak height versus tin (II) concentration (cadmium (II) – triangles; lead (II) – circles). N = 3.119

Figure 5.3: Linear sweep voltammograms resulting from additions of 10 mgL^{-1} bismuth (III) (at - 0.10 V) into a pH 4.3 acetate buffer solution containing 1.03 mgL^{-1} lead (II) (at - 0.34 V) and 0.56 mgL^{-1} cadmium (II) (at - 0.60 V) using both SPE (A) and BDDE (B). Dotted

line equates to optimum concentration of bismuth (III). Deposition potential and time: - 1.2 V (vs. SCE) and 120 seconds respectively. Inset: Corresponding plots of voltammetric peak height versus bismuth (III) concentration (cadmium (II) – triangles; lead (II) – circles). N = 3. 121

Figure 5.4: Linear sweep voltammograms resulting from 10 mgL⁻¹ antimony (III) (at 0.0 V) with additions of tin (II) (at - 0.34 V) (1 – 40 mgL⁻¹) towards 1.03 mgL⁻¹ lead (II) (at - 0.34 V) and 0.56 mgL⁻¹ cadmium (II) (- 0.60 V) in a pH 4.3 acetate buffer solution using both SPE (A) and BDDE (B) (dotted line equates to optimum concentration of antimony (III) and tin (II)). Deposition potential and time: - 1.2 V (vs. SCE) and 120 seconds respectively. Inset: Corresponding plots of voltammetric peak height versus tin (II) / antimony (III) concentration (cadmium (II) – triangles; lead (II) – circles). N = 3. 123

Figure 5.5: Linear sweep voltammograms resulting from additions of 10 mgL⁻¹ and 5 mgL⁻¹ bismuth (III) (at - 0.10 V) and tin (II) (at - 0.34 V) respectively into a solution containing 1.03 mgL⁻¹ lead (II) (at - 0.34 V) and 0.56 mgL⁻¹ cadmium (II) (at - 0.60 V) in a pH 4.3 acetate buffer solution using both SPE (A) and BDDE (B) (dotted line equates to optimum concentration of bismuth (III) and tin (II)). Deposition potential and time: - 1.2 V (vs. SCE) and 120 seconds respectively. Inset: Corresponding plots of voltammetric peak height versus tin (II) / bismuth (III) concentration (cadmium (II) – triangles; lead (II) – circles). N = 3. 125

Figure 5.6: Linear sweep voltammograms resulting from additions of lead (II) (at - 0.34 V) (103.61 to 932.42 µgL⁻¹) and cadmium (II) (at - 0.60 V) (56.46 to 508.14 µgL⁻¹) into a pH 4.3 acetate buffer solution (dotted line) using both a standard-SPE (A) and a bare BDDE (B). Also depicted are the corresponding calibration plots for lead (II) (C) and cadmium (II) (D) at the SPE (squares) and BDDE (circles). Deposition potential and time: - 1.2 V (vs. SCE) and 120 seconds respectively. N = 3. 127

Figure 5.7: Linear sweep voltammograms resulting from additions of lead (II) (at - 0.34 V) (103.61 to 932.42 µgL⁻¹) and cadmium (II) (at - 0.60 V) (56.46 to 508.14 µgL⁻¹) into a pH 4.3 acetate buffer solution (dotted line) containing 5 mgL⁻¹ of antimony (III) (at - 0.0 V) using both an SPE (A) and BDDE (B). Also depicted are the corresponding calibration plots for lead (II) (C) and cadmium (II) (D) at the SPE (squares) and BDDE

(circles). Deposition potential and time: - 1.2 V (vs. SCE) and 120 seconds respectively.

N = 3. 128

Figure 5.8: Linear sweep voltammograms resulting from additions of lead (II) (at - 0.34 V) (103.61 to $932.42 \mu\text{gL}^{-1}$) and cadmium (II) (at - 0.60 V) (56.46 to $508.14 \mu\text{gL}^{-1}$) in to a pH 4.3 acetate buffer solution (dotted line) containing 20 mgL^{-1} of tin (II) (at - 0.34 V) using both an SPE (A) and BDDE (B). Also depicted are the corresponding calibration plots for lead (II) (C) and cadmium (II) (D) at the SPE (squares) and BDDE (circles). Deposition potential and time: - 1.2 V (vs. SCE) and 120 seconds respectively.

N = 3. 130

Figure 5.9: Linear sweep voltammograms resulting from additions of lead (II) (at - 0.34 V) (103.61 to $932.42 \mu\text{gL}^{-1}$) and cadmium (II) (at - 0.60 V) (56.46 to $508.14 \mu\text{gL}^{-1}$) in to a pH 4.3 acetate buffer solution (dotted line) containing 1 mgL^{-1} of bismuth (III) (at - 0.1 V) using both an SPE (A) and BDDE (B). Also depicted are the corresponding calibration plots for lead (II) (C) and cadmium (II) (D) at the SPE (squares) and BDDE (circles). Deposition potential and time: - 1.2 V (vs. SCE) and 120 seconds respectively.

N = 3. 131

Figure 5.10: Linear sweep voltammograms resulting from additions of lead (II) (at - 0.34 V) (103.61 to $932.42 \mu\text{gL}^{-1}$) and cadmium (II) (at - 0.60 V) (56.46 to $508.14 \mu\text{gL}^{-1}$) in to a pH 4.3 acetate buffer solution (dotted line) containing 10 mgL^{-1} of antimony (III) (at 0.0 V) and 20 mgL^{-1} of tin (II) (at - 0.34 V) using both an SPE (A) and BDDE (B). Also depicted are the corresponding calibration plots for lead (II) (C) and cadmium (II) (D) at the SPE (squares) and BDDE (circles). Deposition potential and time: - 1.2 V (vs. SCE) and 120 seconds respectively. N = 3. 132

Figure 5.11: Linear sweep voltammograms resulting from additions of lead (II) (at - 0.34 V) (103.61 to $932.42 \mu\text{gL}^{-1}$) and cadmium (II) (at - 0.60 V) (56.46 to $508.14 \mu\text{gL}^{-1}$) in to a pH 4.3 acetate buffer solution (dotted line) containing 1 mgL^{-1} of bismuth (III) (at - 0.10 V) and 1 mgL^{-1} of tin (II) (at - 0.34 V) using both an SPE (A) and BDDE (B). Also depicted are the corresponding calibration plots for lead (II) (C) and cadmium (II) (D) at the SPE (squares) and BDDE (circles). Deposition potential and time: - 1.2 V (vs. SCE) and 120 seconds respectively. N = 3. 133

Figure 5.12: Calibration plots depicting the response of voltammetric peak height versus lead (II) (A, C & E) / cadmium (II) (B, D & F) concentration over the range of 10 – 150 μgL^{-1} in a solution of a pH 4.3 acetate buffer using the SPE (A & B), GCE (C & D) and BDDE (E & F). In each the plots obtained for the bare electrode material (squares) is overlaid with the response obtained in the presence of 1 mgL^{-1} bismuth (III) (circles). Deposition potential and time: - 1.2 V (vs. SCE) and 120 seconds respectively. N = 3. 137

Figure 5.13: Linear sweep voltammograms resulting from additions of lead (II) (at - 0.34 V) and cadmium (II) (at - 0.60 V) (solid line) into a pH 1.7 HCl solution (dotted line) using a standard-SPE (A). Also depicted are the corresponding calibration plots for lead (II) (B) and cadmium (II) (C) over the concentration ranges of 2-20 μgL^{-1} and 2.2-22 μgL^{-1} respectively. Deposition potential and time: - 1.5 V (vs. SCE) and 240 seconds respectively, with the respective errors bars corresponding to the standard deviation of the procedure. N = 3. 139

Figure 6.1: Optical image of a single side of a back-to-back screen-printed graphite microband (A) and a schematic depiction of the back-to-back configuration demonstrating the electrode lay-out and single point of electrical connection (B). ... 142

Figure 6.2: Image of two bSPEs in the side-by-side configuration comprising of two working, reference and counter electrodes. Distance between the centre of the two working electrodes: 7.5 mm. 143

Figure 6.3: Square wave voltammograms obtained in a solution of 0.02 M (pH 1.7) HCl in the absence (dotted line) and increasing concentration additions of lead (II) ions (5 to 110 μgL^{-1}) and corresponding calibration plots over the range studied using bSPEs (A & C) and b²SPEs (B & D) respectively. Data presented is an average and error bars from three experiments. Deposition potential and time of -1.2 V and 30 seconds respectively. 147

Figure 6.4: Analysis of the data presented in Figure 6.3 in terms of plots of current density (of the peak heights) against increasing concentrations of lead (II) ions utilising the bSPEs (squares) and b²SPEs (circles). Deposition potential and time: -1.2 V and 30 seconds respectively. N = 3. 148

Figure 6.5: Square wave voltammograms (A) for the back-to-back (dotted line) and side-by-side (dashed line) configuration. Solution composition: 100 μgL^{-1} lead (II) ions; 0.02

M HCl. Additionally shown (B) is a plot of peak height vs. increasing concentrations of lead (II) ions. N = 3 Deposition potential and time of -1.2 V and 30 seconds respectively. 150

Figure 6.6 (above): Square wave voltammograms obtained using the b²SPE within 0.02 M (pH 1.7) HCl (solid line) and the simultaneous detection of lead (II), cadmium (II) and zinc (II) at concentrations of 8, 16 and 36 μgL⁻¹ respectively (dashed line). Deposition potential and time of -1.5 V and 120 seconds respectively..... 151

Figure 6.7 (above): Calibration plots of lead (II) (A), and the additional interferents cadmium (II) (B) and zinc (II) (C) using b²SPEs. Data presented is an average and error bars from three experiments. Deposition potential and time of -1.5 V and 120 seconds respectively. 152

Figure 6.8: Square wave voltammograms obtained using b²SPEs (A) in a drinking water sample in the absence (dashed line) and the result of increasing additions of lead (II) ions (solid lines). Standard addition plot (B) for the lead (II) ions within drinking water with corresponding errors bars. N = 3 Deposition potential and time of -1.2 V and 30 seconds respectively. 153

Figure 6.9: Cyclic voltammograms recorded in 1 mM hexaammineruthenium (III) chloride / 0.1 M KCl (A & B) and 1 mM potassium ferrocyanide (II) / 0.1 M KCl (C & D) using the B-CNT-SPE (dotted line) and B²-CNT-SPE (solid line) at scan rates of 5 mV s⁻¹ (A & C) and 100 mV s⁻¹ (B & D) (vs. Ag/AgCl)..... 155

Figure 6.10: Typical cyclic voltammograms obtained in 50 μM dopamine hydrochloride in a pH 7.4 phosphate buffer solution and plots of peak height vs. increasing dopamine concentration (5-49.6 μM) using the B-CNT-SPEs (dotted line & squares) and B²-CNT-SPEs (solid line & circles) at scan rates of 50mVs⁻¹. N = 3 (vs. Ag/AgCl) 157

Figure 6.11: Typical cyclic voltammograms obtained in 100 μM capsaicin in a pH 1.25 phosphate buffer solution (A) and plots of peak height vs. increasing capsaicin concentration (5 - 49.6 μM) (B) using the B-CNT-SPEs (dotted line & squares) and B²-CNT-SPEs (solid line & circles) at scan rates of 50 mV s⁻¹. N = 3 (vs. Ag/AgCl). 158

Figure 6.12: Typical cyclic voltammograms obtained in 100 μM hydrazine in a pH 7.4 phosphate buffer solution (A) and plots of peak height vs. increasing hydrazine

concentration (7.9 – 104 μM) (B) using the B-CoPC-SPEs (dotted line & squares) and B²-CoPC-SPEs (solid line & circles) at scan rates of 100 mV s^{-1} . N = 3 (vs. Ag/AgCl).....159

Figure 7.1: Optical image of the bespoke metallic stencil used throughout this work (A) to fabricate the PDEs. Shown in (B) is the PDE after one draw and the completed PDE with a connecting strip (C). Sellotape[®] was applied to each individual electrode to cover the conductive carbon connections and define the 4 mm working area.....165

Figure 7.2: Typical cyclic voltammograms utilising different pencil grades drawn once (A), three (B), five (C) and ten (D) times recorded in 1 mM hexaammineruthenium (III) chloride / 0.1 M KCl. Scan rate: 50 mV s^{-1} (vs. SCE).166

Figure 7.3: Plots of pencil composition/grade vs. peak height (cathodic current) recorded in 1 mM hexaammineruthenium (III) chloride / 0.1 M KCl as a result of increasing the number of draws. Scan rate: 50 mV s^{-1} (vs. SCE). Data shown is an average and corresponding standard deviation N = 3167

Figure 7.4: Typical cyclic voltammetric responses recorded in 1 mM hexaammineruthenium (III) chloride / 0.1 M KCl (A) and in 1 mM potassium ferricyanide / 0.1 M KCl (B) at 5 mV s^{-1} (dotted line) and 100 mV s^{-1} (solid line) (vs. SCE) using the 6B PDE drawn ten times.....168

Figure 7.5: Typical cyclic voltammetric response using the 6B PDE drawn ten times recorded in 1 mM potassium ferrocyanide / 0.1 M KCl. Scan rate: 100 mV s^{-1} (vs. SCE). Note that this figure reiterates that electrochemical processes which require an electrochemical oxidation step first give rise to featureless voltammetric profiles.169

Figure 7.6 (above): TEM images of the bulk 6B pencil ‘lead’ (used for the fabrication of the PDEs) at increasing magnifications.....170

Figure 7.7 (above): SEM images of 6B PDEs drawn once (A and B) and ten times (C and D).170

Figure 7.8: Raman spectra for the bulk 6B pencil lead (red line; pencil lead analysis as received), 6B PDE drawn once (green line) and ten times (blue line).172

Figure 7.9: 2D (A and D) and 3D (B and E) schematic Raman maps generated from analysis of 6B PDEs drawn once (A, B and C) and ten (D, E and F) times respectively and their corresponding optical images (C and F). Raman intensities were recorded at the characteristic 2D peak occurring ca. 2750 cm^{-1}173

Figure 7.10: Typical cyclic voltammograms (A) recorded in the absence (dotted line) and presence of 500 μM p-benzoquinone (solid line) within a pH 7.4 phosphate buffer solution. Typical calibration plot (B) corresponding to additions of p-benzoquinone over the range of 100 to 1000 μM into a pH 7.4 phosphate buffer solution recorded using a 6B PDE drawn ten times. Error bars indicate the average response and standard deviation $N = 3$. Scan rate: 50 mV s^{-1} (vs. SCE).....175

Figure 7.11: Simultaneous determination of Pb (II) and Cd (II) recorded in 0.1 M HCl (dotted line) utilising a back-to-back 6B PDE drawn ten times. Shown in (A) are the corresponding linear sweep voltammograms with corresponding calibration plots (B) and (C) respectively. Error bars indicate the standard deviation of $N = 3$. Deposition potential and time: -1.2 V (vs. SCE) and 120 seconds respectively.177

Chapter 1 - *Concepts of Electrochemistry*

1.1 Introduction to Electrochemistry

Since the 17th century when the recognition of electrochemistry as a branch of 'chemistry' was established, the utilisation of electrochemistry within everyday technology has become imperative.¹ Such advancement and reliability upon technology allows this branch of chemistry to flourish and expand, not only for the benefit of the scientific community but the general population as well. Electrochemistry is the combination of utilising electricity and interpreting the electrochemical reactions that occur from it.^{1,2} The field of electrochemistry comprises of many applications such: electroanalytical sensors, batteries, fuel cells, solar power and large scale metallic plating to name just a few.^{2,3} With such benefits and possible applications, the study of electrochemistry is vital for a sustainable and prosperous future.

Within the field of electrochemistry the main focal point is not on the bulk solution unlike that of many other areas of chemistry, but on the electrochemical interaction of the electrode and the solution at its surface.^{2,4} Such analysis can be only be obtained if the correct utilisation of an electrochemical cell is carried out, depending on whether a potentiometric or potentiostatic method will depict the electrode setup needed.² The electrochemical cell for a potentiometric method can only occur when two conducting electrodes are present within an electrolytic solution (electrolyte). The two electrodes are denoted as the working and reference electrode.² Within the cell, the working electrode is where the reaction occurs and the reference electrode remaining at a static potential that importantly is not affected by the reaction within the cell.² Alternatively, for a potentiostatic method a three electrode system is employed, with the addition of an auxiliary electrode (counter). The introduction of a counter electrode in combination with the previous electrodes, allows for a current to be passed through the solution and by-pass that of the reference electrode. This creates a system that possesses a higher stability, as the current no longer passes through it.² Figure 1.1 depicts a traditionally used three electrode system compared to a system which has been printed using conductive inks; such a comparison indicates the ability to create

electrochemical setups that are portable, cheap and reproducible. This thesis focuses on the development of screen-printed electrode systems.

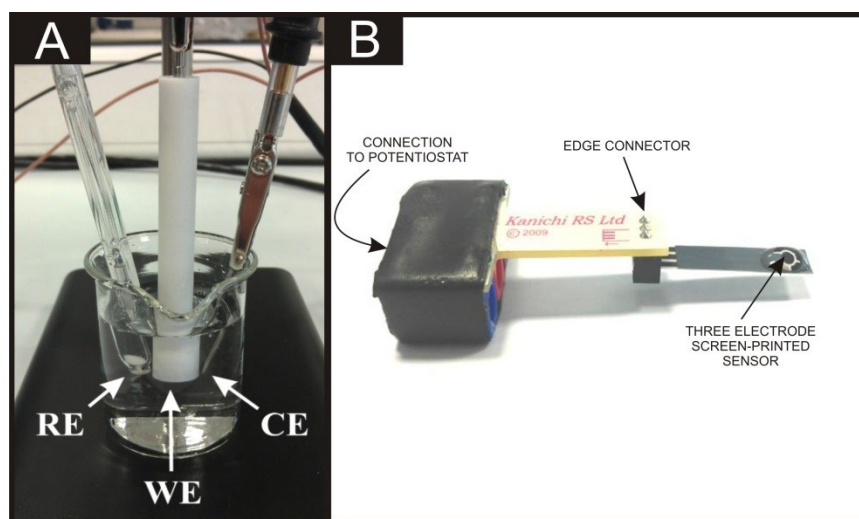


Figure 1.1: A) A typical three electrode system utilising an edge pyrolytic plane working electrode (WE), saturated calomel reference electrode (RE) and a platinum counter electrode (CE). B) A screen-printed electrode with a carbon composite working and counter electrode and an Ag/AgCl reference electrode within an electrolyte solution.

1.1.1 Faradaic and Non-Faradaic Processes

Faradaic and non-faradaic are two types of processes that exist at the electrode when carrying out an electrochemical experiment.^{2,4} These processes are governed by Faraday's law stated within equation (1.1), where eq are the chemical equivalents of the reactants that are oxidised or reduced, Q , is the charge that is transferred across the electrode-solution interface and is given by $Q = it$ (for a stable current) or $Q = \int_0^t i dt$ (for an unstable current) where i is the current, t is the time, F is the Faraday constant (96485.38 coulombs mol⁻¹):^{2,5}

$$eq = \frac{Q}{F} \tag{1.1}$$

This equation indicates that amount of chemical reaction induced by the current flow is proportional to that of the electricity passed through the cell. It is then obvious, that for a Faradaic process to occur, the utilisation of electricity must have caused a reaction over the electrode-solution interface, such reactions are simply denoted as oxidations or reductions.² However, even though there is no chemical reaction occurring, these non-faradaic processes have some very important real world applications as capacitors, as when the potential is altered non-Faradaic processes such

as adsorption and desorption occurs, allowing the flow of capacitive current to be measured.^{2,3}

When utilising potential-controlled techniques the aim is to measure the faradaic current related to the concentration of the analyte. Such responses are measured by recording the electron transfer of the process of the redox couple:^{2,5}



where, O and R are the oxidised and reduced species respectively, of the redox couple. Such reactions will occur within a potential range that allows the electron transfer thermodynamically or kinetically favourable. Thermodynamically controlled systems can utilise the potential of the electrode to establish the activity of the electroactive species (where a^O and a^R represent the activities of the oxidised and reduced forms respectively), according to the Nernst equation:^{2-4, 6, 7}

$$E = E^0 - \frac{RT}{nF} \ln \frac{a^R}{a^O} \quad (1.3)$$

where, R , is the universal gas constant ($8.314 \text{ J K}^{-1} \text{ mol}^{-1}$), T is the temperature (in Kelvin), n is the number of electrons transferred in the reaction, and F is the Faraday constant (mentioned previously in equation (1.1)). In highly dilute aqueous solutions, where such ions do not physically interact with each other, it is assumed that the activity is equal to concentration. The Nernst equation can then be expressed in the following form:^{2, 3, 7}

$$E = E^0 - \frac{RT}{nF} \ln \frac{C^R}{C^O} \quad (1.4)$$

In which C^R and C^O represent the concentration of the reduced and oxidised species respectively. At a temperature of 298 K and standard conditions (additionally considering that $\ln(x) = 2.3\log(x)$) equation (1.4) can be further expressed as:^{2, 3}

$$E = E^0 - \frac{0.059}{n} \log \frac{C^R}{C^O} \quad (1.5)$$

It is possible from these Faradaic processes to plot current vs. potential to obtain a voltammogram (mentioned later). Such characteristics of the voltammograms consist of areas of both non-Faradaic and Faradaic processes.⁷

1.1.2 Effect of Mass Transport within Electrochemistry

With reactions taking place over an electrode-solution interface, the mass transport, or the rate of which an analyte moves towards the electrode surface can affect or in some cases overpower the overall rate of reaction.^{3,6} In general there are three scenarios that can affect the mass transport of the analyte, these are:^{2,3,5,8}

- *Convection*: The movement of the analyte towards the electrode *via* forced movement, such as stirring or increased flow to the electrode by rotation or vibration of the electrode. Additionally, the effect of concentration gradients *i.e.* natural convection of the analyte towards the surface of the electrode can also affect the mass transport.
- *Migration*: The movement of charged ions across the solution under the influence of an electric field caused from the potential difference between the electrodes within the solution.
- *Diffusion*: The movement of both charged and un-charged ions due to a concentration gradient within the solution.

These scenarios can be averted, within many electrochemical techniques the main mode of mass transport desired is that of diffusion as this is deemed the most reproducible and reliable rate of electroactive species transfer which is correspondent to the concentration of the analyte within the bulk solution which does not rely upon any mechanical methodologies.⁸ Simply, forced convection can be minimised by not utilising methods that include stirring or rotation of the electrode. The introduction of a supporting electrolyte (which is not electroactive at the potential desired) is the most effective means to minimise the effect of migration, typically concentrations exceed that of 100 times more concentrated than the target analyte. It is also important to note, that such electrolyte can be used to reduce the overall resistance of the solution.^{2,5}

The mass transport within the electrochemical system is measured by the flux (J). The flux is defined as a number of molecules penetrating a specific area of the electrode over an imaginary plane; the units of the flux are $\text{mol s}^{-1} \text{cm}^{-2}$. In entirely diffusional modes of mass transport the flux can be quantified by Fick's 1st Law:²⁻⁴

$$J(x, t) = -D \frac{\partial C(x, t)}{\partial x} \quad (1. 6)$$

where, J is the flux of the species, $\frac{\partial c}{\partial x}$ is the concentration gradient at distance (x) and time (t) and D is the diffusion coefficient; (it is important to note that the larger the molecule the smaller the diffusion coefficient).^{2, 4, 5} Additionally, the negative sign indicates that such concentration gradient is travelling from a high to low concentration gradient.⁴ Upon introduction of time and distance to this concentration relationship can be defined as Fick's 2nd Law:^{2, 4, 5}

$$\frac{\partial C}{\partial t} = D \frac{\partial^2 C}{\partial x^2} \quad (1. 7)$$

As mentioned previously Fick's 1st Law is only valuable when diffusion is the sole mode of mass transport occurring within the bulk solution. For this situation to occur the submission of the other two modes must be accomplished. The relationship between the three modes is described as the Nernst-Planck equation:^{2, 3, 5}

$$J(x, t) = -D \frac{\partial C(x, t)}{\partial x} - \frac{zFD C(x, t)}{RT} \frac{\partial \phi(x, t)}{\partial x} + CV(x, t) \quad (1. 8)$$

where, D is the diffusion coefficient, $\frac{\partial c}{\partial x}$ is the concentration gradient at the distance (x) and time (t), $\frac{\partial \phi(x, t)}{\partial x}$ is the potential gradient, z is the charge of the electroactive species, and $V(x, t)$ is the hydrodynamic velocity in aqueous media. Note that this relationship is for a one dimensional process.^{2, 3, 5}

It is widely reported that the magnitude of current (i) produced from an electroactive species is proportional to the flux (J) *via* this expression:²⁻⁶

$$i = -nFAJ \quad (1. 9)$$

where, n is the number of electrons, F is Faraday's constant, A is the area of the electrode surface. The combination of equations (1.7) and (1.9) creates an expression that is exhibited from the current response to diffusion of the electroactive species.

$$i = -nFAD \frac{\partial C(x, t)}{\partial x} \quad (1. 10)$$

Upon controlling the convection and migration, diffusion will occur, however the transport of these ions must penetrate a layer created by the electrochemical technique

in place. This layer is known as the Nernst Diffusion Layer depicted in Figure 1.2, it is clear from this that outside the diffusion layer, δ , the concentration of the electroactive species is well-controlled and mixed at a constant bulk concentration. As soon as the analyte passes through the diffusion layer, natural convection no longer occurs due to the stagnating electrode surface, thus the only modes of transport occurring within this zone are diffusional, it is important to note that within experiments these layers can sometimes reach values of tens to hundreds of microns. The thickness of the diffusion layer is also dependent on the time taken to scan between the potentials, *i.e.* the scan rate, ν , therefore the diffusion layer in 2-dimensions can easily be calculated *via* these relationships: ⁴

$$\delta = \sqrt{2Dt} \quad (1.11)$$

$$\text{where: } t = \frac{RT}{F\nu} \quad (1.12)$$

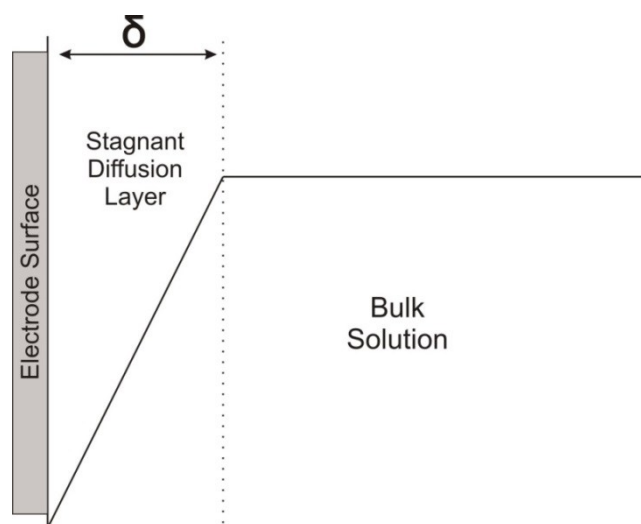


Figure 1.2: Schematic of the Nernst Diffusion Layer

1.1.3 Effect of Electron-Transfer within Electrochemistry

When an electrochemical reaction has sufficient or high values for mass transport, the reaction relies upon the rate at which the electron-transfer occurs between the conduction bands of the oxidised and reduced species; see equation (1.2). The rate of reduction V_{Red} , is given by this relationship, where C^O is the concentration of the analyte at the surface of the electrode: ³

$$V_{Red} = k_{Red}C^O(\mathbf{0}, t) \quad (1.13)$$

The oxidation V_{Ox} , is simply the reverse of the above equation, where C^R is the concentration of the reduced species:

$$V_{Ox} = k_{Ox}C^R(\mathbf{0}, t) \quad (1.14)$$

where k_{Red} and k_{Ox} are the heterogeneous rate constants for the reduction and oxidation half-cells respectively. Such rate constants are dependent on the following simple Butler-Volmer expressions: ³

$$k_{Red} = k^0 \exp\left[\frac{-\alpha nF(E-E^0)}{RT}\right] \quad (1.15)$$

$$k_{Ox} = k^0 \exp\left[\frac{(1-\alpha)nF(E-E^0)}{RT}\right] \quad (1.16)$$

with k^0 representing the standard heterogeneous rate constant (cm s^{-1}) and α is the transfer coefficient. The standard heterogeneous rate constant is an indication of the reaction speed between the electrode material and the analyte of choice; the transfer coefficient relays the symmetry of free energy curve in consideration of the reactants and products. It is important to note, that for symmetrical curves the value of the transfer coefficient is close to 0.5. ³ It is possible upon inspection of equations (1.13) and (1.14) that the overall applied potential of the reaction has an exponential effect upon the electron rate transfer of the reduction and oxidation half-cells. Such conditions of the above equations are when no current is passed through the system, upon the introduction of the flux, j , where $j = k_{red}[C_{Ox}] - k_{ox}[C_{Red}]$, using equations (1.15) and (1.16) the following expression occurs:

$$j = k_{red}^0 \exp\left[\frac{-\alpha nF(E-E^0)}{RT}\right] [C_{Ox}] - k_{ox}^0 \exp\left[\frac{(1-\alpha)nF(E-E^0)}{RT}\right] [C_{Red}] \quad (1.17)$$

1.2 Electrochemical Techniques/Methods

1.2.1 Cyclic Voltammetry

Cyclic voltammetry has become one of the most valuable and widely used techniques within electrochemistry.^{2,3} The main reason behind such dominance is the ability to rapidly understand reactions within the solution, in terms of heterogeneous rate kinetics, coupled chemical reactions and other interesting chemical properties.^{2,3} The process of cyclic voltammetry consists of 'sweeping' the potential at the same rate (*i.e.* scan rate, ν , V s^{-1}) within a triangular waveform shown in Figure 1.3, and measuring the current, i , occurring throughout the experiment. It is important to note that linear sweep voltammetry is the same waveform however the system is not reversed, therefore scanning between E_1 and E_2 . Upon plotting the acquired current against the swept potential, a cyclic voltammogram (CV) is created.^{4,9}

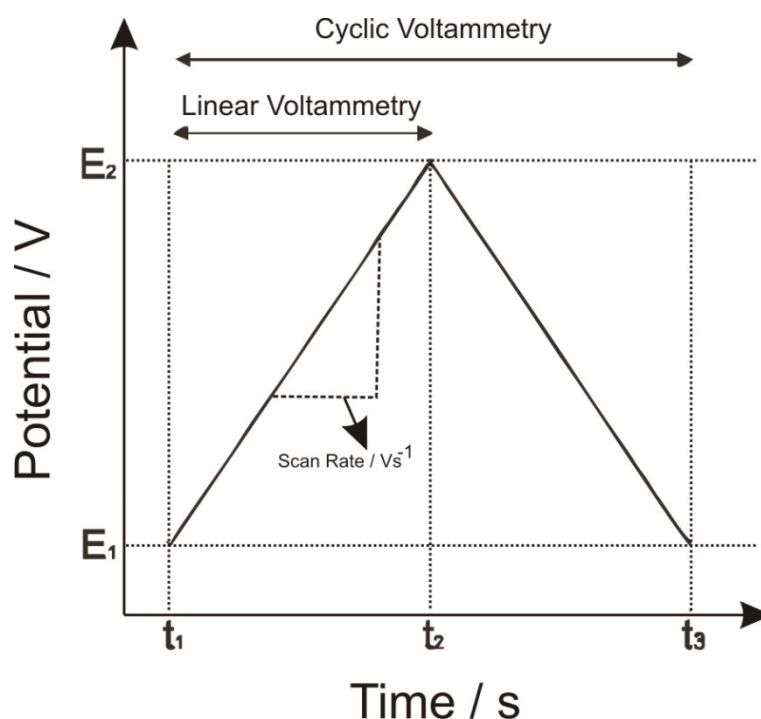


Figure 1.3: The triangular potential waveform used within cyclic voltammetry and linear sweep voltammetry.

A typical CV of 1mM hexaammineruthenium (III) chloride / 0.1 M KCl utilising a graphitic screen-printed electrode (standard-SPE) which possesses an on-board Ag/AgCl

reference and carbon counter is shown in Figure 1.4. As mentioned previously within Chapter 1.1.2, the mode of mass transport is solely that of diffusion due to the suppression of convection and migration, by addition of a supporting electrolyte and minimisation of agitation. Upon inspection of Figure 1.4 it is clear that the potential is started at + 0.2 V, it is important to note that the starting potential has no clear Faradaic process occurring until the potential is swept to - 0.1 V. At this potential a peak occurs as the current increases exponentially until the Ru (III) ions at the surface of the electrode become exhausted, at this moment the current decreases creating a symmetrical peak. Upon sweeping the potential positive (at - 0.7 V), there again is no Faradaic process until the potential reaches - 0.3 V where the Ru (II) at the electrode-solution interface become re-oxidised, creating another symmetrical peak.

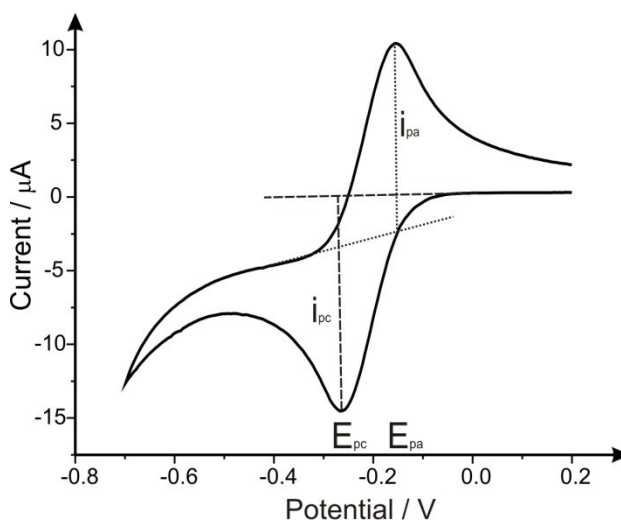


Figure 1.4: A typical cyclic voltammogram within 1 mM hexaammineruthenium (III) chloride/ 0.1 M KCl utilising a standard-SPE. Scan rate: 100 mV s⁻¹. Additionally showing are the peak heights (i_{pa} and i_{pc}) and positions (E_{pa} and E_{pc}) for the (anodic) reduction and (cathodic) oxidation respectively.

It is important to note, that the distance between the two peaks identify if the redox process upon the electrode of choice is reversible, irreversible or quasi-reversible process. Figure 1.5 shows typical CV's of these processes, it is clear that these processes can be analysed qualitatively and quantitatively.

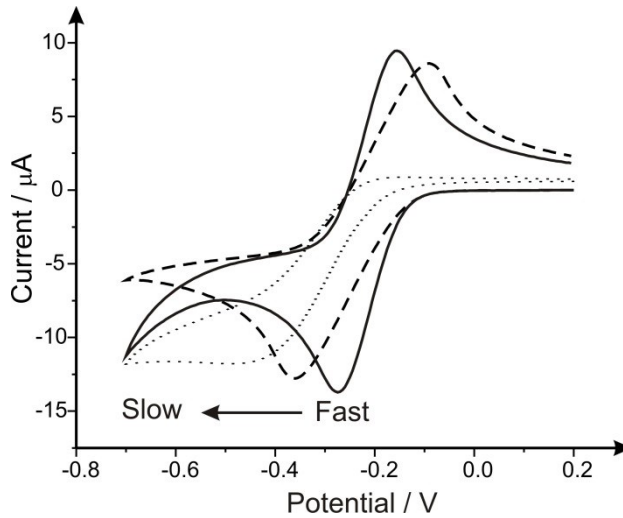


Figure 1.5: Cyclic voltammograms representing a reversible (solid line), quasi-reversible (dashed line) and irreversible (dotted line).

For a reaction that is deemed electrochemically reversible the peak separation (ΔE_p) between the two peak potentials at 298 K is denoted as: ⁷

$$\Delta E_p = E_{pa} - E_{pc} = 0.057/n \quad (1.18)$$

where, n is the number of electrons within the half-reaction. Utilising equation (1.18) the ideal ΔE_p for a reversible electrochemical system must be 57 mV at 298 K, and totally independent of the scan rate. If the ΔE_p is larger than this value but still has two visible peaks for the redox system, this system must be quasi-reversible, and thus controlled by the value of the scan rate. ⁴ The formal potential is related to the peak position and for a reversible system is located in the middle of $E_{pa} - E_{pc}$, and is described as the following:

$$E^0 = \frac{E_{pa} - E_{pc}}{2} \quad (1.19)$$

In the cases where electron-transfer is much slower than that of the mass-transfer process, the peak potential is calculated by the following relationship:

$$E_p = E^0 - \frac{RT}{an'F} \left[0.78 - \ln \frac{k^0}{D^{1/2}} + \ln \left(\frac{an'Fv}{RT} \right)^{1/2} \right] \quad (1.20)$$

where, the E_p is at much higher potential than the E^0 , with the overpotential being related to the k^0 and the α value. The value of E_p becomes larger when the value of αn is decreased causing the CV to become more irreversible.

In addition, the peak position is not the only source of quantitative data expressed within a voltammogram. According to the Randles-Ševčík equation (see below) the peak current can also be obtained and is proportional to the concentration within the bulk solution. For a reversible system the Randles-Ševčík equation is: ^{2, 4, 6}

$$i_p = 0.446FA[C]_{bulk}\sqrt{\frac{FDv}{RT}} \quad (1. 21)$$

which at standard conditions and 298 K leads to:

$$i_p = 2.69 \times 10^5 AD^{1/2}[C]_{bulk}v^{1/2} \quad (1. 22)$$

For a quasi-reversible system the constant is simply replaced with the value of 2.65×10^5 , in the case of an irreversible system the constant also changes however the introduction of the charge transfer coefficient also occurs, which at standard conditions and 298 K leads to:

$$i_p = 2.99 \times 10^5 \sqrt{\alpha} AD^{1/2}[C]_{bulk}v^{1/2} \quad (1. 23)$$

where F is the Faraday constant, n is the number of electrons transferred in the redox process, A is the electrode area (cm^2), D is the diffusion coefficient of the electroactive species ($\text{cm}^2 \text{s}^{-1}$), C is their concentration (mol cm^{-3}) and v is the applied scan rate (V s^{-1}).

In reversible and irreversible situations the electron transfer and mass transport kinetics control the process depending on which is the rate limiting factor. The rate of mass transport is governed by the mass transport coefficient, m_T , which is calculated by: ⁴

$$m_T = \frac{D}{\delta} \quad (1. 24)$$

where, δ is the diffusion layer calculated, *via* equations (1.11) and (1.12). The heterogeneous rate constant, k^0 mentioned previously within Chapter 1.1.3, can be elegantly calculated utilising the cyclic voltammogram. The Nicholson method is an

experimental estimate of the observed, k^0 , for electrochemical redox systems using the following equation: ¹⁰

$$\varphi = k^0 \left[\frac{\pi D n \nu F}{RT} \right]^{-1/2} \quad (1.25)$$

where, ψ , is the kinetic parameter (calculated from the ΔE_p shown in Table 1.1), D is the diffusion coefficient, n is the number of electrons involved in the process, F is the Faraday constant, ν is the applied voltammetric scan rate, R the gas constant and T the temperature.

ψ	$(\Delta E_p)(n) / mV$
20	61
7	63
6	64
5	65
4	66
3	68
2	72
1	84
0.75	92
0.50	105
0.35	121
0.25	141
0.10	212

Table 1.1: Variation of ΔE_p with ψ at 298 K. Reproduced with permission from Ref. ¹⁰.

The kinetic parameter, ψ , is tabulated within Table 1, as a function of peak-to-peak separation (ΔE_p) at a set temperature (298 K) for a one-step, one electron process. The function of $\varphi(\Delta E_p)$, which fits Nicholson's data, is given by: ^{11, 12}

$$\varphi = - \frac{(-0.628 + 0.0021X)}{(1 - 0.017X)} \quad (1.26)$$

where $X = \Delta E_p$ is used to determine φ as a function of ΔE_p from the experimentally obtained voltammetry. From this, a plot of φ against $[\pi D n \nu F / (RT)]^{-1/2}$ can be produced

graphically allowing the k^0 , to be readily determined, however ΔE_p values that exceed 212 mV within the Nicholson table have to rely upon the following equation first introduced Klingler and Kochi: ¹³

$$k^0 = \left[2.18 \left(\frac{D\alpha n F v}{RT} \right)^{1/2} \right] \exp \left[- \left(\frac{\alpha^2 n F}{RT} \right) \Delta E_p \right] \quad (1.27)$$

where, the constants are the same as described in equation (1.27) however, α is assumed to correspond to 0.5.

Upon calculation of the mass transfer coefficient and the standard heterogeneous rate constant, the distinction between a reversible and irreversible process can be illustrated:

$$k^0 \gg m_T \text{ (Reversible process)} \quad (1.28)$$

$$k^0 \ll m_T \text{ (Irreversible process)} \quad (1.29)$$

Such values have limits and therefore the Matsuda and Ayabe parameter, Λ , was introduced within an elegant paper in 1955: ¹⁴

$$\Lambda = \frac{k^0}{\left(\frac{FDv}{RT} \right)^{1/2}} \quad (1.30)$$

Matsuda and Ayabe comment that the ranges between reversible, quasi-reversible and irreversible are presented in Table 1.2:

<i>Classification</i>	<i>Matsuda and Ayabe Ranges</i>
Reversible	$\Lambda \geq 15$ $k^0 \geq 0.3 v^{1/2} \text{ cm s}^{-1}$
Quasi-Reversible	$15 > \Lambda > 10^{-3}$ $0.3 v^{1/2} > k^0 > 2 \times 10^5 v^{1/2} \text{ cm s}^{-1}$
Irreversible	$\Lambda \leq 10^{-3}$ $k^0 \leq 2 \times 10^5 v^{1/2} \text{ cm s}^{-1}$

Table 1.2: A table indicating the Matsuda and Ayabe ranges for reversible, quasi-reversible and irreversible electrode kinetics at 298 K assuming α is 0.5.

1.2.2 Stripping Voltammetry

Stripping voltammetry is one of the most widely used electroanalytical techniques, since it has the potential for low limits of detection of simultaneous metals or other organic substances.^{3,4} There are three types of stripping voltammetry: anodic (ASV), cathodic (CSV) and adsorptive (AdASV). All of these types of stripping voltammetry contain a two-step methodology, the first being a pre-concentration step and the second a 'stripping' step. In the pre-concentration step the movement of the analyte is forced *via* mass transport, therefore appropriate stirring or use of a rotating disk electrode is necessary to improve the mass transport of the analyte. The aim of the pre-concentration step is to 'plate' or deposit the analyte upon the surface of the working electrode, such actions are performed *via* the implementation of a deposition potential (either anodic or cathodic) for a specific time. The stripping step consists of scanning the potential in the opposite direction to that of the pre-concentration step, inducing a Faradaic loss of the analyte upon the surface of the working electrode.⁴ Upon this removal a characteristic peak of the analyte is created, such characteristic peaks are depicted within Figure 1.6 showing a typical response using ASV for the detection of lead (II). These voltammograms exhibit peak current that is proportional to the concentration of the metal ions and therefore allow for utilisation as an analytical technique.

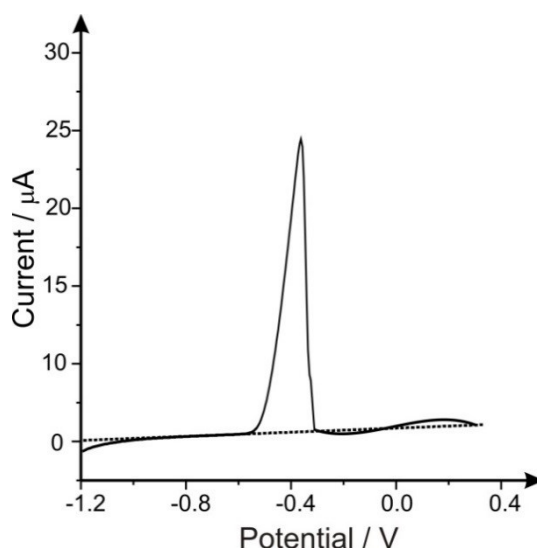


Figure 1.6: A typical anodic stripping voltammogram in the absence (dotted line) and presence of lead (II) (solid line) within 0.1 M acetate buffer solution, utilising a screen-printed electrode. Deposition potential and time: -1.2 V and 120 seconds respectively.

These two steps can be visually represented within the form of chemical equations and are as follows:⁴

Anodic Stripping Voltammetry (ASV)

Pre-concentration Step

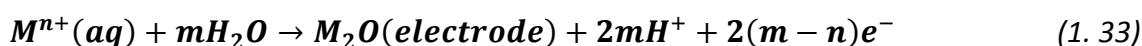


Stripping Step

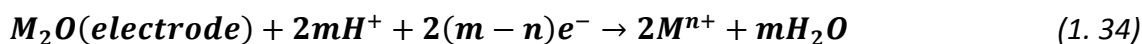


Cathodic Stripping Voltammetry (CSV)

Pre-concentration Step



Stripping Step



Adsorptive Stripping Voltammetry (AdSV)

Pre-concentration Step



Stripping Step



Note: that these equations are a generalisation and that other metals, such as nickel (II) and cobalt (II) have different voltammetric stripping mechanisms, however in this Thesis the consideration of these metals are not relevant and ASV is solely used.

1.2.3 Chronoamperometry

In electroanalytical methodologies where the focus upon the current over a time period is ideal, chronoamperometry is a key experimental technique allowing for the distinction and understanding of the diffusional process occurring at an electrode surface. Such a technique consists of holding the potential at a point where no Faradaic process is occurring, (note that a cyclic voltammogram can identify this) and shifting this to an area where the reaction can proceed spontaneously, all the while measuring the current produced from the electroactive reaction. Depicted in Figure 1.7 A is a typical chronoamperometric waveform, where it is visible that upon sweeping the potential from E_1 to E_2 a change in the peak current can be realised. Additionally shown in Figure 1.7 B, it is clear that upon increasing the concentration of the target analyte the peak current increases. It is also apparent that upon the potential change the current increases dramatically, caused by the creation of a concentration gradient at the electrode surface, in which the flux of the electrochemical species can react rapidly at the surface. Such responses seen in Figure 1.7 B are in agreement with Cottrell equation (1. 37), which relates to the current as a function of time.

$$i(t) = \frac{nFACD^{1/2}}{\pi^{1/2}t^{1/2}} \quad (1. 37)$$

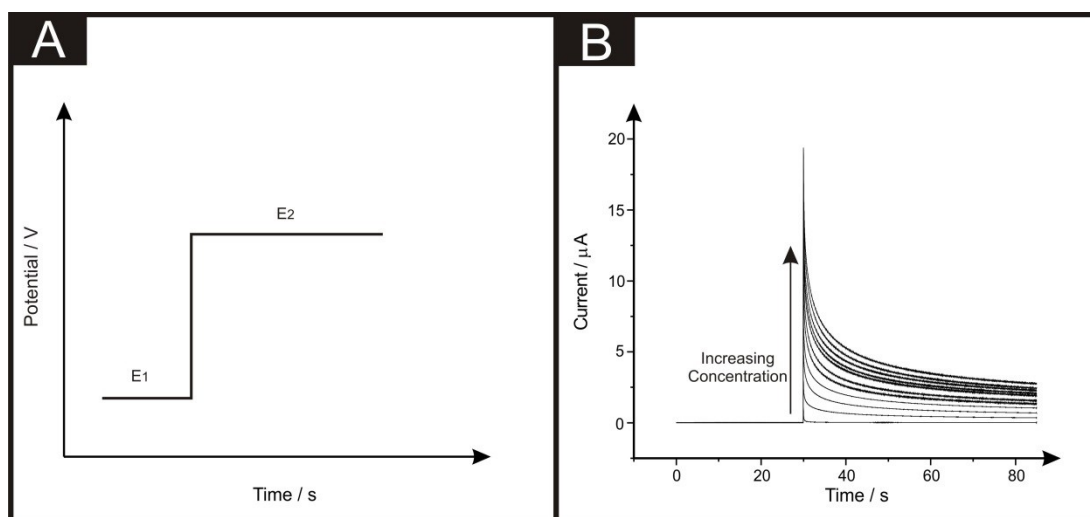


Figure 1.7: A typical chronoamperometric potential waveform (A) and a current-time response for increasing additions of an analyte (B).

1.2.4 Square-Wave Voltammetry

In addition to the previously mentioned electroanalytical tools, square-wave voltammetry is a commonly used technique for the detection of many electroactive analytes, due to its ability to analyse at extremely low limits of detection *i.e.* $1 \times 10^{-8} \text{ mol L}^{-1}$. A square-wave voltammetric profile is created by the sampling of current over forward and reverse pulses, such responses are then plotted over a base staircase potential, with a resultant symmetrical voltammogram being formed, as depicted in Figure 1.8. The creation of these low limits of detection is attributed to the net current of the forward and reverse current being measured, rather than the single current value presented in cyclic voltammetry. Due to this methodological approach, the overall influence of a charging background current can be diminished. Alongside the benefits of a lower limit of detection, the utilisation of an amplitude decreases the overall scan time, to that of a matter of seconds, unlike other voltammetric techniques.^{2, 3, 5}

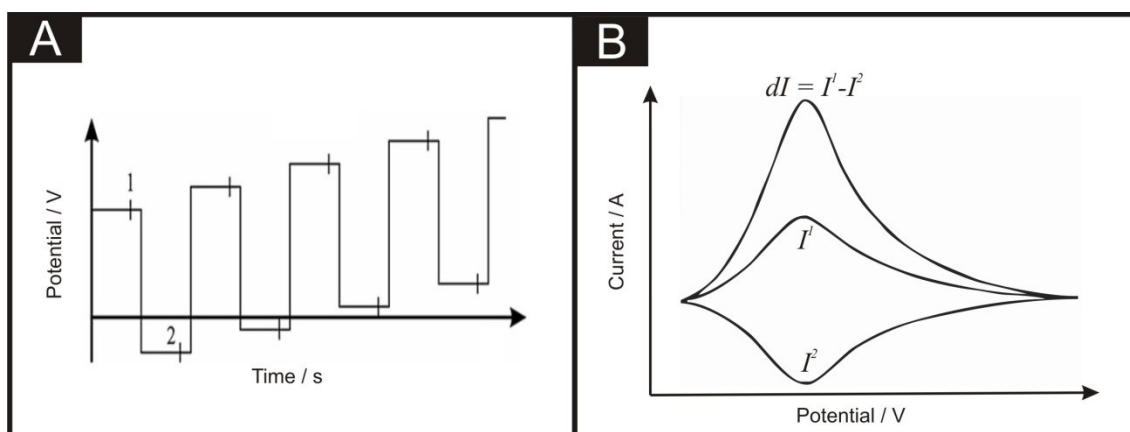


Figure 1.8: Square-wave voltammetric waveform (A) and the resulting voltammetric profile of current versus staircase potential.

1.2.5 Benchmarking Electroanalysis

Throughout this thesis there is a constant theme of screen-printed designs for the application within electroanalysis, therefore consideration of some simple benchmarking techniques must be established. It has been well documented in previous sections of this thesis, the constant relation between the current produced and the concentration of the analyte. The general techniques utilised within this thesis for applications within electroanalysis are potential-controlled techniques, such as cyclic voltammetry, anodic stripping voltammetry and chronoamperometry. In all these cases the peak current caused from the oxidation or reduction of the target analyte, is used as the analytical signal/response, from this concentration controlled peak, a simple plot of the voltammetric peak height as a function of concentration can be constructed. Within the majority of this thesis model electroanalytical systems have been utilised to show proof-of-concept of many electrode configurations using an array of analytes, namely, NADH, citric acid, hydrazine, ascorbic acid, lead (II), cadmium (II), dopamine, capsaicin and benzoquinone. The analytes chosen have been studied and benchmarked against current literature via two methods; these are the analytical linear range and theoretical limit of detection (LOD). The analytical linear range is simply the range of concentrations used throughout the study; the linearity of curve of peak height vs. concentration range is measured through regression of the data points. This value of regression, R^2 is calculated and for totally linear and non-linear curves values of 1 and 0 respectively. However, it is commonly acceptable within analytical techniques for the R^2 value to range between 0.96 and 0.99. Additionally, benchmarking through analysis of the theoretical limit of detection is another simple method for analytical techniques. It is important to note, that this value is solely theoretical and in some cases it would be extremely hard to reach utilising electrochemical setups due to possible limitations of the methodology *i.e.* noise at low signals. Nevertheless, it is a useful tool for analysing the calibration curve. A commonly utilised approach for the calculation of the LOD is *via* a combination of methods described by both the International Union of Pure and Applied Chemistry (IUPAC) and the American Chemical Society (ACS), which utilise the mean signal of the blank, defined as:

$$LOD = \frac{\overline{y_D} - \overline{y_B}}{q_1} = K_{D^{sb}}/q_1 \quad (1.38)$$

where, $\overline{y_D}$ is the signal value and $\overline{y_B}$ is the mean blank signal, K_D is the numerical factor chosen according to the confidence (statistical) level desired. It is commonly acknowledged that the value for K_D , within an array of academic journals, is referred to as 3 and further denoted throughout as the 3-sigma method.¹⁵ Upon creation of a calibration plot that has been repeated and is statistically viable, a LOD value can be calculated *via* the following expression:

$$LOD = 3Sb/m \quad (1.39)$$

where, Sb is the standard deviation of the blank and m is the gradient of the calibration curve. As the creation of the LOD is solely dependent upon on the quality of the calibration curve, therefore if a high quality calibration curve is presented, then the Sb will be low thus creating an improved LOD for the target analyte.

1.2.6 Selection of redox probes

In order to run the cyclic voltammetric experiment described in Section 1.2.1, one needs to select an appropriate electroactive analyte. Typically these probes are classified into inner- and outer- sphere redox probes. There are a whole range of redox probes that exist and that can be utilised and have been studied on highly ordered pyrolytic graphite and glassy carbon electrodes: ¹⁶ IrCl₆, Ru(NH₃)₆, Co(phen)₃, MV, Fe(phen)₃, Fe(CN)₆, Co(en)₃, Ru(en)₃, Fc(COOH)₂, Ru(bpy)₃, Ru(NH₃)₅py, Co(sep), Ru(CN)₆, Mo(CN)₈, W(CN)₈, Fe_(aq), Eu_(aq) and V_(aq).

Outer-sphere redox probes are termed *surface insensitive* such that k^o is not influenced by the surface oxygen-carbon ratio, surface state/cleanliness in terms of a surface coating of a monolayer film of uncharged adsorbates, or specific adsorption to surface groups/sites. There is no chemical interaction or catalytic mechanism involving interaction (*i.e.* an adsorption step) with the surface or a surface group in this case the electrode merely serves as a source (or sink) of electrons and as such outer-sphere systems are sensitive primarily to the electronic structure due to the density of electronic states near the Fermi level.

On the other hand, inner-sphere redox mediators are termed *surface sensitive* in that the k^o is strongly influenced by the state of the electrode surface (surface chemistry and microstructure) *via* specific electro-catalytic interactions that are inhibited significantly if the surface is obscured by adsorbates (or impurities). Such interactions can also depend strongly on the presence (or absence) of specific oxygenated species which give rise to either beneficial or detrimental electrochemical effects.^{17, 18} In this case systems are more largely affected by surface state/structure and/or require a specific surface interaction, being catalysed (or inhibited) by specific interactions with surface functional groups (adsorption sites) rather than the DOS as such systems generally have high reorganisation energies.^{17, 18}

The observation of differing responses when using varied inner- and outer-sphere redox probes allows insights to be deduced regarding the state of the surface structure of the electrode material in question. McCreery^{17, 18} has provided a “road map” for commonly utilised redox probes, as shown in Figure 1.9, which allows

researchers to clarify from experimental observations the redox systems and how they are affected.

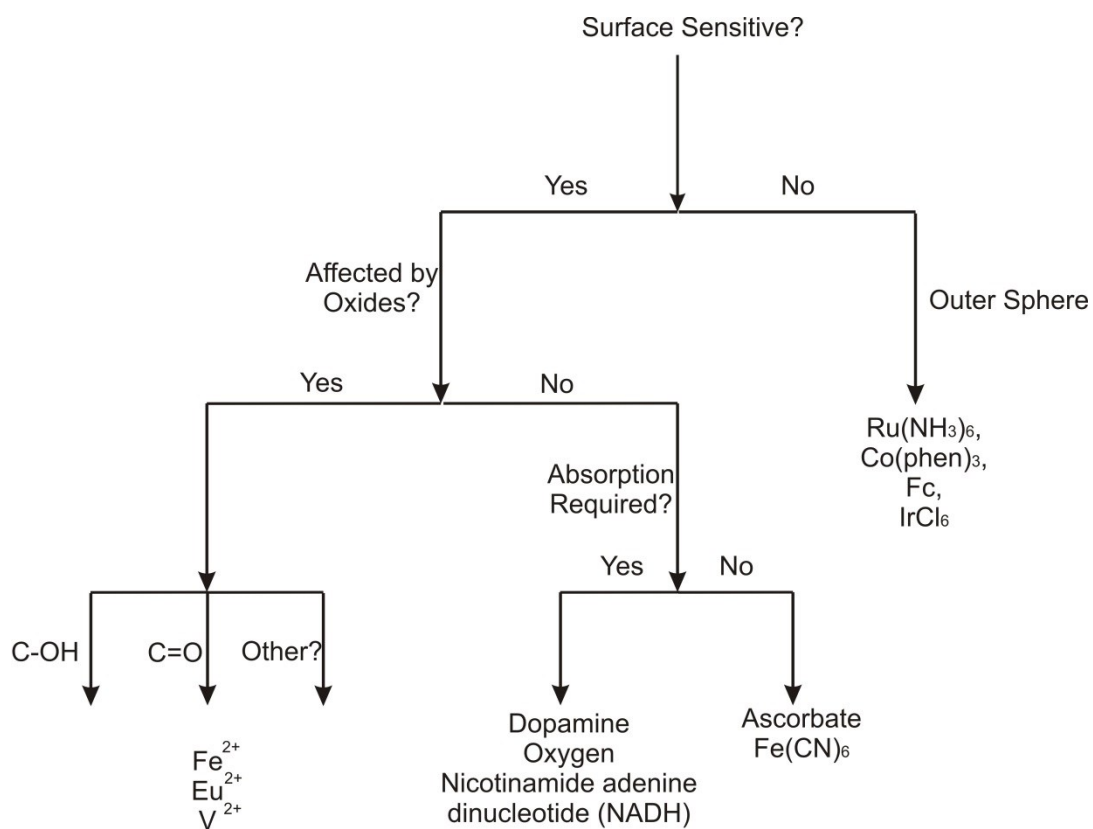


Figure 1.9: Classification of redox systems according to their kinetic sensitivity to particular surface modifications on carbon electrodes. Adapted from Ref¹⁶.

1.2.7 Changing the electrode geometry: macro to micro

As mentioned in Chapter 1, macro- and micro- electrodes can be fabricated *via* screen-printing. At a macroelectrode, electrolysis of the analyte occurs across the entire electrode surface such that the diffusion of the analyte to the electrode or from the electrode surface is termed planar, and the current response is typically described as 'diffusion limited', giving rise to an asymmetric peak as shown in Figure 1.10 A. At the edge of the macroelectrode, where the electrode substrate meets the insulating material defining the electrode area, diffusion to or from the edge of the electrode is effectively to a point. Therefore, the flux, j , and the rate of mass transport are larger at the edge and as such diffusion becomes convergent. This is termed an 'edge effect' which is negligible at a macroelectrode since the contribution of convergent diffusion to the edges of the macroelectrode is inundated by that of planar diffusion to the entire electrode area.

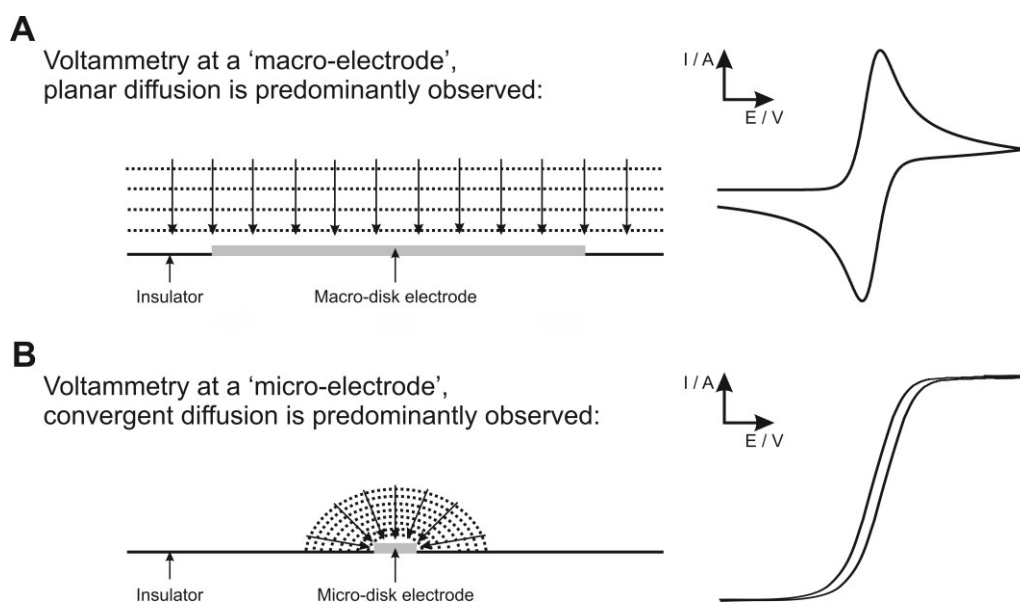


Figure 1.10: The unique differences between the cyclic voltammetric signatures observed at a macroelectrode (A) compared to a microelectrode (B).

As the electrode size is reduced from macro to micro, or even smaller to that of nano, convergent diffusion to the edges of the electrode becomes significant. In this regime a change in the observed voltammetric profile is observed which results in the loss of the peak shaped response, as evident in Figure 1.10 B with that of a sigmoidal voltammogram. The effect of convergent diffusion has the benefit of improvements in

mass transport such that the current density is greater than at a macroelectrode under planar diffusion.

1.3 Common Electrode Materials

Within electrochemical setups the material of the working electrode can improve or impede the desired electrochemical characteristics, since the reaction process occurring within the system take place upon it.⁶ The most common electrodes are highly conductive metals such as gold and platinum, however due to the extreme costs of these materials; low budget research cannot be achieved. In recent decades the utilisation of carbon materials has become a rapidly advancing area of research, due to its availability at a relatively low cost. In general, carbon electrodes are made from a variety of materials such as glassy carbon (GCE), carbon fibres, highly ordered pyrolytic graphite (HOPG), single and multi-walled carbon nanotubes (SWCNTs and MWCNTs respectively) and boron-doped diamonds (BDDE) to name a few.¹⁹ These carbon based electrode systems are not only cost effective, but their utilisation within electroanalysis offers a large potential window, low background current and rich surface chemistry. Nonetheless these benefits do not offer the “fast” electron transfer rates compared to the metallic options; this is due to the species orientation upon the carbon surface. It is important to note, that such carbon electrodes all consist of the same basic sp^2 hybridised six-membered aromatic ring, however each electrode material has a different ratio of edge and basal plane sites, with the edge sites offering a faster electron transfer to that of the basal plane.¹⁹

1.3.1 Carbon Materials

As mentioned previously carbon based materials are one of the most utilised materials within electroanalytical studies. The carbon atom can form an array of allotropes since its electron configuration has a small energy difference between the s-orbital and p-orbitals. Among the many carbon allotropes the crystalline structures of graphite and diamond are common electrode materials.

The graphite structure possesses a hexagonal structure with the carbon atoms in sp^2 hybridised trigonal structure. Graphite is a 'stack' of graphene layers, held together by relatively weak Van der Waals forces. However unlike the graphite structure, diamond allotropes have the atoms arranged within a tetrahedral configuration possessing of a sp^3 hybridised covalent bonded structure. Shown within Figure 1.10 are the visual differences between the bonded structures of graphite and diamond.

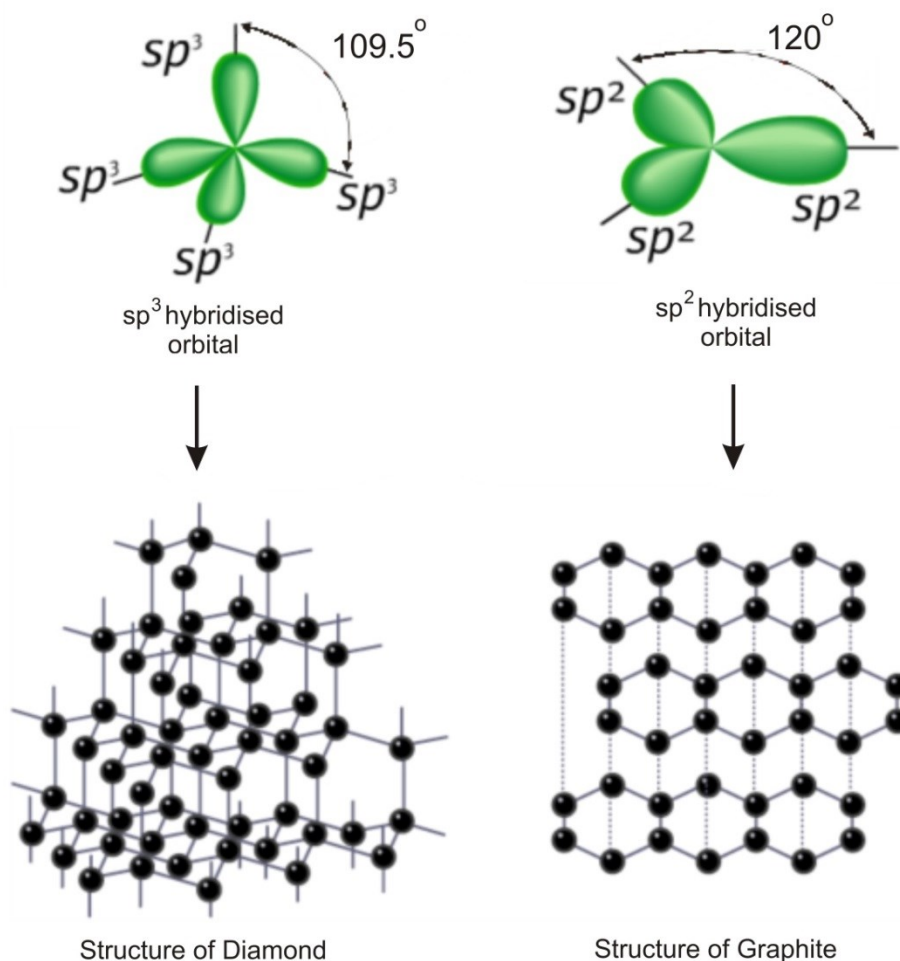


Figure 1.11: Graphite and diamond structures derived from their respective hybridised orbitals of the carbon atoms.

One of the most common graphitic materials within electrochemical research is highly ordered pyrolytic graphite (HOPG). The surface of the HOPG consists of conductive islands of both basal-plane and edge-plane sites. These areas within the graphite structure allow for creation of solely basal (BPPG) and edge plane electrodes (EPPG), offering “slow” and “fast” electron transfer kinetics respectively. A full schematic of the edge and basal plane sites is visualised within Figure 1.11.

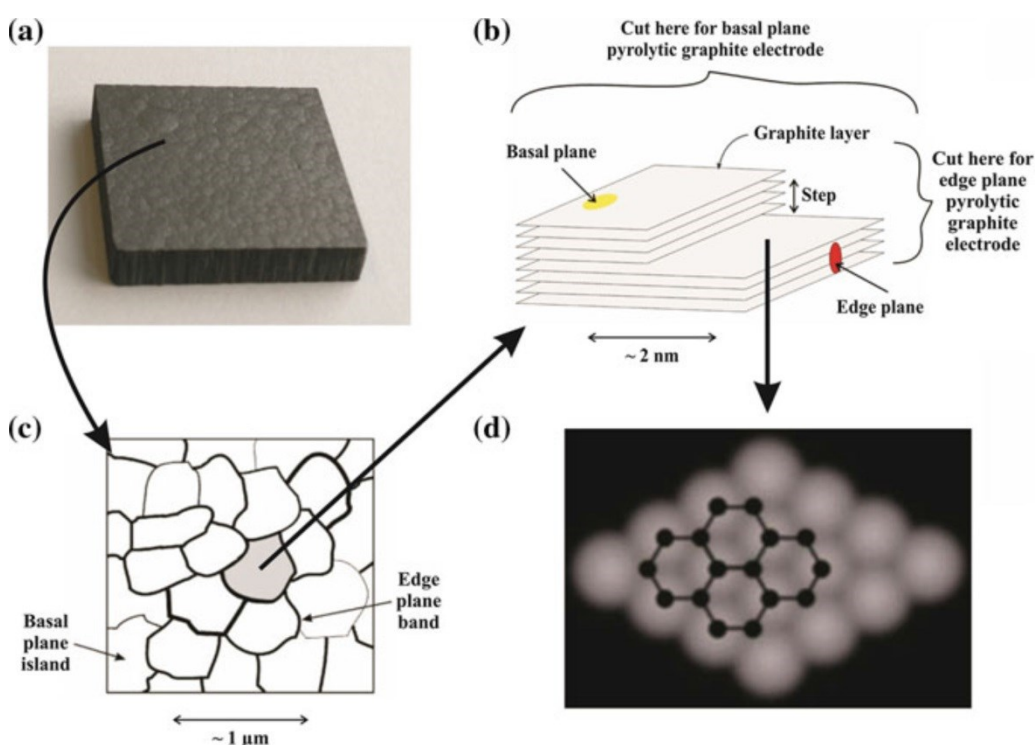


Figure 1.12: a) Image of a commercially available slab of HOPG. b) Schematic of a side-view of a HOPG surface, highlighting its basal plane and edge plane like-sites/defects. c) A representation of a HOPG surface showing the discrete basal plane and edge plane islands. d) A typical STM image of a HOPG surface with the corresponding fragment of the graphene structure superimposed. Reproduced with permission from Ref¹⁵.

Along with the graphite based electrodes, diamond electrodes are commonly used throughout electrochemical setups. It is widely reported and understood that diamond is an impressive insulator, thus utilisation as an electrode is not ideal. However ‘doping’ of the diamond with an electron accepting element such as boron (with doping ranges of the diamond electrode from 10^{19} to 10^{21} atoms/cm³) increases the conductivity and therefore creates an electrode material with a very wide potential range (~ -1.35 to $+2.3$ V vs. a normal hydrogen electrode), low background currents and stable within aggressive organic electrolytes. The popularity of boron doped diamond

electrodes (BDDE) is due to its ability to prevent adsorption upon the reaction of the medium, allowing the reaction of new analyte upon a 'new' potential scan. In addition, as the electrode is based upon a diamond structure, this electrode material is extremely robust and can offer a long electrochemical lifecycle (*if the appropriate cleaning methods are carried out*).

Similarly to the graphitic and diamond surfaces, glassy carbon (GCE) or vitreous carbon electrodes are utilised due their similar heterogeneous rate kinetics to that of EPPG. The manufacture of such electrodes occurs *via* the slow carbonisation of a pre-modelled polymeric resin *e.g* phenol-formaldehyde or polyacrylonitrile, at a temperature of 300-1200°C, removing any oxygen, nitrogen and hydrogen at the resin surface. Unlike that of the graphitic/diamond materials, the GCE has intertwined ribbons of cross-linked graphitic like sheets. It is essential to note, that the GCE is completely pore-less and is not permeable to liquids and gases, allowing the surface to be free from defects and contaminants.

With each of these electrode materials offerings its own kinetics, polishing and general treatment of these electrodes is varied throughout the literature, as such each BDDE, GCE or EPPG can present a different electrochemical response to its other counterparts. It is with this, that this thesis utilises screen-printed platforms which regularly exhibit electrode rate kinetics within the same region of magnitude, providing one shot reproducible electrochemical platforms.

Chapter 2 - *Introduction and Current Applications of Screen-Printed Electrochemical Architectures*

This Chapter will discuss the many electrochemical applications of the screen-printed electrode systems, and analysis the selection of equipment for the fabrication of these novel sensors. This Chapter has contributed to the publication of a Springer Brief on 'Screen-Printing Electrochemical Architectures'. †¹

2.1 History of Screen-Printed Electrodes

Within early electrochemical experiments the utilisation of solid noble metallic electrodes was a necessity, however as electrochemistry comes to the forefront of technology, there has been a greater need for a cheaper alternatives. Carbon based materials have been commonly used as alternative electrode, with the introduction of cheap and affordable approaches such as carbon paste electrodes, which reduce cost significantly but can lack reproducibility.²⁰ Since the early 1990s the fabrication of electrode circuits *via* different printing approaches such as pad-printing, roll-to-roll and screen-printing have been utilised for the use within electrochemistry.^{21,22} Each of these printing methods offers inherent advantages and disadvantages. For example, pad-printing offers a thin-film transfer that can be used in an electrochemical setup; however this process is not ideal for mass production of electrode systems and therefore has been regularly deemed a pre-requisite to the screen-printing technology. The screen-printing process has the ability for the mass production of highly reproducible electrode setups.²³ It is with consideration of this that screen-printed electrodes have revolutionised the field due to their capability to bridge the gap between laboratory experiments with in-field implementation.^{24,25} This is of course compounded by the billion dollar (per annum) glucose sensing market which has benefited from the incorporation of screen-printed electrodes since it now allows individuals to be able to measure their blood glucose levels at home, where an electrochemical result is instantly realised; without recourse to visit a hospital / clinic.^{26,27} This technological approach

¹ C.W.Foster *et al*, Screen-Printed Electrochemical Architectures, Springer, 2015

permits the mass production of highly reproducible electrode configurations and due to its scales of economy.^{27, 28} Such electrode designs offer improvements in sensitivity, signal-to-noise ratios and reduced sample volumes, producing potential replacements for conventional (solid and re-usable) electrode substrates. Further to this, the ease of the mass production of screen-printed sensors enables their use as one-shot sensors, allowing possible contamination to be avoided, and alleviate the need for electrode pre-treatment as is the case for solid electrodes prior to their use.^{24, 29, 30}

Along with the commercially available electrochemical glucose biosensor, these screen-printed electrodes have been regularly utilised for other bio-sensing applications such as the determination of codeine and diazepam within urine samples and beverages respectively,^{31, 32} lactate sensing and cholesterol to name a few.^{33, 34} Additionally DNA sensing using screen-printed electrode systems has become a large focus over the recent decade with much research focusing upon the quantification of mutagenic DNA bases.^{23, 35, 36} Since the developed sensors are low cost, mass produced, and disposable this allows for the rapid non-intrusive detection of radiation damaged DNA.³⁵ Other interesting biological applications include the determination of cancer biomarkers, with focus upon an array of proteins released pre-tumour within the body.³⁷ Figure 2.1 shows a typical drop-cast method for the fabrication of a screen-printed system. In this situation, a range of useful materials can be immobilised upon screen-printed electrodes, *i.e.* biological elements (such as horseradish peroxidase and graphene oxide *etc.*) are incorporated within the chosen modifier.³⁸

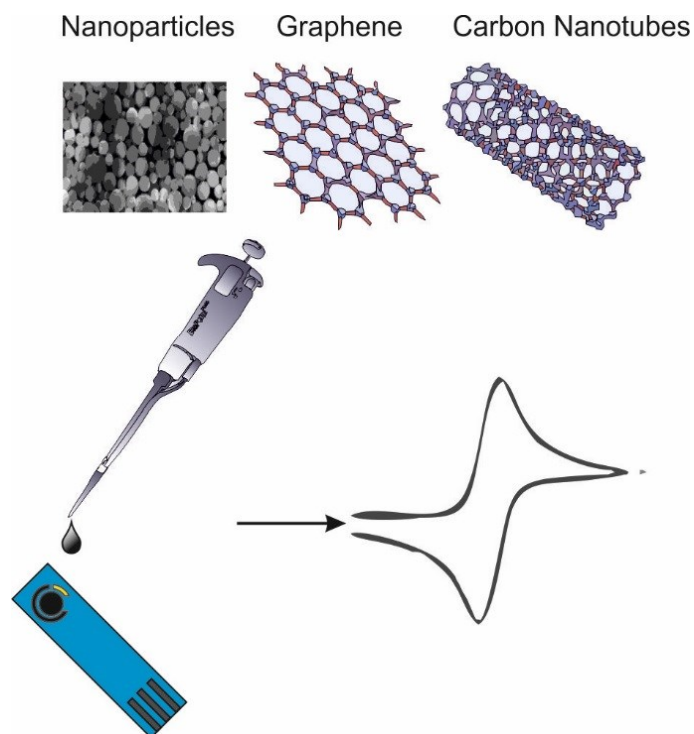


Figure 2.1: Example of a typical drop-cast fabrication upon screen-printed systems and the corresponding electrochemical measurement of a target analyte. Reproduced from Ref³⁸.

It is noted that this method of fabrication is the most common and simplistic technique for the modification of a screen-printed electrode surface. However, this approach can potentially offer a low reproducibility and often the films created are not films, and are in fact macrostructures.³⁹ Utilising the printing technology, the production of reproducible and consistent chemical signatures are acquired. The ability to create a printing medium containing such electrode modifiers gives the user the freedom to produce an even coverage upon the surface.^{29, 40-42} Shown in Figure 2.2 is a typical screen-printed sensor with a printed multi-walled nanotube layer, as the modification is controlled by the parameters dictated within the printing process the creation of a reproducible response for the detection of dopamine is presented.^{36, 43}

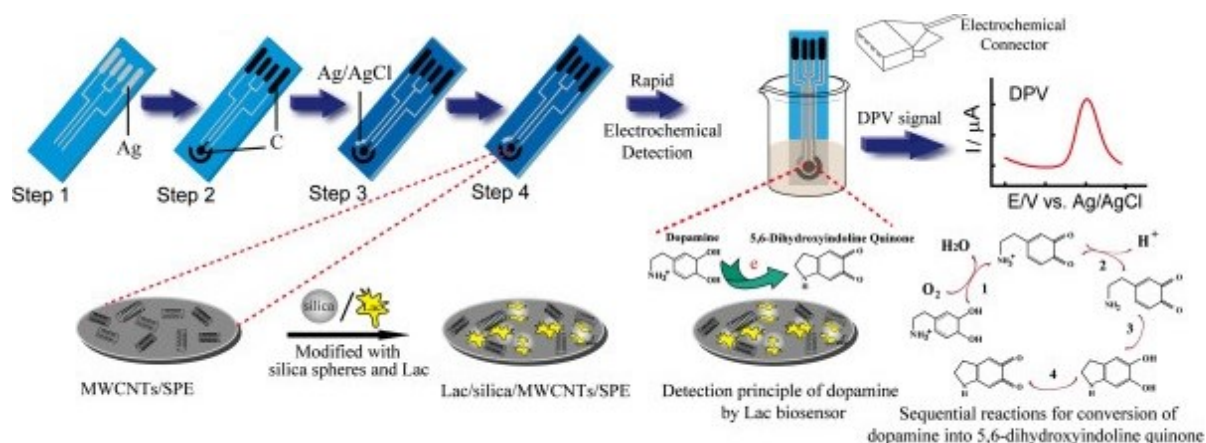


Figure 2.2: Schematic illustration of the screen-printed configuration, the procedures used in the process of MWCNTs-doped SPE fabrication. Reproduced from Ref³⁹.

Not only can these systems be applied to biological systems but the incorporation as analytical sensors for an array of electrochemically active toxins, additives and drugs to name a few, has been explored. It is common that these screen-printed electrodes do not have the same limit of detection as other extremely expensive equipment; however the possibility for the creation of point-of-care sensors is an exciting and rapidly evolving area of research.⁴⁴⁻⁴⁶ For example, regular detection of ‘legal-highs’ has been continuously successful as the electroactive compounds give intense and quantitative signals, for a potential light-weight handheld sensor.⁴⁷ Furthermore, these sensors have also been applied within electrophoretic miniaturised devices due to their benefits such as significant improvement in analysis times, lower consumption of reagents and samples, flexibility, and procedural simplicity.⁴⁸

In addition, these screen-printed systems can be regularly applied as potential solar cells (Figure 2.3 A), with the incorporation of photocatalytic surface groups, in the form of nanoparticles. It is clear within the literature, that screen-printing can directly print onto these substrates easily and can create an even surface coverage.⁴⁹⁻⁵¹ Remaining within the area of the renewable energy, focus upon the utilisation of screen-printed electrodes within a potential fuel cell (Figure 2.3 B) has also been studied by simply screen-printing a minimal amount of the cathode and anode material, potentially reducing the overall fabrication and servicing costs of the *future* fuel cell technology.^{52,}

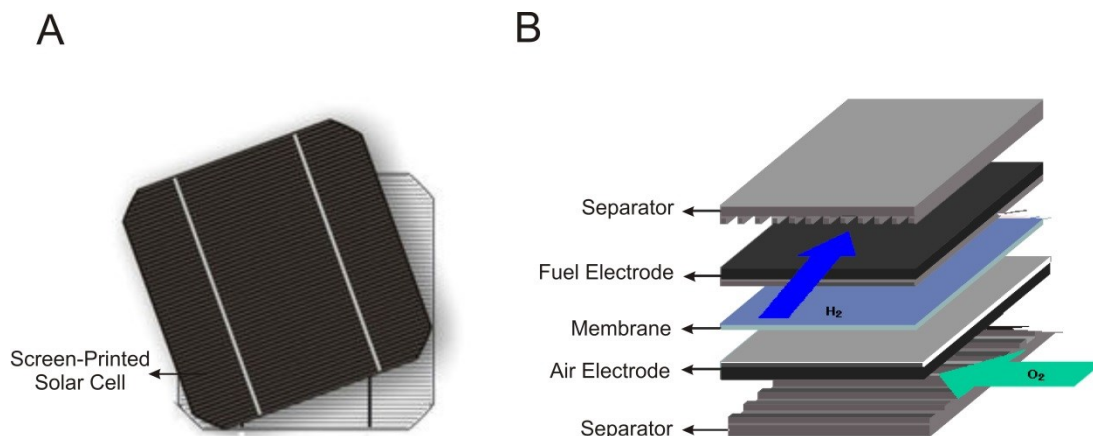


Figure 2.3: Optical image (A) and schematic diagram (B) of a screen-printed solar cell and fuel cell respectively. Adapted from Ref ^{54, 55}.

Along with the need for the creation of energy, the storage of the proposed energy must be upheld and improved for the continuation of technological advancement. In this situation, these novel and exciting electrode systems have also been applied towards the exciting capacitive capabilities of the conductive inks. ^{56, 57} Hallam *et al.* ⁵⁸ utilised screen-printing as a new methodology to fabricate flexible and reproducible supercapacitors *via* the elimination of the interface between the charge collectors and working electrodes, ultimately lead to a higher power density obtained at the printed systems.

With such an array of applications, the literature is compounded with new additions of research utilising screen-printed electrodes, for more information the author directs the reader to some key literature reviews. ^{24, 59, 60}

2.1.1 Screen-Printed Design

Additionally, from the tailoring of the working electrode material through the use of screen-printing techniques, the electrode geometry is also readily manipulated through the incorporation of screen-printing technologies for the fabrication of electrochemical sensing platforms. When designing such electrodes it is convenient to have electrodes which do not require a large sample size, therefore in general the required three-electrodes are fabricated as close as possible and also reduce resistance which can potentially distort the measured voltammetry; the most common electrode configuration is the 3 mm working electrode with on-board reference and counter (see Figure 1.1)

In addition, to macroelectrode architectures, microelectrodes can be designed and fabricated to mimic that of true microelectrode behaviour (*i.e.* near elimination of contributions from planar diffusion rather than solely radial/ convergent diffusion) and further enhancements in the electroanalytical sensing performances. The conversion from macro to microelectrode systems within electrochemical applications, possess some significant advantages, such as: smaller diffusion layer, greater mass transport, lower transient current and are more resistive to the effect of an ohmic drop. These systems also have benefits within the fabrication method, due to the minimal ink utilised within the screen-print.

A variant on the traditional co-planar disc-shaped microelectrode which continues to gather further interest within current literature is the microband electrode. Band electrodes are fabricated to be macroscopic in-length but microscopic in width. These electrode configurations have been reported to offer the additional advantage of allowing larger currents to be obtained compared to a microdisc due to the increased electrode area, whilst the width of the band is still maintained in the micrometre range to ensure that convergent diffusion is still dominant. Generally, these have been fabricated *via* the screen-print method however utilisation of gold and platinum inks are favourable and tend to be printed upon a ceramic substrate, which can offer a lower user ability and applicability within-the-field. Upon this printed electrode, a Pyrex glass slide is attached to reveal a thin microband system.^{61, 62} In adaptation to this, Craston *et al.*⁶³ reported the use of a screen-printed conductive ink (Au/Pt) with an additional

polymer layer upon a ceramic layer, this is then etched in a perpendicular direction of the print, (shown in Figure 2.4) creating a microband-*like* electrode system. Recently, an adapted approach within electroanalytical applications has been carried out by Hart and Zen independently ^{64, 65} where ultramicrobands are fabricated in the aforementioned manner and were targeted towards the sensing of lead in acetate leachates ⁶⁵ and the determination of reduced glutathione. ⁶⁶ However, the reproducibility of the electrodes fabricated in this manner is questionable, due to additional splicing step. ⁶⁷

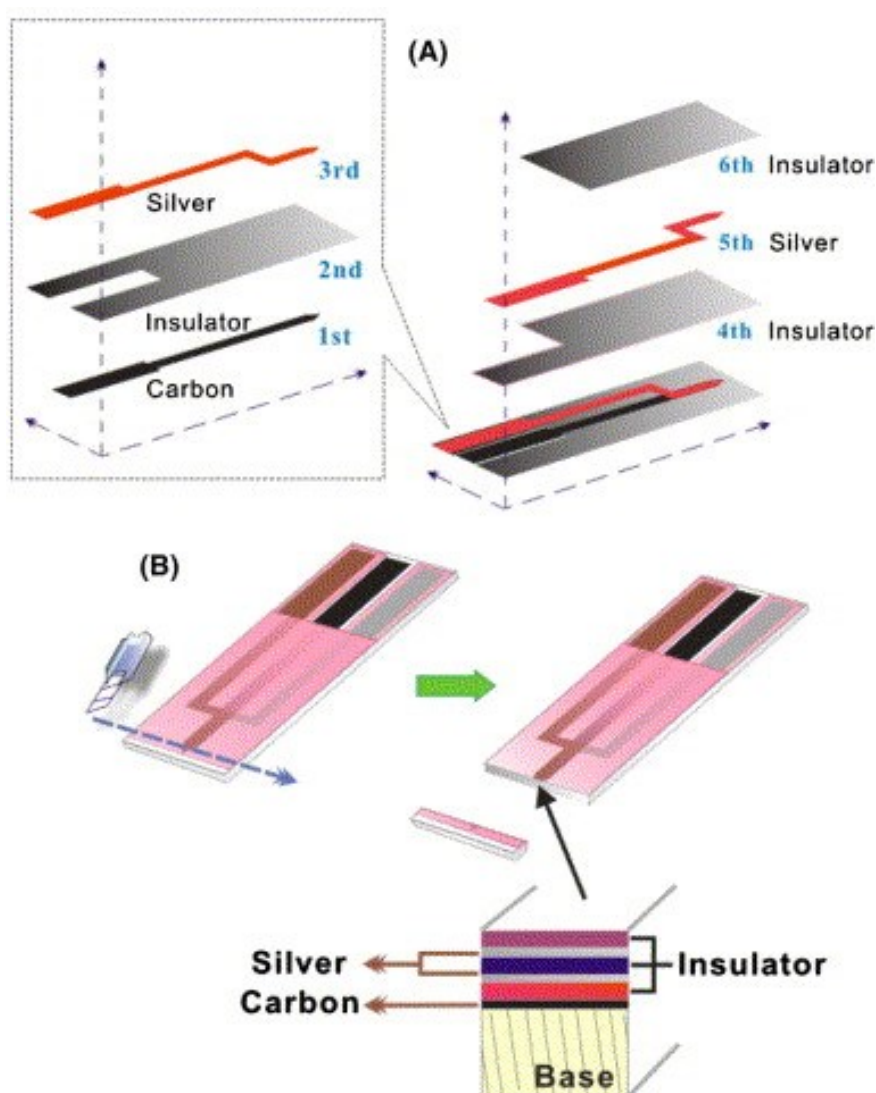


Figure 2.4: (A) A schematic of a layer-by-layer structure of the screen-printed ultramicroelectrode assembly. (B) Cross-sectional diagram the electrode system with a built-in three-electrode configuration. Reproduced with permission from Ref ⁶⁸

Nonetheless, upon utilisation of the appropriate printing parameters this can be completed reproducibly and accurately. Metters *et al.*⁶⁷ reported the use of a V-Mesh (Vecry Mesh) (explained further within section 2.3) for a defined and reproducible screen-printed 50 μM band electrode (shown in Figure 2.5), such an electrode was employed as an electroanalytical sensor towards NADH and chromium (VI).⁶⁷

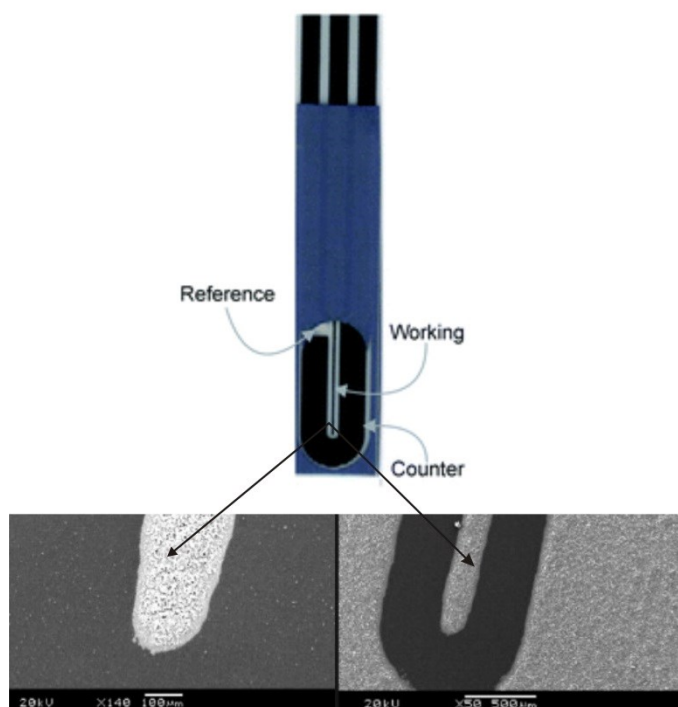


Figure 2.5: Optical and SEM imaging of a 2 cm (length) x 100 μM (width) screen-printed band electrode.

In consideration of the above mentioned limitations of macroelectrodes, the creation of screen-printed array electrodes can be realised for the potential multiple detection of intriguing analytes. Over recent decades these microelectrode arrays can significantly increase the sensitivity of electroanalytical methodologies, due to the increase number of microelectrode disks present within the design.⁶⁹ Rusling *et al.*⁷⁰ have created an immunoassay that can detect a range of cancer biomarker proteins upon a simple microarray electrode design. Shown in Figure 2.6, is an example of a screen-printed electrode microelectrode array and how Rusling *et al.* have modified them with antibodies, which can potentially bind to the cancer biomarker proteins.⁷⁰⁻⁷²

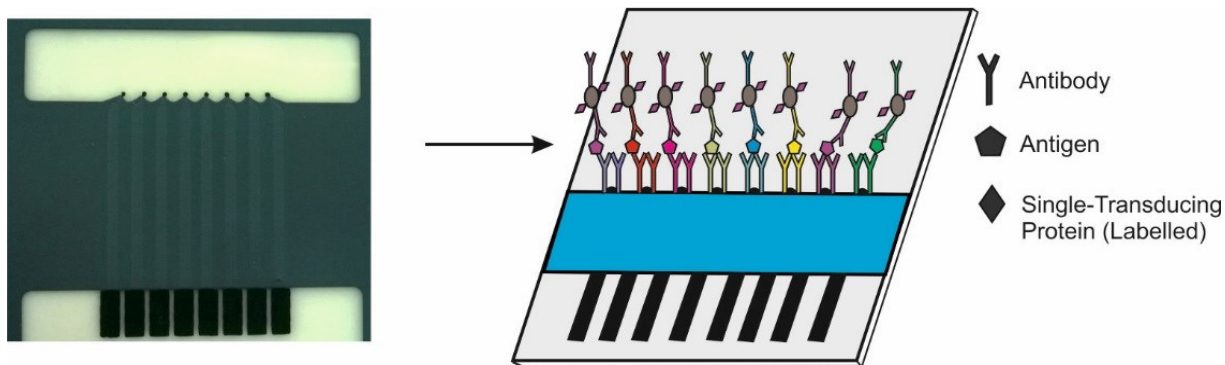


Figure 2.6: Optical image of a microarray screen-printed electrode and schematic of an immunoassay created upon this system.

These arrays allow for the multiple detection of analytes; however, utilisation of recessed arrays can also be accomplished *via* the screen-printing process. Recessed microelectrodes and arrays can be fabricated *via* screen-printing a thicker dielectric layer around the microelectrode, allowing for an extended distance between each electrode and thus create more diffusional independent voltammetric responses (*i.e.* sigmoidal responses), creating advantages such as greater sensitivity, increased current density and improved signal-to-noise ratio.⁷³

2.1.2 Printing Media

The utilisation of a printing medium (*i.e. ink or paste*) within the screen-printing process is vital for the transfer of the printed design, typically these inks or pastes are fabricated using conductive particles within a solvent/binder mixture to allow the transfer of the particulate matter onto the substrate. Such inks can be made readily available and are extremely beneficial to the user as they possess the ability to be manipulated to provide different working electrode compositions.

Wang *et al.*⁷⁴ indicates that the choice of carbon ink should rely upon the application at hand, due to the differences within the electrochemical signals seen with a range of inks.⁷⁴ Such other examples of printable inks, include the fabrication of platinum⁷⁵ and gold⁷⁶ screen-printed sensors which have been applied towards the electroanalytical sensing of chromium species (VI and II) in the case of the gold sensor, and both hydrazine and hydrogen peroxide for the case of the platinum sensor.^{75, 76} Crucially, it was determined that the requirement for electrode potential cycling prior to utilisation (as is the case for bulk noble metal macro electrodes in order to form an oxide upon the electrode surface) was alleviated in the case of the screen-printed sensors owing to the noble metal utilised within the screen-printing process being in the form of an oxide.^{35, 36} Clearly, the removal of such a preparatory step offers significant benefits when considering the development of sensors intended for use outside of the laboratory environment where rapid and facile analysis is imperative (one-step analysis). However, as mentioned previously the metallic options can be costly and the need for carbon based materials has become necessary. In response to this, the utilisation of graphitic based inks for an assortment of applications has been realised. Not only do these inks replicate the electrochemistry of typically used electrodes such as glassy carbon (GCE) and edge plane pyrolytic graphite (EPPG) but they are manufactured at a fraction of the cost. In addition, an array of raw carbon materials can be used, such as carbon-nanotubes,⁴⁰ graphene,²⁹ mediated carbon structures⁷⁷ and nanoparticles⁷⁸ to name a few.

Having the ability to alter the electron transfer capabilities at an electrode surface has a beneficial effect upon the analytical applications. Shown within Figure 2.7, are comparison of the voltammetric behaviour of unmodified screen-printed electrodes

with that of polymeric modified screen-printed electrode; upon the metallic plating of these systems the electrochemistry will be dominated by the metallic properties rather than the underlying electrode.

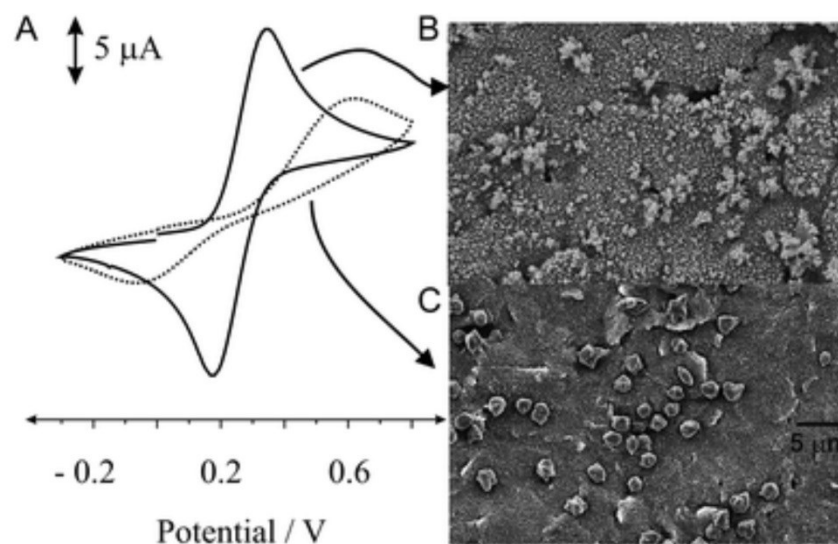


Figure 2.7: Cyclic voltammetric profiles (A) obtained in 1 mM potassium ferrocyanide / 1 M KCl using a copper plated standard SPE (solid line) with that of a bespoke electrochemical platform (dashed line). Scans recorded at 100 mV s^{-1} vs. SCE. SEM images of the copper plated standard (B) and bespoke (C) screen-printed electrochemical platforms. Reproduced from ref⁷⁹ with permission from Elsevier.

Choudhry *et al.*⁷⁹ have shown beneficial electrolytic modification of various electro-catalytic metals where the bespoke modified electrode surface performs as a micron-sized template.⁷⁹ When the metallic ensemble is used over that of an electrolytically modified macroelectrode, a dramatic change within the mass transport occurs enabling a low limit of detection and potential improvements in the analytical performance even with a minimal amount of the electrode surface being covered by the ensemble.

In addition to pure metallic modifications as reported above, the utilisation of metallic oxides can be used. Bismuth oxide is a common oxide form that can be placed within a printable ink for advantageous detection of metal ions, with such modification being *akin* to that of highly toxic mercury electrode systems. Unlike that of an *in-situ* or *ex-situ* modification the fabrication process can create extremely reproducible areas of catalytic material within the composite, rather than on the surface. Such electrode

systems mimic that of the bismuth film electrodes and therefore can be utilised for the array of applications of these electrode systems. ²⁴

2.1.3 Substrate

One aspect of screen-printing technology, particularly in the case of the fabrication of electrochemical devices which is often overlooked, is the selection of the electrode substrate on which the ink is printed upon. Screen-printed electrodes are generally printed upon ceramic^{80, 81} or plastic substrates⁸²⁻⁸⁴ and the need for ultra-flexible sensors has arisen due to the possibility of using the screen-printed electrodes not only just within the laboratory environment but within the scientific field outside its confines applied “into-the-field”. Previous elegant work has seen “biosensors in briefs” being used to sense chemicals such as hydrogen peroxide and NADH;⁸⁵ a case in which ultra-flexible sensors are fundamental in achieving an ideal electrode for such applications. Wang *et al.*⁸⁶ developed wearable electrochemical sensors on underwater garments comprised of the synthetic rubber neoprene. The neoprene-based sensor was evaluated towards the voltammetric detection of trace heavy metal contaminants and nitro-aromatic explosives in seawater samples, with further applications involving the first example of enzyme (tyrosinase) immobilization on a wearable substrate towards the amperometric biosensing of phenolic contaminants in seawater also being described. Furthermore, depicted in Figure 2.8 is the screen-printed fabrication of electrochemical tattoos. Wang and co-workers have demonstrated that temporary transfer tattoo (T3) electrochemical sensors can be fabricated for physiological and security monitoring of chemical constituents leading to the demonstration of ‘electronic skin’, within this report they look at the effect of stretching and friction created on the skin.⁸⁷ Additionally, studies by Wang and co-workers have studied the analysis of sodium within perspiration upon the epidermis, utilising a similar setup as shown in Figure 2.8.⁸⁸

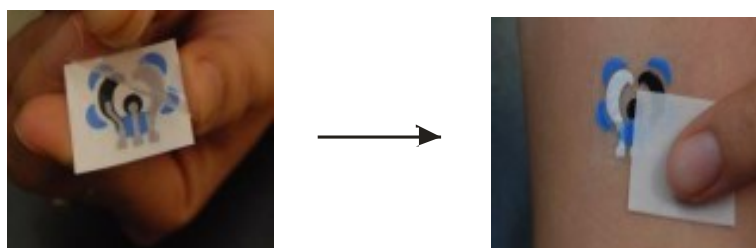


Figure 2.8: Optical images of the electrochemical tattoo upon the substrate and skin. Reproduced from Ref⁸⁷

Other work has explored the effect of mechanical contortion and stress on polymeric sensors comprised of Mylar[®], polyethylene naphthalate and Kapton which was found to be able to withstand such mechanical stress and still function electrochemically.⁸³ In general, a good substrate is simply classed as something that has a good adhesion to the screen-printed ink; the current diversity of substrates, as shown above, is fascinating.

2.2 Screen-Printing Process

The technique of screen-printing is described as the production of thick film hybrids, for applications within many areas of the scientific community, such as circuit boards and electrochemical systems to name a few. Due to the nature of screen-printing the creation of mass-produced thick films can be realised, with the utilisation of relatively cheap and simple designs this process possesses an excellent scales of economy. Additionally it is noted that due to simplicity of the machinery used throughout this process can be altered and changed upon a fundamental understanding of screen-printing.

The process of screen-printing typically consists of five prerequisites to ensure identically reproducible thick films, these are as follows:

- Suitable printing medium
- Mesh screen with an embedded stencil design
- Substrate to print upon
- Flexible and resilient squeegee
- Secure base to prevent movement of substrate within the process.

It is important to note, that suitable printing machinery is required to ensure the desired level of reproducibility is achieved with a high throughput. Nevertheless, there are situations where the printing machinery can impede and become inauspicious to the overall screen-print, it is with these considerations that it is solely reliant on the methodology.

Upon integration of the above mentioned pre-requisites, a print cycle can occur; Figure 2.9 represents the process in three simple steps. The first step consists of placement of the printing media (*i.e.* ink, emulsion or paste) upon the mesh screen, where it is visible that the screen is not in contact with the substrate. Such contact could potentially damage or spoil the print as the substrate would uncontrollably “snap-off” the screen, creating an unclean print. The contact only occurs when the squeegee applies pressure over the screen forcing the printing medium through the stencil design, creating the desired pattern or design in a controlled and efficient manner.

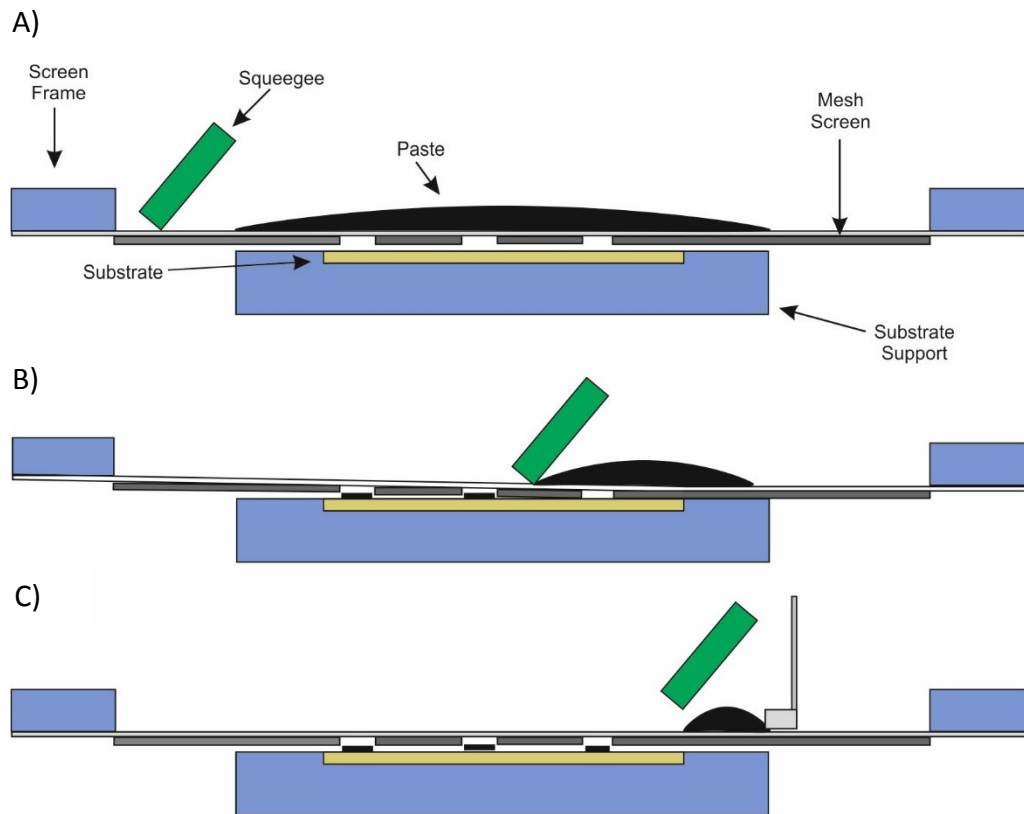


Figure 2.9: Schematic of the Screen-Print Process. A) Placement of the printing media (i.e. ink, emulsion or paste) upon the mesh screen, where it is visible that the screen is not in contact with the substrate. B) The printing medium is passed through the openings in the screen mesh in a controlled manner. C) The print is finished and the stencil design has been transferred onto the substrate.

2.3 Selection of Screen-Printing Equipment

As mentioned previously the prerequisites are vital for the screen-printing process, it is additionally important the selection of this equipment is crucial for maximising reproducibility and outputs. It is with this section that consideration of the screen, squeegee, flood/distribution bar and printing media are discussed.

2.3.1 The Screen

When utilising and designing the screen there are three factors to consider such as the screen frame, stencil design and the screen-mesh. The screen frame typically is fabricated utilising wood or metal, however due to their similarity in pricing they tend to be made from metal, creating a robust and safe foundation. The material used must be able to withstand the pressure created from the tension of the mesh, which in some cases can exceed values of 80 kg. The frame size can be varied however in all cases the screens tend to be either rectangular or square depending on the size of the machine and design at hand. It is due to this that there is no specific ratio or value that corresponds to the perfect design, however it does refer to the inside dimensions of the screen (as the frame is a support for the open mesh area of the screen, calculated by equation (2.1)). There are mainly two types of frames for the screen-printing process these are lightweight cast aluminium and extruded aluminium, dependent on the machine of choice the appropriate composition can be selected.

$$\textit{Open Area} = \frac{(\textit{mesh area})^2}{(\textit{wire diameter} + \textit{mesh opening})^2} \times 100\% \quad (2.1)$$

The screen-mesh has many interesting properties that allow for a perfect screen-printed design, as it acts as a support network to hold the stencil-design in place at all times during the print cycle, even after the pressure has been applied by the squeegee. These characteristics originate from its design and manufacture, the choice of an appropriate material for the mesh can be vital for a precise and detailed screen-print. Shown in Figure 2.10 is an optical image of a screen-mesh showing the woven network of the mesh.

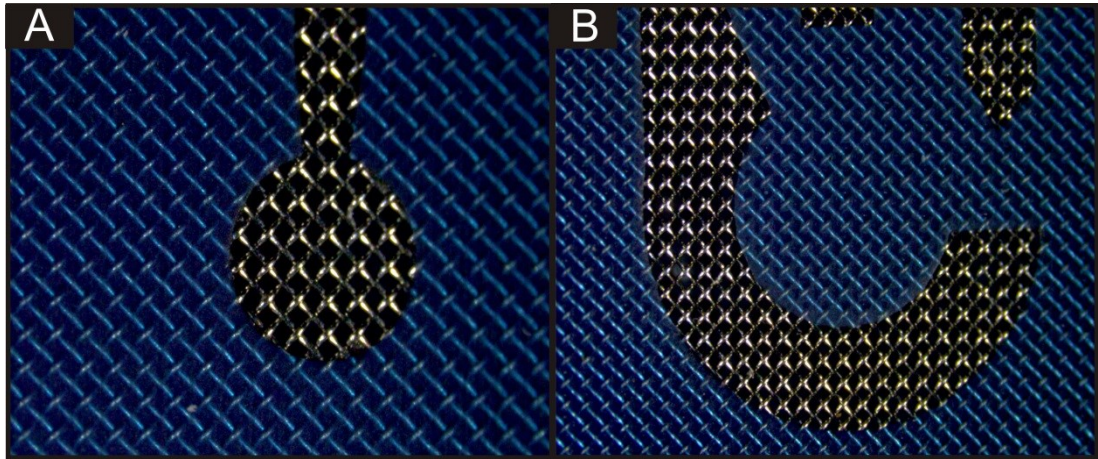


Figure 2.10: Optical image of a stainless steel screen-mesh, for a working electrode (left image) and counter electrode (right image). Magnification x50.

A factor that must be considered upon creation of the mesh screen is the mesh count, M , i.e. the amount of wires per unit of length as shown in Figure 2.11.

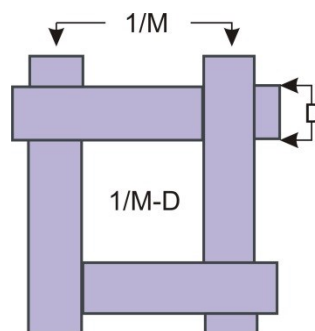


Figure 2.11: Schematic of a mesh opening.

In conjunction with size of the mesh count and wire diameter, D , the mesh opening can be calculated *via* equation (2.2). The mesh opening is a vital measurement that influences the amount and size of the ink that can be passed through the screen.

$$O = \frac{1}{M} - D \quad (2.2)$$

2.3.2 The Squeegee

During a screen-print cycle a highly important factor is the constant movement of the printing media towards the substrate, at a sufficient speed and pressure, this is accomplished by the utilisation of a squeegee. As described in Chapter 2.1.1 the squeegee applies pressure to forcing the ink through the stencil design, creating an even print upon the substrate in a controlled manner.

For the squeegee to complete its necessary tasks, it must be fabricated with materials that are flexible and resilient. The most common material used throughout industry is Polyurethane, it is general practise that squeegees possess an extremely long life and on average can achieve prints of 20,000 before any visible damage occurs. However utilising stainless steel meshes will decrease this as the surface friction applied during cycle will eventually damage the point of contact. During the fabrication of the squeegees many grades of softness are created, it is generally accepted that the softest material creates a larger contact with the screen; therefore this is the more efficient grade to use.

The angle at which the squeegee applies its pressure is also a vital condition for the successful transfer of print media through the stencil design. If the angle is too high the transfer of the printing medium will not be sufficient to fill the print area, therefore creating a thinner application of ink/paste to the substrate below. Additionally if the squeegee is at a much shallower angle the hydrodynamic pressure increases, therefore transferring too much of the ink/paste onto the substrate and potentially blocking and hindering the controlled snap-off. Figure 2.12 exhibits a selection of angles and their advantages/disadvantages, to the screen-printing process.

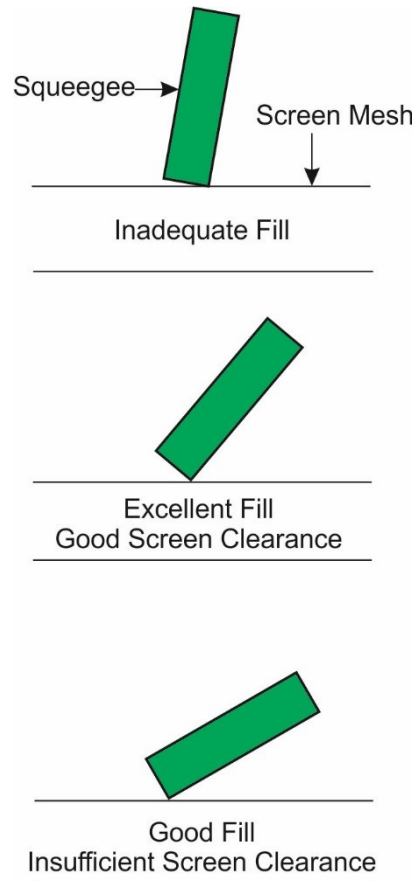


Figure 2.12: Angles of the squeegee and their effect upon the screen-print.

2.3.3 The Flood Bar/Distributor

The distribution of ink/paste is another vital process of the print cycle for a successful print. Typically flood bars are designed from stainless steel and will be slightly longer than the squeegee being utilised, it is then fixed behind the squeegee and upon the first transition of the print cycle the flood bar will transport the ink/paste over the print area. It is paramount that the flood bar is slightly above or touching the screen-mesh, so that it is constantly in touching distance of the ink. In many printing situations the squeegee will remove the excess ink/paste back to the starting position, and the process can be repeated.

2.3.4 Printing Medium

The screen-printed process allows the user to fabricate a variety of geometric designs and shapes; such ability requires the utilisation of a durable, compatible printing medium. Terminology of such media can range from a dye to a simple ink or paste, but in most cases they all will possess the same composition. The viscosity of these 'inks' will determine how successful the print is, as due to the nature of screen-printing the ink must be passed through a specific shape (stencil) keeping its geometric design. The formulation of the specialist inks tend to consist of two components: suitable pigments for the application at hand and an appropriate amount of solvent/binder ratio creating the perfect transport of the pigment.

Upon application of screen-printing some designs or screen-prints may require viscosities that are higher than the ideal, as the majority of quality control issues arise when the ink is more viscous, therefore it is important to ensure that the operation procedure should be modified *via* optimising each step of the manufacture. The ideal screen-printing ink should require no forcing into the open area of the screen, flow readily when moved by the flood bar and not dry within the screen-mesh during the operation. To achieve this perfect consistency, prior mixing of the ink must occur until a smooth fluidic composition is achieved.

In general examination of the composition is performed by utilising a fineness of grind (FOG) gauge (shown in Figure 2.13) for the determination of dispersion, particle size, and fineness of many materials like inks, lacquers, pigments, filler, chocolate to name a few. In this situation, the materials being tested are inks. The gauge may also be used to indicate the presence of undesired large particles in these materials. This tool has an attached scraper, which pulls the material along the sloping groove machined onto the top surface of the gauge. The value for fineness of grind is obtained directly from a scale engraved into the gauge.

Standard Operating Procedures for the Fineness of Grind Gauge

1. Place the gauge on a flat, horizontal and non-slip surface, with the zero mark on the scale closest to the user.
2. Place a considerable amount of material (ink) in the deep end of each groove.

3. Place the scraper on the surface of the gauge behind the material (ink), which is at the deepest groove.
4. Use both hands to hold the scraper and pull along the length of the gauge at a constant speed apply sufficient pressure to clean the excess material (ink) from the edge of the gauge.
5. Stop at a point beyond the zero depth and assess the drawn out material within the next 3 seconds.
6. Note: This avoids inaccurate testing due to evaporation of solvents from materials.
7. The material (ink) should be viewed at right angles to the length of the groove and at an angle of 20 to 30 with the surface of the gauge.
8. Find the first position across the groove 3mm wide which contains 3 to 10 particles/streaks/ scratches of material (ink)
9. Read the position on the scale and record this value.
10. Perform the test three times; afterwards calculate the average value of the result. The average value is the fineness of grind of the material (ink).

The FOG test can be used as a QA/QC measurement for inks used in the screen-printing process.



Figure 2.13: Optical images of fineness of grind gauge. Reproduced from Ref⁸⁹

2.3.5 Curing of the Ink

The nature of the printing media requires a curing step within the fabrication of the design. Generally many failures in the fabrication of conductive inks are reliant upon the poor selection of solvents. It is with this in mind that consideration of the solvents utilised within the 'ink' allow for an ideal curing time and temperature to envisage a situation depicted within Figure 2.14; where it is clear that upon the curing step of the ink the volume starts to decrease, leaving behind a fully conductive 'stack' upon the substrate, in which the polymer within the ink formulation holds the structure of the electrode surface.

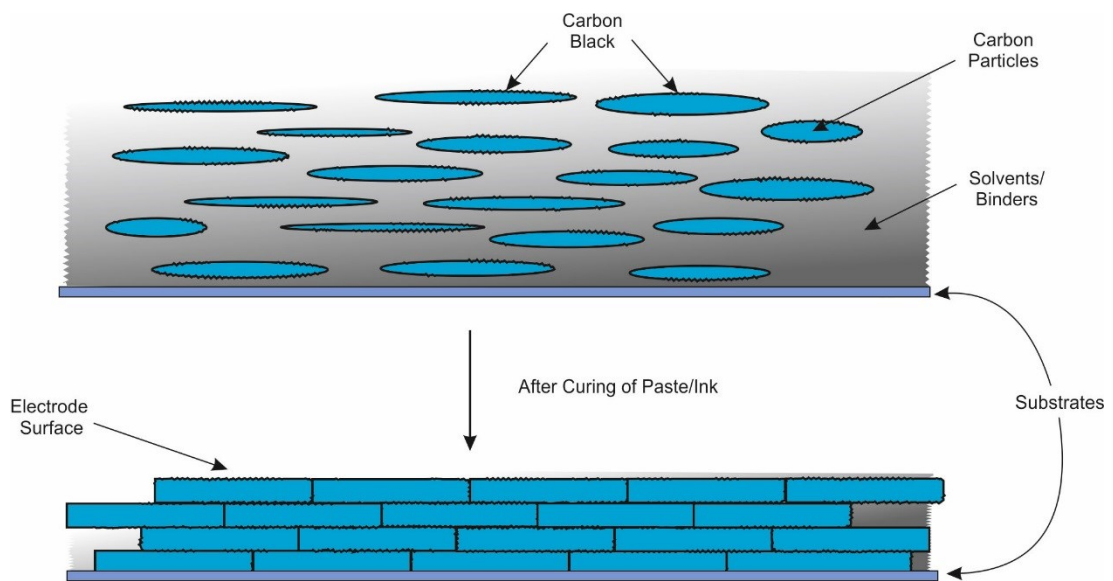


Figure 2.14: Representation of curing of the printing medium upon the conductive layers.

In many cases the manufacturer of the ink will provide the solvents that are the best ratio for working and curing properties, therefore if an amendment is requested consideration of the curing procedure must be endured. Note that an ink has a range of solvents varying from slow and fast evaporation time, to ensure a controlled drying process resulting in a reproducible electrode surface. It is important to note, that the solvent is solely there to create a fluidic support for the conductive paste and thus in most cases a solvent with a lower boiling point would be ideal. The reader should be directed to the Appendices (Table 1) for a detailed troubleshooting guide indicating the common technical problems and how to resolve these issues when utilising the screen-printed process.

2.4 Fabrication of the screen-printed electrodes within this Thesis

The SPEs used throughout this thesis were fabricated in-house with appropriate stencil designs using a microDEK1760RS screen-printing machine (DEK, Weymouth, UK). A previously used ink formulation^{90,91} (Product Codes for each ink are presented within Table 3.1) was first screen-printed onto a range of substrates described within Table 3.1. This layer was cured in a fan oven at 60° C for 30 minutes. Next a silver/silver chloride reference electrode was included by screen-printing Ag/AgCl paste (Product Code: C2040308P2; Gwent Electronic Materials Ltd, UK) onto the plastic substrate. Last a dielectric paste ink (Product Code: P2070423D5; Gwent Electronic Materials Ltd, UK) was printed to cover the connection and define the carbon-graphite working electrode (3 mm diameter), shown within Figure 2.15. After curing at 60° C for 30 minutes the screen-printed electrode is ready to use.

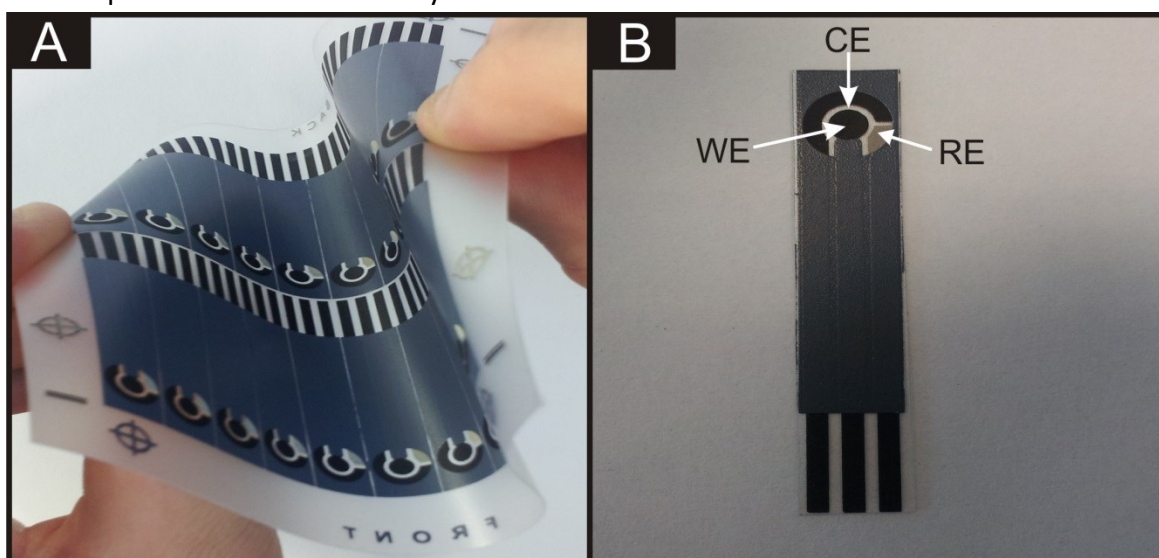


Figure 2.15: Image of a sheet of F-SPE (A) highlighting the ultra-flexible nature of the plastic substrate and fabricated electrode it gives rise to. Image B shows a single F-SPE which has an on-board counter and reference electrode which is used as a single sensor.

Additionally, shown within Table 2.1 are the corresponding values of the heterogeneous rate kinetics for each of the fabricated SPEs throughout this thesis. It is vital to note that these values were calculated *via* the Nicholson method utilising hexaammineruthenium (III) chloride within 0.1 M KCl. Upon the fabrication these SPEs were then benchmarked against the values obtained from their previous counterparts, creating highly reproducible electrode kinetics. If a 'batch' did not meet these quality control requirements they were discarded immediately.

Working Electrode Size (diameter)	Ink - (Product Code)	Substrate	Denotation	Value of $k^0/\text{cm s}^{-1}$
3 mm Macroelectrode	Edge-Plane SPE (Gwent Electronic Materials - C2000802P2)	Polyester (Autostat- 250 μm) Flexible Polyester (Autostat- 150 μm) Sellotaped Desktop Printer Paper (160 g/m^2) Varnished Desktop Printer Paper (160 g/m^2) Tracing Paper (73 g/m^2)	Standard-SPE F-SPE Ps-SPE Pv-SPE T-SPE	1.16×10^{-3} 1.05×10^{-3} 1.15×10^{-3} 1.15×10^{-3} 1.61×10^{-3}
	Cobalt Phthalocyanine Mediated Ink (Gwent Electronic Materials- C2030408P3)	Polyester (Autostat- 250 μm) Flexible Polyester (Autostat- 150 μm) Sellotaped Desktop Printer Paper (160 g/m^2) Tracing Paper (73 g/m^2)	CoPC –SPE CoPC-F-SPE CoPC-P-SPE CoPC-T-SPE	1.15×10^{-3} 1.15×10^{-3} 1.31×10^{-3} 1.02×10^{-3}
100 μM Band	Single Walled Carbon Nanotubes Electrodes (South West NanoTechnologies- VC100)	Polyester (Autostat- 250 μm)	B-CNT-SPE	1.26×10^{-3}

	Cobalt Phthalocyanine Mediated Ink (Gwent Electronic Materials-C2030408P3)	Polyester (Autostat- 250 μm)	B-CoPC-SPE	1.20×10^{-3}
	Edge-Plane SPE (Gwent Electronic Materials - C2000802P2)	Polyester (Autostat- 250 μm)	b-SPE	1.96×10^{-3}

Table 2.1: Product codes, substrate type, value of the heterogeneous rate constant k^0 (cm s^{-1}) and their respective denotation of the screen-printed electrodes used throughout.

2.4.1 Connection of the fabricated screen-printed electrochemical platforms

Researchers can clearly see the allure of utilising screen-printed electrodes and newcomers to the field often fail to obtain reproducible and useful electrochemical measurements which are typically blamed upon the screen-printed electrodes themselves. Others lay the problem with connection to the electrode being difficult, typically utilising crocodile clips and thus obtain electrical noise in the electrochemical signals resulting in unreliable limits the detection, in terms of the analytical sensitivity and limit of detection, towards the target analytical probe. Both such scenarios can result in researchers abandoning the use of screen-printed electrodes. Motivated by these problems, in this Chapter the often overlooked factor of screen-printed electrode experimental setups is explored between the use of an edge connector and the crocodile clips both used in the electrical wiring of the SPEs to the potentiostat/electronics. This Chapter has been published within RSC Analytical Methods (2015,**7**, 1208).

Electrochemical comparison between the two setups of the traditional approach of crocodile clip connection with that of the edge connector, the employment of crocodile clips for electrochemical analysis within a laboratory environment *can produce* near identical responses with that of an edge connector. When one diligently connects the crocodile clips, as shown in Figure 2.16. Appropriate separation of the crocodile *must* be applied to create these responses, shown in Figure 2.17 A and not like that in Figure 2.17 B, the latter gives rise to useless voltammetric signatures while the former gives near perfect and expected voltammetric responses; some researchers obtain such results as presented in Figure 2.17 C and blame the electrode itself without further exploration of the possible problems within the electrochemical system.

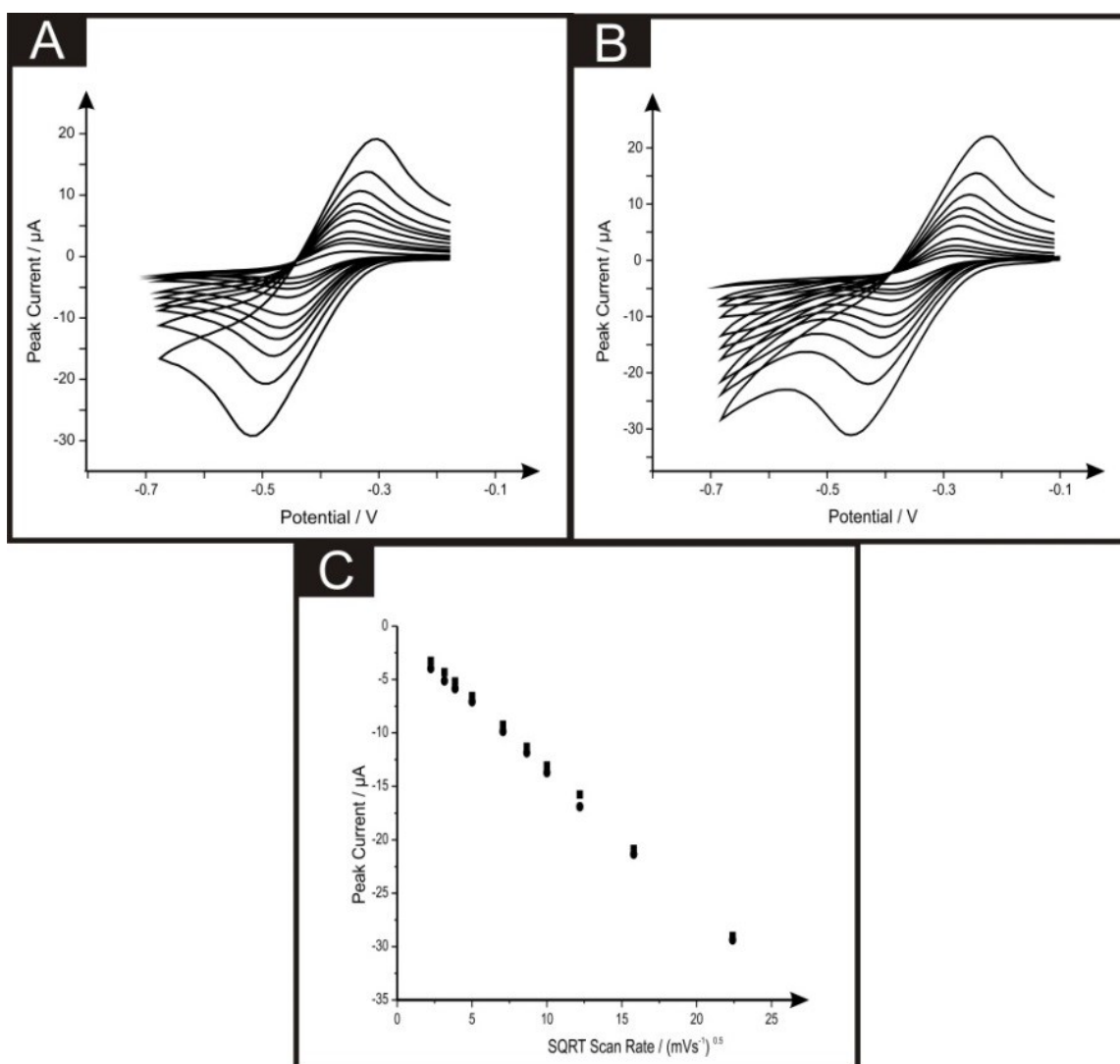


Figure 2.16: Typical cyclic voltammograms using both an edge connector (A) and a crocodile clip setup (B) recorded in hexaammineruthenium (III) chloride/ 0.1 M KCl. Also shown are plots of peak height versus square root of scan rate (C) for the edge connector and crocodile clip setup (squares and circles respectively).

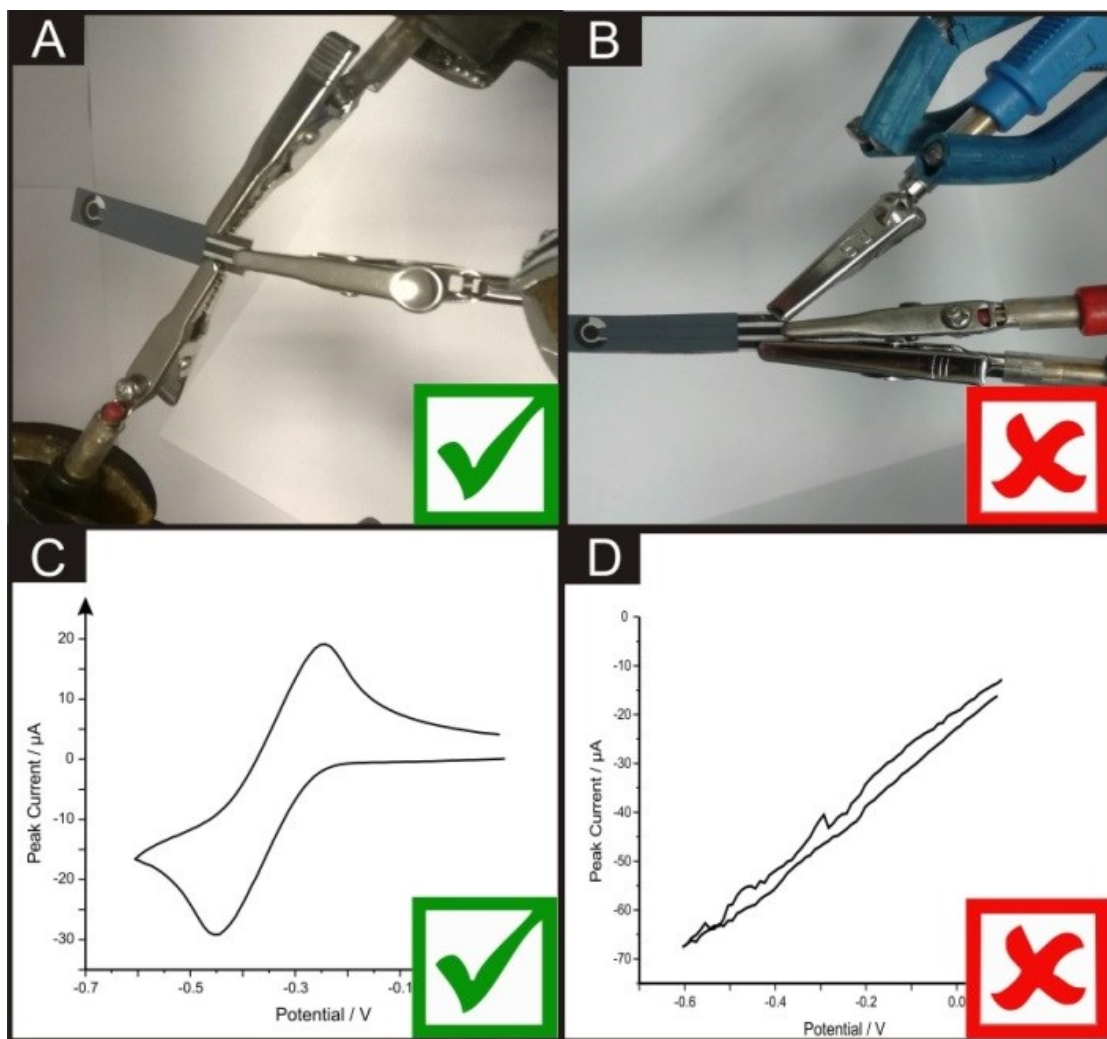


Figure 2.17: Images showing the correct (A) and incorrect (B) way to connect the screen-printed electrodes/sensors to the potentiostat/electrodes utilising crocodile clips, with their corresponding cyclic voltammograms (C & D respectively) recorded in 1 mM hexaammineruthenium (III) chloride/0.1 M KCl.

2.4.2 Quantifying the composition of the screen-printed reference electrode.

The silver/silver chloride reference electrode is printed from an appropriately formulated ink containing (amongst other components) significant amounts of solid silver and silver chloride. A range of silver: silver chloride ratios are available from commercial ink suppliers such as: 40:60; 50:50; 60:40, 70:30; 80:20; 85:15 and 90:10. We show below what effect this has on the voltammetry but note that as the amount of silver increases, the price of the ink substantially increases due to the high cost of silver metal.

The electrochemical process at the reference electrode is as follows:



The appropriate Nernst equation for this process is described by equation (2.4):

$$E = E^0 + \left(\frac{RT}{nF}\right) \ln \left[\frac{[AgCl]}{[Ag][Cl^-]} \right] \quad (2.4)$$

Where, E^0 is the formal potential. Equation (2.4) can be rewritten as:

$$E = E^0 + \left(\frac{RT}{nF}\right) \ln \left[\frac{k}{[Cl^-]} \right] \quad (2.5)$$

Where $k = \frac{[AgCl]}{[Ag]}$

Through investing and separating the logarithmic terms and conversion of base 10 gives:⁹²

$$E = E^0 - 2.303 \left(\frac{RT}{nF}\right) [\log[Cl^-] - \log(k)] \quad (2.6)$$

Assuming the experiment is run at 298 K gives:

$$E = E^0 - 0.0592 \log[Cl^-] + 0.0592 \log(k) \quad (2.7)$$

Hence it can be clearly seen that the electrode potential of this reference electrode decreases by $\sim 59\text{mV}$ for every decade change in chloride ion concentration; not surprisingly one will see that when electroanalytical measurements are reported in the literature that the chloride ion concentration is fixed otherwise the potential will shift accordingly. What is also insightful is that if the ratio (k) of silver:silver chloride in the reference electrode changes then the measured potential will also change. This could happen unexpectedly during printing a large batch that a new reference electrode ink is opened where the ratio of silver:silver chloride is different to that used previously. This would mean that the measured potential would change during the batch and would greatly affect the sensor performance, particularly if the measurement protocol is based upon chronoamperometry. Last, through the use of equation (2.7) the ratio (k) can be experimentally determined to ensure that the ink received from the manufacturer is as claimed. In all experimental procedures additional supporting electrolyte (0.1 M KCl) was added to stabilise this scenario.

Chapter 3 - *Flexibility and Robustness of Screen-Printed Electrodes*

In this Chapter the consideration of objective 2.1; concerning the flexibility of the substrate utilised within the screen-printing process, upon the effect of the electrochemical performance is analysed. This work has been published: *Electroanalysis* (2013, **25**,2275 and 2014, **26**, 262).

3.1 Ultra-Flexible Paper based Electrochemical Sensors: Effect of Mechanical Contortion upon Electrochemical Performance

3.1.1 Introduction

One aspect of screen-printing technology, particularly in the case of the fabrication of electrochemical devices which is often overlooked, is the selection of the electrode substrate on which the ink is printed upon. Screen-printed electrodes are generally printed upon ceramic^{80, 81} or plastic substrates⁸²⁻⁸⁴ and the need for ultra-flexible sensors has arisen due to the possibility of using the screen-printed electrodes not only just within the laboratory environment but within the scientific field outside its confines applied "into-the-field". Previous elegant work has seen "biosensors in briefs" being used to sense chemicals such as hydrogen peroxide and NADH;⁸⁵ a case in which ultra-flexible sensors are fundamental in achieving an ideal electrode for such applications. Wang *et al.*⁸⁶ developed wearable electrochemical sensors on underwater garments comprised of the synthetic rubber neoprene. The neoprene-based sensor was evaluated towards the voltammetric detection of trace heavy metal contaminants and nitro-aromatic explosives in seawater samples, with further applications involving the first example of enzyme (tyrosinase) immobilization on a wearable substrate towards the amperometric biosensing of phenolic contaminants in seawater also being described.

Other work has explored the effect of mechanical contortion and stress on polymeric sensors comprised of Mylar, polyethylene naphthalate and Kapton which was found to be able to withstand such mechanical stress and still function

electrochemically.⁸³ Recently, work within the MMU electrochemical research group have studied the different electrochemical properties of ultra-flexible screen-printed paper-based sensors (standard desktop printing paper) against that of the more traditional polyester-based screen-printed electrodes determining that little deviation with regard to the electrochemical capabilities of the sensors is noted between the two variants, even after extreme mechanically contortion.^{93, 94}

3.1.2 Experimental Section

All chemicals used were of analytical grade and were used as received without any further purification and were obtained from Sigma-Aldrich. All solutions were prepared with deionised water of resistivity not less than 18.2 M Ω cm. Voltammetric measurements were carried out using an Emstat (Palm Instruments BV, The Netherlands) potentiostat. Experiments carried out throughout this study contained a three electrode system, using the SPEs that were fabricated as described within section 3.3. All experiments were carried out using an external counter and reference, a platinum wire and saturated calomel electrode (SCE) respectively to allow comparison with the electroanalytical field.

3.1.3 Results and Discussion

Electrochemical benchmarking of the SPEs utilising potassium ferrocyanide (II) and hexaammineruthenium (III) chloride, upon mechanical contortion

Figure 3.1 depicts optical images of the three screen-printed sensors fabricated (as described within the Experimental Section) which are utilised in this study. The polymer-based screen-printed sensor (denoted throughout as standard-SPE) and both the paper-based screen-printed electrodes are modified using Sellotape™ (denoted throughout as ps-SPE) and a clear nail varnish (denoted throughout as pv-SPE). The Sellotape™ and clear nail varnish are required in order to cover / insulate the carbon screen-printed connections and thus define the screen-printed working electrode ensuring only the desired electrode area is able to interact with the solution since it has been found that although paper-based sensors can yield highly competitive results when applied into analytical protocols, they are susceptible, as would be expected, to wetting and solution absorption which over time can lead to the connections of the sensors being compromised.¹¹ Also shown in Figure 3.1 B and C are the two contortion angles to which the sensors were placed under mechanical stress during the study; 45 and 90° respectively. It is important that these contortion angles were chosen to examine the utility of the connection upon mechanical contortion therefore the effect of delamination was not considered.

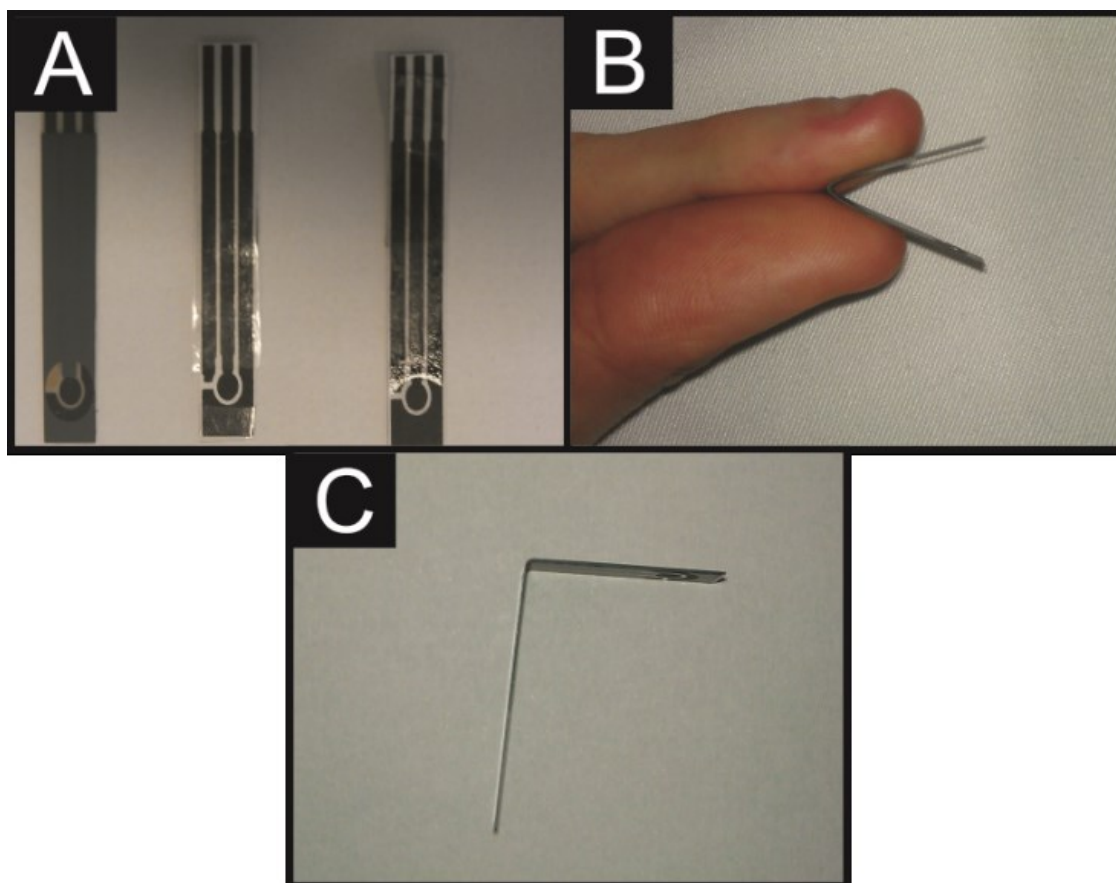


Figure 3.1: Photographs of: (A) The standard polymer-based screen-printed electrode (standard-SPE) (left), the Sellotape™ coated paper-based screen-printed sensor (ps-SPE) (middle) and the clear nail varnish coated paper-based screen-printed sensor (pv-SPE) (right). The contortion angles of 45 and 90° utilised throughout this investigation are shown in (B) and (C) respectively.

The electrochemical activity as a function of applied mechanical stress / contortion utilising the redox probe potassium ferrocyanide (II) was explored. The first consideration was the effect upon the cyclic voltammetric responses observed at the standard-SPE, which are shown in Figures 3.2 A and B following mechanical stress at angles of 45 and 90° respectively for fixed contortion times of 5, 10 and 60 minutes, chosen to recreate the effect of a sensor under constant strain within an in-the-field application. Figure 3.2 C depicts a plot of peak-to-peak separation (ΔE_p) versus contortion time at the two angles (45 and 90°). Note the peak-to-peak separation indicates the degree of reversibility of the heterogeneous electron transfer where the smaller the value, the faster the electron transfer rate. Figure 3.2 C indicates the detrimental effect upon the electrochemical reversibility of the electrode material occurring as a result of mechanical stress / contortion and contortion time where the electrochemical performance deteriorates.

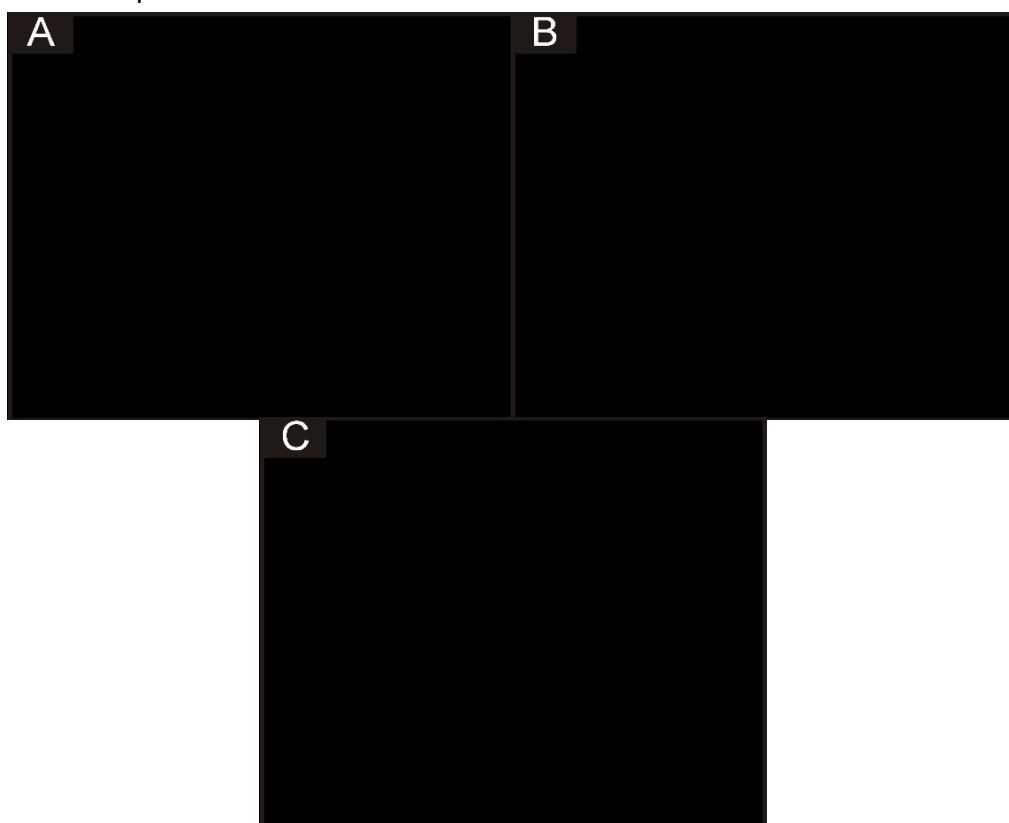


Figure 3.2: Cyclic voltammetric responses obtained at standard-SPE contorted at angles of (A): 45 and (B): 90°, recorded in 1 mM potassium ferrocyanide (II) / 0.1 M KCl. Contortion times of 60 (dashed line), 10 (dash-dotted line), 5 (dotted line) and 0 minutes (solid line) were utilised for each of the standard-SPEs. Scan rate: 100 mV s⁻¹. Also shown is the effect of contortion time for the two angles upon voltammetric peak-to-peak separation (ΔE_p): 45° (squares) and 90° (circles). N = 3.

Next, the paper-based sensors were explored with the effect of contortion angle and time upon electrochemical performance being studied utilising the redox probe potassium ferrocyanide (II). Figures 3.3 A and B show the cyclic voltammetric responses obtained utilising a ps-SPE. As has been previously reported⁹⁵ the electrochemical resistivity (and resultant ΔE_p) is greater at the ps-SPE compared to that at the standard-SPE prior to mechanical stress. Upon the introduction of mechanical stress at the fixed angles for the given contortion times there is a less of a change from the un-treated ΔE_p (320 mV) with a maximum peak-to-peak separation of 365 and 470 mV being observed at angles of 90 and 45° respectively (Figure 3.3 C). Although as seen in Figure 3.3 C, the ΔE_p shifts to a greater value when contorted at 45° rather than 90°, the amount of time the electrodes are subjected to this stress has little bearing on the overall peak positions.

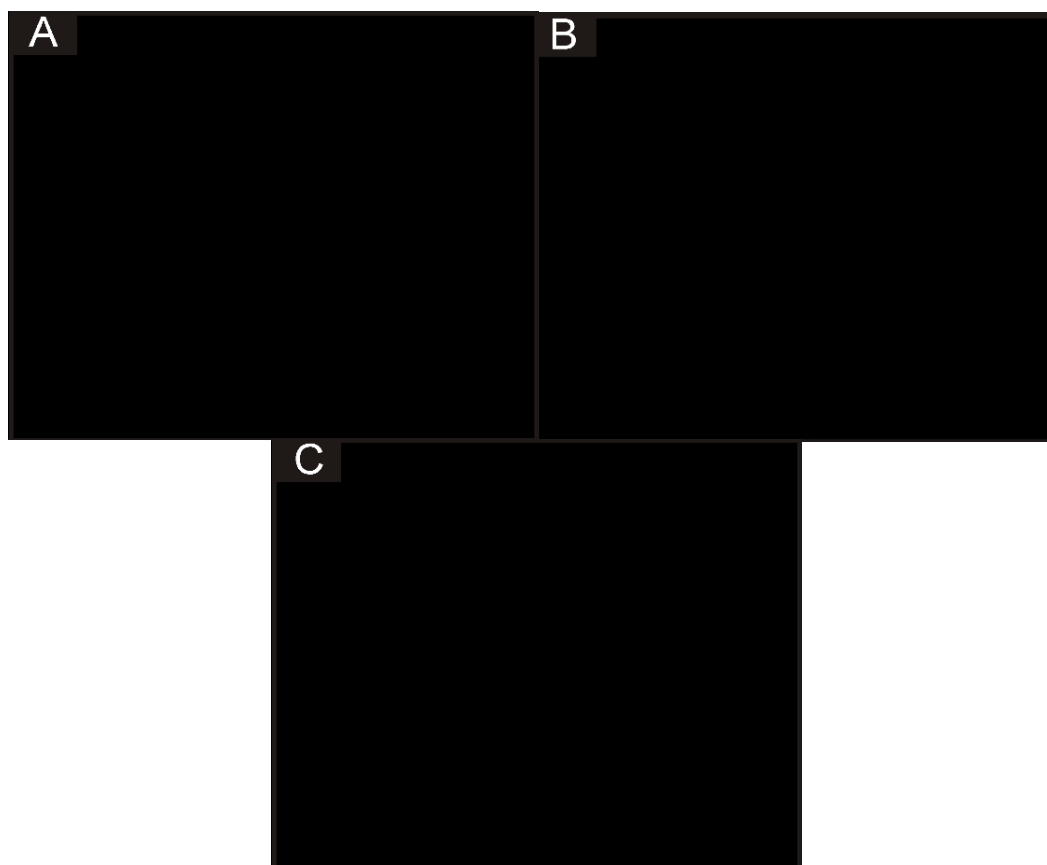


Figure 3.3: Cyclic voltammetric responses for ps-SPE contorted at angles of (A): 45 and (B): 90°, recorded in 1 mM potassium ferrocyanide (II) / 0.1 M KCl. Contortion times of 60 (dashed line), 10 (dash-dotted line), 5 (dotted line) and 0 minutes (solid line) were utilised for each of the standard-SPEs. Scan rate: 100 mV s⁻¹. Also shown is the effect of contortion time for the two angles upon peak-to-peak separation (ΔE_p): 45° (squares) and 90° (circles). N = 3.

Similarly, the cyclic voltammograms obtained when utilising the pv-SPEs, as shown in Figures 3.4 A and B, show the same electrochemical behaviour as is noted at the ps-SPE; the overall peak potential does become slightly larger for the electrodes contorted at 45°, but however for 90° there is little movement as you can evident in Figure 3.4 C. Evidently, comparisons may be drawn between the two sets of data, suggesting that the polymer-based substrate utilised for the standard-SPE are much more susceptible to mechanical stress. It is important to note that although these paper-based sensors offer greatest resilience in relation to mechanical stress over the pre-set periods, the initial voltammetry (prior to mechanical stress) exhibited by the sensors in terms of ΔE_p is larger than at the polymer-based sensor when utilising the redox probe potassium ferrocyanide (II); the polymer-based screen-printed sensor exhibit a ΔE_p value of ~ 205 mV which is in excellent agreement with previous literature⁹⁶ while the paper-based sensors exhibit greater voltammetric peak-to-peak separations of 425 and 355 mV for the pv- and ps-SPE, respectively.

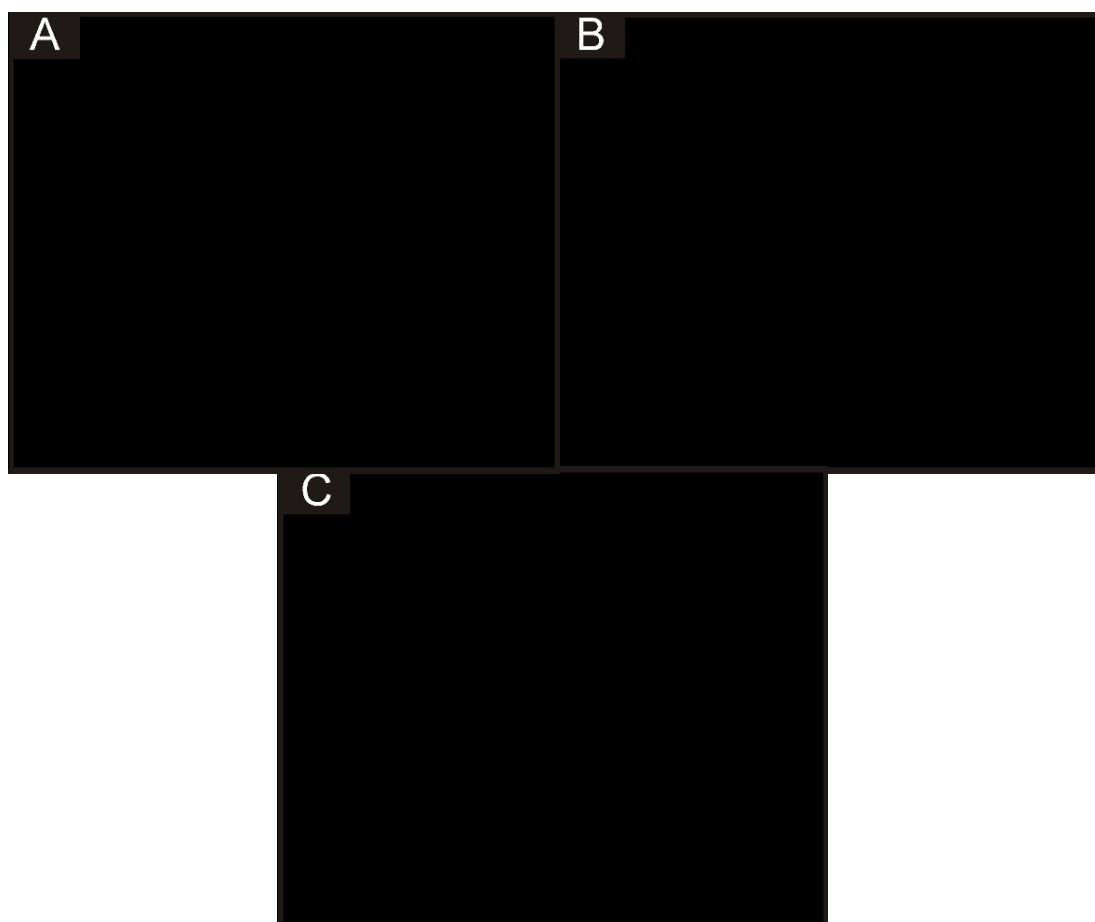


Figure 3.4: Cyclic voltammetric responses for pv-SPE contorted at angles of (A): 45 and (B): 90°, recorded in 1 mM potassium ferrocyanide (II) / 0.1 M KCl. Contortion times of 60 (dashed line), 10 (dash-dotted line), 5 (dotted line) and 0 minutes (solid line) were utilised for each of the standard-SPEs. Scan rate: 100 mV s⁻¹. Also shown is the effect of contortion time for the two angles upon peak-to-peak separation (ΔE_p); 45° (squares) and 90° (circles). $N = 3$.

To allow for comparisons and further understanding the studies relating to the effect of contortion time and angles upon the electrochemical performance and characteristics of the three electrodes, the outer-sphere electrochemical probe hexaammineruthenium (III) chloride was also utilised. When comparing the overall resulting peak-to-peak separation at the three sensors following contortion time at the two angles, less change is noted compared with that seen when utilising the electrochemical probe potassium ferrocyanide (II). From the sensors explored in this study it is clear through assessment of this data that the standard-SPE (screen-printed upon the plastic substrate) demonstrates the greatest susceptibility to contortion with a positive correlation between contortion time and peak-to-peak separation with the same trends, (that is a positive correlation between the resultant peak-to-peak separation and contortion time are noted) for both the ps- and pv-SPE's although these paper-based sensors offered greater resilience in relation to contortion time and degrees over that of the standard-SPE since at longest contortion time and angle (45°), there is no significant deviation from the initial electrodes response before being contorted.

Evaluation of the mechanical contortion towards reduced dihydronicotinamide adenine dinucleotide (NADH)

Next, the effect of mechanical stress upon the screen-printed electrochemical sensors was evaluated using the electrochemical oxidation of NADH (dihydronicotinamide adenine dinucleotide reduced form) to the corresponding oxidized form (NAD⁺). This electrochemical probe receives considerable attention owing to its very important role as a cofactor in many naturally occurring enzymatic reactions, and mainly because of the potential application in over 300 NAD⁺/NADH-dependent dehydrogenase-based biosensors^{95, 97-102} and thus its electrochemical characteristic are hugely important. First the effect of mechanical stress upon the standard-SPE towards the sensing of 100 μM NADH in a pH 7 phosphate buffer solution using cyclic voltammetry following mechanical stress at angles of 45 and 90° at fixed contortion times of 5, 10 and 60 minutes. As observed in Figure 3.5 A at a contortion angle of 90°

over the studied time period there is no significant change in the voltammetric peak current until 60 minutes where a slight reduction in the voltammetric peak height with an additional shift in the oxidative peak potential to a slightly more electropositive potentials occurs. However, following a more severe contortion at an angle of 45°, the electrochemical response at the standard-SPE is more severe following a time of 60 minutes at which point the voltammetric peak is completely lost; clearly this is a limitation if these standard-SPE are used as the basis of biosensors in environments where mechanical contortion might be encountered. In contrast, the initial electrochemical oxidation peak potential occurs at higher potentials at the ps- and pv-SPE compared to the standard-SPE; this potentially could be detrimental when these are applied into real sensing applications, but the full extent of this problem is yet to be fully explored. As observed in Figures 3.6 and 3.7, the effect of mechanical contortion in terms of applied angles and times reveals there is a reduction in the peak magnitude at both ps- and pv-SPE as contortion time increases, with no shift in peak potential to higher overpotential. The largest effect on the electrochemical activity occurs when the electrode is contorted for a time of 60 minutes being contorted at an angle of 45°.

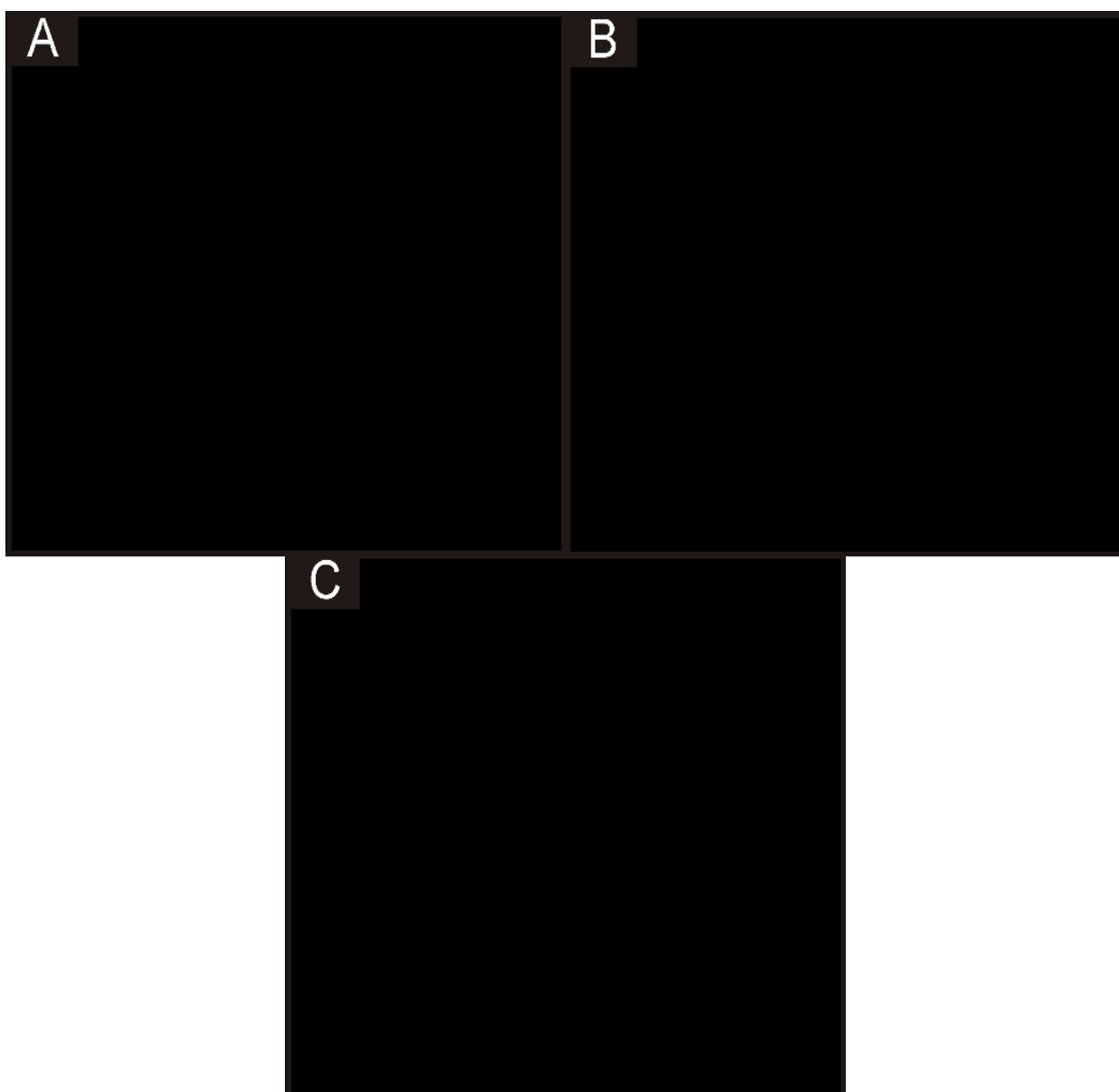


Figure 3.5: Cyclic voltammetric responses for standard-SPE contorted at angles of (A): 45° and (B): 90°, recorded in 100 μM NADH in pH 7 phosphate buffer. Contortion times of 60 (dashed line), 10 (dash-dotted line), 5 (dotted line) and 0 minutes (solid line) were utilised for each of the standard-SPEs. Scan rate: 100 mV s^{-1} . Also shown is the effect of contortion time for the two angles upon the voltammetric peak potential (E_p): 45° (squares) and 90° (circles). $N = 3$.

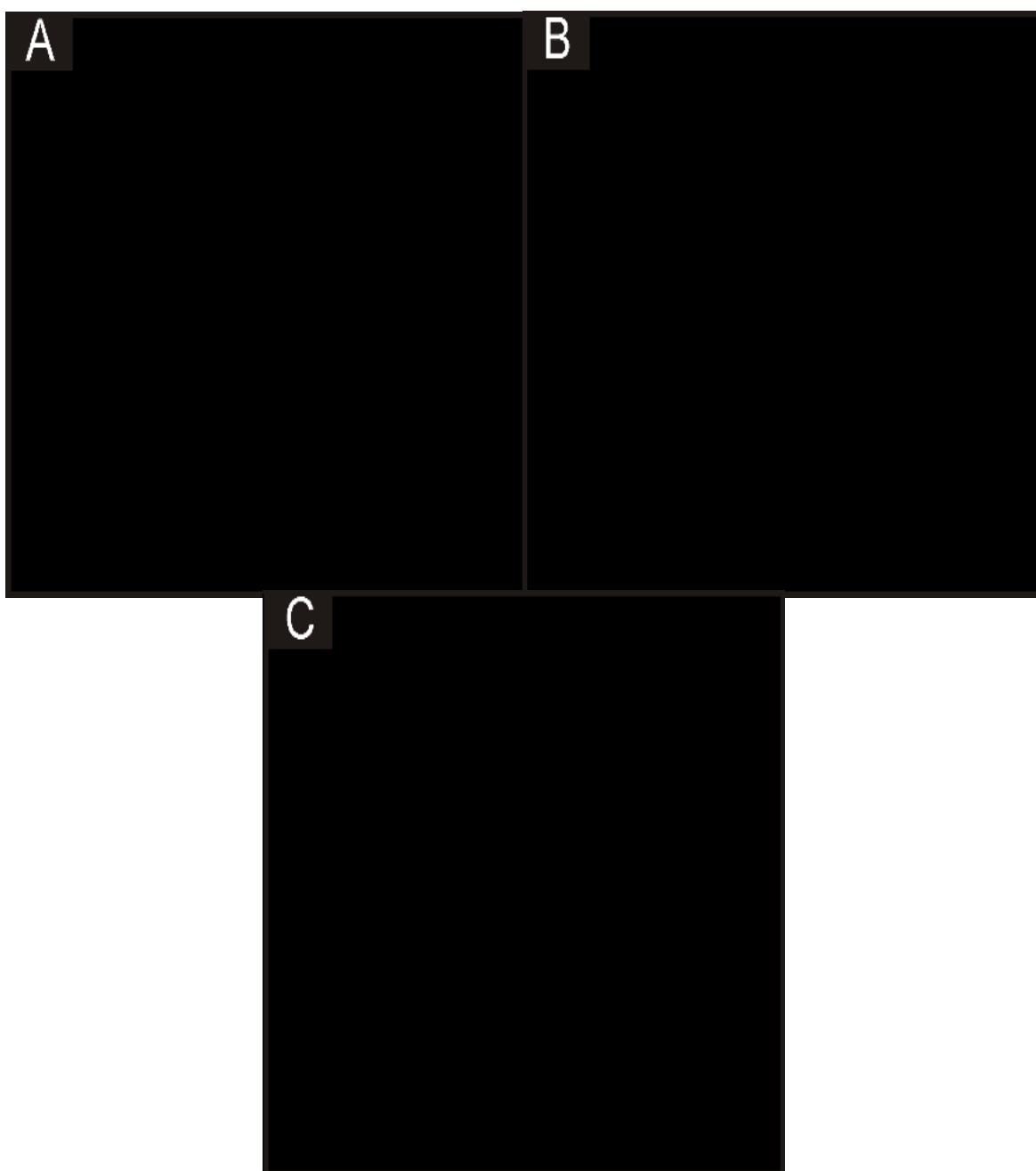


Figure 3.6: Cyclic voltammetric responses for ps-SPE contorted at angles of (A): 45 and (B): 90°, recorded in 100 μM NADH in pH 7 phosphate buffer. Contortion times of 60 (dashed line), 10 (dash-dotted line), 5 (dotted line) and 0 minutes (solid line) were utilised for each of the standard-SPEs. Scan rate: 100 mV s^{-1} . Also shown in (C) is the effect of contortion time for the two angles upon the voltammetric peak potential (E_p): 45 (squares) and 90° (circles). $N = 3$.

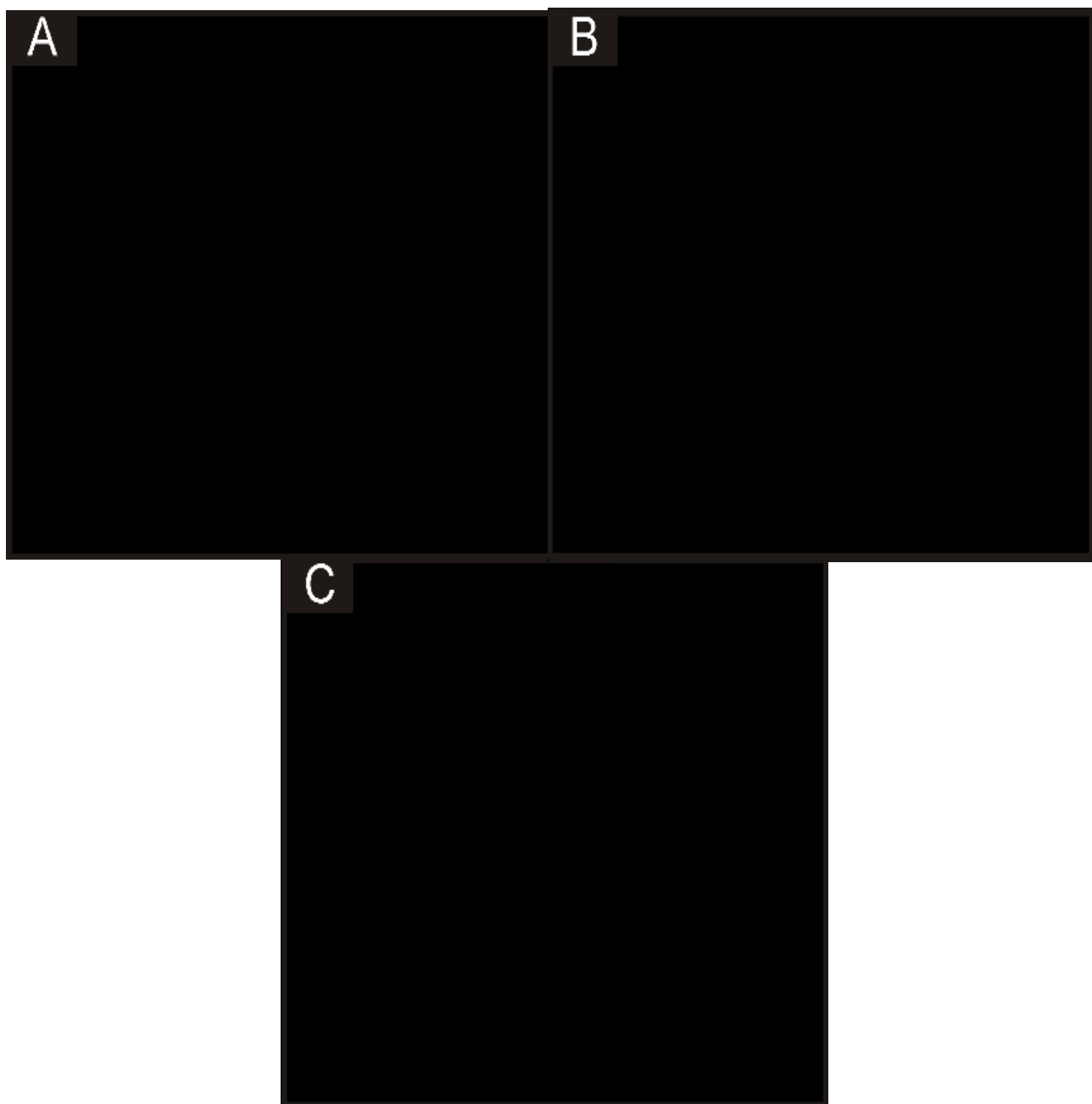


Figure 3.7: Cyclic voltammetric responses for pv-SPE contorted at angles of (A): 45 and (B): 90°, recorded in 100 μM NADH in pH 7 phosphate buffer. Contortion times of 60 (dashed line), 10 (dash-dotted line), 5 (dotted line) and 0 minutes (solid line) were utilised for each of the standard-SPEs. Scan rate: 100 mV s^{-1} . Also shown in (C) is the effect of contortion time for the two angles upon the voltammetric peak potential (E_p): 45 (squares) and 90° (circles). $N = 3$.

In comparison of the all the screen-printed electrodes evaluated with the NADH/NAD⁺ probe (Figures 3.5-3.7), the mechanical contortion has an effect on the electrochemical performance/activity depicted in a reduction in voltammetric peak height. Additionally, the potential shift occurs at a lesser extent for the ps- and pv- SPEs than at of the standard-SPEs. This is clearly related to the material used where the underlying paper-based SPEs are inherently more flexible than those on polymeric-based substrates. A payoff for this more flexible nature is that the electrochemical performance (in terms of the peak height/shape and potential) is worse than at the standard-SPEs which is likely due to adhesion of the carbon screen-printed inks to the respective substrates. In order to gain further insights into the effect of mechanical stress / contortion, surface analysis was carried out. Figure 3.8 shows that damage can be observed to the conductive track which is where the impact of the mechanical contortion occurs. It is noted, that this is far from a quantitative approach and hard to prove unambiguously. However with the electrochemical observations (using electrochemical probes), it is apparent that origin of the unfavorable effects upon the electrochemical performance/activity is due to the conductive path/track being altered/broken during the mechanical force/stress.

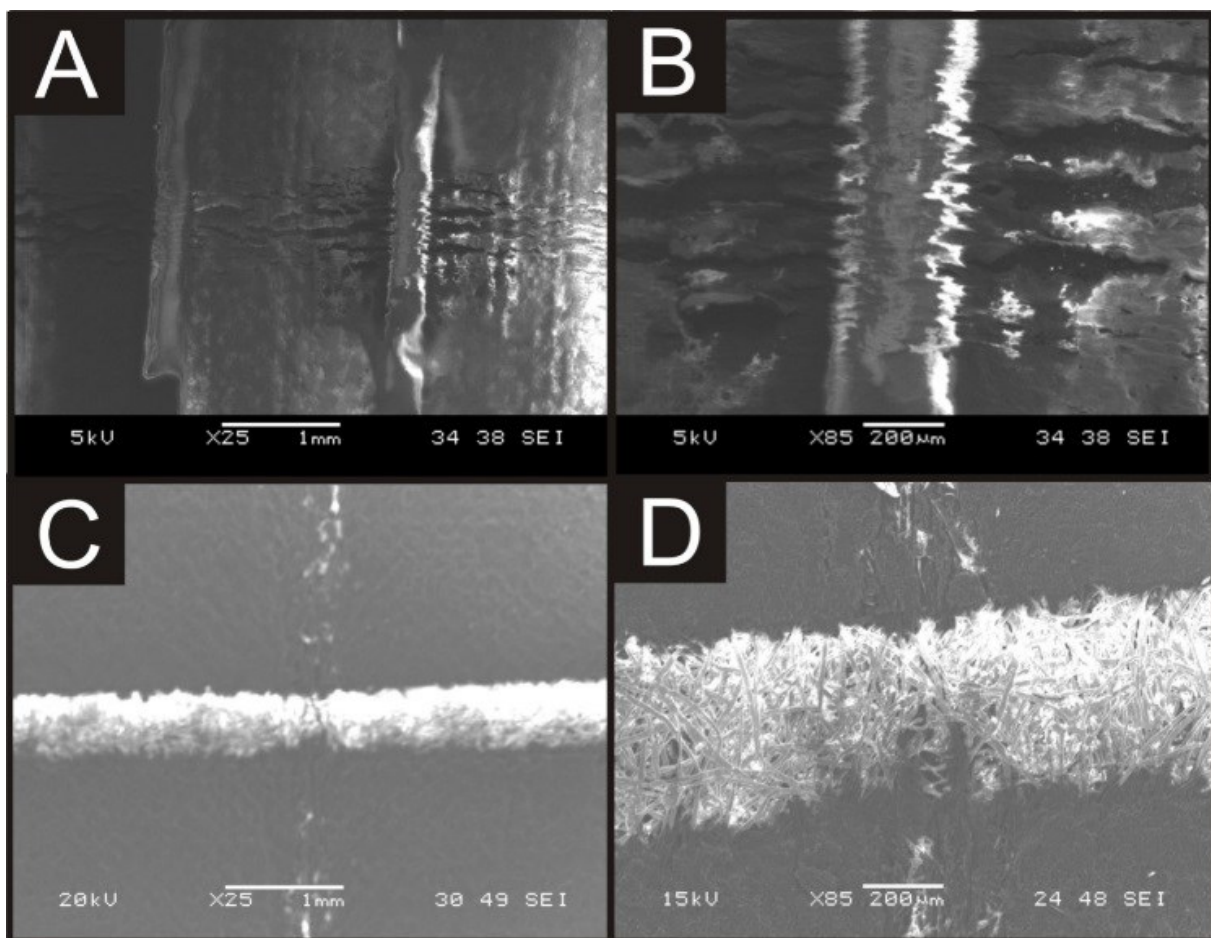


Figure 3.8: SEM images of the conductive track of a carbon screen-printed electrodes on polyester-substrates (A and B) and a paper-based substrate (C and D, prior to coating with nail varnish and Sellotape™ respectively), following 60 minutes contorted at an angle of 45° at magnifications of x 25 (A & C) and x 85 (B & D).

Finally, the effect of *repeated* mechanical stress upon the three SPE sensors was analysed. For continuity, the same electrochemical probes, potassium ferrocyanide (II) and NADH were utilised. The sensors underwent mechanical stress at an angle of 45°, the most aggressive contortion angle, though in this instance rather than time, the effect of the number of contortion/bends was explored over a range of 0 to 100 contortions.

In the case of the redox probe potassium ferrocyanide (II), Figure 3.9 reveals that the ps-SPE demonstrates minimal effects in terms of electrochemical performance as a result of mechanical stress with the voltammetric peak current, and additionally both the peak-to-peak separation, remaining largely unchanged up to 100 contortions at an angle of 45°. In contrast, the pv-SPE, was found to exhibit a decrease in the observed voltammetric peak current over the number of contortions studied and an increase in the peak-to-peak separation upon 100 contortions. The standard-SPE was determined to perform the worse with complete loss of electrochemical response.

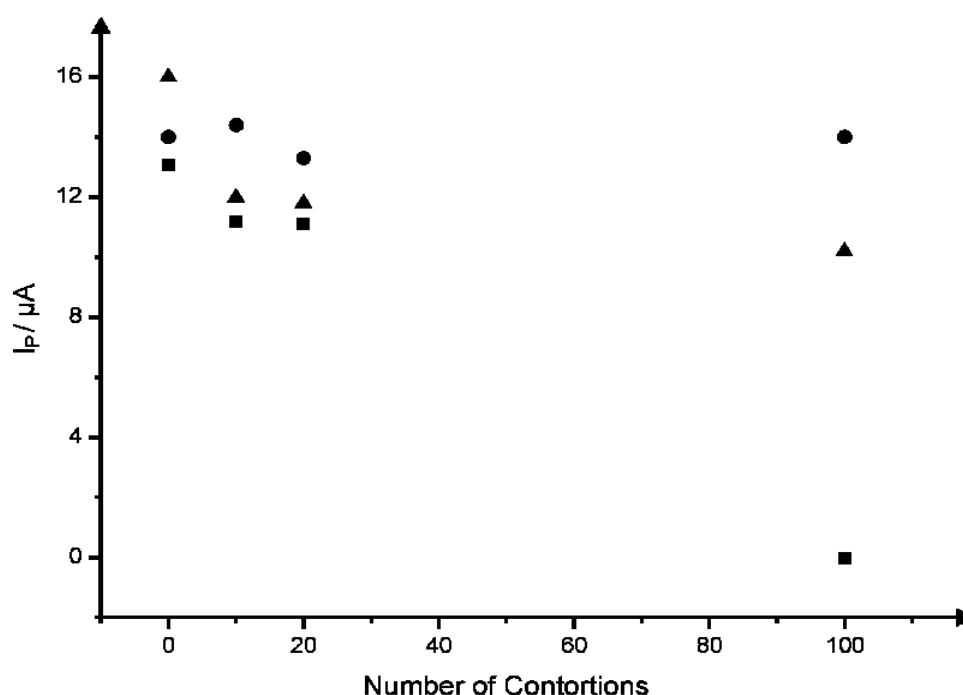


Figure 3.9: The effect of numerous and consecutive contortions to an angle of 45° on voltammetric peak current (I_p), in a solution of 1 mM potassium ferrocyanide (II) / 0.1 M KCl when utilising the standard-SPE (squares), ps-SPE (circles) and pv-SPE (triangles). Scan rate: 100 mV s⁻¹. N = 3.

When used for the monitoring of 100 μM NADH in a pH 7 phosphate buffer solution, the sensors demonstrated behaviour close to that observed in potassium ferrocyanide (II) with the paper-based sensors providing a more robust performance. Figure 3.10 depicts plots of voltammetric peak currents derived from cyclic voltammetric analysis in the solution of NADH after the set numbers of contortion applied to the sensors. As was the case for potassium ferrocyanide (II), the ps-SPE is shown to offer the most stable electrochemical performance in relation to repeated mechanical stress. Evidently when utilising the ps-SPE where after 20 contortions there is an increase in the

voltammetric peak current and additionally a shift in the peak potential to a more electropositive potential. Further to this after 100 contortions the voltammetric signal is found to diminish greatly.

The other paper-based sensor, the pv-SPE, exhibited a decrease in the recorded voltammetric peak current but notably, no change in the oxidative peak potential. Unlike the ps-SPE, the pv-SPE was found to fail after 100 contortions with no signal or voltammetric peak being recorded. Once more it was confirmed that of the sensors utilised, the standard-SPE, printed upon the polymer substrate was most susceptible to the effects of mechanical stress with notable effects on the voltammetric peak current after 20 contortions and a shift in the voltammetric potential, to that of a more electropositive region, for the oxidation of NADH occurring after 10 contortions. Further to this, as was noted for the ps-SPE, no signal was observed after 100 contortions suggesting that the electrical connections of the electrode had been compromised.

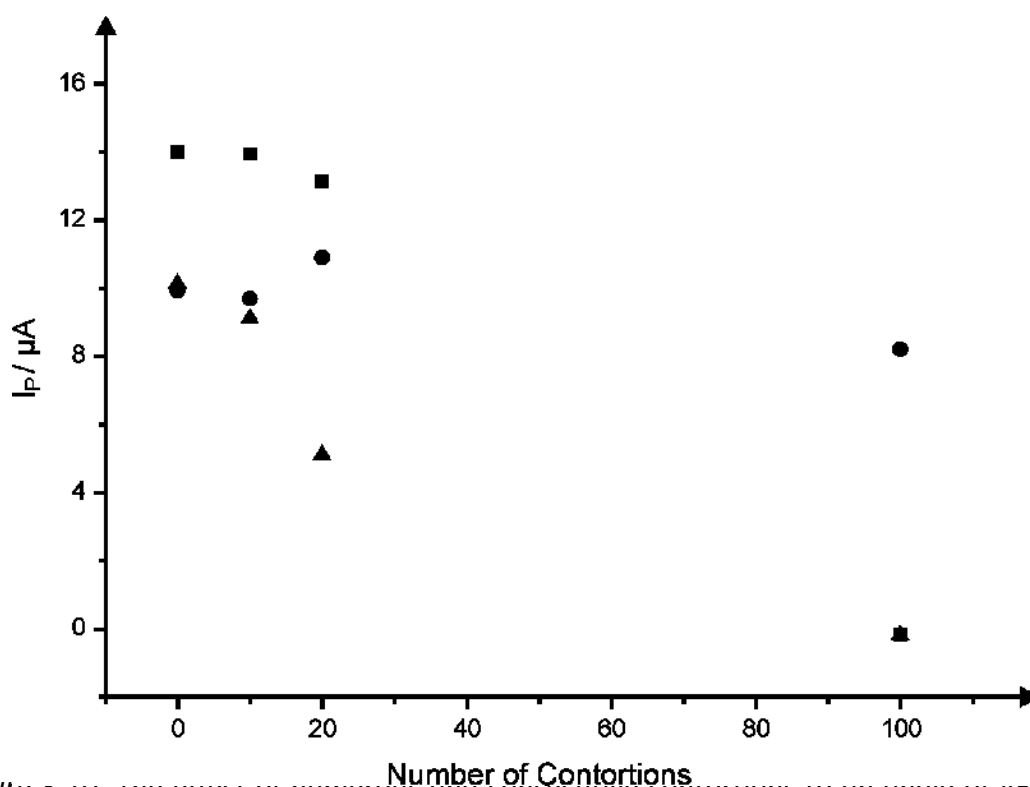


Figure 5.10. The effect of numerous and consecutive contortions to an angle of 45° on voltammetric peak current (I_p), in a solution of $100 \mu M$ NADH in a pH 7 phosphate buffer solution when utilising the standard-SPE (squares), ps-SPE (circles) and pv-SPE (triangles). Scan rate: $100 mV s^{-1}$. $N = 3$.

3.1.4 Conclusions

It has been demonstrated in this Chapter that screen-printed electrodes based upon a polyester substrate are not as flexible and durable as initially thought. Throughout the literature there has been an over running theme that screen-printed electrodes had no limitations and were seen as very flexible as they are easy to manipulate but this study proves that excessive mechanical contortion and stress can have very detrimental effects upon the electrochemical response/activity. However, this study has also shown the ultra-flexibility of paper based screen-printed which can undergo mechanical contortion/stress and are potentially useful for use in such environments where this would be encountered, such as in single-use wearable or “on-body” sensors. However, the downside is that the initial electrochemical response at the paper-based sensors is worse in comparison to the polymeric based sensors, in terms of peak characteristics (height, potential, shape) which is likely due to the way the ink is adhered to the surface.

The next section considers the application of these flexible substrates and introduces for the first time an ultra-flexible polyester alternative to that paper electrodes.

3.2 Ultra-Flexible Screen-Printed Graphitic Electroanalytical Sensing Platforms

3.2.1 Introduction

It was previously reported within section 3.1 that a limitation of the paper-based sensors was due to the absorption of water via the cellulose substrate where wicking of the solution occurred causing shorting of the electrical circuit. Therefore insulation of the sensor with Sellotape™ is required,⁹³ a problem not faced by previously used polyester-based substrates.

In this section, alternative substrates for screen-printed electrodes are explored. The consideration of the often overlooked factor of screen-printed electrodes fabricated upon an alternative to both the traditionally utilised ceramic- and polyester-based substrates by considering paper-, tracing-paper based substrates and additionally a *new* ultra-flexible polyester-based sensor (150 µm thick polyester substrate). This ultra-flexible polyester substrate demonstrates electrochemical performances equalling previously reported polyester⁹³ and paper-based sensors⁹⁴ towards the redox probes hexaammineruthenium (III) chloride and potassium ferrocyanide (II), even after extensive mechanical contortion. Throughout this section, the comparison of these ultra-flexible polyester screen-printed electrodes against other flexible paper-based screen-printed electrodes is made in areas such as electrochemical performance, kinetics and mechanical manipulation. Application of these ultra-flexible screen-printed electrodes is reported for the first time for electroanalytical sensing, where the working electrode is modified with the electrocatalyst cobalt (II) phthalocyanine (CoPC). This system is benchmarked towards the model analytes citric acid and hydrazine, demonstrating excellent sensing capabilities when compared to previously reported screen-printed electrodes.

Two new configurations of ultra-flexible electrochemical sensing platforms that do not need excessive insulation to prevent water ingress are explored.⁹³ To that end tracing paper and ultra-flexible polyester substrates have been explored, for the first time.

3.2.2 Results and Discussion

Substrate Optimisation utilising Electrochemical redox probes: potassium ferrocyanide (II), hexaammineruthenium (III) chloride and NADH

First the electrochemical characterisation of the graphitic SPEs was benchmarked using the electrochemical redox probes potassium ferrocyanide (II) and hexaammineruthenium (III) chloride. Figure 3.11 depicts scan rate studies for the ultra-flexible SPE (F-SPE) towards potassium ferrocyanide (II) and hexaammineruthenium (III) chloride.

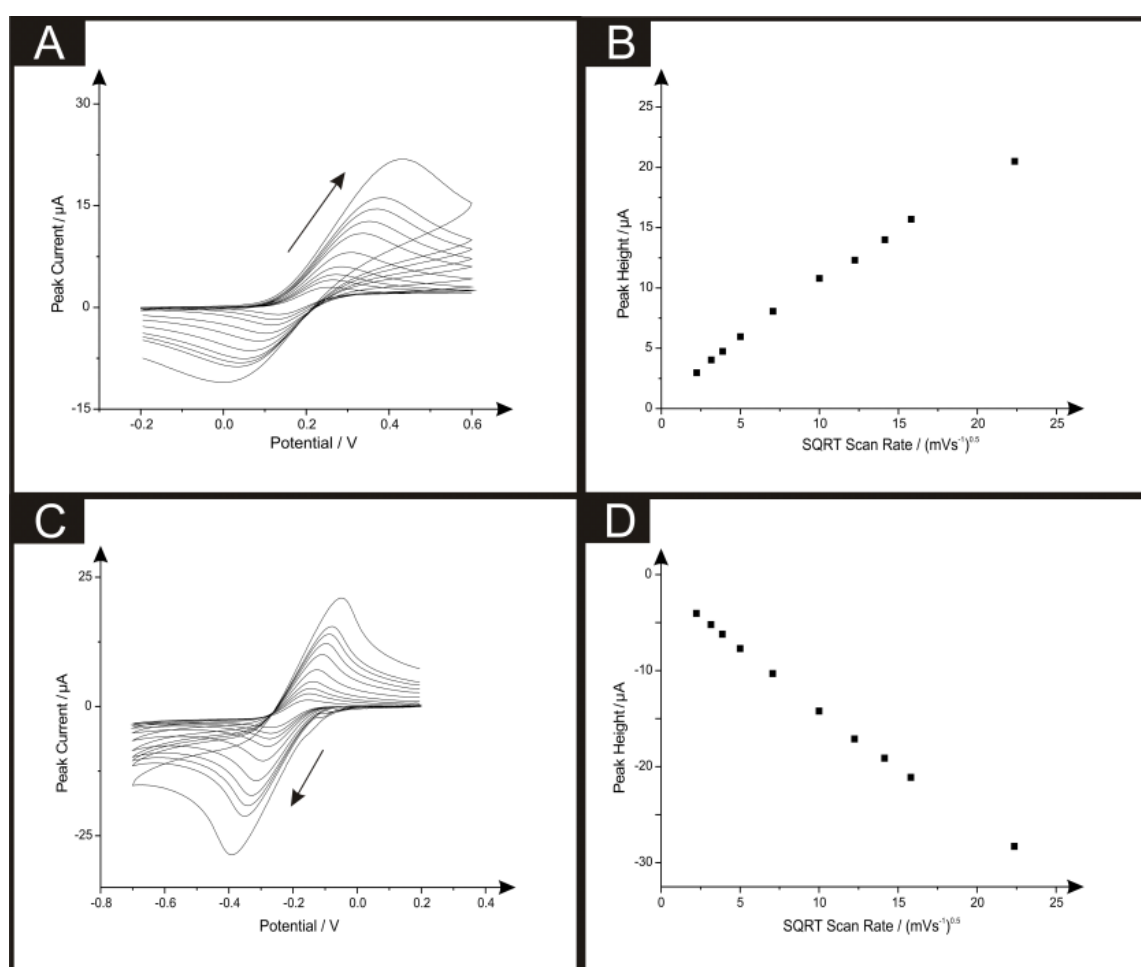


Figure 3.11: Typical cyclic voltammograms and a plot of peak height vs. square root of scan rate for increasing scan rates (5 mV s^{-1} to 500 mV s^{-1}) using a F-SPE (A & B respectively) recorded in 1 mM potassium ferrocyanide (II) / 0.1 M KCl and 1 mM hexaammineruthenium (III) chloride / 0.1 M KCl (C & D).

The heterogeneous rate transfer constants were calculated for both redox probes using the Nicholson method described in equation (1.26). It is noted that such values (shown in Table 2.1) are in agreement with prior work using graphitic screen-printed electrodes upon polyester substrates⁹⁴ suggesting that the printed sensors are electrochemically useful and the underlying/supporting electrode material has no effect on the electrochemical response compared to other polyester electrodes. Within this study it is found that the SPEs printed upon the tracing paper deteriorated significantly upon prolonged exposure to the aqueous solution resulting in deformed and un-useable electrodes; therefore any future electrode characterisations were carried out using standard-SPEs, F-SPEs and P-SPEs.

Previously, the mechanical contortion of paper-based and polyester SPEs have been studied, where it was found that in the case of the latter, the electrochemical capabilities decreased dramatically upon electrode contortion, while the paper-based sensors exhibited a greater resilience as evaluated with the analyte NADH.⁹³ The cyclic voltammetric response towards the electrochemical oxidation of NADH was found to exhibit a clear defined oxidation peak at $\sim +0.45$ V (vs. SCE) for the standard-SPE and $\sim +0.50$ V for P-SPE and F-SPE all recorded at a scan rate of 100 mV s^{-1} . Figure 3.12 depicts the electrochemical performance of P-SPE, F-SPE and standard-SPEs (utilising a new electrode after each addition) towards additions ($10 \text{ }\mu\text{M}$ to $100 \text{ }\mu\text{M}$) of NADH into a pH 7.5 phosphate buffer solution (PBS). From inspection of Figure 3.12 and the electroanalytical performances of the electrodes, it is clear there are no major differences between the F-SPE and standard-SPE in terms of electrochemical performance, however the P-SPE shows a slightly reduced performance towards the sensing of NADH: P-SPE: $I_p / \mu\text{A} = 9.95 \times 10^{-3} \mu\text{A M}^{-1} + 0.18 \text{ }\mu\text{M}$; $R^2 = 0.98$, $N = 10$; F-SPE: $I_p / \mu\text{A} = 1.17 \times 10^{-2} \mu\text{A M}^{-1} + 0.28 \text{ }\mu\text{M}$; $R^2 = 0.98$; $N = 10$; standard-SPE: $I_p / \mu\text{A} = 1.37 \times 10^{-2} \mu\text{A M}^{-1} + 0.06 \text{ }\mu\text{M}$; $R^2 = 0.98$, $N = 10$). It is believed that this is likely due to active electrode area available to adhere to the underlying substrate. The limit of detection (3σ) for NADH sensing using the P-SPE, standard-SPE and F-SPE is found to correspond to $2.95 \text{ }\mu\text{M}$, $1.90 \text{ }\mu\text{M}$, and $2.43 \text{ }\mu\text{M}$, which is in good agreement to previous electroanalytical sensing of NADH, utilising paper-based sensors ($1.8 \text{ }\mu\text{M}$)⁹⁴ indicating that screen-printed

electrodes fabricated using this new electrode substrate (ultra-flexible plastic) are potentially electroanalytically useful.

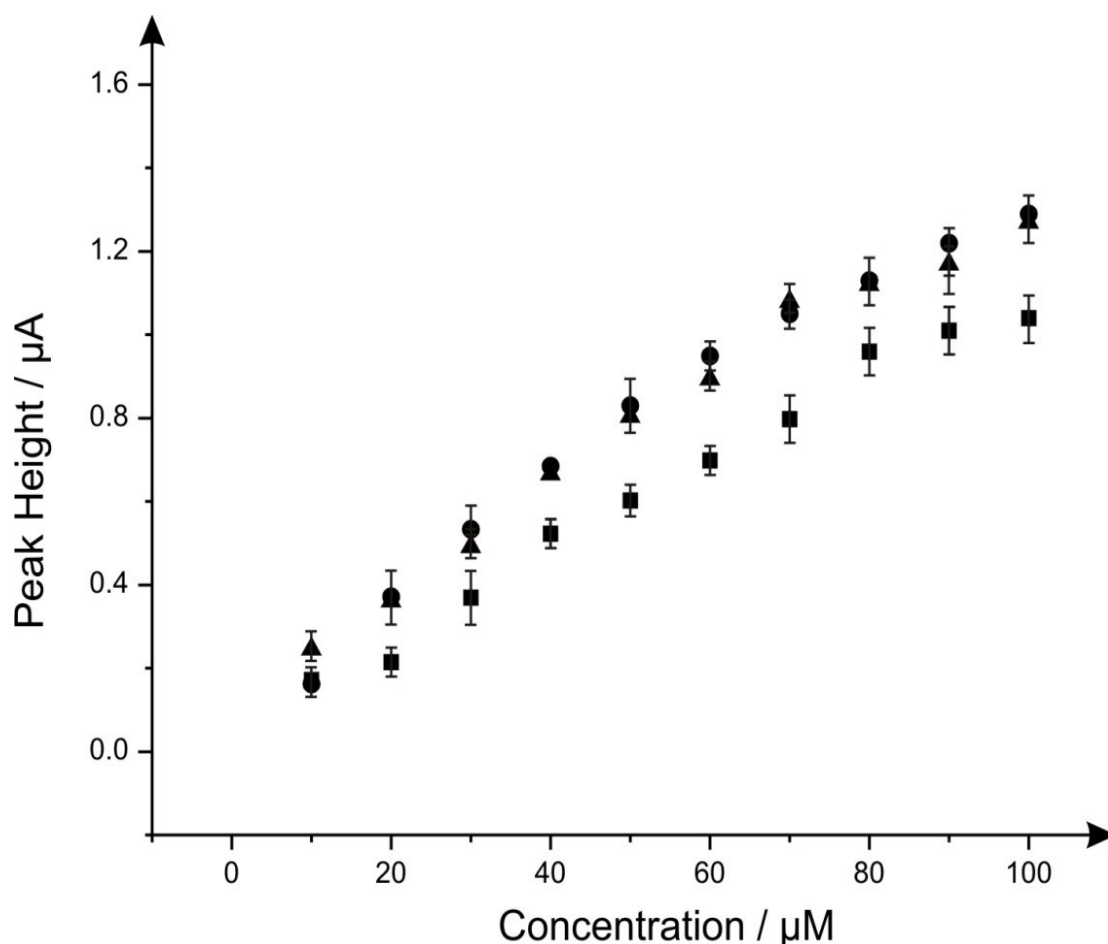


Figure 3.12: Calibration plots resulting from the additions of NADH (10 to 100 μM) into pH 7.5 PBS using new P-SPEs (squares), standard-SPEs (circles) and F-SPEs (triangle) after each addition. Scan rate: 100 mV s^{-1} using cyclic voltammetry. $N = 3$.

Figures 3.13 A, B, C depict cyclic voltammetric responses for P-SPE, F-SPE and standard-SPE which have been mechanically contorted numerous times and are then evaluated towards the electrochemical oxidation of NADH. It is apparent that the standard-SPEs show a relatively large decrease in voltammetric peak height (I_p / μA) compared to that of the P-SPEs and F-SPEs (see Figure 3.13 D). These results provide a clear indication that such substrate replacement could be utilised instead of the previously used flexible paper-based sensors since they can be mechanically contorted

yet still provide useful electrochemical performances. These ultra-flexible polyester substrates have a significant advantage over paper-based sensors as they do not need to be further insulated with Sellotape™ as is the case for the paper-based sensors whilst still offering exceptional flexibility and electrochemical capabilities.

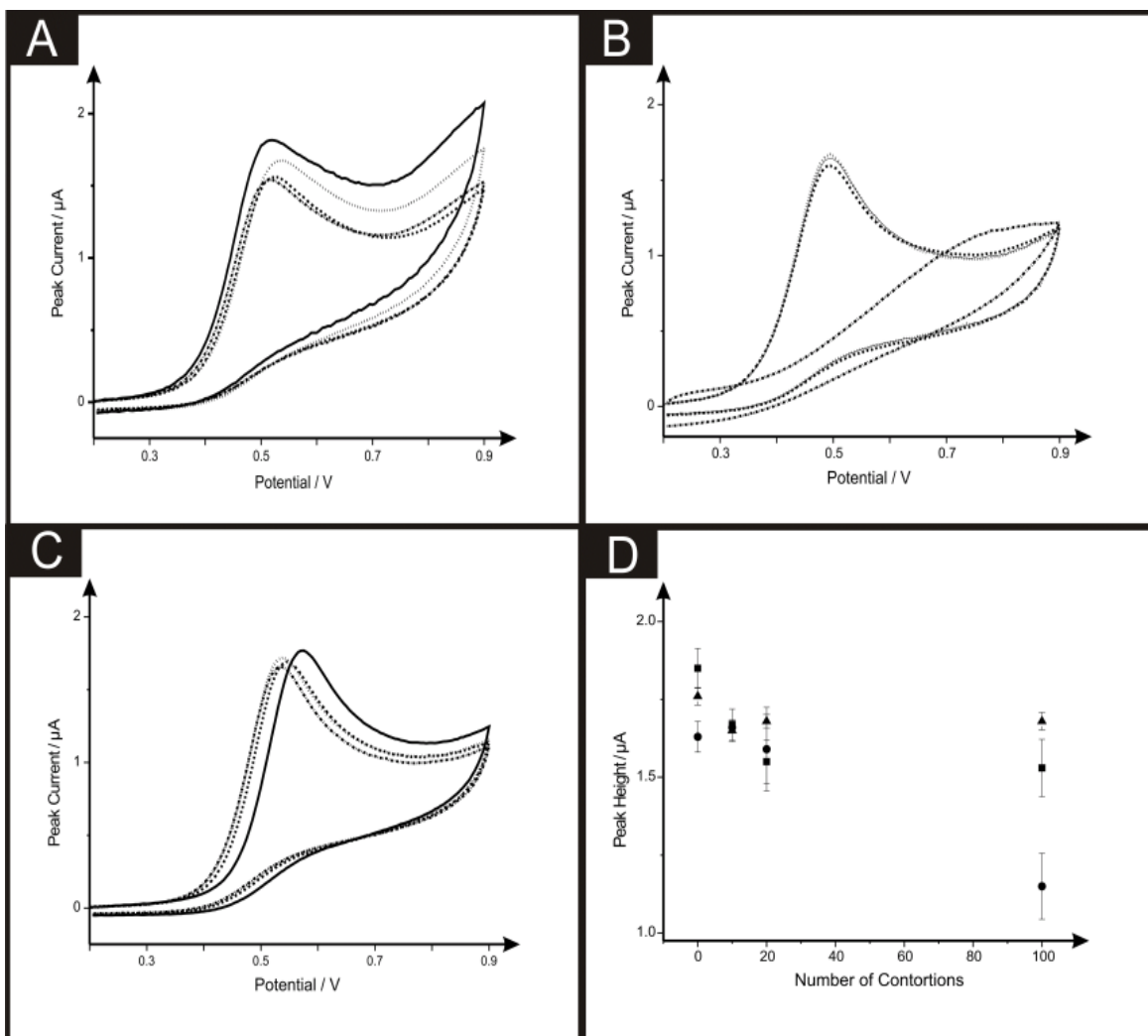


Figure 3.13: Cyclic voltammograms depicting the effect of mechanical contortion upon the voltammetric response when contorted at an angle of 45° over a range of 0 (solid line), 10 (dashed line), 20 (dotted line), 100 contortions (dash-dotted line) towards the P-SPE (A), standard-SPE (B), F-SPE (C) recorded in a solution of $100 \mu\text{M}$ NADH in a pH 7.5 PBS. Also shown is a plot showing peak height ($I_p/\mu\text{A}$) vs. number of contortions (D) for P-SPE (squares), standard-SPE (circles), F-SPE (triangles). Scan rate: 100 mV s^{-1} . $N = 3$.

Effect of Mechanical Contortion upon a CoPC modified SPE: Detection of Citric Acid

The analytical detection of the model analytes was next performed utilising the two different substrates, printing paper and the ultra-flexible polyester, when the working electrode contained the electrocatalyst, CoPC; to the best of our knowledge such sensor configurations have not been reported. The first analyte explored is citric acid, which is a weak acid that is regularly used within the food and beverage industry (as an additive), however due to its excellent chelating properties it is used within other industries such as metal plating, textiles and water softening.¹⁰³ Honeychurch and co-workers have reported the first example of a CoPC modified carbon screen-printed electrode (printed upon a PVC support) towards the electrocatalytic sensing of citric acid.¹⁰⁴ Figure 3.14 shows the voltammetric responses for the oxidation of citric acid where it is clear that in comparison to the standard-SPE the only voltammetric signals obtained are at the CoPC modified carbon working electrodes with an oxidation peak varying from $\sim + 1.00$ V (vs. SCE) to $\sim + 1.20$ V (vs. SCE). It is clear that prior to the oxidation peak (at the previously stated potentials), there is an initial oxidation of Co^{2+}PC to Co^{3+}PC . In addition to this peak, there is also an oxidation peak upon the reverse scan implying that there is still further oxidation of the $\text{Co}^{2+} / \text{Co}^{3+}$ couple.

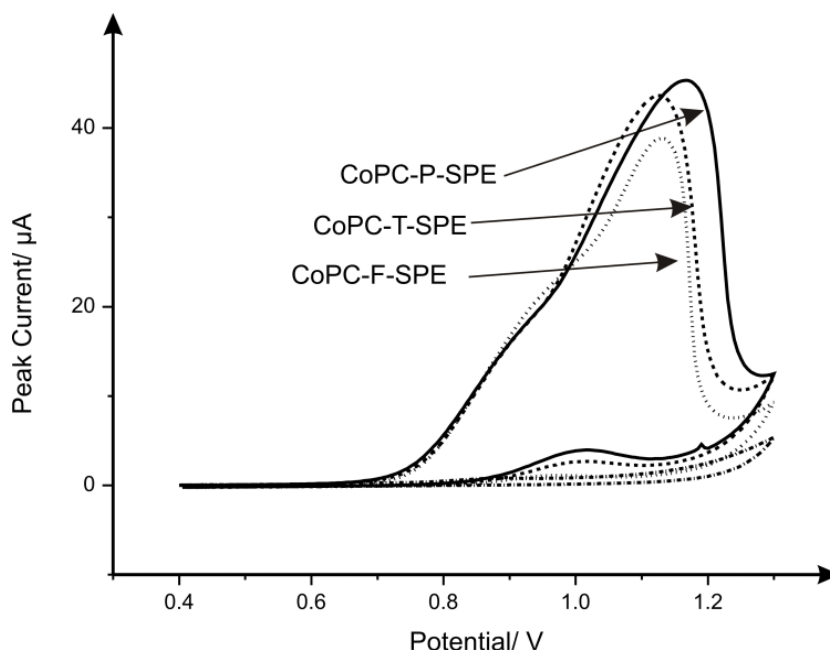
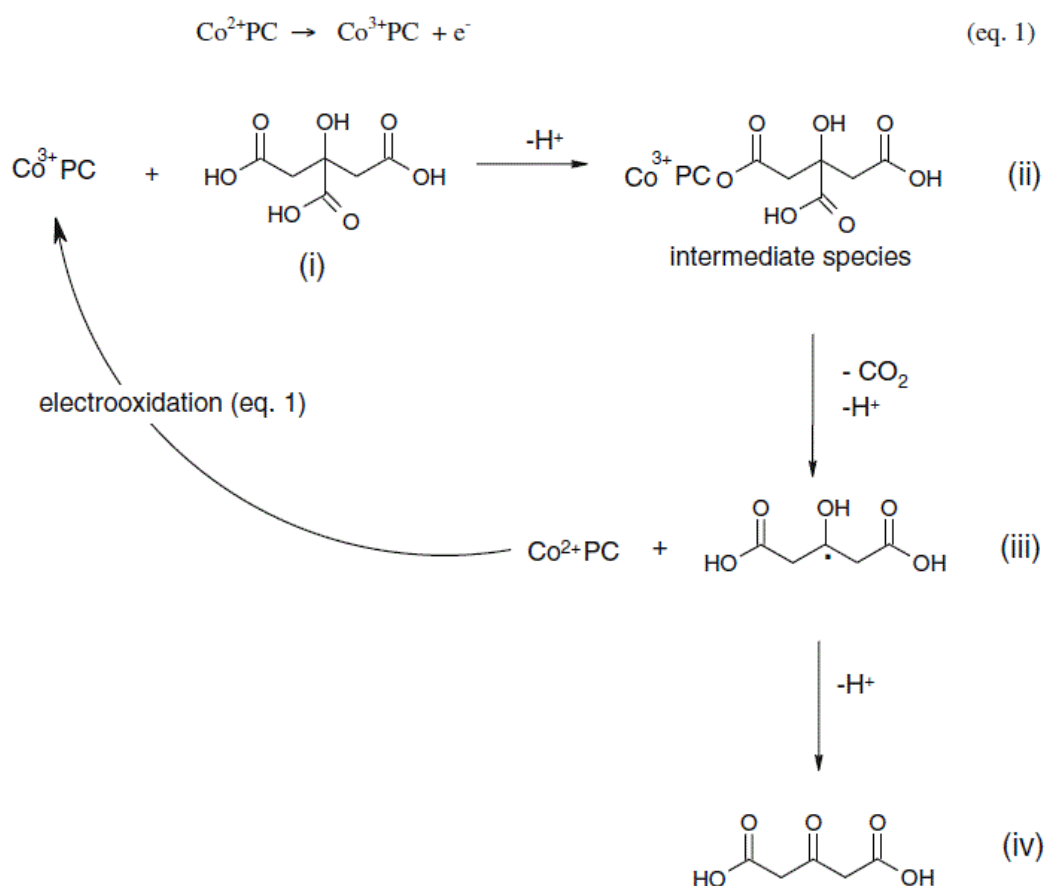


Figure 3.14: Cyclic voltammograms show the response of the CoPC-P-SPE (solid line), CoPC-T-SPE (dotted line) and CoPC-F-SPE (dashed line) recorded in a pH 7.5 PBS containing 10 mM citric acid. Scan rate: 100 mV s^{-1} . Also shown is the response of the blank (standard SPE, no CoPC) showing that the electrochemical response is due to the CoPC contained within the working electrode.

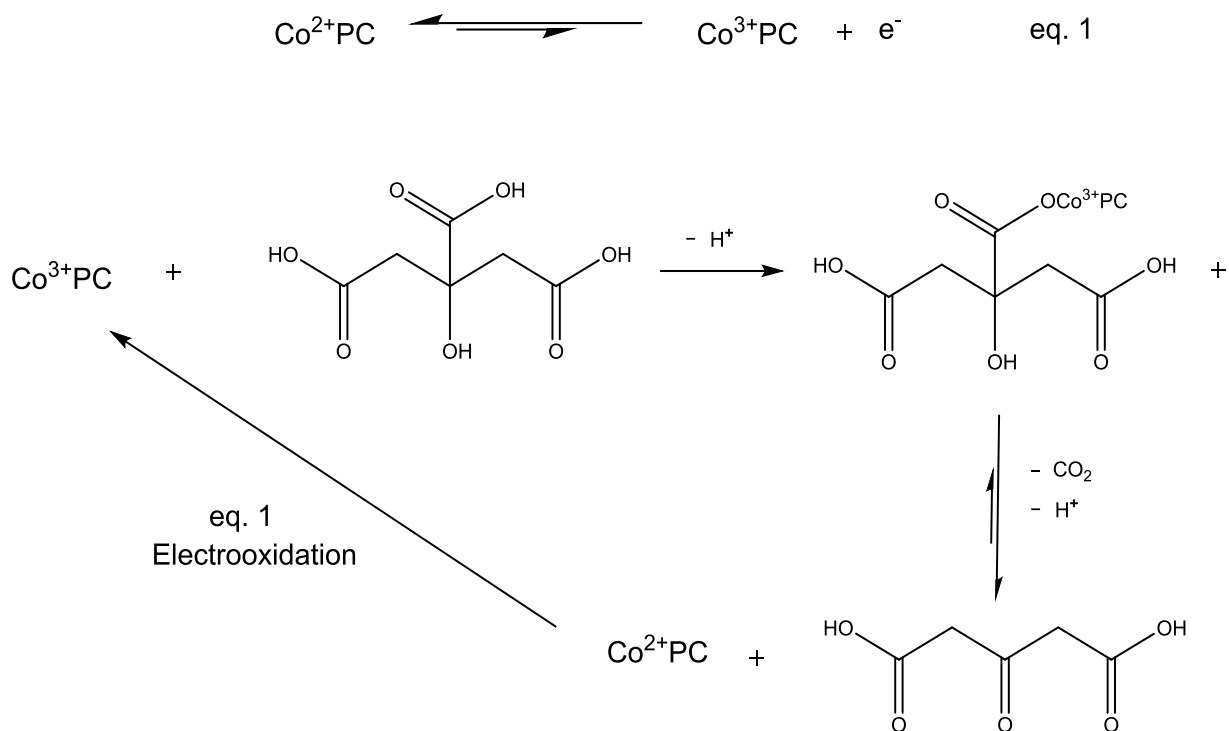
Next, attention was turned to exploring the effect of pH upon the electroanalytical response of 10 mM citric acid using the CoPC SPEs. Gradient values of 59.93 mV / pH for CoPC-P-SPEs, 60.82 mV / pH for CoPC-T-SPEs and 56.18 mV / pH for CoPC-F-SPEs were obtained which is in good agreement with Honeychurch *et al.*¹⁰⁴ who reported a value of 60.70 mV / pH using CoPC-SPEs. Such gradient values obtained are close with that expected for an equal proton and electron system ($59 \text{ mV per pH unit at } 298\text{K}$) as deduced from equation (3. 1):

$$E_{f,eff}^0 = E_f^0 \left(\frac{A}{B} \right) - 2.303 \frac{mRT}{nF} \text{pH} \quad (3. 1)$$

where E_f^θ is the formal potential, m is the number of protons, n is the number of electrons. It is noted, that the pK_a values for the carboxylic groups of citric acid are 3.13, 4.76 and 6.40¹⁰⁴ but voltammetric peaks for the catalytic oxidation of citric acid could be readily identified across the entire pH range studied as has been reported previously by Honeychurch *et al.*¹⁰⁴. Honeychurch *et al.* postulated the electrochemical mechanism to be a EC' type reaction, as shown in scheme 1 A¹⁰⁴ however here is a revised mechanism (presented in scheme 1 B) which suggests that the CoPC molecule attaches upon the carboxylic acid group which is closest to the hydroxyl group (α -carbon) to enable its oxidation, as seen within literature.^{105, 106}



Scheme 1 A (above): Reaction mechanism reported by Honeychurch *et al.*¹⁰⁴ for the electrocatalytic oxidation of citric acid using CoPC-SPEs.



Scheme 1 B (above): New proposed reaction mechanism of the electrocatalytic oxidation of citric acid using CoPC-SPEs.

Focus next turned to the exploring the electroanalytical response of citric acid within a model system utilising the CoPC-SPEs; pH 7.5 was chosen based on previous work.¹⁰⁴ Figures 3.15 A, B and C show the resultant calibration plots ($I_p^{\text{Ox}} / \mu\text{A}$ vs. citric acid concentration) for the three CoPC-SPEs used throughout which gave rise to the following analytical data: CoPC-P-SPE: $I_p / \mu\text{A} = 0.80 \mu\text{A mM}^{-1} + 1.50 \text{ mM}$; $R^2 = 0.95$, $N = 10$; CoPC-T-SPE: $I_p / \mu\text{A} = 0.93 \mu\text{A mM}^{-1} + 0.03 \text{ mM}$; $R^2 = 0.94$, $N = 10$; CoPC-F-SPE: $I_p / \mu\text{A} = 1.04 \mu\text{A mM}^{-1} - 0.52 \text{ mM}$; $R^2 = 0.99$, $N = 10$. Interestingly, the ultra-flexible polyester substrate yields an improved response for the detection of citric acid, however due the rapid deterioration of the paper-based sensors the practicality of CoPC-P-SPEs and CoPC-T-SPEs was questionable therefore CoPC-F-SPEs are the ideal substrate platform for this analyte. The limit of detection (3σ) for citric acid was calculated to be 0.37 mM for CoPC-F-SPEs compared to 0.78 mM for CoPC-P-SPEs, 0.85 mM for CoPC-T-SPEs. Honeychurch *et al.*¹⁰⁴ reported a similar limit of detection of 0.20 mM using CoPC-SPEs, whilst Nascimento *et al.*¹⁰⁷ showed a slightly improved limit of detection of 0.11 mM with the incorporation of the CoPC within a carbon paste electrode. Note that

Nascimento *et al.* used a flow injection amperometric analysis method was utilised accounting for the improved limit of detection.

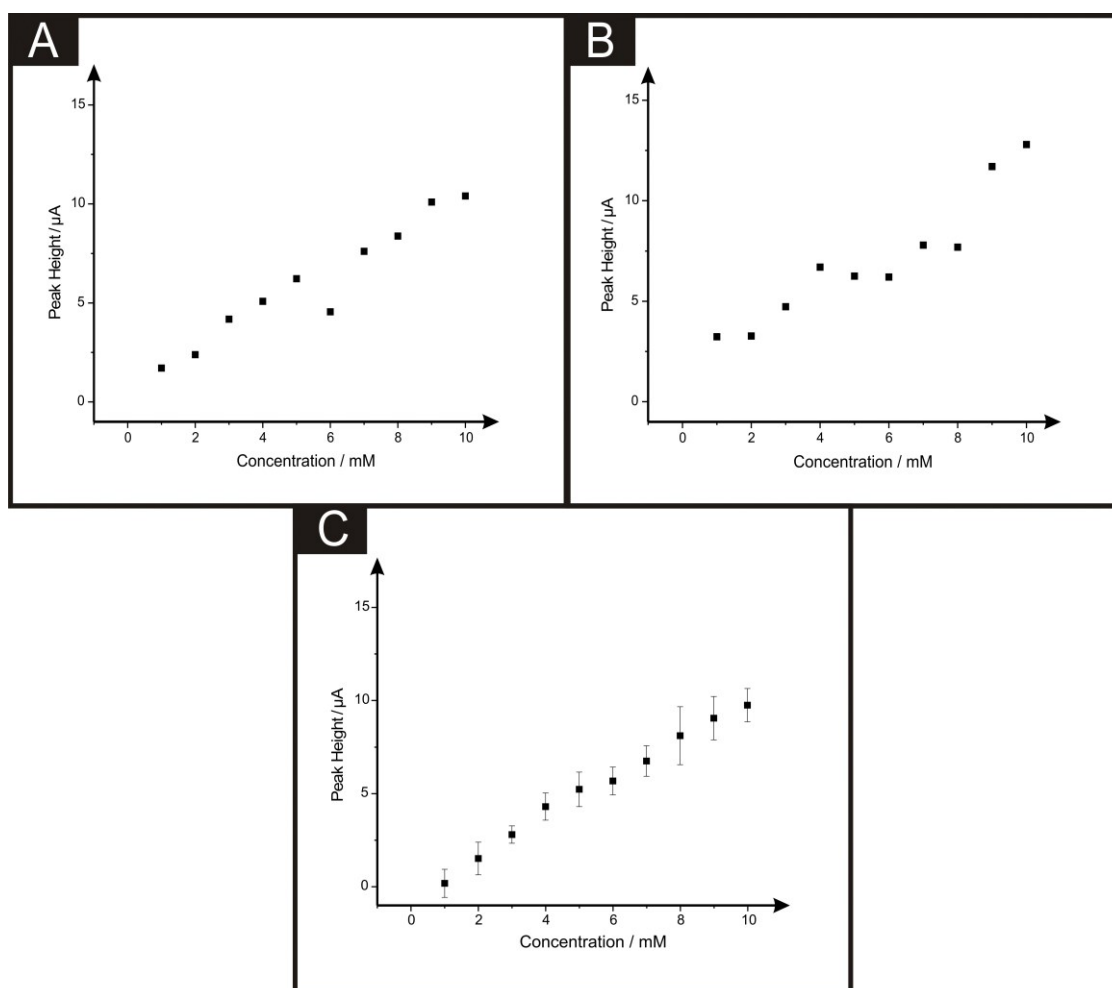


Figure 3.15: Calibration plots resulting from the additions of citric acid (1 to 10 mM) / pH 7.5 PBS using a different CoPC-P-SPE (A), CoPC-T-SPE (B) and CoPC-F-SPE (C) following every addition. Scan rate: 100 mV s^{-1} . $N = 3$.

Effect of Mechanical Contortion upon a CoPC modified SPE: Detection of Hydrazine

The electrochemical detection of hydrazine was next considered. Hydrazine has many uses within a plethora of key industries as a blowing agent, due to its immense capabilities as a reducing agent. However, there have been extensive reports focusing on its detrimental effects upon the human body, such as: irritation of the eyes, nose, and throat, dizziness, headache, nausea, pulmonary oedema, seizures, and coma in humans.¹⁰⁸⁻¹¹⁰ The electrochemical determination of hydrazine was trialled using the CoPC-F-SPEs, which were selected as they were deemed the most robust of the fabricated sensors. Figure 3.16 A shows the effect of 1 mM hydrazine using the CoPC-F-SPEs at a set scan rate of 100 mV s^{-1} showing an oxidation peak at +0.50 V, thus clarifying successful electrocatalytic oxidation of the compound, hydrazine.

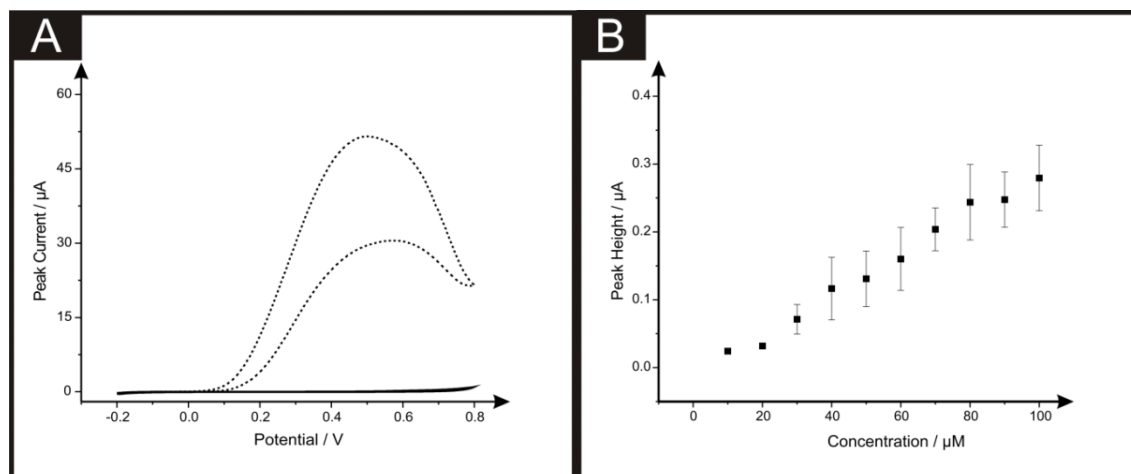
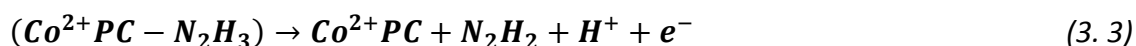


Figure 3.16: Cyclic voltammograms (A) showing a blank solution of pH 7.5 PBS (solid line) and in the presence of 1mM hydrazine / pH 7.5 PBS using CoPC-F-SPE (dashed line). B is a calibration plot showing the consequent additions of hydrazine (10 to 100 μM) into pH 7.5 PBS using a different CoPC-F-SPE following each addition of hydrazine. Scan rate: 100 mV s^{-1} . $N = 3$.

Typically for the detection of hydrazine, modified carbon electrodes are readily used¹⁰⁸ and there are many reports clarifying the successful detection of hydrazine upon modification of an electrode with transition metals.^{108, 111, 112} Zagal *et al.* have reported many articles on the effects of CoPC and derivatives upon the reaction with hydrazine and they have proposed a redox-catalysis mechanism involving $\text{Co}^{3+} / \text{Co}^{2+}$ and the electrochemical reduction by the analyte of CoPC is shown in equations (3. 2) and (3. 3).



A scan rate study was performed with the response of the CoPC-F-SPEs shown in (Figure 3.15). A plot of voltammetric peak height vs. square root of scan rate yields a linear response with hydrazine ($I_p/\mu\text{A} = 1.17 \mu\text{A} / (\text{V s}^{-1})^{1/2} + 9.45 \mu\text{A}$, $R^2 = 0.95$, $N = 10$). A plot of log peak height against log scan rate was also found to be linear (see Figure 3.15 C) with a gradient of 0.47 observed ($\log I_p / \log \mu\text{A} = 0.47 (\log \mu\text{A} / \log \nu) + 0.81 \log \mu\text{A}$, $R^2 = 0.995$, $N = 11$). Both responses indicate a diffusion controlled process.

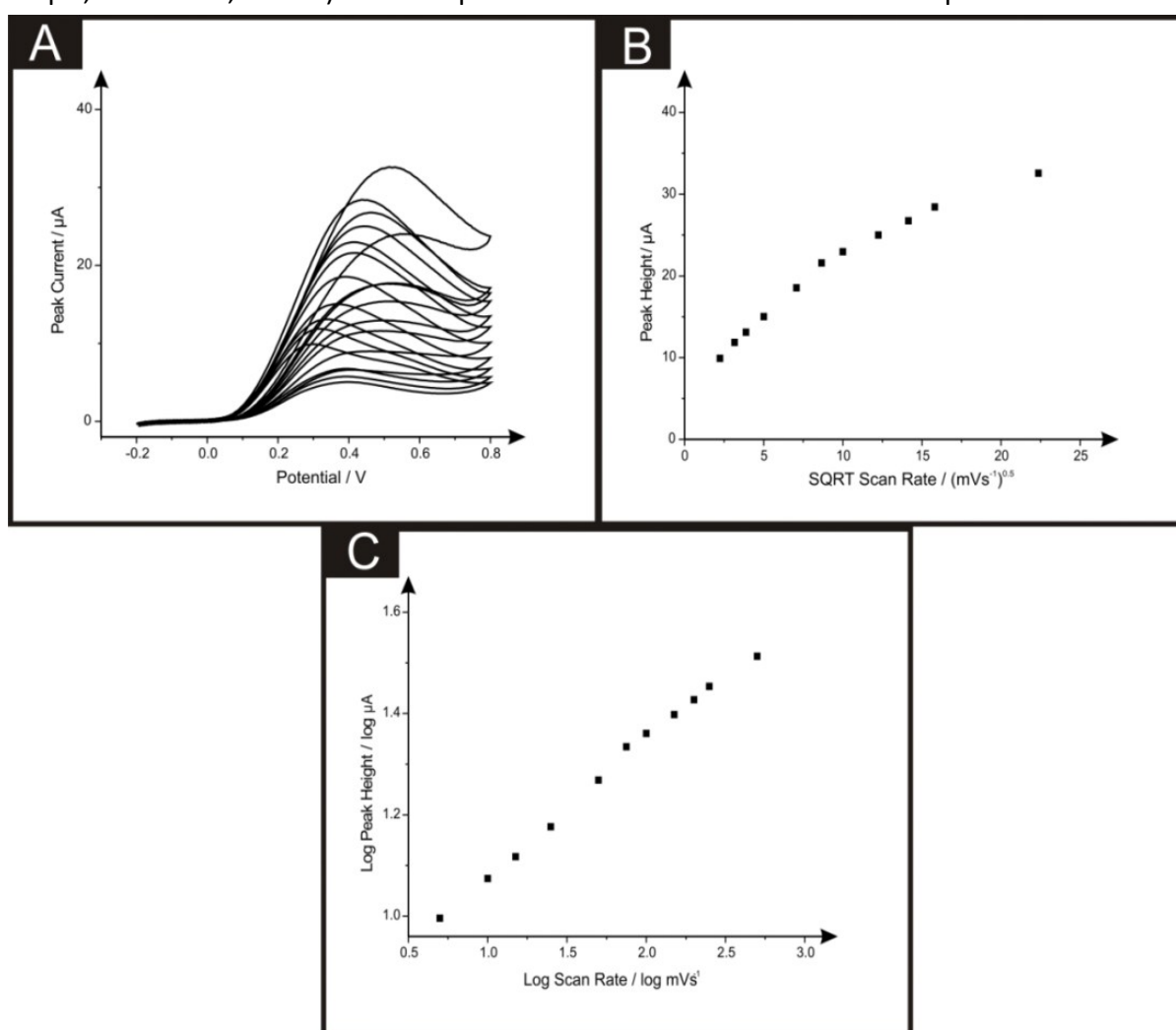


Figure 3.17: Cyclic voltammograms (A) performed over the range 5 to 500 mV s^{-1} recorded in a solution of 1mM hydrazine in pH 7.5 PBS using a different CoPC-F-SPE at each scan rate. Parts (B) and (C) show plots of the square root of the scan rate vs. peak height and logarithm of the peak height vs. logarithm of scan rate respectively. $N = 3$

Additions of hydrazine into a pH 7.5 phosphate buffer solution were next explored using the CoPC-F-SPEs. Figures 3.16 B show linear responses for the additions of (10 μM to 100 μM) hydrazine with the following analytical data found: CoPC-F-SPE: $I_p / \mu\text{A} = 3 \times 10^{-3} \mu\text{A} \mu\text{M}^{-1} - 0.04 \mu\text{M}$; $R^2 = 0.99$, $N = 10$. A limit of detection (3σ) was determined to correspond to 6.21 μM which is comparable to values of 4.60 μM previously reported by Ardakani *et al.*,¹¹⁷ using Alizarin as a mediator on a glassy carbon electrode, and also work provided by Sun *et al.*¹¹⁸ who reported a limit of detection of 1.00 μM for the direct oxidation of hydrazine using a boron-doped diamond film electrode. The first use of a CoPC derivative as a mediator towards hydrazine was reported by Ozoemena *et al.*¹¹⁹ who showed a limit of detection of 1 μM which is also in good comparison to the value determined from using the CoPC-F-SPEs. The catalytic rate constant for this system towards hydrazine was calculated to be $2.07 \times 10^5 \text{ M}^{-1} \text{ s}^{-1}$, again indicating a catalytic behaviour of the CoPC toward the target analyte.

Lastly, consideration of the voltammetric profiles recorded for the analytes citric acid and hydrazine towards the electrocatalytic effect of Co^{2+}PC with additional analysis of the cyclic voltammograms shown for all model analytes, (Figures 3.14 and 3.16). An alternative mechanism to those previously described for the oxidation of Co^{2+}PC to Co^{3+}PC , has been constructed explaining the cyclic voltammetry. As readily observed in these Figures a general trend of an additional oxidation peak upon the reverse sweep of the potential is seen at $\sim + 1.00 \text{ V}$ (citric acid) and $\sim + 0.40 \text{ V}$ (hydrazine); the origin of which has never been explained or addressed. Primarily in all these cases, the $\text{Co}^{2+} / \text{Co}^{3+}$ redox couple has a significantly smaller electrochemical response when not *in-situ* with model analytes, such as citric acid and hydrazine.



In the presence of an analyte, the reaction shifts to the right due to consumption of Co^{3+}PC . The electrochemical reaction becomes "visible" with the presence of a pre/shoulder peak prior the oxidation peak of the CoPC/analyte complex. Once the analyte has been oxidized the Co^{3+}PC is released from the complex with the analyte and it gets reduced, usually during this EC process. The Co^{2+}PC formed before, during the

reverse scan is giving an oxidation peak due to the half oxidation reaction above, since new analyte reaches the electrode surface (diffusion) and forces the Co^{2+}PC to get oxidized, seen in equation (3. 4). Figure 3.18 shows the effect of a secondary scan, towards the chosen model analytes, it is clear that upon the second scan the electrochemical response decreases, this is due to the system becoming diffusion limited after the first scan.

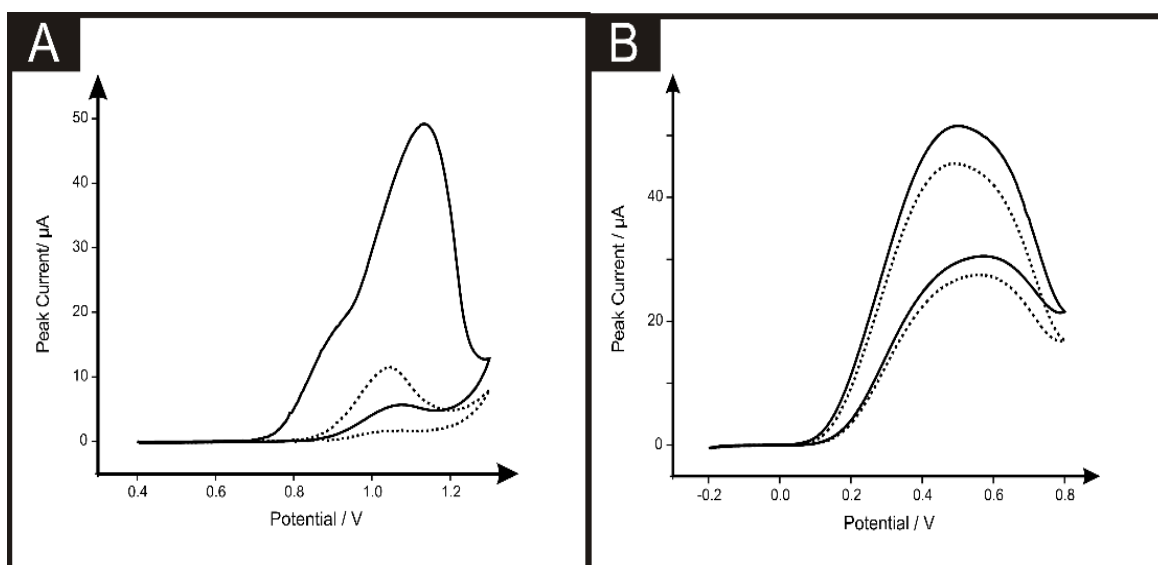


Figure 3.18: Cyclic voltammograms showing both the first (solid line) and second (dashed line) voltammetric scans upon the CoPC-F-SPEs utilising the model analytes (A) 10 mM citric acid in PBS pH 7.5 and (B) 1 mM hydrazine in PBS pH 7.5. Scan rate: 100 mV s^{-1} .

3.2.3 Conclusions

The development and evaluation of screen-printed electrodes with particular consideration upon the substrate of the foundation of the electrochemical sensors has been explored. The electrodes fabricated from the substrates, ranging from paper to ultra-flexible polyester materials, have not only been extensively interrogated with regard to their reproducibility and stability when placed under duress (as would be the case particularly for wearable sensors) and electrochemical performance through the utilisation of well-characterised redox probes, but also for the mediated determination of citric acid and hydrazine through the utilisation of a CoPC ink. It is found that the flexible plastic substrates can be used as an alternative to screen-printed electrode printing upon traditionally used (thicker) polyester and ceramic substrates since they give rise to comparable useful electrochemical performances and offer an ultra-flexible screen-printed sensing platform.

It is hoped that the development of such electrode substrates for use with screen-printing techniques could allow for the development of not only a plethora of novel sensing devices, but also potentially facilitate the further development of electrochemical devices which may have previously been limited by either the less flexible configurations comprising thicker polyester or ceramics, or the problems posed by the use of paper-based sensors owing to wetting. A critical comparison of substrate choice has been analysed for the first time, and introduces an ultra-flexible polyester as an alternative for paper based, which require extensive waterproofing treatment prior to application.

The next Chapter elaborates upon the utilisation of CoPC as electrocatalytic modifier upon carbon electrodes and for the first time compares the traditional drop-cast method with the screen-printed electrode systems used throughout this Chapter.

Chapter 4 - CoPC Modified Screen-Printed Electrodes

In this Chapter, consideration of objective 2.2 is demonstrated with the comparison of drop-casted and bulk modified screen-printed electrodes, which are benchmarked in terms of electroanalytical capabilities and electrochemical performances. Such work has been published within *Sensors* (2014, **14**, 21905).

4.1 Cobalt Phthalocyanine Modified Electrodes Utilised in Electroanalysis: Nano-Structured Modified Electrodes vs. Bulk Modified Screen-Printed Electrodes

4.1.1 Introduction

The importance of electrocatalysis continues to be a major interest to chemists and engineers since the ability to provide a 'clean' system which does not contaminate or foul the electrode surface is vital in a range of applications such as electroanalytical sensors, corrosion chemistry and energy conversion devices (*i.e.* hydrogen fuel cell and batteries) to name just a few.^{120, 121} The utilisation of organometallic compounds containing transition metals such as iron, cobalt and copper phthalocyanines has been a significant focal point.¹²²⁻¹²⁴ These macrocyclic compounds have been reported to exhibit electrocatalytic responses compared to the underlying (bare) supporting electrode substrate. For example the sensing of hydrogen peroxide has been extensively studied using metal phthalocyanines,¹²⁵⁻¹²⁷ and elegant work reported by Ozoemena *et al.*¹²⁸ have shown that a cobalt phthalocyanine (CoPC) - cobalt (II) tetraphenylporphyrin (CoTPP) - glucose oxidase - nafion layer modified glassy carbon can be usefully utilised for the sensing of glucose. Additionally, similar work by T. Kondo *et al.*¹²⁹ have reported a similar method utilising a boron-doped diamond electrode as the underlying electrode. Note that in both cases, electrocatalysis (*via* the modified CoPC electrodes) towards the sensing of hydrogen peroxide produced from the enzymatic reaction is reported compared to the bare underlying/supporting electrode substrate.^{128, 129} Other studies by Wring *et al.*¹³⁰ have reported CoPC to be electrocatalytic towards the analytes coenzyme A and reduced glutathione. CoPC has also been used extensively towards the sensing of hydrazine where in many cases the literature highlights its excellent

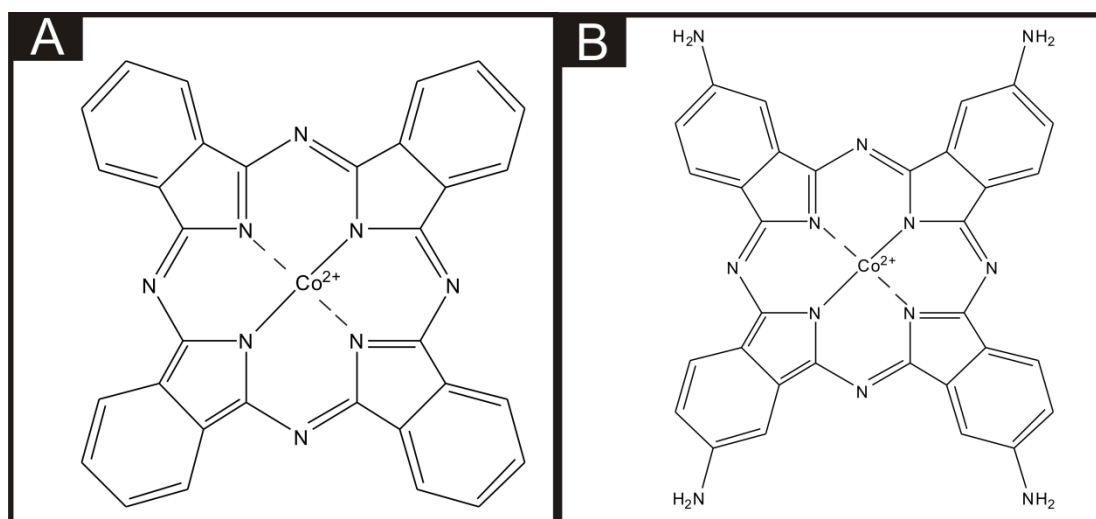
electrocatalytic properties,¹³⁰⁻¹³³ while additionally other toxic nitrogenous compounds such as aziprotryne¹³⁴ and amitrole¹³⁵ have been targeted.

Throughout the literature it is apparent that there are differences in the utilisation of metal phthalocyanines as an electrocatalytic material. There is a vast amount of literature concerning the drop casting technique of a dispersion of phthalocyanines (for example, CoPC within a suitable solvent) onto the surface of carbon based electrodes, and this technique has been utilised towards the sensing of many analytes with much prevail. For example, Caro *et al.*¹³⁶ studied the electrocatalytic effect of CoPC towards the sensing of nitrite using a CoPC modified vitreous carbon electrode. Other studies by Matemadombo *et al.*¹³⁷ have reported the sensing of L-ascorbic acid and have compared the use of surface modified graphitic screen-printed electrodes and a rotating disk electrode, with significant findings in favour for the use of screen-printed electrodes with electrocatalysis reported utilising the CoPC. Work by Wang *et al.*¹³⁸ explored the effect of nano-CoPC (shown in scheme 2 A) towards L-ascorbic acid as an ionophore, with promising electrocatalytic effects compared to a bare glassy carbon electrode. Similar studies by Agboola *et al.*¹³⁹ and Pillay *et al.*¹⁴⁰ have examined the effect of nano-CoPC towards analytes such as epinephrine, dopamine and ascorbic acid where in both instances improved electrochemical responses when combined with single-wall carbon nanotubes supported upon an EPPG have been demonstrated.^{139, 140} Such approaches are reported to encompass numerous benefits such as alterations in mass transport, a large specific surface area, high selectivity and control over microelectrode environment.¹⁴¹ Other work has reported bulk sulfonated-CoPC in a polypyrrole matrix for ammonia gas sensing,¹⁴² multi-walled carbon nanotubes-cobalt phthalocyanine (MWCNTs-CoPC) nanocomposites¹⁴³ and a graphene oxide-CoPC hybrid material as a new electrocatalyst for the electrooxidation of L-cysteine, to name just a few.¹⁴⁴

In addition to the above approaches, where bulk and CoPC nanoparticles are drop-casted onto the desired electrode surface, an alternative is the use of bulk-CoPC screen-printed electrodes (CoPC-SPEs) where the CoPC is incorporated into the ink used to fabricate the screen-printed electrodes allowing the mass production of reproducible CoPC modified screen-printed electrodes. Such electrodes have been explored towards

the sensing of model analytes such as citric acid and hydrazine, resulting in an electrocatalytic response when utilising the CoPC modified electrodes compared to graphitic SPEs and give rise to highly reproducible, one-shot economical and disposable electrode configurations.^{145, 146}

Within current literature, there has been no direct comparison of drop casting nano-CoTAPC (shown in scheme 2 B) and CoPC powder upon electrode surfaces with that of using CoPC-SPEs. Consequently in this section, the critical comparison of CoPC-SPEs with that of drop casted nano-CoTAPC electrodes is considered towards the model analytes L-ascorbic acid oxygen and hydrazine.



Scheme 2 - Molecular structures of the CoPC complexes used in this study, (A) shows CoPC structure incorporated within the ink of the screen-printed electrodes (CoPC SPEs), while (B) shows the nano-CoTAPC with amine groups bonded at each benzene ring of the conjugated system.

4.1.2 Experimental Section

All chemicals used were of analytical grade and were used as received without any further purification and were obtained from Sigma-Aldrich. All solutions were prepared with deionised water of resistivity not less than 18.2 MΩ cm. Voltammetric measurements were carried out using an Emstat (Palm Instruments BV, The Netherlands) potentiostat. Experiments carried out throughout this study contained a three electrode system, using the SPEs that were fabricated as described within section 3.3.

The CoPC nanoparticles (termed nano-CoTAPC herein) have a slightly different molecular structure than the CoPC used in the CoPC SPEs (as shown in scheme 2). The nano-CoTAPC were synthesized as described previously¹⁴⁷ with a slight modification. Briefly, 0.15 g CoTAPC was dissolved in 5 mL of 98% concentrated sulfuric acid. The solution was then added drop-by-drop into a vigorously stirred 300 mL aqueous solution containing 0.45 g hexadecyltrimethyl ammonium-chloride (CTACl; C₁₆H₃₃N(CH₃)₃Cl)-CTAB). The resulting solution was centrifugally separated. The obtained sedimentation was washed repeatedly to neutralise with water. It was then dried in air to obtain the nano-CoTAPC powder. The above mentioned working electrodes were modified with nano-CoTAPC which had been dispersed into a solvent - water mixture of ethanol-water (50:50) at an amount of 0.5 mg / mL and gently sonicated before used. The aliquots (μL) were then pipetted onto the desired electrode surface and then the electrode was placed into an oven to evaporate the solvent mixture at 40° Celsius for 2 minutes. Note that this method was compared to air/room drying at room temperature, where in the case of room temperature drying the modification tended to disperse to the edge of the working electrode; additionally this method took longer for the evaporation to take place. Consequently this drying method was utilised as such effects were not obtained. Additionally the use of CoPC powder from Sigma-Aldrich was also used to modify the standard-SPEs, using the method described previously.

Scanning electron microscope (SEM) images and surface element analysis were obtained with a JEOL JSM-5600LV model having an energy-dispersive X-ray microanalysis package. Raman analysis was carried out using the Thermo Scientific™ DXR Raman.

4.1.3 Results and Discussion

Comparison of the of the nano-CoPC, CoPC-SPE and standard-SPE towards their electroanalytical detection of L-ascorbic acid

In this Chapter, the critical exploration of bulk-cobalt (II) phthalocyanine modified screen-printed electrodes (CoPC-SPE) and drop casted CoPC nanoparticles modified screen-printed electrodes (nano-CoTAPC SPE) are compared. Figure 4.1 A displays a typical SEM image of a bare unmodified standard-SPE where the electrode surface is free of any CoPC and is in agreement with prior work.¹⁴⁵ Figure 4.1 B shows a typical SEM image of CoPC-SPE where in comparison to the standard-SPE (Figure 4.1 A) there appears to be no significant morphological differences. Figure 4.1 C & D show a typical SEM images of a nano-CoTAPC modified screen-printed electrode where the CoPC nanoparticles have been drop cast (20 & 70 μg respectively) onto the electrode surface, it is apparent that at high masses of nano-CoTAPC we witness large areas of clumping, creating a non-uniform surface. Therefore the surface has led to a heterogeneous surface with an uneven coverage of nano-CoTAPC which has resulted in areas of both excessively rich and dilapidated levels of CoPC – in effect the nano-CoTAPC has coalesced on the electrode surface to form larger micron sized CoPC particles. This observation (Figure 4.1 C) in surface morphology is in contrast to that of the CoPC-SPE (Figure 4.1 B); such observations have been similarly reported by Kozub *et al.*¹²⁴ using CoPC drop cast modified edge plane and basal plane pyrolytic graphitic electrodes. As the nano-CoTAPC SPEs are experimentally tailored with differing amounts of nano-CoTAPC, each modified electrode surface will have a different CoPC coverage. The coverage of the electrode surface can be calculated using equation (4. 1):

$$\Gamma = Q/nFA \quad (4. 1)$$

where, Γ , is the coverage of CoPC immobilised upon the desired electrode surface, Q , is the charge taken from the integration of the oxidation wave resulting from the Co^{2+/3+} couple recorded in a pH 7.4 PBS at slow scan rates, n is the number of electrons taking place in the electrochemical process, F is the Faraday constant and A , is the geometrical electrode area (without recourse to any surface roughness corrections).

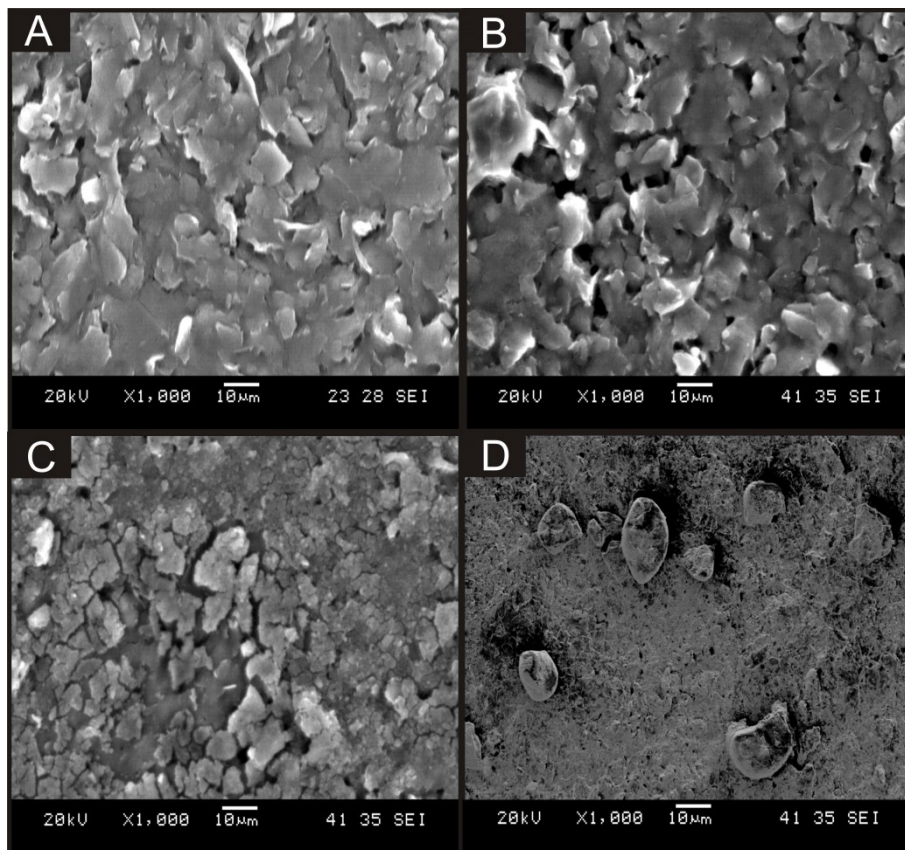


Figure 4.1: Typical SEM images of a bare standard-SPE (A), CoPC-SPE (B) and a standard-SPE modified with 20 μg and 70 μg nano-CoTAPC (C & D respectively).

Through the use of equation (4.1), a CoPC coverage value was found to correspond to $3.39 \times 10^{-14} \text{ mol cm}^{-2}$ for the CoPC-SPEs while for the nano-CoTAPC SPEs, values between 1.16×10^{-11} to $5.80 \times 10^{-15} \text{ mol cm}^{-2}$ were obtained for immobilised CoPC masses of 5×10^{-4} and $7 \times 10^{-1} \mu\text{g}$ respectively. Note that the CoPC in the CoPC SPEs cannot be easily changed and a new ink formulation would need to be developed by the ink supplier. Given that CoPC is a square planar molecule with a size of *ca.* $1.2 \text{ nm} \times 1.2 \text{ nm}$,¹⁴⁸ it is possible to estimate that 1 cm^2 of monolayer CoPC (on an ideally flat surface) should comprise a coverage of $1.2 \times 10^{-10} \text{ mol cm}^{-2}$ CoPC molecules. In comparison of this theoretical value to that the deduced coverage values, the latter are ~ 10 times smaller for nano-CoTAPC SPEs. However as shown in Figure 4.1, sub-monolayer's of CoPC are not observed, but rather microcrystalline structures. This will affect the electrical communication with the underlying graphitic electrode surfaces since these are comprised of edge plane and basal plane sites where the former are electrochemically

active “microbands” and the latter are electrochemically inert. As such, only CoPC crystals located on top of edge plane defects contribute to the electrochemical current, consequently not all of the immobilised nano-CoTAPC will be electrically wired. In terms of the bulk modified CoPC, only the surface layer is accessible to the solution and hence the rest of the electrode containing the bulk of the incorporated CoPC is likely not wired electrically. In this configuration CoPC reduces the percolation pathways depending upon its conductivity and might be detrimental to the electrochemical performance. As such, this likely explains the discrepancies observed in the deduced coverages. Additionally in comparison to that of the drop casted nano-CoTAPC electrode, the CoPC-SPEs have a fixed surface CoPC distribution which cannot be easily altered and this might be a potential disadvantage.

Comparison of the of the nano-CoPC, CoPC-SPE and standard-SPE towards their electroanalytical detection of L-ascorbic acid

Attention was first directed to exploring the electrochemical detection of L-Ascorbic acid (Vitamin C) which has been reported previously at nano-CoPC modified glassy carbon electrodes.¹³⁸ L-Ascorbic acid is a naturally occurring molecule which plays a vital part within mammalian metabolism as an antioxidant and is commonly used as an electroanalytical probe due to its ability to be oxidised at low potentials.^{149, 150} however the electrochemical oxidation of this molecule can lead to interferences with other molecules such as dopamine, NADH and sodium nitrite when applied into real sample analysis.^{123, 149-154}

The modification of a standard-SPE with nano-CoPC (see Experimental section 4.1.2) and explore this nano-CoPC modified SPE towards the sensing of L-Ascorbic acid was next considered. Figure 4.2 A shows a typical cyclic voltammetric profile where two voltammetric peaks are observed at + 0.30 V vs. SCE and + 0.90 V vs. SCE, where the former is not evident in the absence of L-Ascorbic acid suggesting that this new peak is due to the electrocatalysis of CoPC. Figure 4.2 B shows the effect of increasing amounts (mass immobilised on the supporting electrode surface) of nano-CoPC upon the voltammetric peak height (+ 0.30 V vs. SCE) towards the electrochemical detection of L-Ascorbic acid which shows that the peak current on the initial modification of the standard-SPE (5 µg) as the underlying electrode becomes ever more blocked by the

nanoparticles. It was noted that modifications over 20 μg result in a plateauing effect as the working electrode becomes saturated. Comparison of the origin of the electrocatalytic peak with that observed at Figure 4.2 B, the direct electrochemical oxidation of L-Ascorbic acid was observed at bare electrodes, as shown in the Figure 4.3 which demonstrates that the electrochemical oxidation of L-Ascorbic acid is observed at + 0.30 V vs. SCE, + 0.80 V vs. SCE, + 0.90 V vs. SCE for bare standard-SPEs, GCE and BDDE respectively.

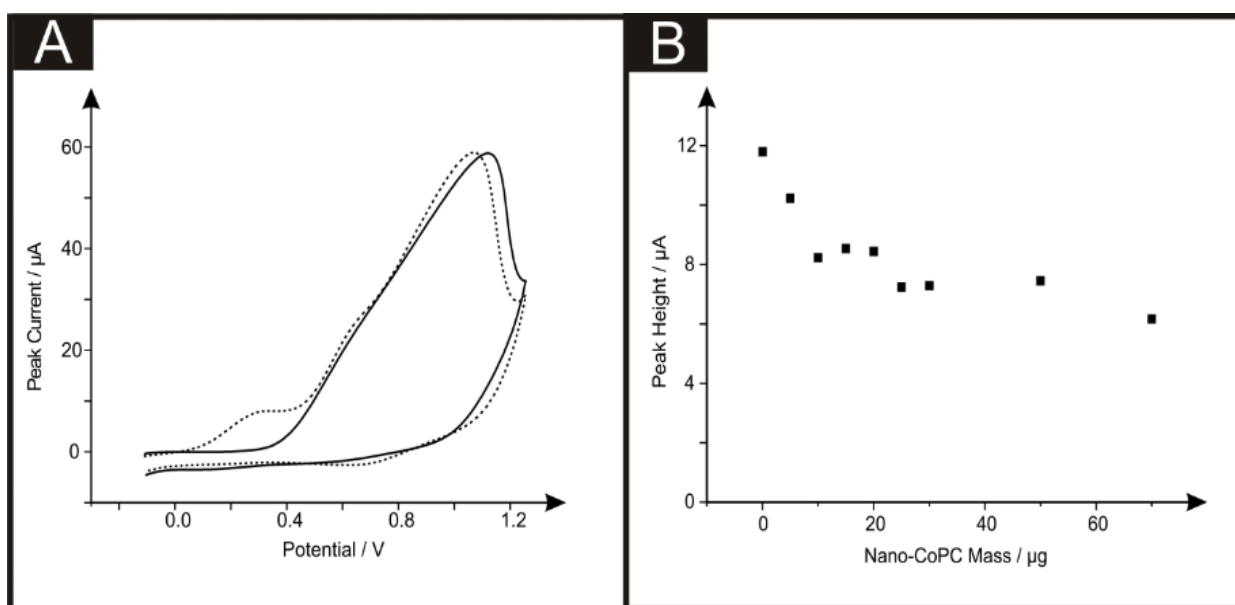


Figure 4.2: Cyclic voltammograms (A) in the presence (dashed line) and absence (solid line) of 1 mM L-Ascorbic acid in pH 7.4 PBS utilising a standard-SPE modified with 20 μg nano-CoPC. (B) shows the corresponding plots of peak height (using peak at $\sim + 0.30$ V vs. SCE) utilising a varied amount (mass) of nano-CoPC. Scan rate: 100 mV s^{-1} . $N = 3$.

Thus, it is summarised that the peak observed in Figure 4.2 A at + 0.30 V vs. SCE is the response of underlying electrode, with that at + 1.00 V vs. SCE being that of the $\text{Co}^{2+/3+}$ couple.

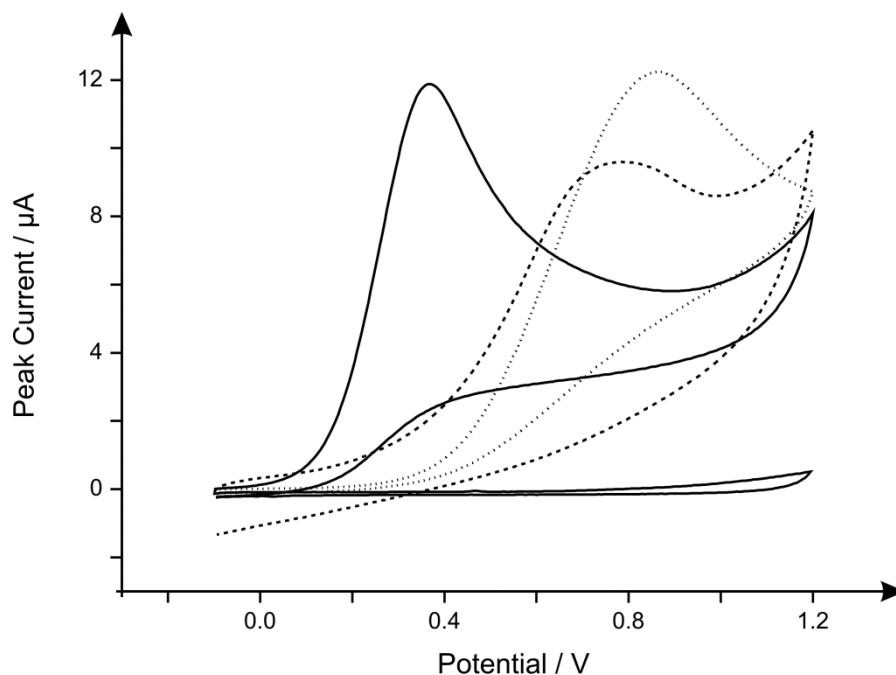


Figure 4.3: Typical cyclic voltammograms utilising a standard-SPE (solid line), GCE (dashed line) and BDDE (dotted line) in a blank pH 7.4 PBS and in the presence of 1 mM L-Ascorbic acid. Scan rate: 100 mV s⁻¹.

Consideration was next turned towards the use of the CoPC SPEs which have recently been scrutinised towards L-Ascorbic acid.¹⁵⁵ The effect of changing the concentration of L-Ascorbic acid was next explored with subsequent additions of the analyte into a pH 7.4 PBS, over a concentration range of 100 µM to 1000 µM. Figure 4.4 shows a comparison between the standard-SPE, nano-CoPC and the CoPC-SPEs where it is clear from the calibration plots that the nano-CoPC SPEs exhibit two linear ranges; 100 to 600 µM and 600 to 1000 µM (nano-CoPC SPE, lower range: $I_p / \mu\text{A} = 1.58 \mu\text{A} \mu\text{M}^{-1} + 0.56 \mu\text{M}$, $R^2 = 0.99$, $N = 6$, higher range: $I_p / \mu\text{A} = 1.55 \mu\text{A} \mu\text{M}^{-1} + 0.55 \mu\text{M}$, $R^2 = 0.92$, $N = 4$. CoPC-SPE: $I_p / \mu\text{A} = 1.29 \times 10^1 \mu\text{A} \text{mM}^{-1} + 1.81 \text{mM}$, $R^2 = 0.97$, $N = 9$) and one linear range for the standard-SPE ($I_p / \mu\text{A} = 1.47 \times 10^1 \mu\text{A} \text{mM}^{-1} - 1.29 \text{mM}^{-1}$, $R^2 = 0.98$, $N = 9$). The CoPC-SPEs and standard-SPEs show exceptional electrochemical performance over the chosen concentration range compared to that of the nano-CoPC SPE as such modifications upon the underlying electrode 'block' the signal as it has become saturated on the surface. The CoPC-SPEs have the advantage of not only containing CoPC, but being a homogenous mixture when screen-printed onto the electrode surface. The limit of detection (3σ) was found to correspond to 65 µM for standard-SPEs

and 70 μM for nano-CoPC SPEs, compared to that of the CoPC SPEs which exhibited a limit of detection of 85 μM , therefore there appears to be no electrocatalysis of L-Ascorbic acid upon modification with CoPC. This is the first comparison of

This observation that the electrocatalytic oxidation of L-Ascorbic acid *via* CoPC modification¹³⁸ can be reproduced upon the bare underlying electrode, is reported for the first time.

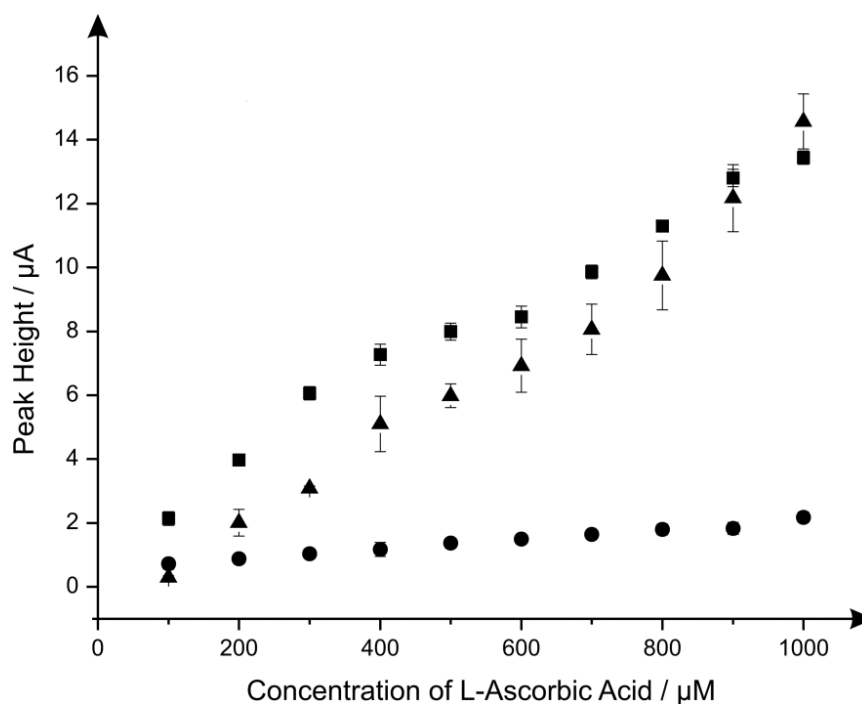


Figure 4.4: Calibration plots with error bars for L-Ascorbic acid over the concentration range 100 to 1000 μM within a pH 7.4 PBS using a nano-CoPC SPEs (circles), CoPC-SPEs (squares) after each scan and a standard-SPE (triangles), a utilising the voltammetric peak obtained at + 0.30 V vs. SCE. Scan rate: 100 mV s^{-1} using cyclic voltammetry, $N = 3$.

Comparison of the of the nano-CoPC, CoPC-SPE and standard-SPE towards the oxygen reduction reaction

To explore the possible catalytic effect of the CoPC-SPEs, focus turned towards the electrochemical reduction of oxygen, which has previously been reported to be electrocatalytic with CoPC modified electrodes.^{132, 156-161} Figure 4.5 A shows cyclic voltammograms for the reduction of oxygen, where a clear reduction peaks are evident using a nano-CoPC SPE (- 0.45 V vs. SCE), CoPC SPE (- 0.40 V vs. SCE) and a bare standard SPE (- 0.50 V vs. SCE) which are in good agreement with previous literature concerning the reduction of oxygen.^{132, 156, 157, 159} Figure 4.5 B illustrates a coverage study upon a standard-SPE, it is clear that above 30 μg of nano-CoPC modified upon the surface of the standard-SPE, saturation is reached and therefore the peak height value starts to plateau off. Voltammetric peak potential is also analysed in Figure 4.3 C where a shift in the peak potential from more negative to more electropositive regions is depicted upon modification with the nano-CoPC.

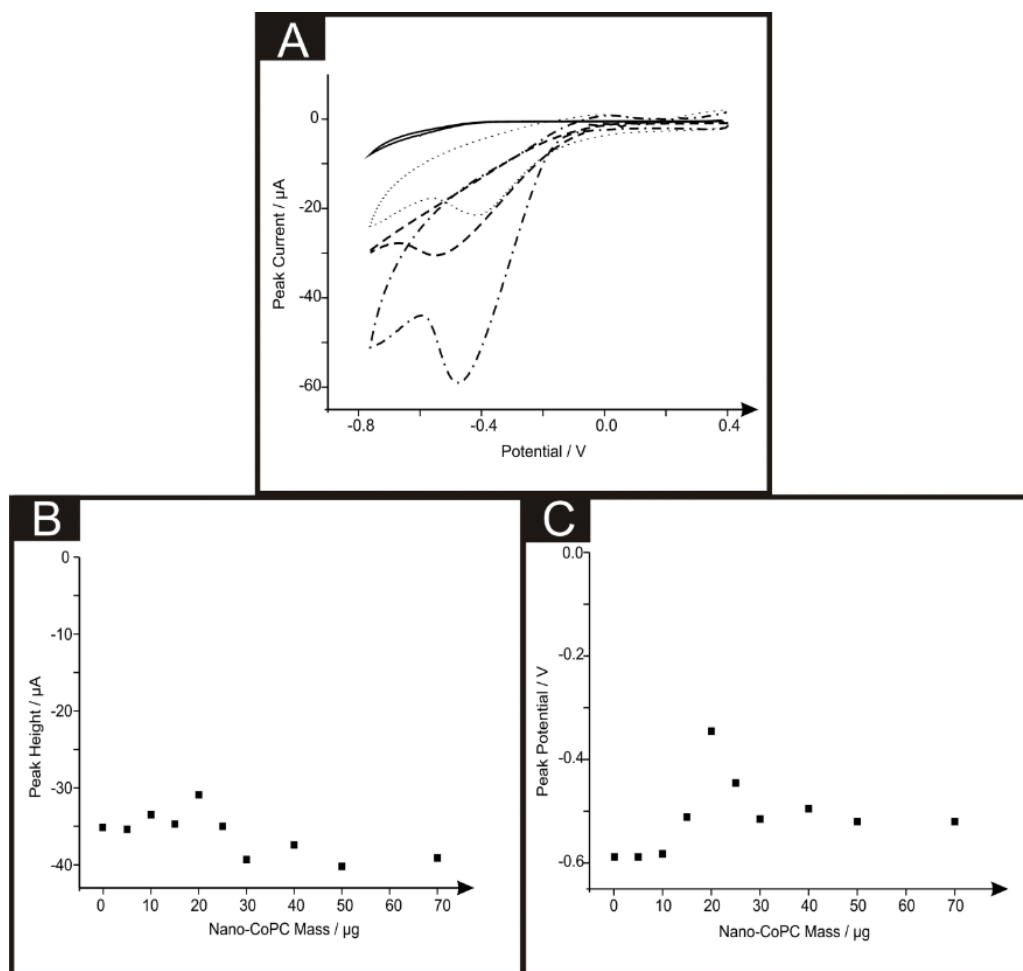


Figure 4.5: Cyclic voltammograms (A) in a nitrogen degassed (solid line) and an oxygen saturated 0.1 M H_2SO_4 solution utilising a standard-SPE (short dashed line), CoPC SPE (dotted line) and a standard-SPE modified with 20 μg nano-CoPC (dotted-dashed line). Corresponding plots of coverage of nano-CoPC mass vs. peak height (B) and peak potential (C). Scan rate: 100 mV s^{-1} .

Tafel analysis involving the analysis of the voltammograms corresponding to the electrochemical reduction of oxygen plotted as peak potential, E_p , vs. \log_{10} current (I) was constructed for the standard-SPE and CoPC-SPEs utilising the following equation:

$$b = \frac{2.303RT}{\alpha n' F} \quad (4. 2)$$

where b (V) is the slope of E_p against $\log_{10} I$, α is the electron transfer coefficient, F is the Faraday constant and n' is the number of electrodes transferred in the rate determining step. Using equation (4. 2), Tafel analysis revealed a gradient of 315 mV giving an $\alpha n'$ value of 0.18 for the CoPC SPEs and a gradient of 134 mV with a corresponding $\alpha n'$ value of 0.44 for the nano-CoPC SPE, for the standard-SPEs a gradient of 124 mV was obtained resulting in a similar $\alpha n'$ value of 0.47. It is apparent that such CoPC modifications lead to slight improvements in the voltammetric peak height likely

due to an increase in surface area, but no electrocatalytic effects are observed using CoPC modified electrodes.

Comparison of the of the nano-CoPC, CoPC-SPE and standard-SPE towards the electrocatalytic detection of hydrazine

Next, study of the carcinogenic analyte, hydrazine, previously studied in Chapter 4.2, showing CoPC has vast electrocatalytic properties. Figure 4.6 shows the cyclic voltammetric response of hydrazine utilising the nano-CoPC SPE. It is apparent that the standard-SPE gives no distinctive oxidation peak towards this analyte however upon CoPC modification, a large oxidation peak at 0.90 V vs. SCE in the absence of hydrazine is observed, confirming that this is the response for the Co^{2+/3+} couple, also shown is the response in the presence of hydrazine (0.30 V vs. SCE), thus confirming that the nano-CoPC are acting as an electrocatalyst, towards hydrazine, such findings are in agreement with previous literature, utilising CoPC-SPEs.¹⁴⁵

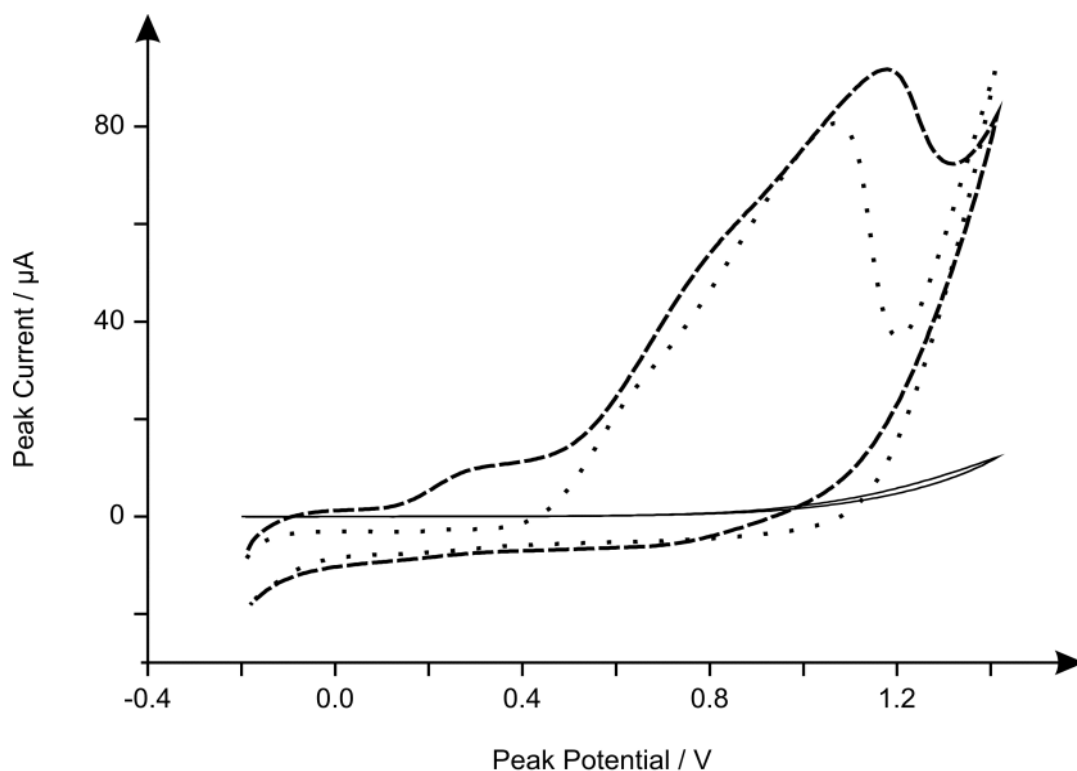


Figure 4.6: Cyclic voltammograms comparing the electrochemical oxidation of hydrazine utilising a standard SPE (solid line) and 20 μg nano-CoPC SPEs in the presence and absence (dashed line and dotted line) of 500 μM hydrazine in a pH 7.4 PBS. Scan rate: 100 mV s^{-1}

Figures 4.6 A and B depict cyclic voltammetry and plots of peak height respectively, as a function of the mass of nano-CoPC modified upon the surface of the standard-SPE, upon excessive modification ($> 30 \mu\text{g}$) of the working electrode causes reduced electrochemical performance, proven with a decrease of peak height (*viz.* Figure 4.7 A). Dilution of the nano-CoPC was next analysed *via* the same study, it is visible in Figure 4.8 that a catalysed peak is still present even at a masses of $5.00 \times 10^{-4} \mu\text{g}$.

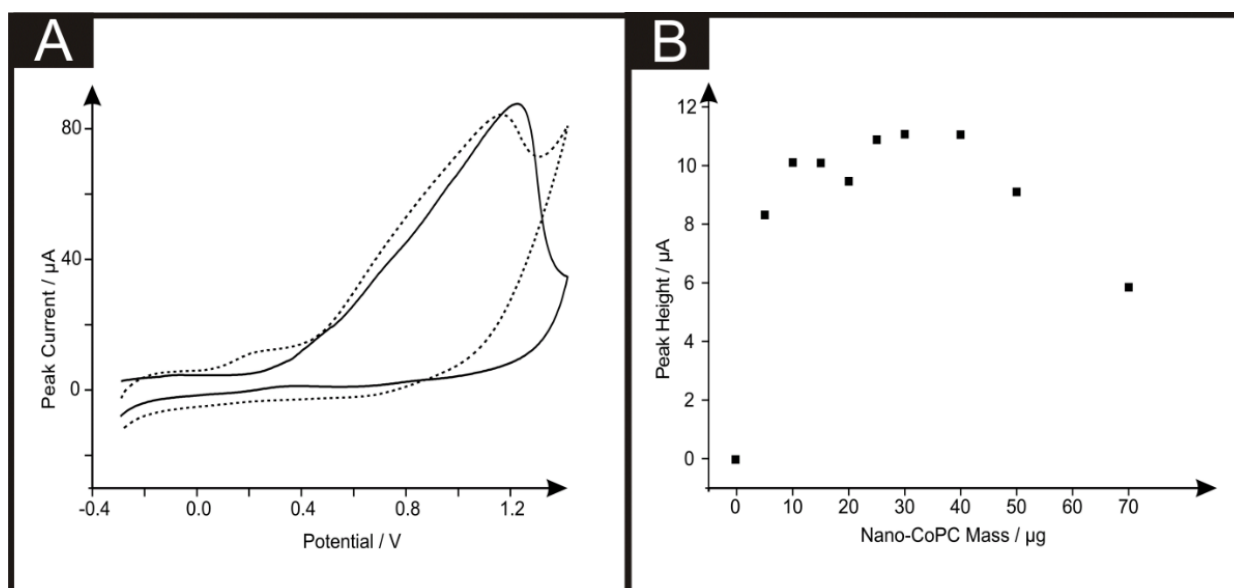


Figure 4.7: Cyclic voltammograms (A) in the presence (dashed line) and absence (solid line) of 500 μM hydrazine in pH 7.4 PBS utilising a standard-SPE modified with 20 μg nano-CoPC. Corresponding plots of nano-CoPC mass vs. peak height (B). Scan rate: 100 mV s^{-1} . $N = 3$.

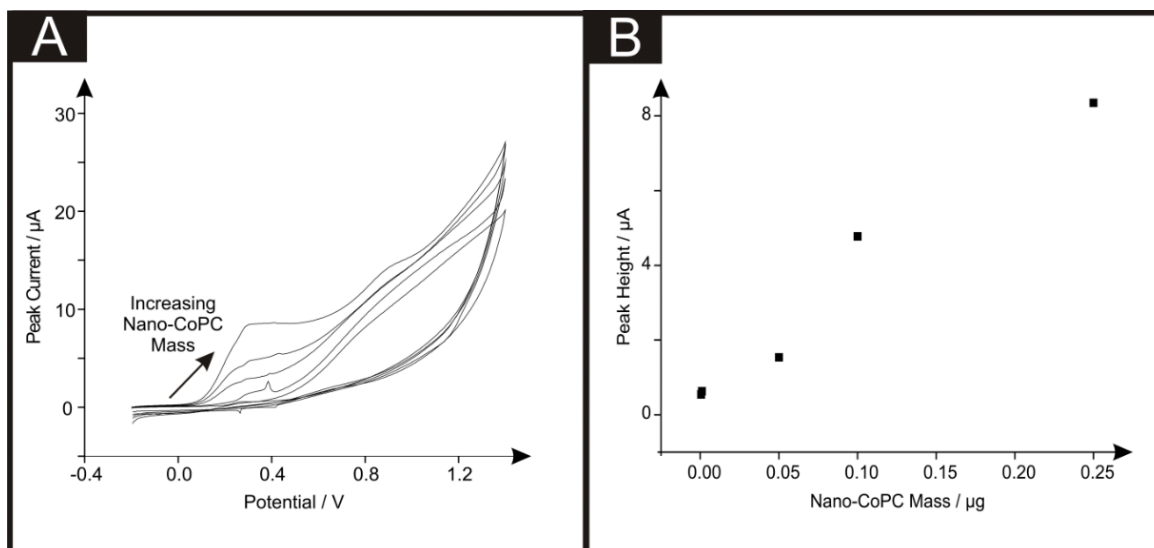


Figure 4.8: Cyclic voltammograms (A) and plots of diluted nano-CoPC mass vs. peak height (B) in the presence of 500 μM hydrazine in pH 7.4 PBS utilising a standard-SPE as the underlying electrode surface. Scan rate: 100 mV s⁻¹. N = 3.

Additions of hydrazine into a pH 7.4 PBS were next explored using the nano-CoPC SPEs and CoPC SPEs. Figure 4.9 illustrates the electroanalytical detection of hydrazine, for both SPEs over concentration range of 10 μM to 100 μM (nano-CoPC SPE: $I_p / \mu\text{A} = 3.00 \times 10^{-3} \mu\text{A} \mu\text{M}^{-1} - 0.79 \mu\text{M}$, $R^2 = 0.98$, $N = 9$; CoPC-SPE: $I_p / \mu\text{A} = 3.00 \times 10^{-3} \mu\text{A} \mu\text{M}^{-1} - 0.40 \mu\text{M}$, $R^2 = 0.98$, $N = 9$). Upon inspection of the analytical data for nano-CoPC SPE, two linear ranges were determined with the first linear range (10 to 40 μM) giving rise to a limit of detection (3σ) of 9.00 μM compared to that of the CoPC-SPEs with a value corresponding to 6.21 μM, which is better than CoPC polymeric modified electrodes¹³³ and similar to other related cobalt phthalocyanine structures.¹⁶²

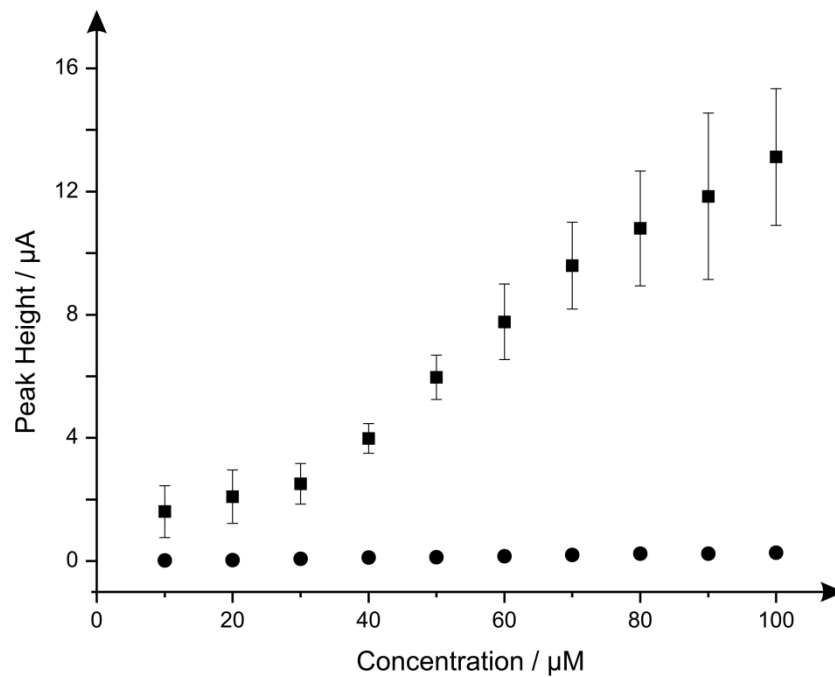


Figure 4.9: Calibration plots showing nano-CoTAPC SPE (squares) and CoPC-SPE (circles) towards subsequent additions of (10 μM to 100 μM) hydrazine into pH 7.4 PBS, utilising a new electrode after each addition. Scan rate: 100 mV s^{-1} . $N = 3$

4.2.4 Conclusions

CoPC modified electrodes prepared by drop casting CoPC nanoparticles onto a range of carbon based electrode substrates are critically compared with that of CoPC bulk modified screen-printed electrodes towards the sensing of the model analytes L-ascorbic acid, oxygen and hydrazine. Coverage analysis of both CoPC configurations found that the drop casted nano-CoTAPC showed 10 times less than the literature value obtained from the charge of the system for a CoPC monolayer, however SEM analysis and coverage values suggest microcrystalline structures therefore indicating that the immobilised CoPC on the surface are generally nonconductive and the residing edge plane sites/defects on the underlying electrode are the electrochemically active regions; however the amount of CoPC upon the surface can easily be changed to optimise the detection of the model analyte under investigation. In terms of the bulk modified CoPC, the surface layer is accessible to the solution and hence the rest of the electrode containing the bulk of CoPC is “dead space” as the electrocatalytic species cannot access this. As these electrodes are screen-printed using a mediated CoPC ink the amount of CoPC cannot be easily changed, however such techniques produce highly reproducible economical disposable one-shot sensors.

It is reported that that no electrocatalysis occurs at both types of CoPC electrode configurations towards the detection of L-ascorbic acid, and it is clear that the bare underlying electrode provides suitable voltammetric signals for the analytical detection. It seems that such realisation provides new insights into previous literature reports suggesting “electrocatalysis”, without any clear control experiments. The electrochemical reduction of oxygen in acidic medium has been reported showing minor electrocatalysis, however an improvement in peak height is witnessed due to a larger CoPC surface area upon the electrode surface. On the other hand true electrocatalysis is observed toward hydrazine where no such voltammetric features are witnessed on the bare underlying electrode substrate, obtaining a first linear range (10 μM to 30 μM) giving rise to a limit of detection (3σ) of 9.00 μM compared to that of the linear range obtained (10 μM to 100 μM) for bulk-CoPC SPEs (utilised within Chapter 4.2) with a corresponding limit of detection of 6.21 μM .

The clear advantage of the nano-CoTAPC is that differing coverages can be utilised and tailored to give rise to a variable reproducibility. In the bulk-CoPC SPE's, this is minimal due to their fabrication approach where the amount of electrocatalyst.

This Chapter has expressed a clear comparison of the advantages and disadvantages of utilising the bulk modified screen-printed electrode system over that of the traditional drop-cast approach. Objective 2.2 has been achieved and the consideration of an *in-situ* electrochemical metallic modification is next explored within Chapter 6 towards the detection of lead (II) and cadmium (II).

Chapter 5 - *In-situ Modified Screen-Printed Electrode Systems*

In this Chapter, further extension of objective 2.2 is considered, with the comparison of the 'traditional' standalone electrode systems to that of the screen-printed electrode setup. It is demonstrated for the first time a clear and precise electrode study utilising an array of *in-situ* metallic modifiers towards the simultaneous detection of lead (II) and cadmium (II). Such work has been published within RSC Analyst (Sept 2015, Accepted).

5.1 Metallic Modified (bismuth, antimony, tin and combinations thereof) Film Electrodes.

5.1.1 Introduction

The mercury film and related electrodes were the backbone of early electrochemistry, particularly for the sensing of metal ion species.¹⁶³ Mercury films provide the inherent advantage of offering improvements over bare electrode materials,¹⁶⁴ similarly the ability to incorporate other metals for the formation of mercury amalgams is also unique.¹⁶⁴ However the toxicity of mercury, with concentrations as little of $1 \mu\text{gL}^{-1}$ possessing the ability to cause serious harm, as defined by the World Health Organisation (WHO),¹⁶⁵ has become an issue which outweighs its potential use; this is exemplified by mercury being banned within Norway, Sweden and Denmark,^{166, 167} and more recently 140 countries agreed on the Minamata Convention by the United Nations Environment Program (UNEP) to prevent emissions.¹⁶⁸

The proposed alternative, touted as an environmentally green species, is bismuth which has been widely adapted by researchers as a replacement for mercury film electrodes where the use of an *ex-situ* or *in-situ* modified bismuth electrode has been reported to give rise to significant electroanalytical improvements over that of a bare electrode.¹⁶⁹⁻¹⁷³ The advantageous analytical properties of bismuth-film electrodes, roughly comparable to those of mercury-film electrodes, are attributed to the property of bismuth to form "fused alloys" with heavy metals, which may be analogous to the amalgams that mercury forms with a similar sensitivity^{169, 174, 175} (usually ppb or lower).^{176, 177} Table 2 (within the appendices) demonstrates the almost unquantifiable

plethora of bismuth modified electrodes for electroanalytical applications, giving insights into the vast and in some instances, the highly repetitive utilisation of bismuth.

Bismuth is not the only replacement for mercury electrodes, it has been reported recently that the utilisation of antimony, tin and mixtures of, can replicate the voltammetry seen by these bismuth and mercury electrodes.¹⁷⁸⁻¹⁸⁰ Antimony modified electrodes have been previously utilised for the fabrication of potentiometric pH sensors^{181, 182} with initial attempts directed to its use a carbon paste electrode (CPE) modified with Sb_2O_3 in combination with Anodic Stripping Voltammetry (ASV).¹⁸³ More recently, a new promising type of metal-film electrode, the antimony-film electrode, has been reported and has been claimed to perform on a par with mercury-film electrodes and bismuth-film electrodes in ASV.¹⁸⁴⁻¹⁸⁶ The available toxicological data regarding the health effects of antimony and its compounds are limited and inconclusive but toxicity is highly dependent on their speciation.¹⁸⁷ The relevant data published by different regulatory agencies indicate that antimony is much less toxic than mercury and therefore antimony-film electrodes are proposed to be more environmentally-friendly than their mercury counterparts.^{188, 189} Interestingly and most notably, antimony-film electrodes have been constructed utilising a microelectrode as the underlying electrode substrate reporting detection limits of 1.9 and 3.1 μgL^{-1} for the sensing of cadmium (II) and lead (II) respectively.¹⁹⁰ Table 2 (within the appendices), provides a thorough literature overview of the reports of the use of antimony films.

Tin is utilised much less frequently though some notable applications have been reported (see Table 2 within the appendices).¹⁹¹⁻¹⁹³ The data released by government agencies indicate that the toxicity of inorganic tin and inorganic tin salts normally used to generate tin-film electrodes is low,¹⁹⁴⁻¹⁹⁶ these electrodes can therefore potentially serve as environment-friendly sensors and, as such, more data is needed to assess their analytical utility in ASV. As is evident from inspection of Table 2 (within the appendices), a vast array of underlying electrode materials have been employed for modification using such metallic films, with graphitic electrode materials often being favoured.^{91, 166, 173, 197-199} Of those available, the most commonly utilised underlying material is glassy carbon (GCE)¹⁹⁹⁻²⁰⁴ with boron-doped diamond (BDDE)^{172, 197, 198} and screen-printed graphite electrodes (SPEs)^{91, 197, 205} also being utilised. The sensing of heavy metals such

as cadmium (II) and lead (II), amongst others (see Table 2 in the appendices), has become of a huge interest within the field of electrochemistry particularly the development of sensors which offer the ability to identify heavy metals simultaneously, even at trace levels. A plethora of literature exists exploring the use of many electrode surfaces with many modifications, all with very intriguing results,^{171, 206-210} many of which are highlighted in Table 2 (within the appendices). However even with the ability to sense at trace levels there are always ways to try and improve the sensitivity and practicality of the analytical protocol. Since the introduction of bismuth modified electrodes the choice of electrolyte has been a pH 4 acetate buffer solution, the utilisation of such supporting electrolyte has been of little discussion within literature, with many research groups recreating the conditions needed for a mercury plated electrode.²¹¹ However a simple pH study by Wang *et al.*²¹² has shown that at pH 4 the best response for the sensing of heavy metals is obtained. It is apparent that within neutral or slightly alkaline conditions bismuth may become hydrolysed and therefore the electrochemical process can be compromised.²¹³



In this Chapter, the exploration of the electroanalytical detection of lead (II) and cadmium (II) in aqueous solutions with modifications of the underlying electrode surface with the reported electrocatalytic surfaces of antimony (III), bismuth (III) and tin (II) *in-situ* modified electrodes and their combinations. It is demonstrated that the observed voltammetric response is dependent upon the chosen electrode substrate. This therefore means that when an electrode substrate exhibiting slow electron transfer kinetics is utilised, modification using bismuth (III) gives an impression of improved electroanalytical performance over the underlying substrate. On the other hand, if an electrode substrate with fast electron transfer properties is utilised in combination with film modified electrodes, a not so discernible difference is often observed. In fact it is revealed that a simple pH change and utilising a standard-SPE can give rise to optimal electroanalytical performances and questions the need to modify an electrode substrate in the first place, due to the capability of a standard-SPE to sense to below the

concentration levels set by the WHO for lead (II) and cadmium (II). Such work is of key importance for those concerned with the development of disposable metal sensors.

5.1.2 Experimental Section

All chemicals used were of analytical grade and were used as received without any further purification and were obtained from Sigma-Aldrich. All solutions were prepared with deionised water of resistivity not less than 18.2 M Ω cm. Voltammetric measurements were carried out using an Emstat (Palm Instruments BV, The Netherlands) potentiostat. Experiments carried out throughout this study contained a three electrode system, using a boron doped diamond electrode (BDDE), a glassy carbon electrode (GCE) and screen-printed electrodes (SPE) as the defined working electrodes. The SPEs were fabricated as described within section 3.3. All experiments were carried out using an external counter and reference, a platinum wire and saturated calomel electrode (SCE) respectively to allow comparison within the electroanalytical field.

The heterogeneous rate transfer constants were calculated for both redox probes using equation (1.26). The k^0 value for the BDDE was $7.87 \times 10^{-4} \text{ cm s}^{-1}$ and for the GCE of $1.48 \times 10^{-3} \text{ cm s}^{-1}$ utilising hexammineruthenium (III) chloride. It is noted that such values are in agreement with prior work using SPEs.²¹⁴

5.1.3 Results and Discussion

Antimony in-situ modified electrodes for the determination of lead (II) and cadmium (II)

The modification of electrodes for an improved electrochemical performance has been a particular interest within many electroanalytical applications, and has been at the spearhead of electrochemistry over the recent years.²¹⁵⁻²¹⁷ Initially inspired by recent work exploring the beneficial modification of electrode materials, such as that reported by Toghil *et al.*²¹⁸ describing the modification of a BDDE with antimony (III) for the sensing of lead (II) and cadmium (II), we endeavour to obtain further insights into the beneficial use of electrode modification with a view to deconvoluting the existing literature through the understanding of when an electrode modification truly offers an improved electrochemical performance, or in fact in some instances a simplified analytical protocol using a bare, unmodified electrode might be superior.

Exploration of the utilisation of different metal modifications and combinations thereof for the monitoring of lead (II) and cadmium (II) is considered; selected as these are undoubtedly the most commonly studied metal ion species (see Table 2 within the appendices). As described earlier, one such metal utilised for the improved sensing of lead (II) and cadmium (II), are antimony film modified electrodes,²¹⁹⁻²²² in consideration of this the determination of the most beneficial concentration of antimony (III) is analysed. In this scenario, antimony (III) is reduced *in-situ* at the electrode surface prior to the electrochemical deposition of cadmium (II) and lead (II) and therefore provides an “electrocatalytic” surface as widely reported in the literature.²¹⁸

Figure 5.1 shows additions of antimony (III) into a pH 4.3 acetate buffer solution containing 1.03 mgL⁻¹ lead (II) and 0.56 mgL⁻¹ cadmium (II). Using linear sweep voltammetry (LSV), it is clearly depicted in Figure 5.1, that both cadmium (II) and lead (II) are detectable at the two electrode materials utilised without the need for antimony (III); with stripping peaks for cadmium (II) and lead (II) being recorded at - 0.60 V and - 0.34 V respectively. Upon the addition of increasing concentrations of antimony (III) both the BDDE and SPE exhibit a clear stripping peak (0.0 V) for antimony which, as would be expected, is observed to increase in magnitude with increasing antimony (III) concentrations. Interestingly, at the SPE it is evident that the antimony deposited on the surface does not significantly effect that of the overall response of the target analytes,

whilst Figure 5.1 B however shows the response obtained for the BDDE, at which there seems to be a dramatic change towards the overall electrochemical response which is consequently different to that of previous literature using a BDDE.²¹⁸ In light of these findings utilising both the SPE and BDDE, an optimised antimony (III) concentration of 5 mgL⁻¹ was determined owing to the greatest peak height response (see Figure 5.1 A and 5.1 B inset) of the concentrations studied at the two electrode materials for the determination of lead (II) and cadmium (II). At this optimum, antimony (III) concentration of 5 mgL⁻¹, the modified BDDE exhibits a peak height increase of 258 % and 311 % for lead (II) and cadmium (II) respectively, however the modified SPE experiences a decrease of 14 % for lead (II) but a 10 % increase for cadmium (II) compared to the respective unmodified electrodes (the optimised concentration is emphasised by the utilisation of a dotted line in Figures 5.1 A and 5.1 B).

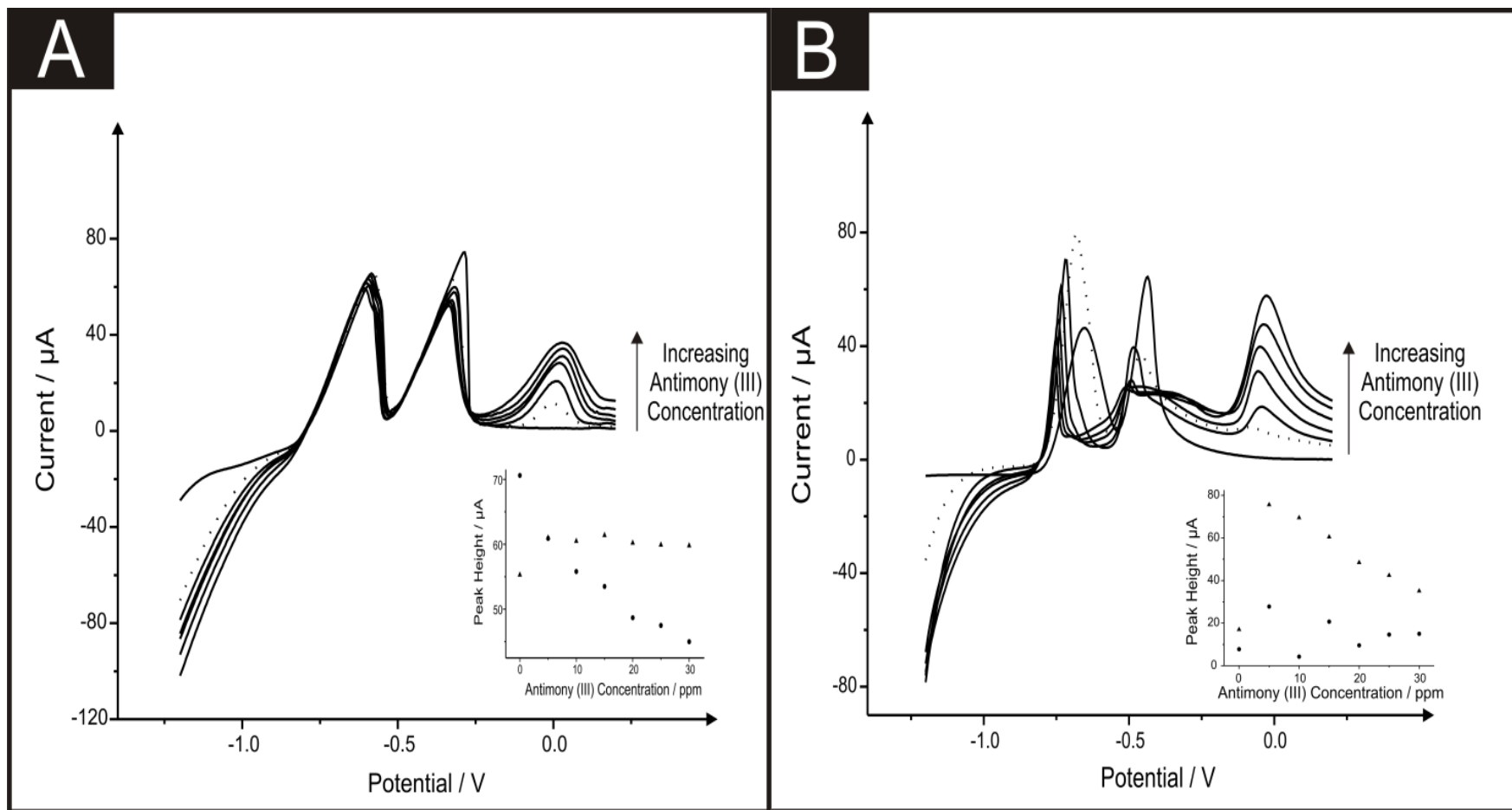


Figure 5.1: Linear sweep voltammograms resulting from additions of 5 mgL^{-1} antimony (III) (at 0.0 V) into a $\text{pH } 4.3$ acetate buffer solution containing 1.03 mgL^{-1} lead (II) (at -0.34 V) and 0.56 mgL^{-1} cadmium (II) (at -0.60 V) in a using both SPE (A) and BDDE (B). Dotted line equates to the optimum concentration of antimony (III). Deposition potential and time: -1.2 V (vs. SCE) and 120 seconds respectively. Inset: Corresponding plots of voltammetric peak height versus antimony (III) concentration (cadmium (II) – triangles; lead (II) – circles) $N = 3$.

Tin in-situ modified electrodes for the determination of lead (II) and cadmium (II)

Attention was next turned towards the detection of lead (II) and cadmium (II) with the use of tin (II). Tin film modified electrodes have been reported within the previous literature with GCE and a carbon paste electrode (CPE) to provide satisfactory results are towards the determination of cadmium (II).^{178, 192} Figure 5.2 shows the additions of tin (II) into a solution of pH 4.3 acetate buffer containing 1.03 mgL^{-1} lead (II) and 0.56 mgL^{-1} cadmium (II), where again it should be noted that detection of both metal species can be seen without any modification. As depicted in Figure 5.2 A the stripping of both cadmium (- 0.60 V) and lead (- 0.34 V) are affected by the introduction of increasing concentrations of tin (II); particularly for the case of the lead (II) stripping at - 0.34 V. This striking response for the stripping of lead at both the BDDE and SPE is understandable as both tin (II) and lead (II) typically exhibit similar peak potentials which can cause some misinterpretation of voltammetric results. However, it is clear through inspection of Figure 5.2 B that BDDE can give rise to two separate peaks for tin (II) and lead (II) at lower concentrations at which separation of the two species voltammetrically is possible. Due to this noted interference arising from the overlapping of the tin (II) and lead (II) voltammetric peaks at high tin (II) concentrations the lowest tin (II) concentration of 20 mgL^{-1} was determined to be the optimum modification concentration (see Figure 5.2 A and 5.2 B inset). At this optimum tin (II) concentration of 20 mgL^{-1} , the modified BDDE exhibits a peak height increase of 42 % and 23 % for lead (II) and cadmium (II) respectively, however the modified SPE experiences an increase of 14 % for lead (II) and a 8 % increase for cadmium (II) compared to the respective unmodified electrodes (the optimised concentration is emphasised by the utilisation of a dotted line in Figures 5.2 A and 5.2 B).

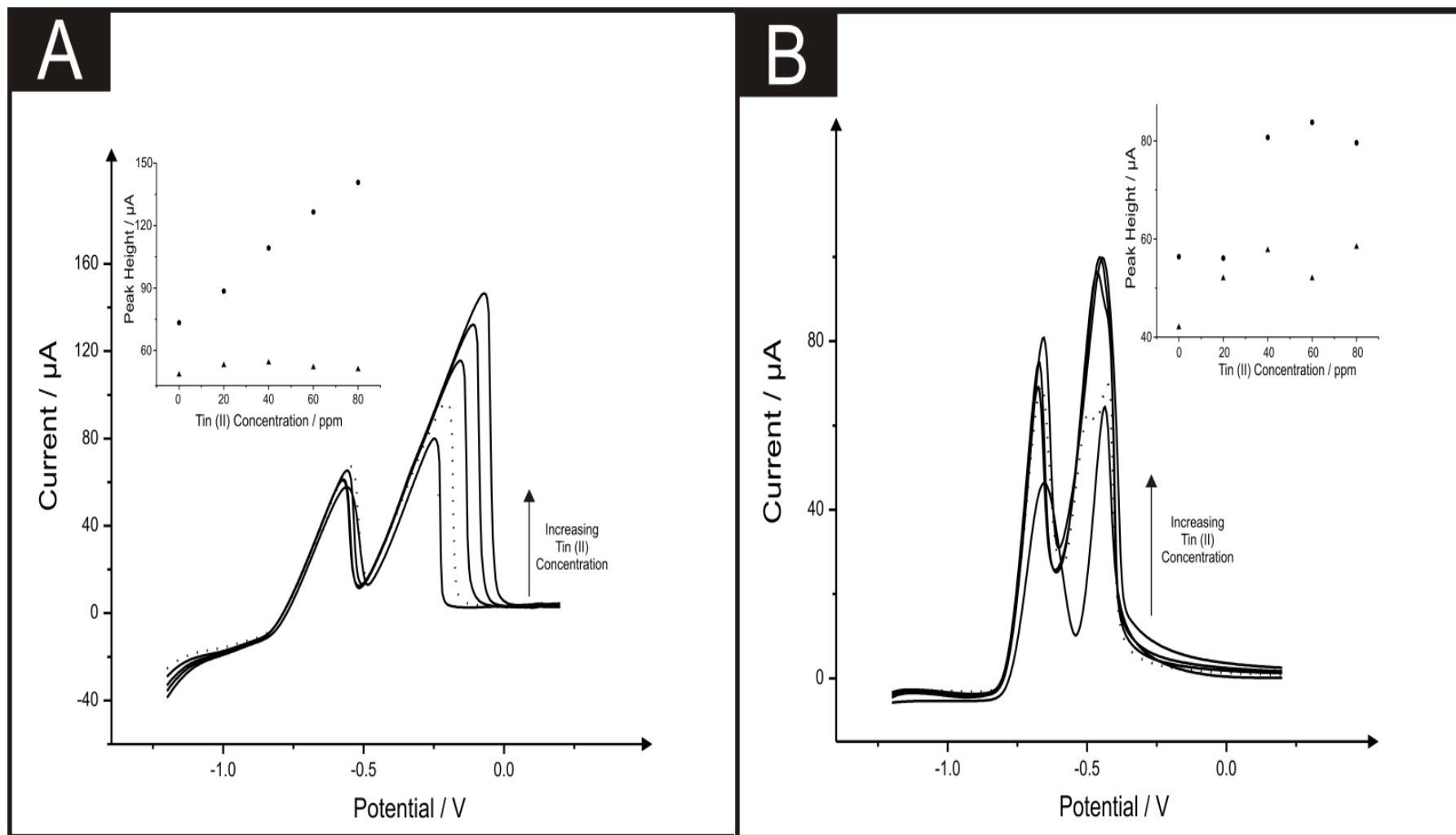


Figure 5.2: Linear sweep voltammograms resulting from additions of 20 mgL^{-1} tin (II) (at -0.34 V) into a pH 4.3 acetate buffer solution containing 1.03 mgL^{-1} lead (II) (at -0.34 V) and 0.56 mgL^{-1} cadmium (II) (at -0.60 V) using both SPE (A) and BDDE (B). Dotted line equates to optimum concentration of tin (II). Deposition potential and time: -1.2 V (vs. SCE) and 120 seconds respectively. Inset: Corresponding plots of voltammetric peak height versus tin (II) concentration (cadmium (II) – triangles; lead (II) – circles). $N = 3$.

Bismuth in-situ modified electrodes for the determination of lead (II) and cadmium (II)

Next, the attention turned to the use of the 'green' metal bismuth; this has been covered in literature vigorously, not only as a standalone film electrode but with different alloys such as bismuth-tin and bismuth-antimony on many electrodes such as graphite, CPE, BDDE, GCE and SPE.^{169, 172, 223} The effect of bismuth (III) concentration on the determination of 1.03 mgL⁻¹ lead (II) and 0.56 mgL⁻¹ cadmium (II) in a pH 4.3 solution acetate buffer was next analysed, to find the optimum level of bismuth (III) for the detection of the two heavy metals when using the BDDE and SPE. It is important to note that this choice of buffer solution was chosen due to the vast amount of reports that claim that this is ideal solution for bismuth modified electrodes.^{211, 224}

Figure 5.3 shows the effect bismuth (III) (- 0.10 V) has upon the detection of cadmium (II) and lead (II), where on SPE and BDDE (Figure 5.3 A and B respectively) a large concentrated addition of bismuth (III) is observed to cause a severe hindrance to the overall electrochemical response with regards to the two analytes. From the range of bismuth (III) modification concentrations trailed a concentration of 1 mgL⁻¹ was determined as the optimum concentration for further analytical studies as upon addition of bismuth (III) into the solution the lead (II) voltammetric peak reduces in magnitude whereas in contrast the voltammetric peak for cadmium (II) is seen to increase; particularly for the SPE (see Figure 5.3 A and 5.3 B inset). As a result of this, a concentration of 1 mgL⁻¹ bismuth (III) was selected as the most appropriate for further analytical studies, with the same concentration being applied to the BDDE to allow for sufficient and fair performance comparison. At this optimum bismuth (III) concentration of 1 mgL⁻¹, the modified BDDE exhibits a peak height decrease of 52 % and 2 % for lead (II) and cadmium (II) respectively, however the modified SPE experiences an increase of 6 % for lead (II) and a 7 % increase for cadmium (II) compared to the respective unmodified electrodes (the optimised concentration is emphasised by the utilisation of a dotted line in Figures 5.3 A and 5.3 B).

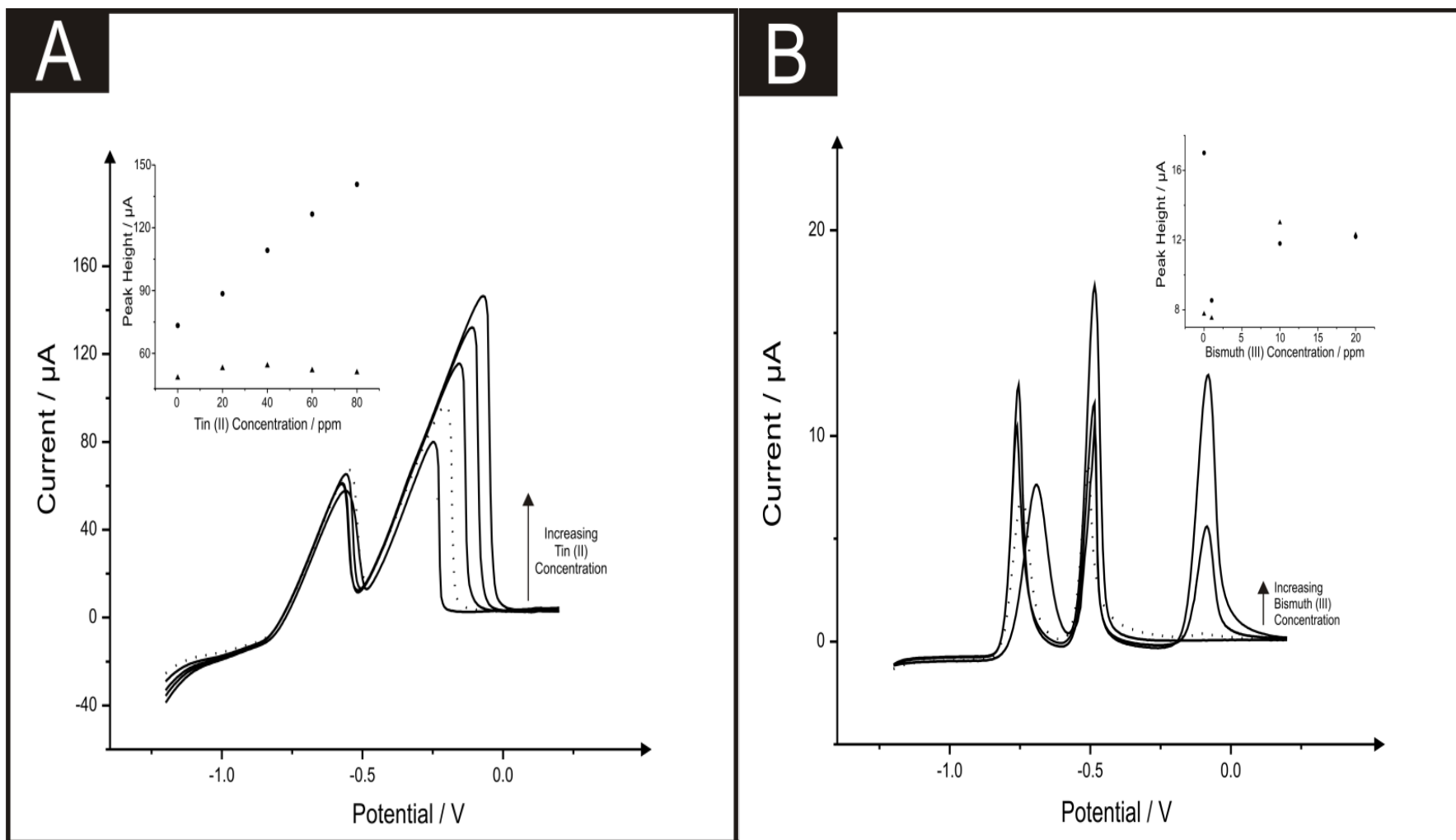


Figure 5.3: Linear sweep voltammograms resulting from additions of 10 mgL^{-1} bismuth (III) (at -0.10 V) into a $\text{pH } 4.3$ acetate buffer solution containing 1.03 mgL^{-1} lead (II) (at -0.34 V) and 0.56 mgL^{-1} cadmium (II) (at -0.60 V) using both SPE (A) and BDDE (B). Dotted line equates to optimum concentration of bismuth (III). Deposition potential and time: -1.2 V (vs. SCE) and 120 seconds respectively. Inset: Corresponding plots of voltammetric peak height versus bismuth (III) concentration (cadmium (II) – triangles; lead (II) – circles). $N = 3$.

Alloy Combination modified electrodes for the determination of lead (II) and cadmium (II)

In addition to the abovementioned modifications, the incorporation and utilisation of metals of interest for the enhanced determination of heavy metal species such as cadmium (II) and lead (II) as discussed earlier herein there is potential, as has been described in prior literature,^{169, 225, 226} for the utilisation of alloy combinations for improved electrochemical determination of certain analytically relevant species. Considering this, the viability for the utilisation of a tin (II) / antimony (III) alloy was analysed. Once more different concentrations and ratios of the two species comprising the alloy were trialled in attempts to determine the most appropriate concentrations for use when determining the two analytes cadmium (II) and lead (II). Figure 5.4 depicts the voltammetric responses arising from varying concentrations of the alloy at a fixed cadmium (II) and lead (II) concentration at both the SPE and the BDDE. Inspection of the voltammetric responses and corresponding calibration plots depicted (inset for each) reveals that in both the case of the SPE and the BDDE, the alloy and its composition are of key importance. As such, when considering the most appropriate or optimised alloys formation to be utilised for consequential analytical applications it was decided that the tin (II) / antimony (III) alloy composed of 20 mgL⁻¹ tin (II) and 10 mgL⁻¹ antimony (III) was most appropriate when utilising the BDDE as the peak heights for both cadmium (II) and lead (II) were much greater than the other combinations trialled. In the case of the SPE the same alloy combination was chosen as it was clearly notable that this was the most suitable alloy combination which allowed for the yielding of a voltammetric signal which did exhibit a more Gaussian-type voltammetric profile in comparison to the other combinations explored, and therefore offered improved determination of the two analytes. At these optimum concentrations of tin (II) and antimony (III) of 20 mgL⁻¹ and 10 mgL⁻¹ respectively, the modified BDDE exhibits a peak height increase of 110 % and 192 % for lead (II) and cadmium (II) respectively, however the modified SPE experiences an increase of 30 % for lead (II) and a 34 % increase for cadmium (II) compared to the respective unmodified electrodes (the optimised concentration is emphasised by the utilisation of a dotted line in Figure 5.4 A and 5.4 B).

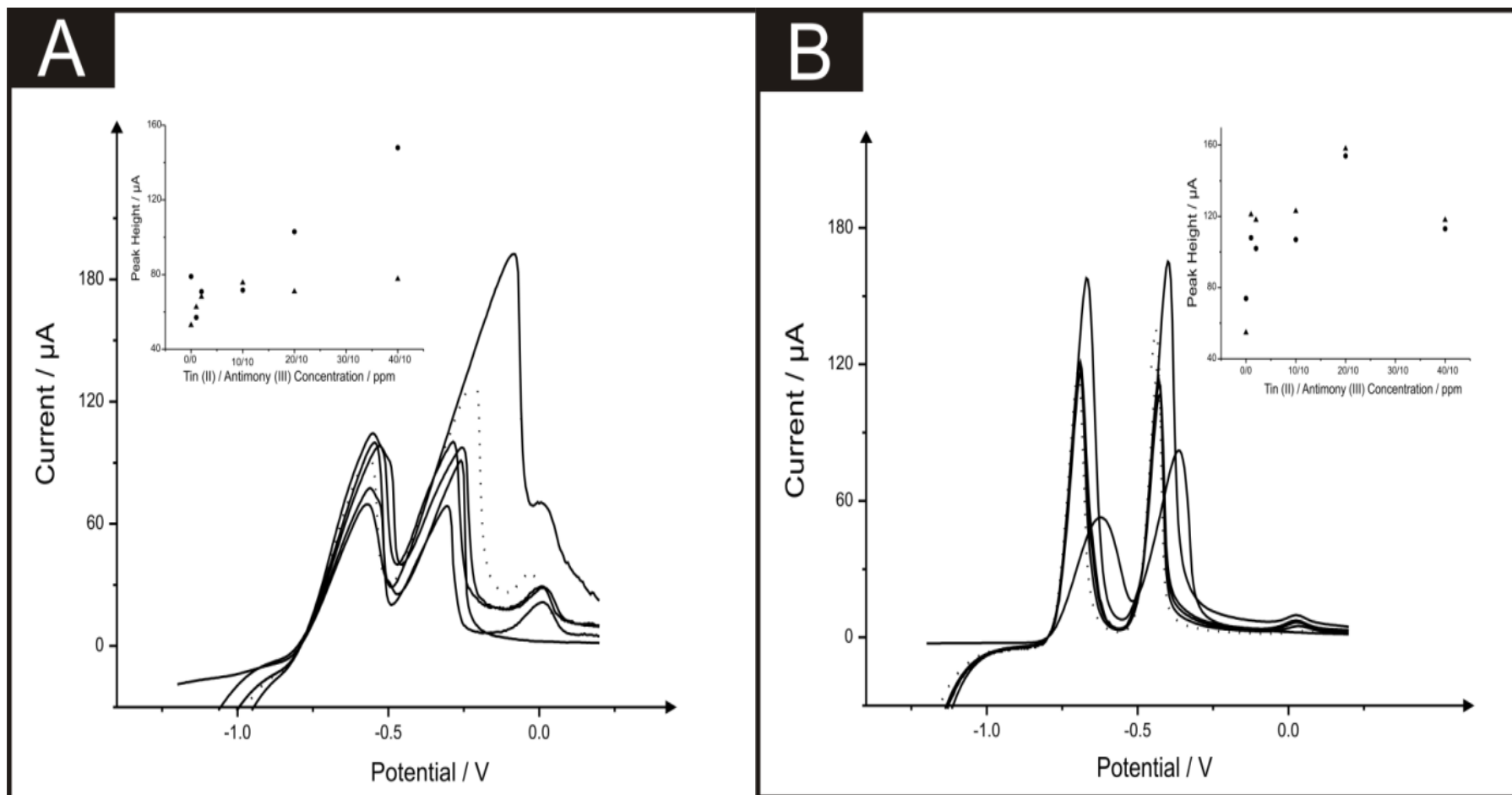


Figure 5.4: Linear sweep voltammograms resulting from 10 mgL^{-1} antimony (III) (at 0.0 V) with additions of tin (II) (at -0.34 V) ($1 - 40 \text{ mgL}^{-1}$) towards 1.03 mgL^{-1} lead (II) (at -0.34 V) and 0.56 mgL^{-1} cadmium (II) (-0.60 V) in a pH 4.3 acetate buffer solution using both SPE (A) and BDDE (B) (dotted line equates to optimum concentration of antimony (III) and tin (II)). Deposition potential and time: -1.2 V (vs. SCE) and 120 seconds respectively. Inset: Corresponding plots of voltammetric peak height versus tin (II) / antimony (III) concentration (cadmium (II) – triangles; lead (II) – circles). $N = 3$.

The second of the two alloy configurations examined for the determination of cadmium (II) and lead (II) was a bismuth-tin alloy. Figure 5.5 A and B show the addition of four heavy metals into a pH 4.3 acetate buffer solution, towards SPE and BDDE respectively. Here you can see the BiSn-SPE gains what seems to be a larger lead (II) peak however it is actually that of the tin (II) addition, thus shows that the SPE being used cannot define the peaks, as seen previously with the additions of tin (II). Figure 5.5 B shows interesting voltammetric data as on the addition of the alloy, the peak shifts more negative and becomes much more defined.

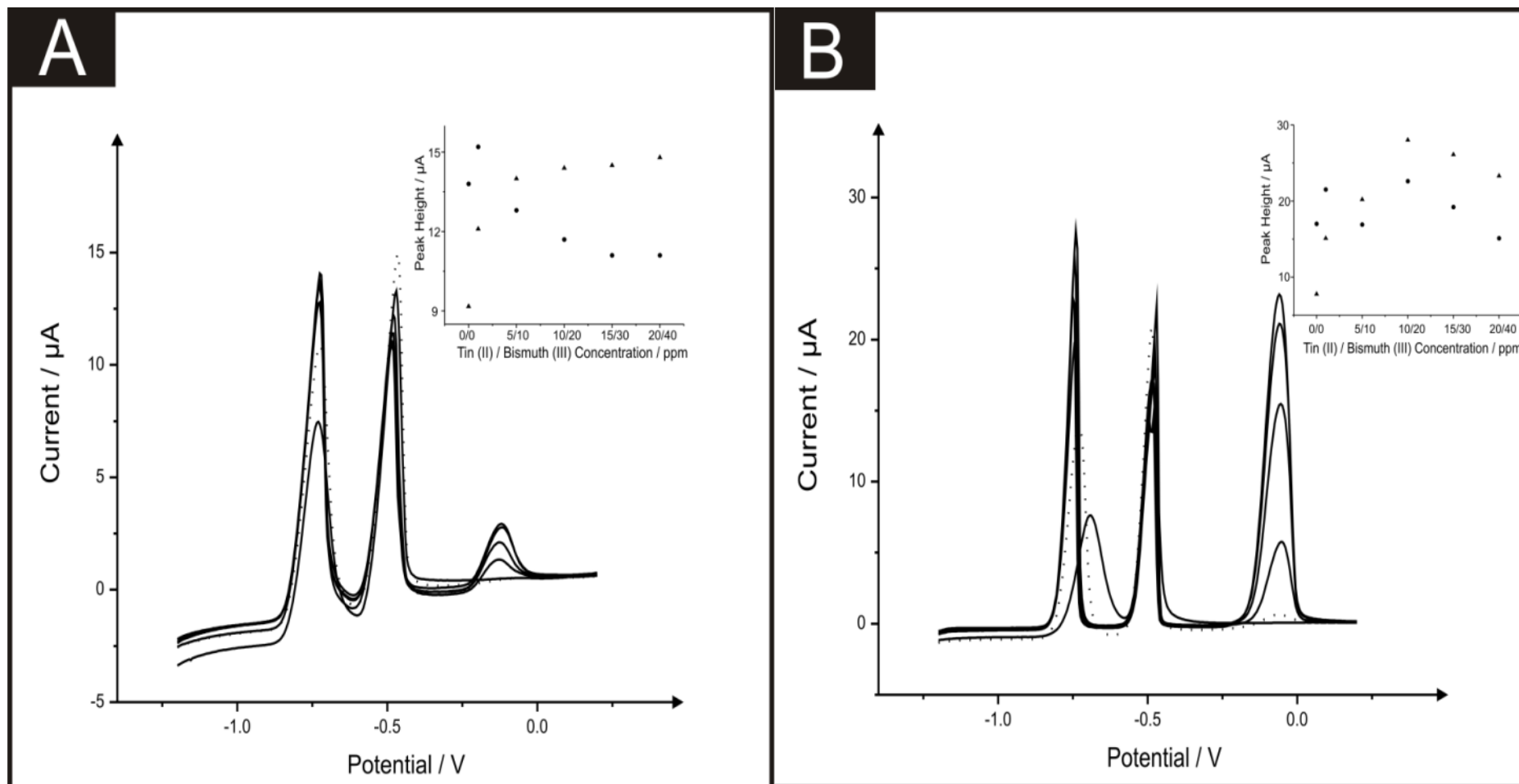


Figure 5.5: Linear sweep voltammograms resulting from additions of 10 mgL^{-1} and 5 mgL^{-1} bismuth (III) (at -0.10 V) and tin (II) (at -0.34 V) respectively into a solution containing 1.03 mgL^{-1} lead (II) (at -0.34 V) and 0.56 mgL^{-1} cadmium (II) (at -0.60 V) in a pH 4.3 acetate buffer solution using both SPE (A) and BDDE (B) (dotted line equates to optimum concentration of bismuth (III) and tin (II)). Deposition potential and time: -1.2 V (vs. SCE) and 120 seconds respectively. Inset: Corresponding plots of voltammetric peak height versus tin (II) / bismuth (III) concentration (cadmium (II) – triangles; lead (II) – circles). $N = 3$.

Electrochemical sensing capabilities of lead (II) and cadmium (II) using an optimised in-situ bismuth modified electrode

After determination of the optimum concentration of each of the modifiers present in solution when considering the determination of lead (II) and cadmium (II) steps were next taken to explore the potential to utilise these protocols for the simultaneous determination of both lead (II) and cadmium (II) in solution over a range of concentration. Once again, the responses obtained at the bare unmodified BDDE electrode are compared and contrasted not only with the electrochemical performance obtained in the presence of the modifier, but as a comparison to this conventional electrode SPEs are once again utilised, allowing us to compare practicality within the electroanalytical field and sensitivity towards the target analytes. Figures 5.6 through to 5.11 depict the responses obtained at both the BDDE and SPEs both unmodified (in the absence) and presence of the modifiers under investigation (bismuth, antimony, tin and their alloys) for the simultaneous measurement of both lead (II) and cadmium (II) in the ranges of 103.61 to 932.42 μgL^{-1} and 56.46 to 508.14 μgL^{-1} respectively. Inspection of Figure 5.6 clearly reveals that in the case of the two bare, unmodified sensors the SPE offers greater electrochemical performance and in turn sensitivity towards the determination of the two analytes.

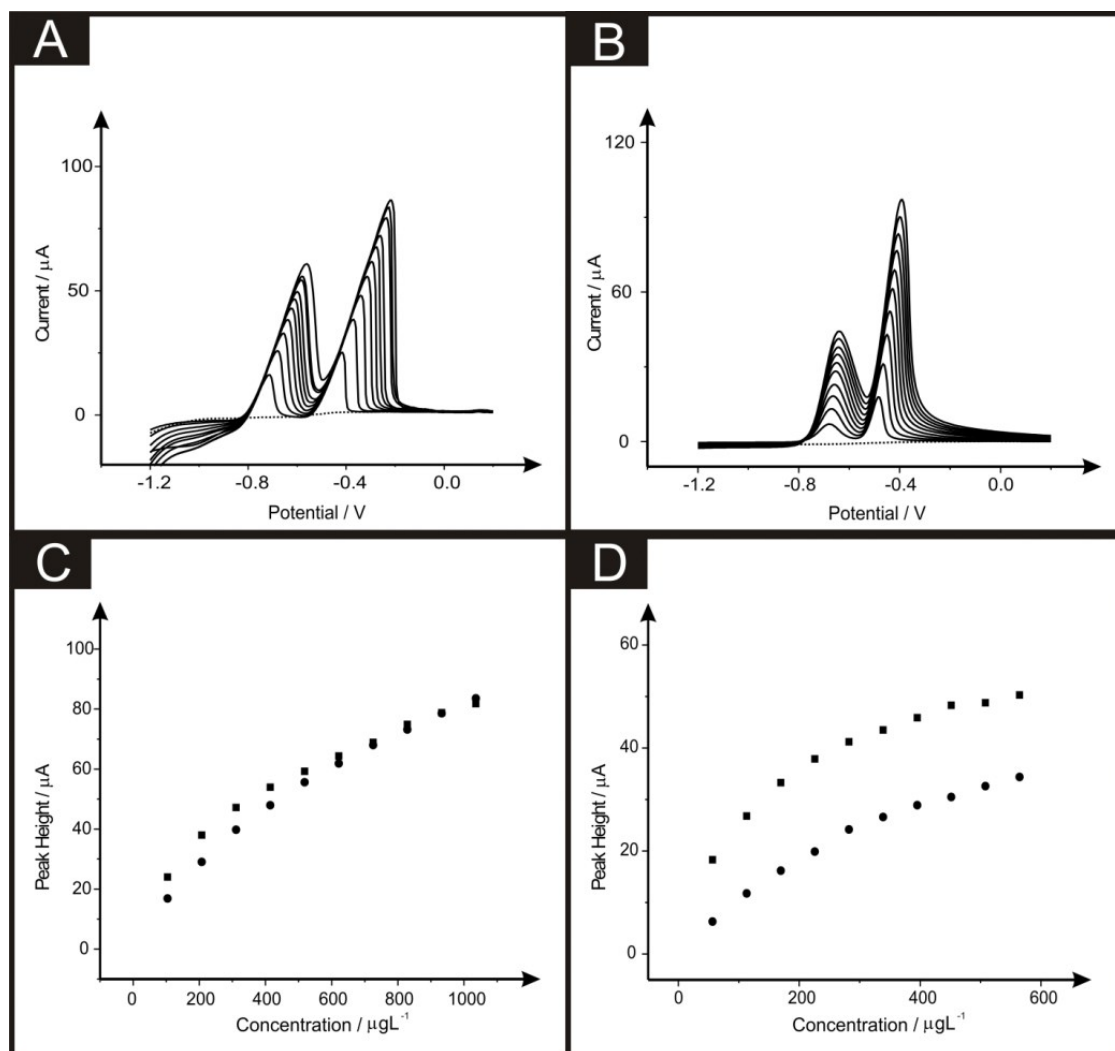


Figure 5.6: Linear sweep voltammograms resulting from additions of lead (II) (at -0.34 V) (103.61 to 932.42 μgL^{-1}) and cadmium (II) (at -0.60 V) (56.46 to 508.14 μgL^{-1}) into a pH 4.3 acetate buffer solution (dotted line) using both a standard-SPE (A) and a bare BDDE (B). Also depicted are the corresponding calibration plots for lead (II) (C) and cadmium (II) (D) at the SPE (squares) and BDDE (circles). Deposition potential and time: -1.2 V (vs. SCE) and 120 seconds respectively. $N = 3$.

Though upon the introduction of bismuth (III) to improve the electrocatalytic performance (Figure 5.7) a superior response is noted at the BDDE in comparison to that of the bismuth (III) modified SPE, though importantly this improvement is arguably not sufficient enough to suggest that the presence of bismuth (III) is of merit or practical worth at either of the two electrode materials with a very minimal improvement observed over the responses obtained at bare electrodes.

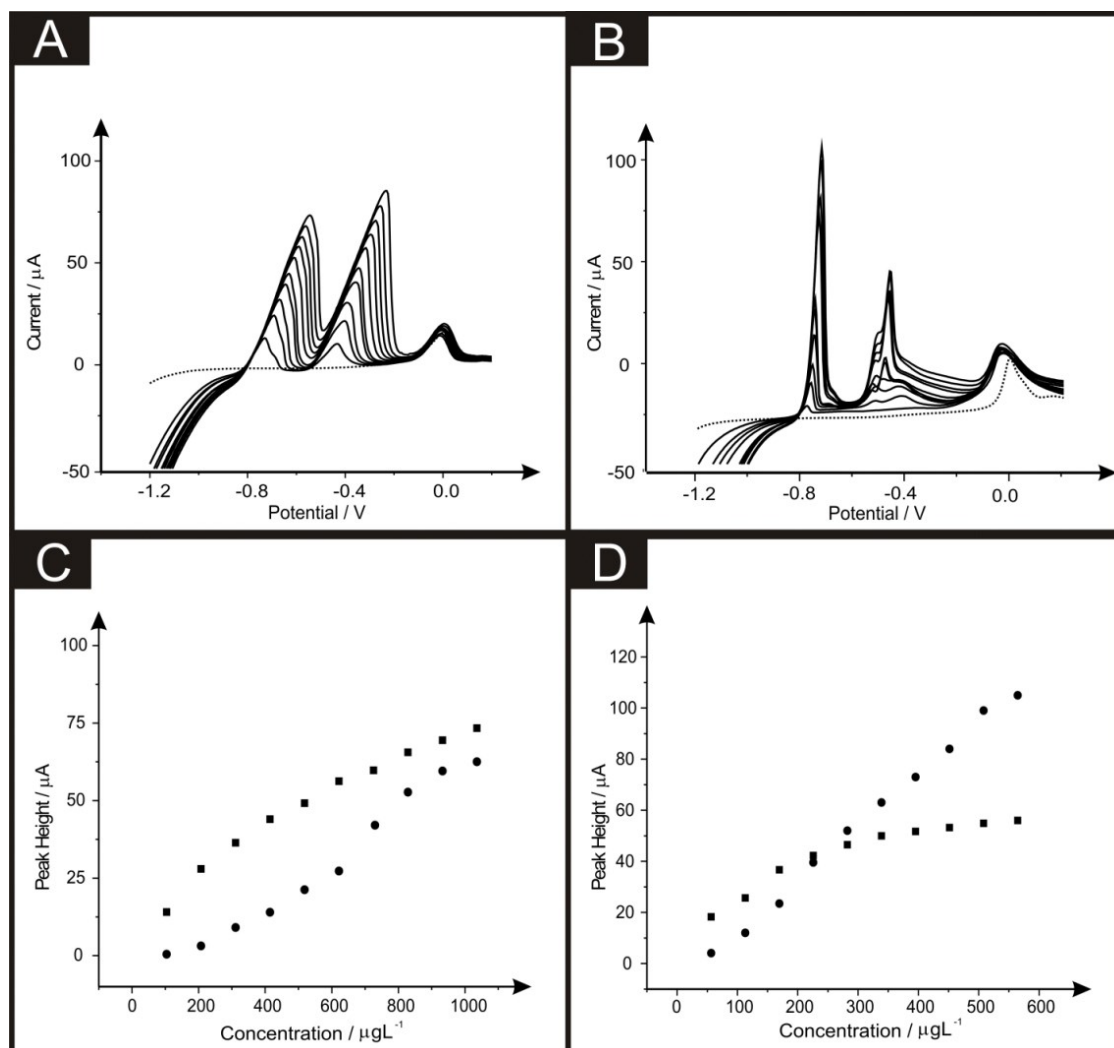


Figure 5.7: Linear sweep voltammograms resulting from additions of lead (II) (at - 0.34 V) (103.61 to $932.42 \mu\text{gL}^{-1}$) and cadmium (II) (at - 0.60 V) (56.46 to $508.14 \mu\text{gL}^{-1}$) into a pH 4.3 acetate buffer solution (dotted line) containing 5 mgL^{-1} of antimony (III) (at - 0.0 V) using both an SPE (A) and BDDE (B). Also depicted are the corresponding calibration plots for lead (II) (C) and cadmium (II) (D) at the SPE (squares) and BDDE (circles). Deposition potential and time: - 1.2 V (vs. SCE) and 120 seconds respectively. $N = 3$.

This improvement with regards to the performance of the BDDE towards the determination of lead (II) and cadmium (II) is noted not only at the bismuth modified sensor (Figure 5.7), but also throughout the range of modifications utilised as portrayed in Figures 5.8 to 5.11. Such an electrochemical performance is in agreement with that previously reported in a plethora of papers where electrodes such as BDDE and GCE which exhibit typically slow kinetics are modified in order to improve the electrochemical performance.^{169, 172, 227-229} However, it is important to consider that a more suitable approach could perhaps be to elect to utilise an electrode material such as EPPG (or edge plane-like screen-printed electrodes such as the SPEs reported herein) which will offer suitably desirable electron transfer kinetics and in turn electrochemical performance without recourse for pre-treatment and/or modification. Interestingly, when considering further the response obtained at the SPE upon the introduction of each of the modifiers the response is detrimentally affected with a noticeable reduction in the recorded voltammetric peak height for the two analytes. For the case of this electrode material it could be considered that the presence of these modifiers which have been extensively reported to improve the electrochemical performance of electrode materials could in fact be blocking the electrode surface of the SPE resulting in this reduced performance.

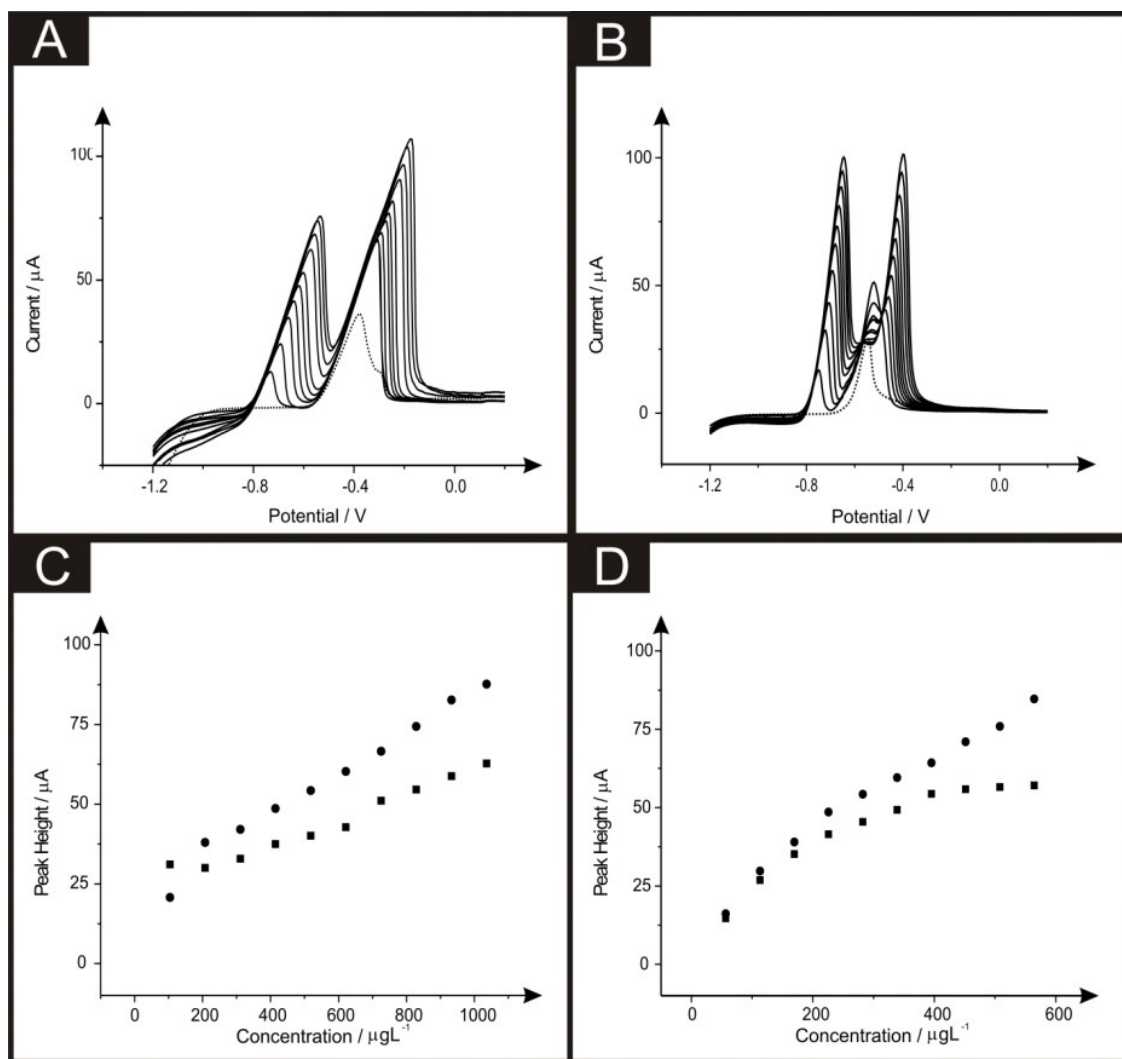


Figure 5.8: Linear sweep voltammograms resulting from additions of lead (II) (at - 0.34 V) (103.61 to $932.42 \mu\text{gL}^{-1}$) and cadmium (II) (at - 0.60 V) (56.46 to $508.14 \mu\text{gL}^{-1}$) in to a pH 4.3 acetate buffer solution (dotted line) containing 20mgL^{-1} of tin (II) (at - 0.34 V) using both an SPE (A) and BDDE (B). Also depicted are the corresponding calibration plots for lead (II) (C) and cadmium (II) (D) at the SPE (squares) and BDDE (circles). Deposition potential and time: - 1.2 V (vs. SCE) and 120 seconds respectively. $N = 3$.

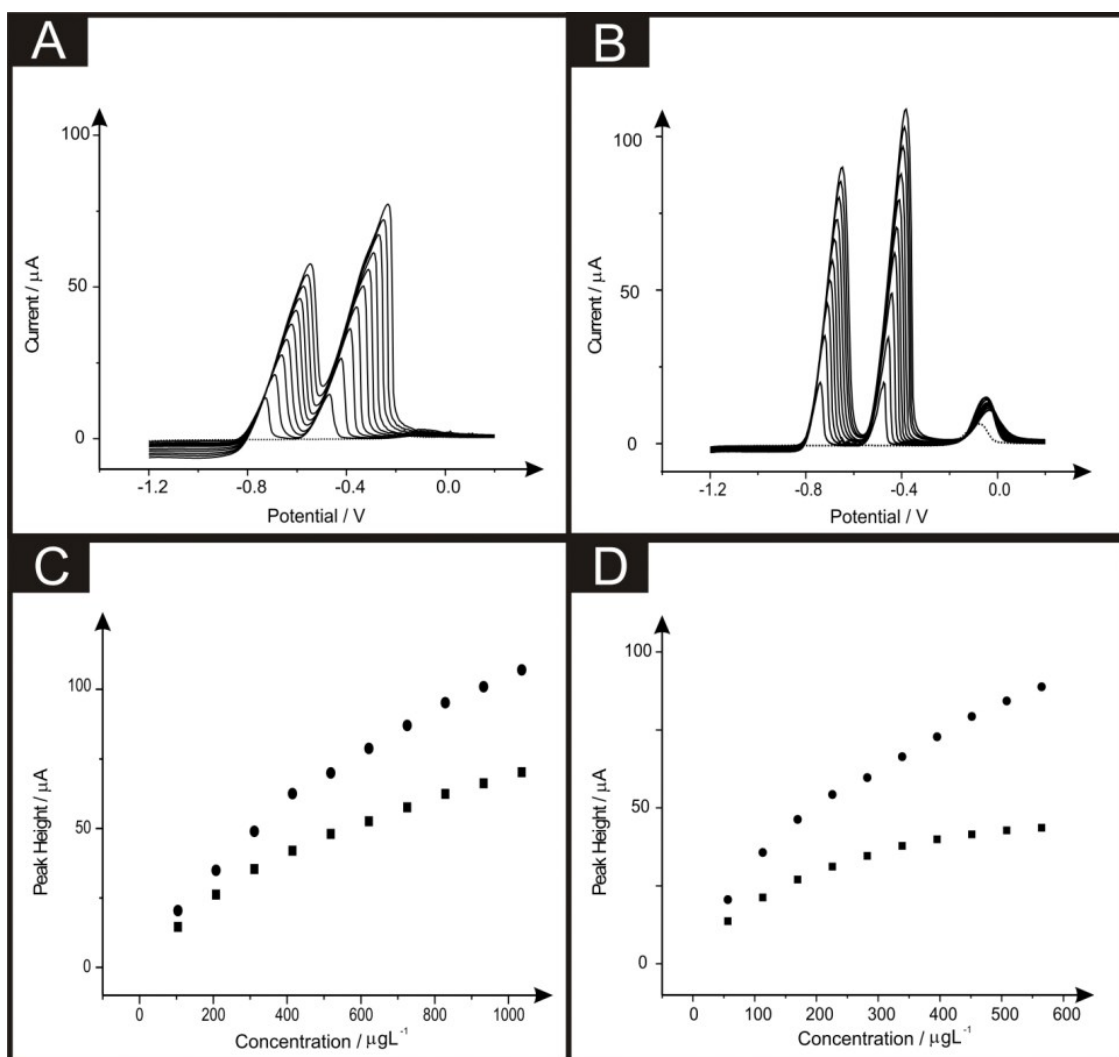


Figure 5.9: Linear sweep voltammograms resulting from additions of lead (II) (at - 0.34 V) (103.61 to $932.42 \mu\text{gL}^{-1}$) and cadmium (II) (at - 0.60 V) (56.46 to $508.14 \mu\text{gL}^{-1}$) in to a pH 4.3 acetate buffer solution (dotted line) containing 1 mgL^{-1} of bismuth (III) (at - 0.1 V) using both an SPE (A) and BDDE (B). Also depicted are the corresponding calibration plots for lead (II) (C) and cadmium (II) (D) at the SPE (squares) and BDDE (circles). Deposition potential and time: - 1.2 V (vs. SCE) and 120 seconds respectively. $N = 3$.

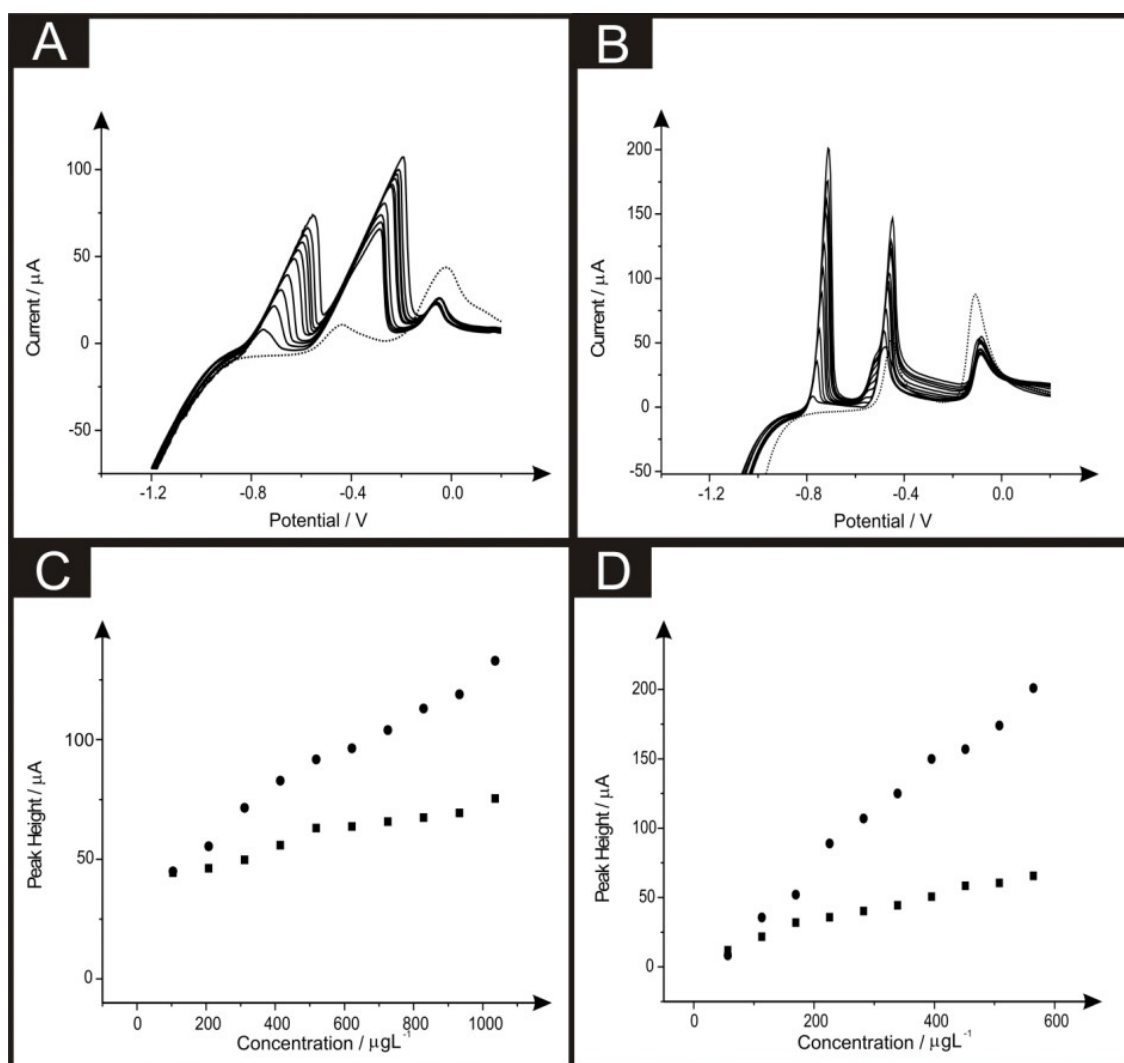


Figure 5.10: Linear sweep voltammograms resulting from additions of lead (II) (at - 0.34 V) (103.61 to $932.42 \mu\text{gL}^{-1}$) and cadmium (II) (at - 0.60 V) (56.46 to $508.14 \mu\text{gL}^{-1}$) in to a pH 4.3 acetate buffer solution (dotted line) containing 10mgL^{-1} of antimony (III) (at 0.0 V) and 20mgL^{-1} of tin (II) (at - 0.34 V) using both an SPE (A) and BDDE (B). Also depicted are the corresponding calibration plots for lead (II) (C) and cadmium (II) (D) at the SPE (squares) and BDDE (circles). Deposition potential and time: - 1.2 V (vs. SCE) and 120 seconds respectively. $N = 3$.

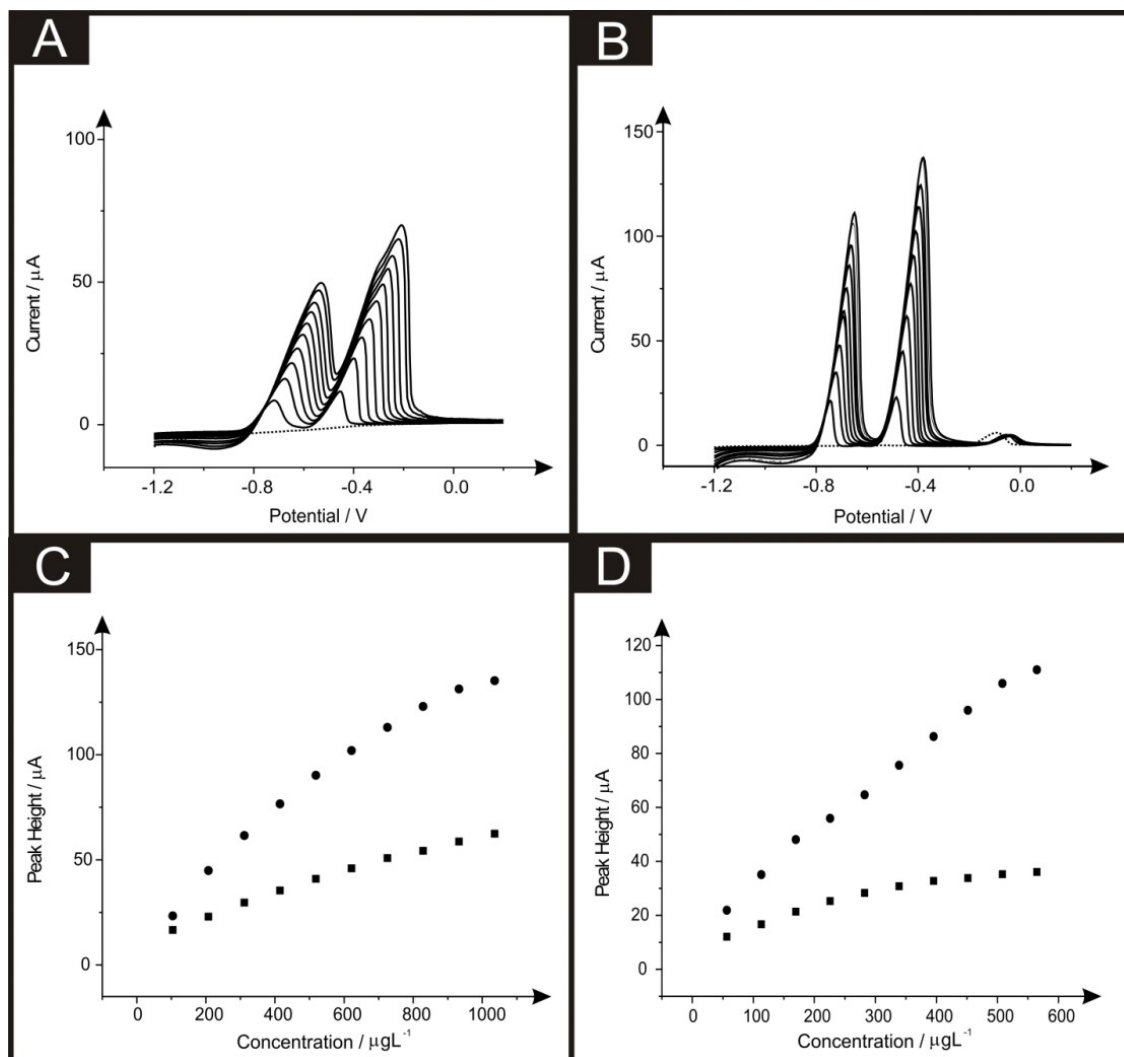


Figure 5.11: Linear sweep voltammograms resulting from additions of lead (II) (at - 0.34 V) (103.61 to $932.42 \mu\text{gL}^{-1}$) and cadmium (II) (at - 0.60 V) (56.46 to $508.14 \mu\text{gL}^{-1}$) in to a pH 4.3 acetate buffer solution (dotted line) containing 1 mgL^{-1} of bismuth (III) (at - 0.10 V) and 1 mgL^{-1} of tin (II) (at - 0.34 V) using both an SPE (A) and BDDE (B). Also depicted are the corresponding calibration plots for lead (II) (C) and cadmium (II) (D) at the SPE (squares) and BDDE (circles). Deposition potential and time: - 1.2 V (vs. SCE) and 120 seconds respectively. $N = 3$.

Individual determination of lead (II) and cadmium (II) utilising an in-situ modified and unmodified electrodes

Next, attention was turned to the monitoring of the two analytes, lead (II) and cadmium (II) at low levels relevant to real world applications, utilising SPE, GCE and BDDE. Comparisons were sought between the response and sensitivity achievable at the unmodified and *in-situ* bismuth (III) modified electrodes in order to derive the real benefits offered by such modifications over existing unmodified electrode materials. In this case, the two analytes were monitored singularly rather than simultaneously to assess the true capabilities of the analytical protocols for the determination of the analytes at low-levels.

The response at the electrodes were first considered with additions of lead (II), over the concentration range 10 – 150 μgL^{-1} , being made into a solution of pH 4.3 acetate buffer using both the unmodified electrodes but also measurements in the presence of 1 mgL^{-1} bismuth (III). As is depicted in Figure 5.10 A both the bare and bismuth (III) modified SPE exhibit virtually identical electrochemical behaviour, however at higher concentrations the standard-SPE possesses greater sensitivity. The resultant calibration plots of voltammetric peak height versus lead (II) concentration being linear over the analytical range studied (SPE: $I_p / \mu\text{A} = 0.044 \mu\text{A} / \mu\text{gL}^{-1} - 0.101 \mu\text{A}$; $R^2 = 0.96$; $N = 11$; SPE in the presence of bismuth (III) $I_p / \mu\text{A} = 0.036 \mu\text{A} / \mu\text{gL}^{-1} + 0.152 \mu\text{A}$; $R^2 = 0.97$; $N = 11$). The limit of detection (3σ) for the determination of lead (II) at the unmodified SPE was calculated to be 0.079 μgL^{-1} with a slight improvement determined in the presence of bismuth (III) offering a limit of detection (3σ) of 0.035 μgL^{-1} . Similarly, when the determination of lead (II) at these low levels was examined utilising a GCE electrode a linear response was once again noted for both the bare electrode ($I_p / \mu\text{A} = 0.007 \mu\text{A} / \mu\text{gL}^{-1} + 0.034 \mu\text{A}$; $R^2 = 0.98$; $N = 11$) and in the presence of bismuth (III) ($I_p / \mu\text{A} = 0.013 \mu\text{A} / \mu\text{gL}^{-1} + 0.317 \mu\text{A}$; $R^2 = 0.86$; $N = 11$) with both sensors; as seen in Figure 5.10 C. Comparable calibration plots are once again evident, as is the case when utilising the SPE, with the limit of detection (3σ) at the bare GCE being calculated to be 0.216 μgL^{-1} which as would be expected does not deviate substantially from that obtained at the GCE in the presence of bismuth (III) of 0.138 μgL^{-1} . Clearly in the case of both the SPE and the GCE the presence of bismuth (III) yields little improvement in terms of the limit

of detection over that of the respective bare electrode materials. However, in terms of sensitivity ($\mu\text{A}/\mu\text{gL}^{-1}$) it is clear that the standard-SPE and bismuth (III) modified GCE are superior. The utilisation of the BDDE saw a slight increase within the peak height for all concentrations concerned (shown in Figure 5.12 E) when the electrode is modified with bismuth (III) (BDDE: $I_p / \mu\text{A} = 0.007 \mu\text{A} / \mu\text{gL}^{-1} - 0.084 \mu\text{A}$; $R^2 = 0.95$; $N = 11$; BDDE in the presence of bismuth (III): $I_p / \mu\text{A} = 0.009 \mu\text{A} / \mu\text{gL}^{-1} + 0.044 \mu\text{A}$; $R^2 = 0.98$; $N = 11$) the limit of detections (3σ) were calculated to correspond to 0.342 and $0.299 \mu\text{gL}^{-1}$ in the presence and absence of bismuth (III) respectively. As with lead (II) the relevance of the utilisation of the *in-situ* modifier bismuth (III) for the determination of cadmium (II) was explored at the SPE, GCE and BDDE. Additions of cadmium (II) over the concentration range $10 - 150 \mu\text{gL}^{-1}$ were made into a solution of pH 4.3 acetate buffer at the SPE, GCE and BDDE in the absence (bare) and presence of bismuth (III). As is shown in Figure 5.12 B a linear response is obtained for both the standard-SPE ($I_p / \mu\text{A} = 0.156 \mu\text{A} / \mu\text{gL}^{-1} - 1.787 \mu\text{A}$; $R^2 = 0.98$; $N = 11$) and SPE in the presence of bismuth (III) ($I_p / \mu\text{A} = 0.079 \mu\text{A} / \mu\text{gL}^{-1} + 0.365 \mu\text{A}$; $R^2 = 0.95$; $N = 11$) the two calibration plots show that upon modification of bismuth (III) there is a detrimental effect upon the peak height achieved. The limit of detection (3σ) determined at the standard-SPE was $0.016 \mu\text{gL}^{-1}$ which is slightly improved to a limit of detection (3σ) of $0.050 \mu\text{gL}^{-1}$ when employing the SPE in the presence of bismuth (III). Notably however, unlike the case for the determination of lead (II) at both electrode substrates and cadmium (II) when utilising the SPE, when the GCE was applied towards the determination of cadmium (II) in the presence and absence of the bismuth (III) modifier an increase in the resultant calibration plots and consequently limits of detection was evident. As is clear from Figure 5.12 D in contrast to the observations for the determination of cadmium (II) at the SPE (and both SPE and GCE for the determination of lead (II)) the presence of bismuth (III) results in an increase in the sensitivity of the analytical protocol compared to that obtained at the bare GCE. Although both the responses in the presence and absence of bismuth (III) allow for a linear electroanalytical response over the concentration range under investigation ($I_p / \mu\text{A} = 0.014 \mu\text{A} / \mu\text{gL}^{-1} + 0.018 \mu\text{A}$; $R^2 = 0.99$; $N = 11$ and $I_p / \mu\text{A} = 0.007 \mu\text{A} / \mu\text{gL}^{-1} + 0.029 \mu\text{A}$; $R^2 = 0.97$; $N = 11$ respectively) a greater sensitivity is clear at the bismuth (III) modified GCE as is reflected in the limit of detection (3σ) of $0.31 \mu\text{gL}^{-1}$ and $0.40 \mu\text{gL}^{-1}$

calculated for in the presence and absence of bismuth (III) respectively. Upon utilisation of the BDDE saw an additional increase within the sensitivity of the protocol (shown in Figure 5.12 F) when the electrode is modified with bismuth (III) (BDDE: $I_p / \mu\text{A} = 0.007 \mu\text{A} / \mu\text{gL}^{-1} - 0.083 \mu\text{A}$; $R^2 = 0.95$; $N = 11$; BDDE in the presence of bismuth (III): $I_p / \mu\text{A} = 0.013 \mu\text{A} / \mu\text{gL}^{-1} - 0.190 \mu\text{A}$; $R^2 = 0.98$; $N = 11$) the limit of detections (3σ) were calculated to correspond to $0.35 \mu\text{gL}^{-1}$ and $0.41 \mu\text{gL}^{-1}$ in the presence and absence of bismuth (III) respectively.

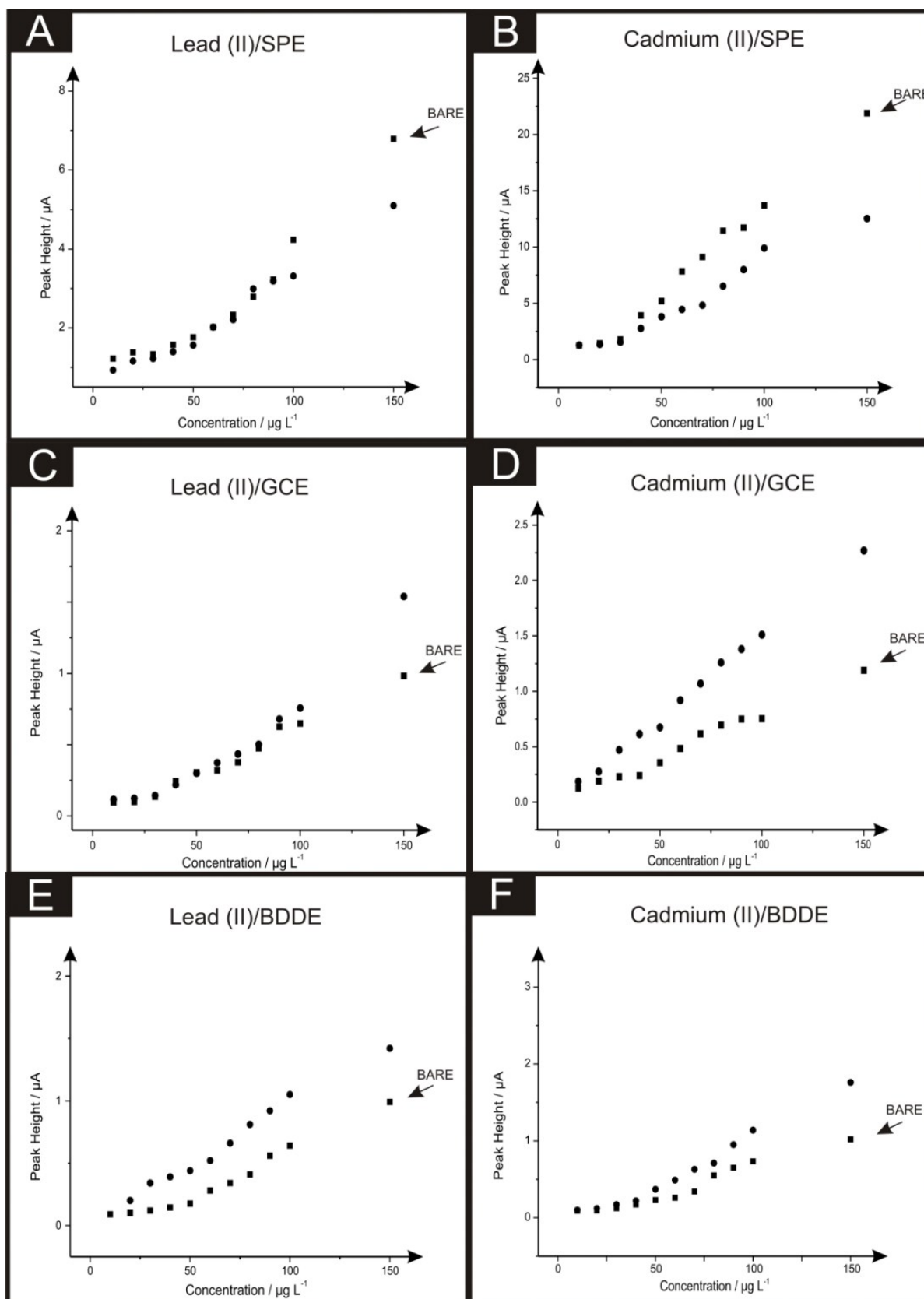


Figure 5.12: Calibration plots depicting the response of voltammetric peak height versus lead (II) (A, C & E) / cadmium (II) (B, D & F) concentration over the range of 10 – 150 $\mu\text{g L}^{-1}$ in a solution of a pH 4.3 acetate buffer using the SPE (A & B), GCE (C & D) and BDDE (E & F). In each the plots obtained for the bare electrode material (squares) is overlaid with the response obtained in the presence of 1 mg L^{-1} bismuth (III) (circles). Deposition potential and time: - 1.2 V (vs. SCE) and 120 seconds respectively. $N = 3$.

Simultaneous determination of lead (II) and cadmium (II) utilising an in-situ modified and unmodified electrodes at WHO levels

Individual analyses of such analytes are redundant if one cannot reach lower concentration levels than that recommended by the WHO therefore such analysis of reaching these limits were realised. Figure 5.13 A shows simultaneous detection for the increasing concentrations of lead (II) and cadmium (II) within a solution containing 0.1 M HCl. The change in buffer was considered due to the detrimental effect of the bismuth (III) towards the overall sensitivity of the standard-SPE. Shown in Figures 5.13 B and C are calibration plots that reach concentration levels of 2-20 μgL^{-1} for lead (II) and 2.2-22 μgL^{-1} for cadmium (II) (within ideal conditions), which are lower than that recommended by the WHO, with values corresponding to 10 μgL^{-1} and 3 μgL^{-1} for lead (II) and cadmium (II) respectively within drinking water. Upon inspection of the data it is clear that in this situation a higher theoretical limit of detection is reached compared to that seen in the previous section utilising an acetate buffer solution, with the values corresponding to 1.2 and 1.0 μgL^{-1} for lead and cadmium respectively. Even though such values are higher, this scenario exhibits the simultaneous detection of both analytes, with no further modification upon the SPE used throughout, therefore offering an exceptionally portable, cheap and reproducible electrochemical sensor.

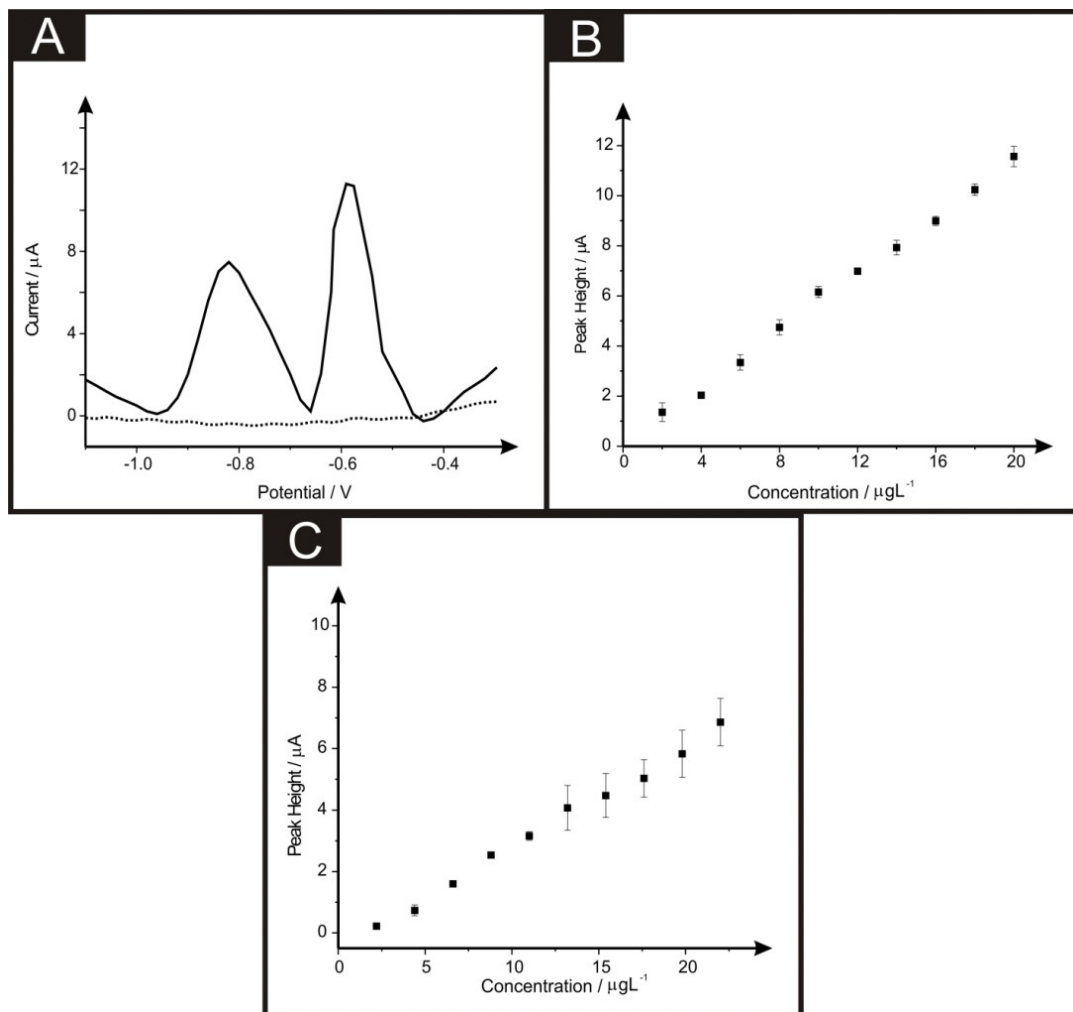


Figure 5.13: Linear sweep voltammograms resulting from additions of lead (II) (at -0.34 V) and cadmium (II) (at -0.60 V) (solid line) into a pH 1.7 HCl solution (dotted line) using a standard-SPE (A). Also depicted are the corresponding calibration plots for lead (II) (B) and cadmium (II) (C) over the concentration ranges of $2\text{--}20\text{ }\mu\text{gL}^{-1}$ and $2.2\text{--}22\text{ }\mu\text{gL}^{-1}$ respectively. Deposition potential and time: -1.5 V (vs. SCE) and 240 seconds respectively, with the respective errors bars corresponding to the standard deviation of the procedure. $N = 3$.

5.1.4 Conclusions

The consideration of electrochemically metallic modified electrodes and combinations, thereof towards the sensing of the heavy metal species lead (II) and cadmium (II), has been reported. In this section, the ‘improvements’ upon the electrochemical response using these metallic modifiers are only ever observed when the underlying electrode substrate exhibits slow electron transfer properties, such as BDDE and GCE. In comparison when such underlying electrode substrate exhibits fast electron transfers kinetics (such as the graphitic screen-printed electrodes used throughout), the improvements are not apparent and in some cases can lead to a detrimental effect upon the electroanalytical response. Therefore, it is clear that modifications upon graphitic SPEs are not necessary, when looking for improved electroanalytical sensing of both lead (II) and cadmium (II). Furthermore *in-situ* bismuth modified electrodes routinely utilise a pH 4 acetate buffer solution in order for the metallic film to be stable²¹³, which can create a problem at low concentrations of heavy metals due to its high background current.²¹¹ The above mentioned standard-SPE system allows for the use of a pH 1.7 0.1 M HCl solution, with the detection of the target analytes (cadmium (II) and lead (II)) at levels below that set by the World Health Organisation (WHO) using a bare graphite SPE, without the requirement of the use of bismuth other metallic modified electrodes. Last, one should not forget that potentially the morphology of the metallic modified electrodes will likely be different on each electrode substrate and is also likely a contributing factor. Nevertheless, the voltammetric performances are insightful to indicate the resulting electroanalytical performances and this work clearly shows that generally metallic modified electrodes are not required to reach WHO levels.

This Chapter has thoroughly examined the *in-situ* metallic modification over the bare counterparts, it has shown that clear metallic benefits can only be demonstrated when utilising a slow electrode surface. This is the first examination of these *in-situ* metallic modifiers which have been reported throughout the literature as beneficial electrode materials.

The next Chapter electrochemically analyses the creation of innovative designs for electroanalytical applications.

Chapter 6 - *Screen-Printed Designs to improve Electroanalytical Responses*

This Chapter explores the utilisation and application of improved screen-printed systems, by the creation of intelligent designs, as described within objective 2.3. Such work has been published within RSC Analyst (2015, **140**, 4130) and Electroanalysis, (2015, In Press).

6.1 Screen-Printed Back-to-Back Electroanalytical Sensors

6.1.1 Introduction

Recently, the introduction of a screen-printed back-to-back electrode configuration was realized, in which both sides of a plastic substrate were screen-printed upon, converting this “dead-space” into a further electrochemical sensor which results in improvements in the analytical performance;²³⁰ Figure 6.1 depicts the concept where screen-printed microband electrodes are fabricated “back-to-back”.²³⁰

In this Chapter, the exploration of the screen-printed back-to-back electrode configuration towards the sensing of the heavy metal lead (II) ions is considered for the first time. These screen-printed microband electrode back-to-back configurations exhibit analytically useful sensing capabilities with improvements in the electroanalytical sensitivity observed over that of the traditionally employed single microband electrodes. Proof-of-concept is demonstrated for the sensing of lead (II) ions at analytically useful levels within model conditions and is demonstrated to successfully quantify lead (II) ions in drinking water which is independently validated with ICP-OES; the analytical utility of the proposed back-to-back microband electrode is demonstrated to quantify lead (II) ions in drinking water at WHO levels.

In addition to the electroanalytical detection of lead (II) ions, the exploration and integration of SWCNTs and CoPC inks have also been explored, towards dopamine, capsaicin and hydrazine for the first time utilising these simplistic designs.

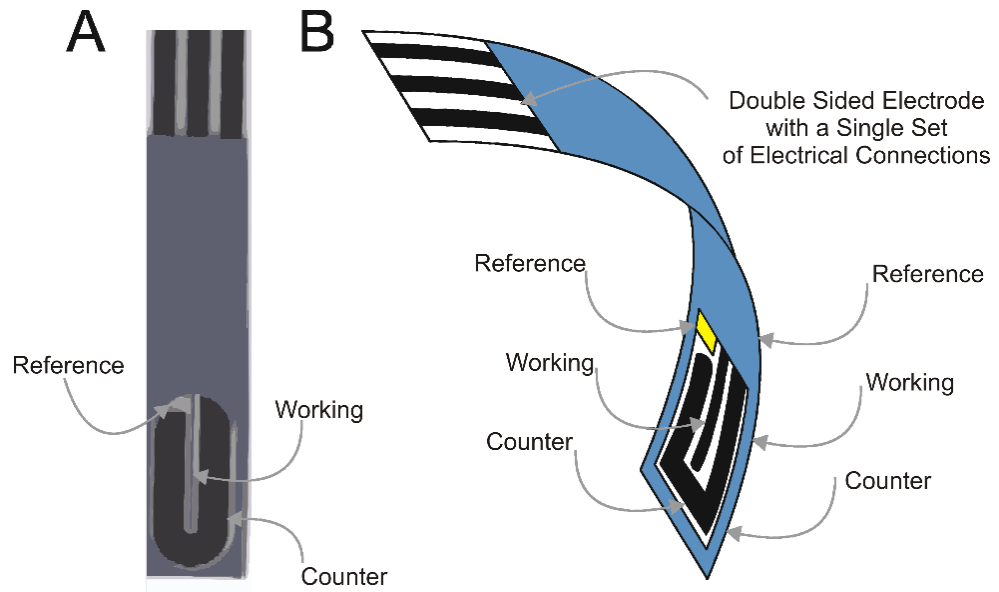


Figure 6.1: Optical image of a single side of a back-to-back screen-printed graphite microband (A) and a schematic depiction of the back-to-back configuration demonstrating the electrode lay-out and single point of electrical connection (B).

6.1.2 Experimental Section

All chemicals used were of analytical grade and were used as received without any further purification and were obtained from Sigma-Aldrich. The solutions were prepared with deionised water of resistivity not less than 18 M Ω cm. All measurements were performed with a Palmsens (Palm Instruments BV, The Netherlands) potentiostat.

All measurements were conducted using a screen-printed graphite microband three electrode configuration (bSPE) consisting of a geometric working electrode (100 μ m diameter and 20 mm length), fabricated in the same way as section 3.3. In this configuration the sensor is printed only upon one side. There are two options to achieve the back-to-back configuration. The first is that the above approach is repeated on the back side of the polyester substrate²³⁰ or two electrode can be taken and placed back-to-back, herein the latter approach is utilised for simplicity. From this point onwards when the electrodes are back-to-back, a superscript "2" is introduced, such that in the case of a single microband electrode (bSPE) in the back-to-back configuration becomes denoted as b²SPE. Additional side-by-side experiments were performed with the microband electrodes printed in a side-by-side configuration as demonstrated in Figure 6.2.

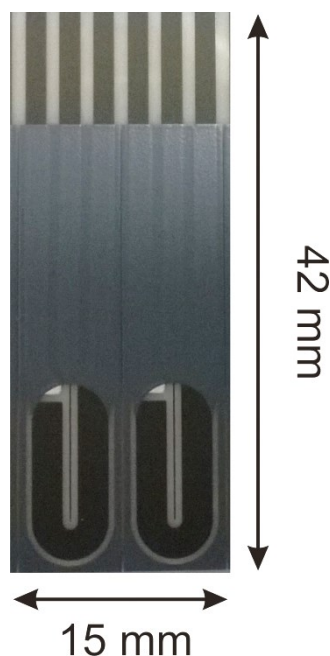


Figure 6.2: Image of two bSPEs in the side-by-side configuration comprising of two working, reference and counter electrodes. Distance between the centre of the two working electrodes: 7.5 mm.

Square wave anodic stripping voltammetry (SWASV) was used throughout this work for the determination of lead (II) ions with a deposition potential of – 1.2 V. The following buffer solutions were utilised and explored in this work: solution A: contained a combination of 2.50 M ammonium acetate (pH 7.0), 1.55 M acetic acid (pH 4.3) and 0.02 M phenol in ethanol solution²³¹ ; solution B: contained a combination of 2.50 M ammonium acetate (pH 7.0) and 1.55 M acetic acid (pH 4.3) ²³¹ ; solution C: 0.10 M sodium acetate buffer solution (pH 4.5) and solution D: 0.02 HCl solution (pH 1.7). Drinking water was obtained from a drinking water tap (Manchester City Centre, Manchester, UK) which was run for a minute before a sample being obtained. The sample was then stored at room temperature and used within a day of sampling. Prior to electroanalytical measurements the drinking water samples were simply modified to pH 1.7 with HCl.

Inductively Coupled Plasma/Optical Emission Spectrometry (ICP-OES) experiments were carried out using a Thermo Scientific DUO iCAP 6300 ICP Spectrometer, exhibiting a relative standard deviation of 2.7 %, used to validate against the electroanalytical method presented within this chapter.

6.1.3 Results and Discussion

Electroanalytical Heavy Metal Ion Sensing

First the optimised solution characteristics for the anodic stripping voltammetric determination of lead (II) ions are explored. Four solutions of differing compositions (see Experimental section) were utilised using the b²SPE with a fixed concentration of 2 mgL⁻¹ of lead (II) ions and a deposition potential and time of -1.2 V and 60 seconds respectively. In this approach the lead (II) ions are accumulated in the form of lead (0) through the application of the negative (deposition) potential, at a selected time following which the potential is swept positive. This process results in the deposited metal lead upon the electrode surface to be electrochemically stripped back to lead (II) ions giving rise to a voltammetric stripping peak, the analytical signal, where the peak height (and area) of the response is proportional to lead (II) ion concentrations.²³² It is found that a distinctive stripping peak is observed at a peak potential of - 0.60 V (vs. Ag/AgCl), such responses are typical of that seen within literature.²³³⁻²³⁸ The average current density (taken from the peak current/electrode geometric area) for the lead stripping peak was 13.60 $\mu\text{A cm}^{-2}$ (solution A), 417.5 $\mu\text{A cm}^{-2}$ (solution B), 542.6 $\mu\text{A cm}^{-2}$ (solution C) and 1037 $\mu\text{A cm}^{-2}$ (solution D). These results show that the optimal solution for the electroanalysis of lead (II) ions is solution D (0.02 HCl solution; pH 1.7) which is used herein.

Further optimisation was next performed, in order to find the optimal deposition time utilising square wave anodic stripping voltammetry (SWASV) using 5 $\mu\text{g L}^{-1}$ of lead (II) ions in a 0.02 M HCl solution (pH 1.7). This concentration is chosen since as it is below that indicated by the WHO, where lead (II) levels within drinking water are recommended to be limited to 10 $\mu\text{g L}^{-1}$.²³⁹ Optimisation of the deposition times were next explored using both the bSPE and b²SPE. It became apparent that the optimum results are obtained when a deposition time of 30 seconds is employed with further deposition times found to result in a plateauing of the observed current density response, as the metal no longer plates upon the electrode surface but the existing plated metal. Through the application of a deposition time of 30 seconds, the current density is found to correspond to 3.40 and 17.55 $\mu\text{A cm}^{-2}$ utilising the bSPE and b²SPE configuration respectively. Such values indicate that the b²SPE exhibits a ~ 5 times

improvement over that of a single bSPE indicating the advantageous use of the back-to-back configuration.

The analytical efficacy of the b²SPE configuration was next explored towards the sensing of lead (II) ions, utilising SWASV and compared to a single microband (bSPE). Figure 6.3 depicts the response from additions of lead (II) ions made over the concentration range of 5-110 µg L⁻¹ using both electrode configurations. Analysis of the SWASV profiles in the form of plots of peak height (I_H) vs. concentration are found to be linear over the concentration range with the following linear regression: bSPE: $I_H / \mu\text{A} = 8.00 \times 10^{-3} \mu\text{A}/\mu\text{g L}^{-1} + 2.90 \times 10^{-3} \mu\text{A}$; $R^2 = 0.99$; $N = 10$; b²SPE: $I_H / \mu\text{A} = 0.06 \mu\text{A}/\mu\text{g L}^{-1} + 0.31 \mu\text{A}$; $R^2 = 0.99$; $N = 10$. Analysis of the current density using both electrode configurations is depicted in Figure 6.4 where the b²SPE exhibits a greater analytical response over the bSPE towards the detection of lead (II) ions over the concentration range used. The limit of quantification (LOQ) was found to correspond to 5.00 µg L⁻¹ for both cases, with values for the limit of detection (LOD) (3σ) for the b²SPE showing a ~3 times improvement in comparison to the bSPE, with values corresponding to 1.01 and 3.70 µg L⁻¹ respectively.

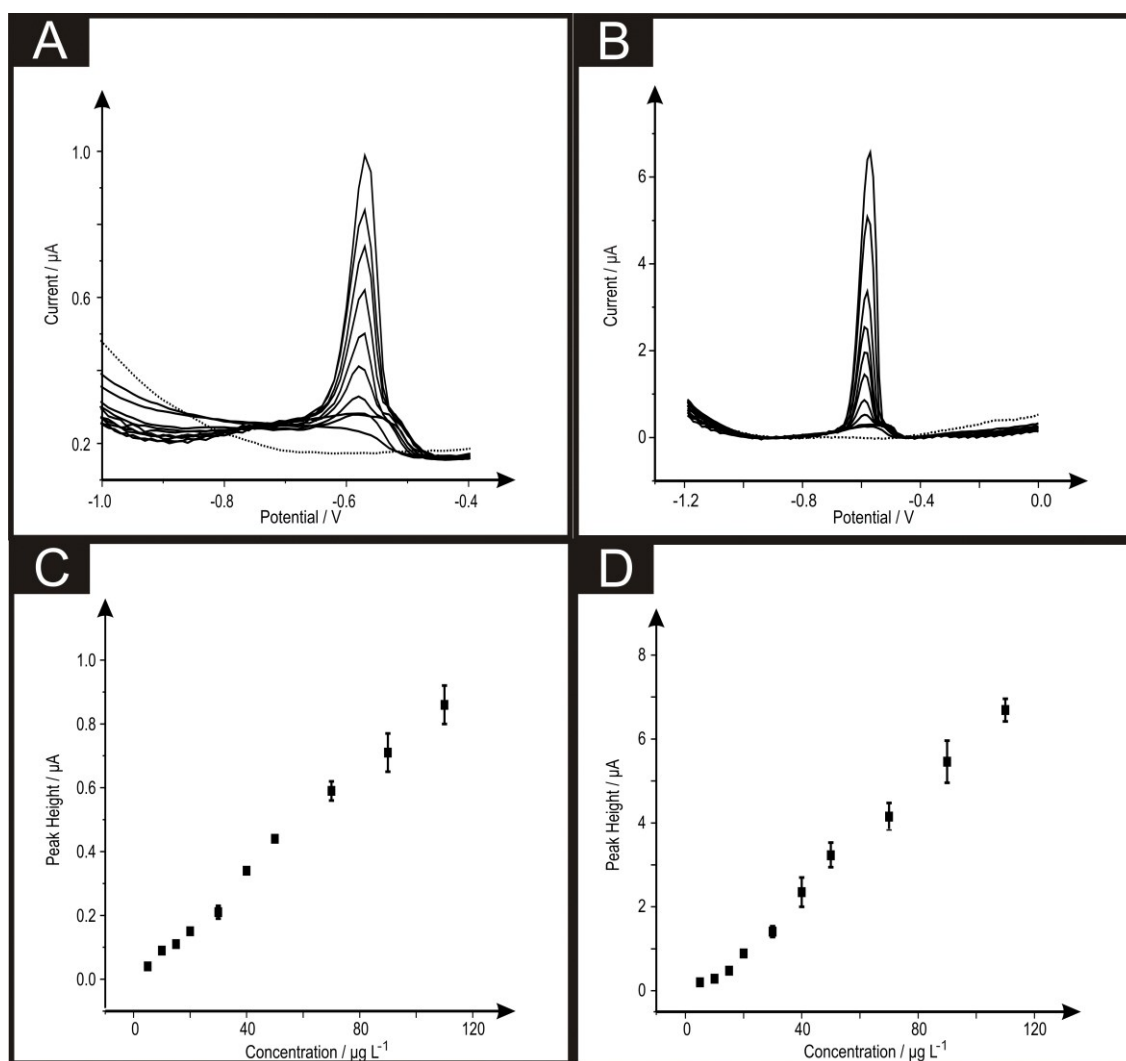


Figure 6.3: Square wave voltammograms obtained in a solution of 0.02 M (pH 1.7) HCl in the absence (dotted line) and increasing concentration additions of lead (II) ions (5 to 110 $\mu\text{g L}^{-1}$) and corresponding calibration plots over the range studied using bSPEs (A & C) and b²SPEs (B & D) respectively. Data presented is an average and error bars from three experiments. Deposition potential and time of -1.2 V and 30 seconds respectively.

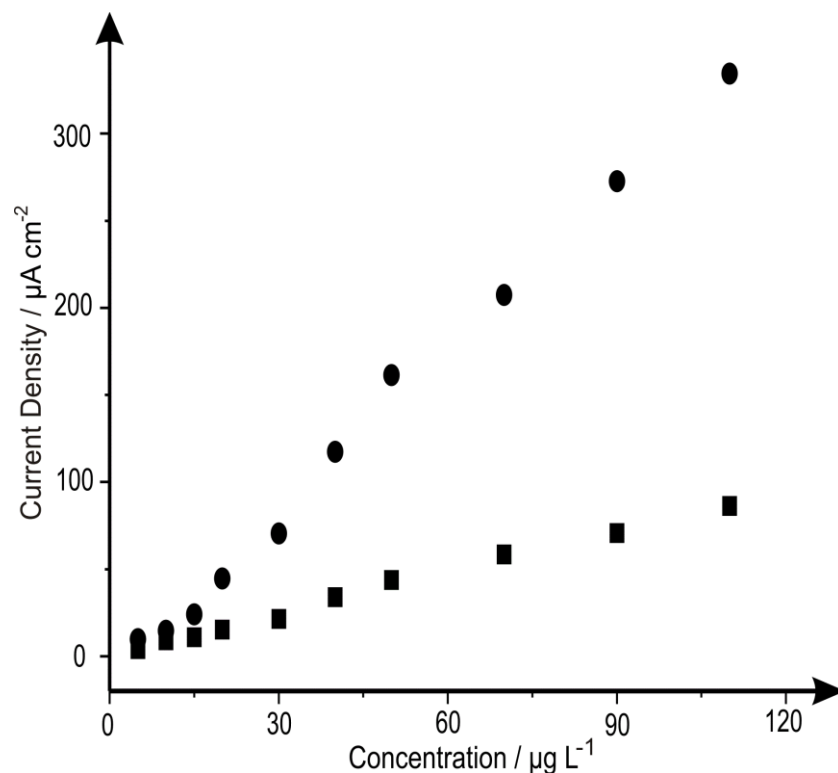


Figure 6.4: Analysis of the data presented in Figure 6.3 in terms of plots of current density (of the peak heights) against increasing concentrations of lead (II) ions utilising the bSPEs (squares) and b²SPEs (circles). Deposition potential and time: -1.2 V and 30 seconds respectively. $N = 3$

The improvement in the current density through the use of the back-to-back configuration is a key advantage of using this novel geometry. The reason for the improvement was thought that in the use of the back-to-back design, the electrode area is consequently doubled without resulting in any increase in unwanted capacitive currents (due to the nature of a microband design), with improvements in the analytical performance observed with the analytical sensitivity (gradient of a plot of peak height/analytical signal against concentration) and the corresponding limit-of-detection being reduced.²³⁰ The microband electrodes are advantageous since due to their geometric shape, have an additional contribution from radial diffusion in addition to planar diffusion. This change in mass transport promotes enhanced rates of mass transport of electroactive species to the electrode surface, reduced double-layer capacitance, and less susceptibility to ohmic losses.²³² These characteristics make it possible to perform analysis with enhanced sensitivity on short time scales under time independent conditions. In the case of the back-to-back configuration, the electrically

wiring of two microband electrodes back-to-back and hence this induces an additional improvement within the sensitivity of the electrodes performance; this is exemplified earlier in this paper where a five times improvement in the current density is evident for the sensing of lead (II) ions using the back-to-back configuration over that of a single microband electrode. This results in improvements in the analytical performance with a greater sensitivity observed (see Figure 6.4) with a lower limit of detection achievable for the case of the b²SPE over that of the bSPE.

It is also important to note that as previously mentioned by Metters *et al.*²³⁰ the back-to-back configuration allows for an ideal electrode configuration where diffusion zones do not overlap or interfere with each other which would be the case if two electrodes were wired in unison and placed in the solution side-by-side (see Figure 6.2). To prove this insight for the sensing of lead (II) ions, a comparison between the side-by-side and the back-to-back configuration (see Figure 6.1) was explored. Figure 6.5 A shows comparative SWASV of both configurations at a concentration of lead (II) ions at 100 µgL⁻¹, it is clear that the peak height in the case of the side-by-side configuration is significantly hindered compared to that of the back-to-back. Additionally shown in Figure 6.5 B are the resultant calibration curves for the side-by-side configuration over the lead (II) ion concentration range of 100-598 µgL⁻¹, the range of which is limited by this configuration. These results are further verified by the vast difference within the LOD (3σ) for the side-by-side configuration compared to the back-to-back configuration, with values corresponding to 31 and 1.1 µgL⁻¹ respectively. Note the high LOD and large error bars are a result of diffusional zones between the working electrodes of the side-by-side overlap where the microbands electrode deplete the same region of solution.²⁴⁰⁻
²⁴² In the case of the back-to-back electrodes, diffusional zones will likely never interact which is an advantage of using this novel electrode configuration.

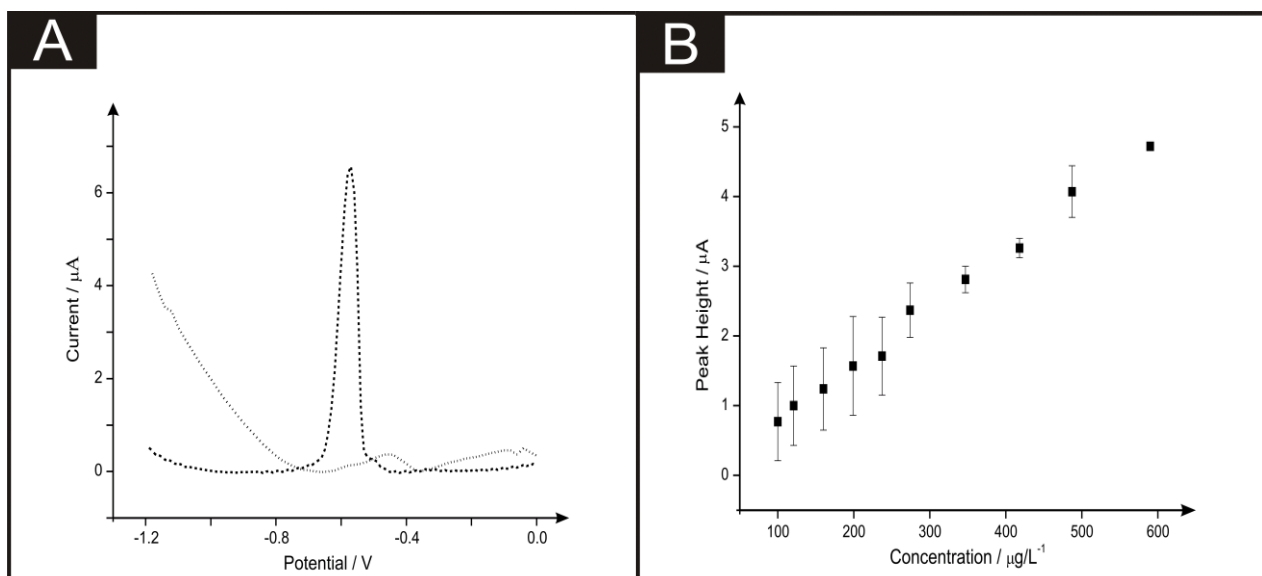


Figure 6.5: Square wave voltammograms (A) for the back-to-back (dotted line) and side-by-side (dashed line) configuration. Solution composition: $100 \mu\text{g/L}^{-1}$ lead (II) ions; 0.02 M HCl. Additionally shown (B) is a plot of peak height vs. increasing concentrations of lead (II) ions. $N = 3$ Deposition potential and time of -1.2 V and 30 seconds respectively.

It is important when analysing heavy metals that the response you are obtaining is that of the metal you desire, therefore the analysis of common interferences of lead (II) (cadmium (II) and zinc (II)) are now considered. Figure 6.6 depicts the response obtained from a b^2SPE sensor, for the simultaneous detection of lead (II), cadmium (II) and zinc (II), it is clear that three separate peaks are observed with peaks forming at -0.6 V , -0.8 V and -1.0 V respectively. Such responses are in agreement with literature concerning the simultaneous detection of these analytes.²⁴³⁻²⁴⁵ Upon analytical analysis (Figure 6.7) of the cadmium and zinc the lower linear range was utilised to calculate the LOD which was found to correspond to 0.3 and $32 \mu\text{g/L}^{-1}$ respectively, which for cadmium is very competitive however this system isn't ideal for zinc ion detection compared to many others,²⁴⁶ nonetheless in this case the focus solely upon the effect of interference not analytical competency. Returning to the analytical performance of the b^2SPE sensor, its response is benchmarked against the current literature and against the WHO recommended limit, as presented in Table 3 (within the appendices). It is clear that the b^2SPE sensor is competitive against other electrochemical configurations. What is of

interest is that in the majority of cases, lengthy deposition times are utilised and very few are applied or validated in real samples.

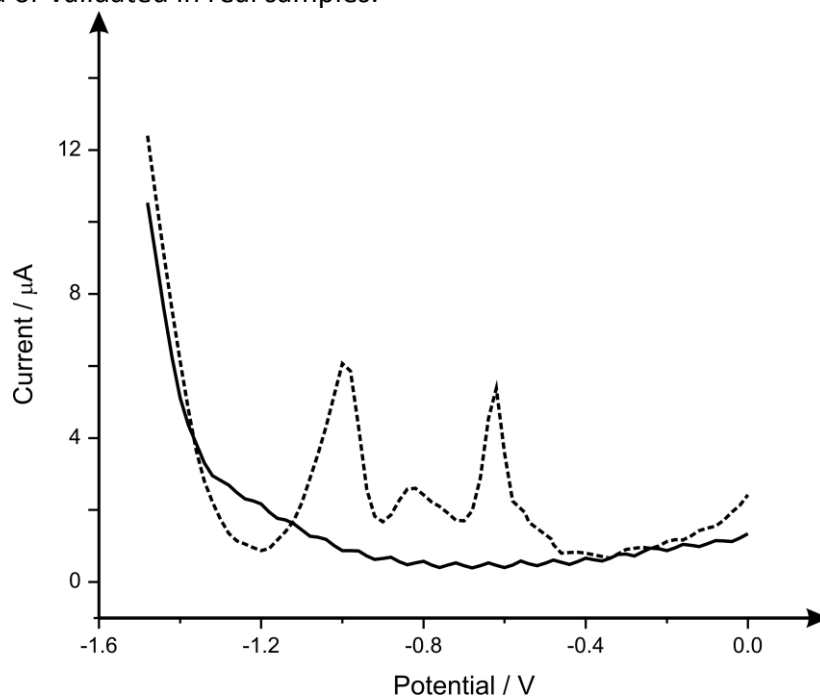


Figure 6.6 (above): Square wave voltammograms obtained using the $b^2\text{SPE}$ within 0.02 M ($\text{pH } 1.7$) HCl (solid line) and the simultaneous detection of lead (II), cadmium (II) and zinc (II) at concentrations of 8 , 16 and $36\ \mu\text{gL}^{-1}$ respectively (dashed line). Deposition potential and time of -1.5 V and 120 seconds respectively.

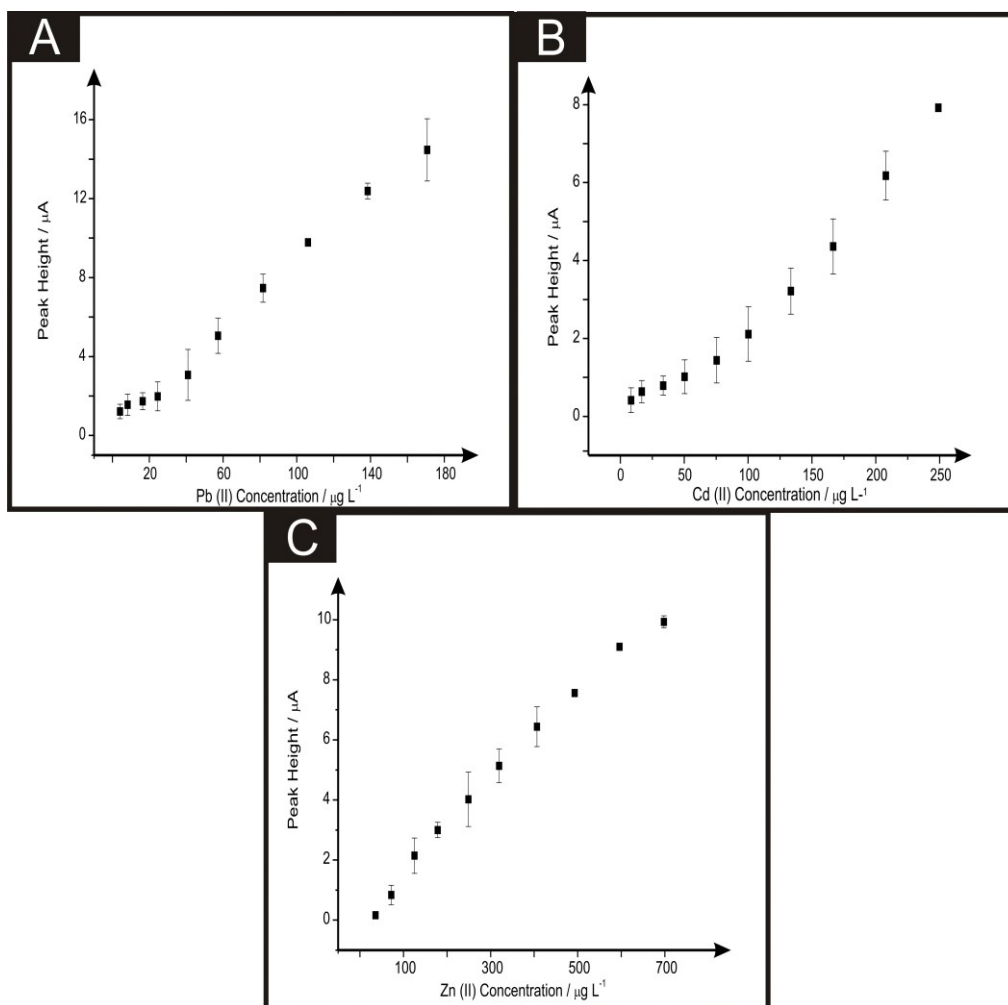


Figure 6.7 (above): Calibration plots of lead (II) (A), and the additional interferents cadmium (II) (B) and zinc (II) (C) using b^2 SPEs. Data presented is an average and error bars from three experiments. Deposition potential and time of -1.5 V and 120 seconds respectively.

The detection of lead (II) ions within drinking water was next explored using the b^2 SPE; real sample analysis was undertaken to see if the proposed electroanalytical protocol has any potential interferents. Using SWASV the determination of lead (II) ions within drinking water *via* the standard addition protocol. A typical standard addition plot and voltammograms are shown in Figure 6.8. The fitting of the data in Figure 6.8 revealed the following linear regression: $I_H/\mu\text{A} = 0.03 \mu\text{A}/\mu\text{g L}^{-1} + 0.08 \mu\text{A}$; $R^2 = 0.99$; $N = 10$. The concentration of lead (II) ions within the drinking water sample was calculated from the lower linear range resulting from the standard addition plot and was found to be $2.8 (\pm 0.3) \mu\text{g L}^{-1}$. The obtained value was compared with Inductively Coupled Plasma - Optical Emission Spectrometry (ICP-OES) (further details can be found in the experimental section). Results obtained *via* ICP-OES correspond to $2.5 (\pm 0.1) \mu\text{g L}^{-1}$. The excellent agreement between the proposed electrochemical protocol and independent laboratory analysis indicates the usefulness of the proposed electrochemical sensing protocol.

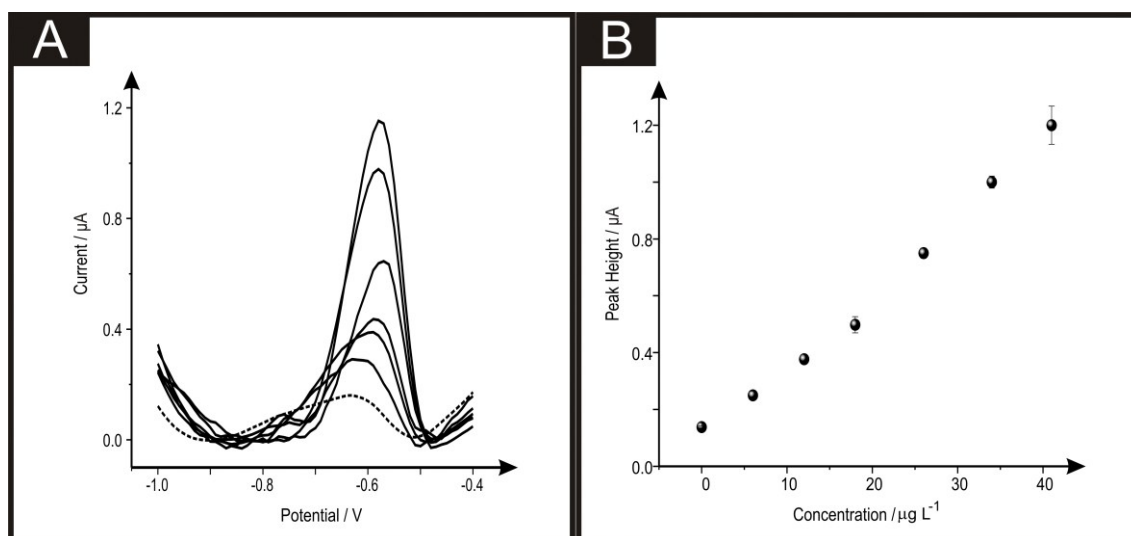


Figure 6.8: Square wave voltammograms obtained using b^2 SPEs (A) in a drinking water sample in the absence (dashed line) and the result of increasing additions of lead (II) ions (solid lines). Standard addition plot (B) for the lead (II) ions within drinking water with corresponding errors bars. $N = 3$ Deposition potential and time of -1.2 V and 30 seconds respectively.

Extending the Potential Applications of the Simplistic Design

The B-CNT-SPEs and B²-CNT-SPEs were fabricated as described in the experimental section and were initially electrochemically characterised using the redox probes hexaammineruthenium (III) chloride and potassium ferrocyanide (II); note the single “B” indicates a standard one-sided sensor while the “B²” indicates the sensors are back-to-back (see Figure 6.1).

Figure 6.9 depicts the observed cyclic voltammetric responses obtained using the B-CNT-SPEs and B²-CNT-SPEs where it is clear that the voltammograms presented show a typical sigmoidal response at the lower scan rate of 5 mV s⁻¹ for both analytes, compared to that at the faster scan rate of 100 mV s⁻¹. Analysis of the effect of scan rate upon the voltammetric response was explored over the scan rate range of 5 to 400 mV s⁻¹ where analysis of the observed peak height plotted against the square root of scan rate produced a linear response for the B-CNT-SPEs and B²-CNT-SPEs with the two redox probes over the entire scan rate range explored: Hexaammineruthenium (III) chloride: $I_p / \mu\text{A} = -5.39 \times 10^{-1} \mu\text{A} / (\text{V s}^{-1})^{1/2} - 1.99 \mu\text{A}$; $R^2 = 0.99$ and $I_p / \mu\text{A} = -1.05 \mu\text{A} / (\text{V s}^{-1})^{1/2} - 4.03 \mu\text{A}$; $R^2 = 0.99$. Potassium ferrocyanide (II): $I_p / \mu\text{A} = 4.12 \times 10^{-1} \mu\text{A} / (\text{V s}^{-1})^{1/2} + 1.10 \mu\text{A}$, $R^2 = 0.99$ and $I_p / \mu\text{A} = 7.89 \times 10^{-1} \mu\text{A} / (\text{V s}^{-1})^{1/2} + 4.03 \mu\text{A}$, $R^2 = 0.99$, $N = 10$ for the B-CNT-SPEs and B²-CNT-SPEs respectively; such response indicate diffusional electrochemical processes. Furthermore, analysis of log₁₀ peak current versus log₁₀ scan rate was performed in order to ensure the semi-infinite diffusion model was governed by the Randles–Ševčík equation. In all cases the gradients were found to be in the range 0.46 - 0.55 indicating no thin-layer effects which can be commonly observed with carbon nanotube electrodes where the redox probe is trapped within solvent pockets of the porous network of the nanotubes.¹⁵ What is of note is that in comparison of the gradients observed for the scan rate studies using the redox probes is that a significant improvement is evident in terms of the voltammetric peak height with an average improvement over the entire scan rate range studied of ~ 1.98 for both redox probes. It is readily evident from inspection of Figure 6.9 that at slow scan rates a steady-state type voltammetric profile is observed where upon faster scan rates, the voltammetric profile becomes peak-shaped. This change in the voltammetric profile is related to the diffusion layer thickness over the microscopic dimension of the band since as the scan

rate is increased linear diffusion predominates resulting in peak shaped voltammetry. This is because the fabricated microelectrode is not a true microelectrode and the contribution from linear/planar diffusion is still significant. However, what is interesting is that nearly a two-times increase in the current is observed (viz Figure 6.9) when a single microband (B-CNT-SPE) is compared to that of a the back-to-back configuration (B²-CNT-SPE) which is due to the electrodes being connected in unison but have no electrochemical interaction with one another and hence effectively an array has been produced where the current is therefore a multiple of the number electrodes, in this case, two.

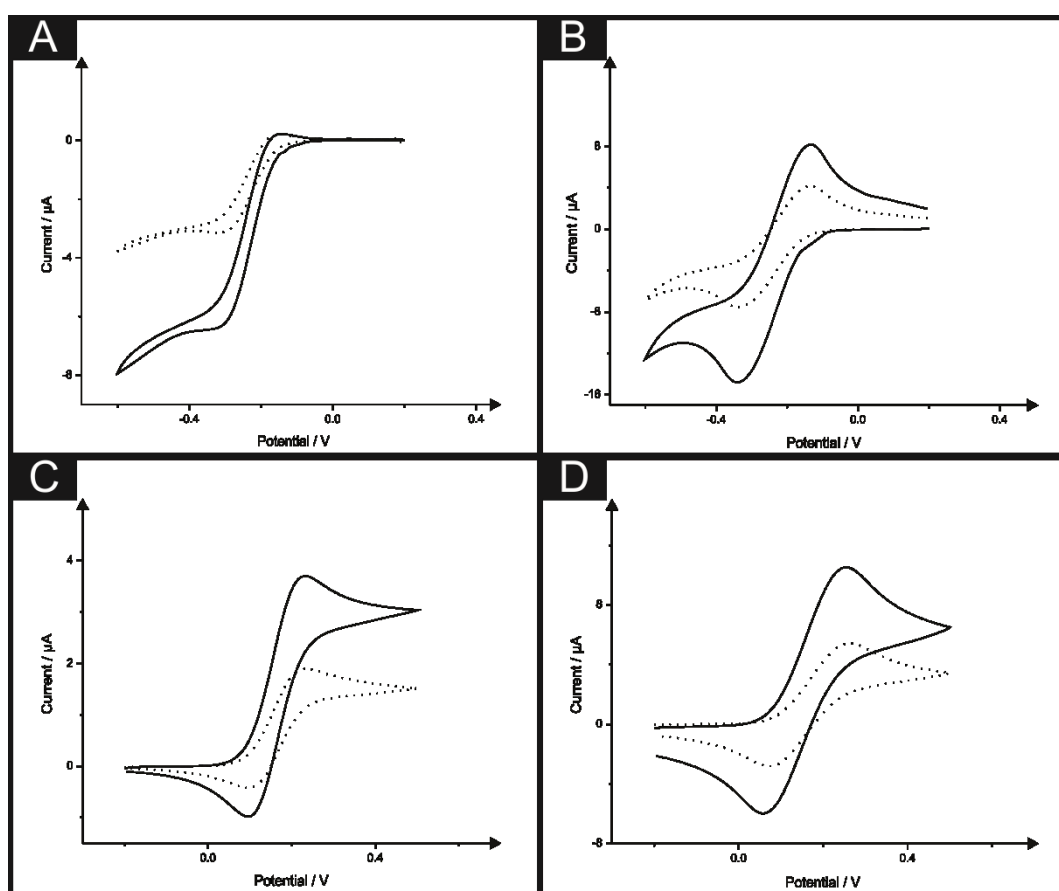


Figure 6.9: Cyclic voltammograms recorded in 1 mM hexaammineruthenium (III) chloride / 0.1 M KCl (A & B) and 1 mM potassium ferrocyanide (II) / 0.1 M KCl (C & D) using the B-CNT-SPE (dotted line) and B²-CNT-SPE (solid line) at scan rates of 5 mV s⁻¹ (A & C) and 100 mV s⁻¹ (B & D) (vs. Ag/AgCl).

Next, attention was turned to electrochemically characterising the B²-CNT-SPEs using the electroactive analyte dopamine (DA). In this section the use of DA as a model analyte for the benchmarking of these novel SPE configurations is considered. Analysis of a phosphate buffer solution (PBS) containing 50 μM DA was first carried out utilising B-CNT-SPEs and B²-CNT-SPEs. Figure 6.10 A depicts cyclic voltammograms of DA, it is clear that an oxidation peak is present at 0.0 V which is in good agreement with literature, representing carbon/graphite electrode surface.²⁴⁷⁻²⁵⁰ Scan rate studies (over the range of 5 to 400 mV s⁻¹) using both electrode configurations was performed with analysis of the voltammetric responses in the form of peak height vs. square root scan rate was found to be linear in both cases, suggesting a diffusional controlled process operating at each electrode surface; B-CNT-SPEs: $I_p / \mu\text{A} = 6.09 \times 10^{-1} \mu\text{A} / (\text{V s}^{-1})^{1/2} + 3.72$, $R^2 = 0.99$, $N=10$. B²-CNT-SPEs: $I_p / \mu\text{A} = 1.08 \mu\text{A} / (\text{V s}^{-1})^{1/2} + 7.40$, $R^2 = 0.99$, $N = 10$. Importantly, as desired, the voltammetric signal, with regards to observed gradient, is noted to double (~ 1.9 times improvement) upon utilisation of the B²-CNT-SPEs over the B-CNT-SPEs as is depicted in Figures 6.10 A.

Next the electroanalytical utility of the B-CNT-SPEs over the B²-CNT-SPEs was explored with additions of DA into a pH 7.4 PBS, over a concentration range of 5 to 49.6 μM. Figure 6.10 B show analysis of the voltammetric peak height (signal) plotted against concentration where it is clear that a linear response arises for both electrode configurations: B-CNT-SPEs: $I_p / \mu\text{A} = 10.6 \times 10^{-3} \mu\text{A}/\mu\text{M}^{-1} + 0.02 \mu\text{M}$, $R^2 = 0.99$, $N = 3$. B²-CNT-SPEs: $I_p / \mu\text{A} = 20.1 \times 10^{-3} \mu\text{A}/\mu\text{M}^{-1} + 0.06 \mu\text{M}$, $R^2 = 0.99$, $N = 10$. Importantly the voltammetric signal, in terms of the analytical sensitivity is noted to double (~ 1.9 times improvement) upon implementation of the B²-CNT-SPEs over the B-CNT-SPEs (see Figure 6.10 A), such a response indicates the benefit of using the back-to-back configuration. The limits of detection (3σ) for dopamine are found to correspond to 11.1 μM and 1.13 μM for B-CNT-SPEs and B²-CNT-SPEs respectively, compared to other literature concerning modified carbon electrodes these values are very competitive. Valentini *et al.*²⁵¹ explored the electroanalytical capabilities of graphene modified macroelectrodes with limit of detection of 4.00 μM, however upon utilisation of CNT modified macroelectrode SPEs Moreno *et al.*²⁵² exhibited a value corresponding to 0.015 μM, which is due to the utilisation of adsorptive stripping voltammetry.

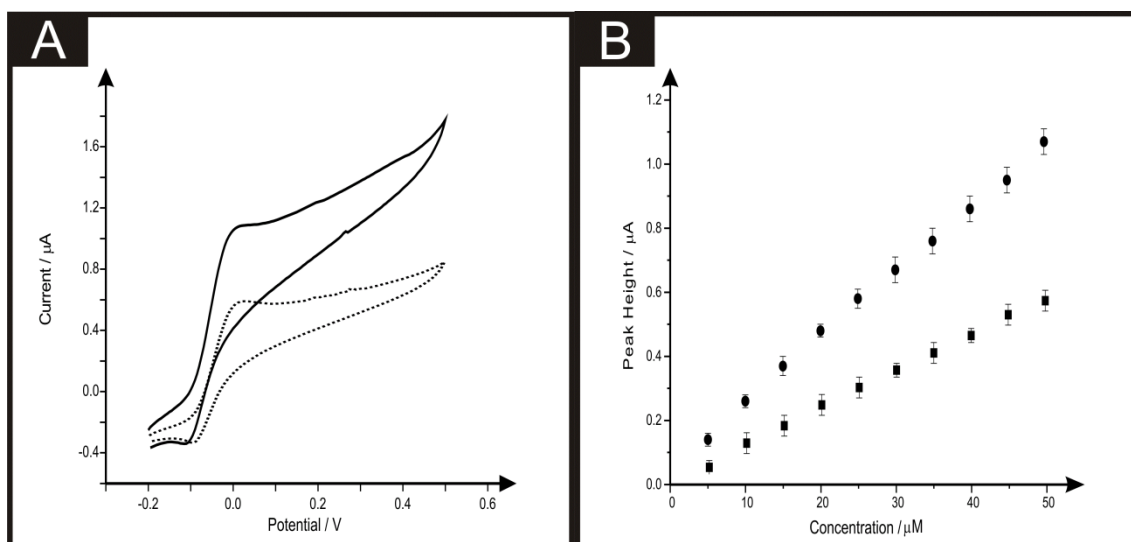


Figure 6.10: Typical cyclic voltammograms obtained in 50 μM dopamine hydrochloride in a pH 7.4 phosphate buffer solution and plots of peak height vs. increasing dopamine concentration (5-49.6 μM) using the B-CNT-SPEs (dotted line & squares) and $\text{B}^2\text{-CNT-SPEs}$ (solid line & circles) at scan rates of 50mVs^{-1} . $N = 3$ (vs. Ag/AgCl)

The focus is now turned to benchmarking the back-to-back configurations with another interesting analyte, capsaicin, which is a natural defence mechanism contained within chilli peppers to prevent mammalian intrusion by eliciting a burning sensation upon contact with the skin by “activating sensory neurons that convey information about noxious stimuli to the central nervous system”.⁴⁰ The potency of the burning sensation is related to the concentration of the various capsaicin present within the chilli pepper consumed. The capsaicin can be used as a topical analgesic for the treatment of post-herpetic neuralgia (shingles), additionally the capsaicin can exhibit combative effects against cholesterol and obesity, and for the treatment of peptic ulcers, back pain, and urinary incontinence.^{40, 253-255}

Figure 6.11 A depicts cyclic voltammetric profiles obtained for capsaicin where the electrochemical oxidation is coupled to an irreversible homogeneous chemical step, which results in the hydrolysis of the 2-methoxy group to form an σ -benzoquinone unit in the structure of capsaicin.⁴⁰ Consequently, the σ -benzoquinone part of the capsaicin falls in a redox electrochemical loop with catechol, this effect has been elegantly explained in literature.^{40, 254} Importantly, as desired, the voltammetric signal, with regards to observed peak height, is noted to double (~ 1.77 times improvement) upon implementation of the $\text{B}^2\text{-CNT-SPEs}$ over the B-CNT-SPEs as is depicted in Figure 6.11 A. A calibration curve over a concentration range of 5 to 49.6 μM , (utilising the reduction peak at $\sim +0.20$ V, as the analytical peak), for both electrode configurations is depicted

in Figure 6.11 B, with an improved current witnessed upon utilisation of a back-to-back configuration, it is apparent that there are two linear ranges for both configurations. In both case the lower linear arises between 5 and 24.9 μM and the upper from 24.9 to 49.6 μM ; B-CNT-SPEs lower linear range: $I_p / \mu\text{A} = 26.24 \times 10^{-3} \mu\text{A}/\mu\text{M}^{-1} + 0.12 \mu\text{M}$, $R^2 = 0.99$, $N = 5$. B-CNT-SPEs upper linear range: $I_p / \mu\text{A} = 26.40 \times 10^{-3} \mu\text{A}/\mu\text{M}^{-1} + 0.06 \mu\text{M}$, $R^2 = 0.99$, $N = 5$. B²-CNT-SPEs lower linear range: $I_p / \mu\text{A} = 46.15 \times 10^{-3} \mu\text{A}/\mu\text{M}^{-1} + 0.01 \mu\text{M}$, $R^2 = 0.99$, $N = 5$. B²-CNT-SPEs upper linear range: $I_p / \mu\text{A} = 46.52 \times 10^{-3} \mu\text{A}/\mu\text{M}^{-1} + 1.16 \mu\text{M}$, $R^2 = 0.99$, $N = 5$. Utilising the lower linear ranges the limit detection were found to correspond to 0.18 μM for the back to back configuration. Such analytical techniques towards capsaicin utilising the B and B²-CNT-SPEs are reported for the first time. Therefore comparisons can only be made towards that of a macroelectrode response, utilised by Randviir *et al.*⁴⁰ and Kachosangi *et al.*²⁵⁴ with limit of detection values corresponding to 0.77 and 0.31 μM .

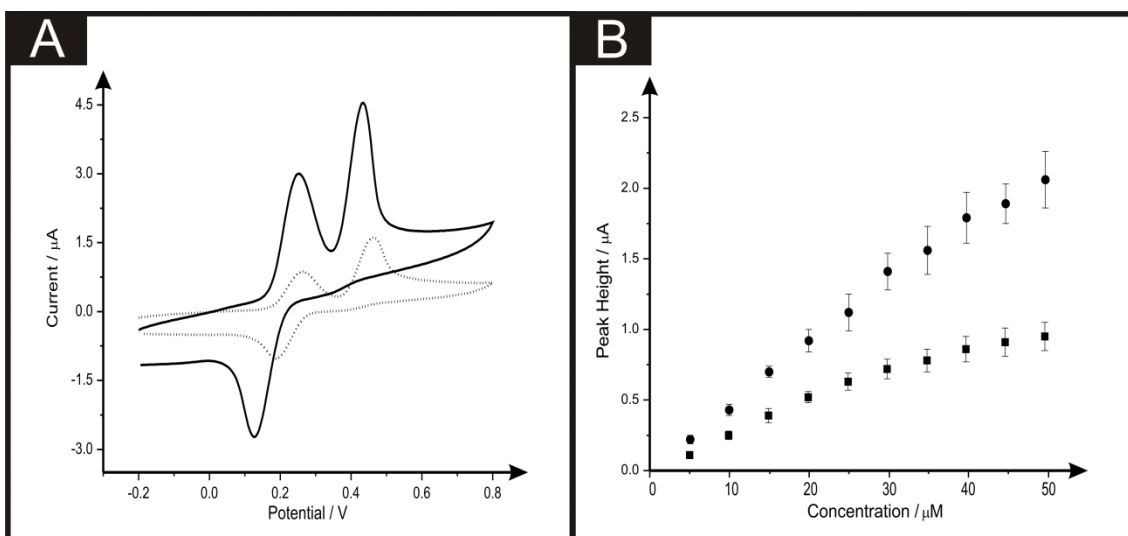


Figure 6.11: Typical cyclic voltammograms obtained in 100 μM capsaicin in a pH 1.25 phosphate buffer solution (A) and plots of peak height vs. increasing capsaicin concentration (5 - 49.6 μM) (B) using the B-CNT-SPEs (dotted line & squares) and B²-CNT-SPEs (solid line & circles) at scan rates of 50 mV s^{-1} . $N = 3$ (vs. Ag/AgCl).

In all the above examples the back-to-back configuration utilises the 'dead space' of the screen-printed sensor and has been shown that the electrode can conveniently be modified with carbon nanotubes and has electroanalytical benefits.²³⁰ Further expansion of the back-to-back configurations was undertaken with CoPC since has previously been shown to be electrocatalytic towards hydrazine. Figure 6.12 A shows a comparison between both electrodes, with the back-to-back configuration exhibiting a

much higher peak current than witnessed previously throughout, in this case there is a 12.7 times improvement compared to the B-CoPC-SPEs, this could be explained by the complex mechanism in which CoPC reacts with hydrazine, such mechanism has been previously explained in section 4.2. Consequent additions of hydrazine within a pH 7.4 PBS were next realised, Figure 6.12 B shows plots of peak height vs. increasing concentration of hydrazine (7.9-104 μM). In both cases it is clear that linear plots are observed, however it is apparent as previously seen throughout and in Figure 6.12 A, there is an extreme increase in the sensitivity of the back-to-back configuration: B-CoPC-SPEs: $I_p / \mu\text{A} = 0.55 \times 10^{-3} \mu\text{A}/\mu\text{M}^{-1} - 4.10 \times 10^{-3} \mu\text{M}$ $R^2 = 0.99$, $N = 10$. B²-CoPC-SPEs: $I_p / \mu\text{A} = 7.01 \times 10^{-3} \mu\text{A}/\mu\text{M}^{-1} - 1.60 \times 10^{-3} \mu\text{M}$ $R^2 = 0.99$, $N = 10$.

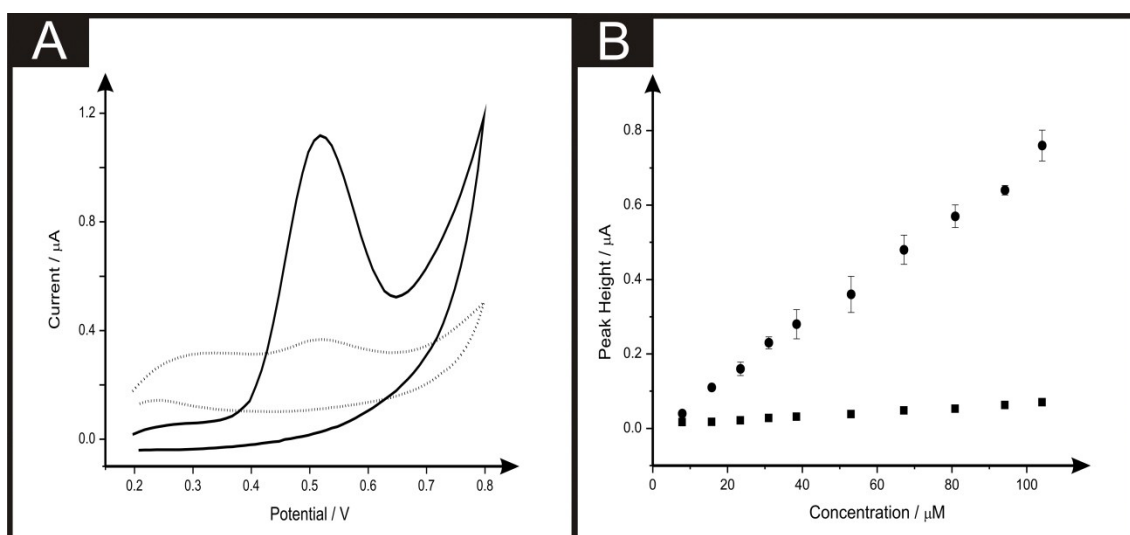


Figure 6.12: Typical cyclic voltammograms obtained in 100 μM hydrazine in a pH 7.4 phosphate buffer solution (A) and plots of peak height vs. increasing hydrazine concentration (7.9 – 104 μM) (B) using the B-CoPC-SPEs (dotted line & squares) and B²-CoPC-SPEs (solid line & circles) at scan rates of 100 mV s^{-1} . $N = 3$ (vs. Ag/AgCl).

This is reiterated in the limits of detection (3σ) for each of the electrodes, with such values corresponding to 2.90 and 4.78 μM for the B²-CoPC-SPEs and B-CoPC-SPEs respectively. The utilisation of a CoPC mediator towards the sensing of hydrazine was reported by Ozoemena *et al*¹¹⁹ with such values for the limit of detection corresponding to 1 μM , using a macroelectrode system, it is important to note that values obtained in this work for the first time are carried out with CoPC derived microband SPEs.

6.1.4 Conclusions

Reported is the first example of using the back-to-back electrode configuration towards the sensing of heavy metal ions using SWASV. It is found that in comparison to a single commonly utilised microband electrode that the back-to-back configuration allows a five times improvement in the analytical sensitivity over that of a single microband, and thus create an excellent alternative to that of a standalone microband electrode setup. Proof-of-concept is demonstrated towards the sensing of an unknown concentration of lead (II) ions found within a sample of drinking water, which upon utilisation of the standard addition method presented a concentration that was independently verified with ICP-OES, was found to be within a similar range. This novel screen-printed back-to-back electrode configuration shows extreme promise for the generic sensing of heavy metal ions. Additionally, this electroanalytical design has been explored towards the electrochemical sensing of dopamine, capsaicin and hydrazine. It has been demonstrated that the back-to-back orientation is a simple approach to facilitate improvements in the electroanalytical response, as observed by a doubling of the analytical response, (gradient of a plot of signal against concentration) with improvements in the limits of detection. Due to the nature of screen-printing with the range of inks that are currently available^{29, 256, 257} the electrode composition can be readily changed which demonstrates the versatility of the back-to-back configuration.

The improved electroanalytical performance of intelligent and novel back-to-back screen-printed sensors has been demonstrated over the single electrode setup. Such designs can minimalise wasted space and amplify the current exhibited within electrochemical reaction. The work presented within this Chapter meets and exceeds that described within objective 2.3.

The next Chapter introduces a possible future electrochemical graphitic platforms, which can be applied within electroanalytical scenarios.

Chapter 7 - *Simplistic Electrode Fabrication Methods*

This Chapter demonstrates for the first time a ‘new’ concept for the design and fabrication of low cost, portable electrode configurations, utilising commercially available pencil drawn electrodes. Such work further exceeds the objectives of the creation of new electrode designs for electroanalytical applications.

7.1 Pencil It In: Pencil Drawn Electrochemical Sensing Platforms

7.1.1 Introduction

There is currently an enormous global interest towards the design, synthesis and fabrication of improved analytical sensing platforms. Electrochemically derived sensors attract attention due to their ability to convert chemical information into an electrical signal and through careful design can give rise to sensitive, selective, experimentally simple and low cost sensors.²⁵⁸ Over recent decades the expansion of carbon based electrochemistry has received a significant focus due to these materials satisfying the aforementioned demands, with a particularly large wealth of knowledge being obtained within the fields of highly ordered pyrolytic graphite,^{16, 259} mono- and few- layer graphene,²⁶⁰⁻²⁶² and carbon nanotubes.^{263, 264} The utilisation of ‘popular’ carbon based materials offers exciting advances within electrochemistry, such as the cost effective production of electrodes that exhibit a similar or enhanced performance to that of the traditional noble metal based alternatives.²⁶⁵ With electrochemists constantly searching for new electrode configurations, focus has now turned to the readily available hand-drawn pencil graphitic electrodes (PDEs),²⁶⁶⁻²⁶⁸ where one can potentially draw their own electrode providing a rapid and extremely cost-effective approach for the production of electrochemical sensing platforms.

Commercial pencils (and consequently PDEs) contain a high percentage of graphite, making these an excellent ‘cheap’ electrode material, where the pencil itself is used as an electrode.²⁶⁶⁻²⁶⁸ Previous literature has been orientated around pencils being used as static standalone electrodes, with many electrochemical applications reported, such as towards the detection of ascorbic acid,²⁶⁹ dopamine,²⁷⁰ flavonoids,²⁷¹ and morphine.²⁷² However, utilising such standalone pencils as working electrodes is not without its drawbacks, such as their large/bulky nature and the lack of tailorability within the design

and control of the working area. One innovative solution is to utilise PDEs, which satisfy the mass requirement for the miniaturisation of electrochemical systems, in addition to allowing vast adaptability and regulation of the working area; the potential ability to draw one's electrode onto a variety of surfaces is extremely attractive. As such, the nature of PDEs potentially allows for extremely simple, effective, low cost and portable sensors to be developed.

Recently, the interest in utilising PDEs has grown and this is evident through the emergence of literature reports which are overviewed in Table 4 (within the Appendices), with many research groups focusing upon either characterising the electrochemical properties of the PDEs or utilising them towards specific sensing applications^{266, 269, 272} with insufficient/inadequate characterisation being provided in each case. Table 4 (within the Appendices) provides a thorough literature overview, where for example, Dossi *et al.*²⁷³ have studied the performance of PDEs upon paper substrates towards the detection of ascorbic acid, with additional work utilising cobalt (II) phthalocyanine doped- PDEs, where the cobalt (II) phthalocyanine has been mixed with the bulk pencil "lead", and placed within a similar pencil setup and explored for the electrocatalytic detection of cysteine and hydrogen peroxide.²⁷³ Other work from this group has explored the detection of analytes such as potassium ferrocyanide,²⁷⁴ 1,2-hydroxybenzene,²⁷⁵ dopamine and paracetamol.²⁷⁶ Honeychurch has elegantly demonstrated the electrochemical detection of lead (II) within real-canal-water samples using PDEs hand-drawn upon polyvinylchloride substrates.²⁶⁶ Although such studies highlight the use of PDEs as a potentially plausible option towards future reproducible, cost effective and simple sensors, many of the examples highlighted in Table 4 (within the Appendices) fail to adequately characterise the underlying electrochemical (and physicochemical) properties present and furthermore overlook the use of control experiments. Another key point to note is that in cases where it is claimed that PDEs are being utilised, in actual fact in the case mentioned previously, a homemade graphite paste electrode type set-up (for example see: [273] and [277]) is being implemented, with incorporation of the 'lead' from a pencil, which as such should not strictly be classified as a PDE.

Inspired by the recent reports of utilising PDEs and the considerations noted above, in this Chapter the fabrication, characterisation (physicochemical and electrochemical) and implementation (electrochemical sensing) of various PDEs upon a flexible polyester substrate, is reported. The electron transfer properties of our hand-drawn electrodes towards hexaammineruthenium (III) chloride and potassium ferricyanide are explored, performing control experiments to achieve the optimum performance in terms of the number of 'draws' when fabricating a specific PDE and vary the pencil graphite content/composition used to draw the PDEs, namely, 6B, 5B, 4B, 3B, 2B, B, HB, H, 2H; such control experiments are rarely performed in the literature. Finally, the electroanalytical performance of our PDEs towards the detection of *p*-benzoquinone and the simultaneous detection of lead (II) and cadmium (II) are explored for the first time utilising PDEs.

7.1.2 Experimental Section

All chemicals used were of analytical grade and were used as received without any further purification from Sigma-Aldrich. The solutions were prepared with deionised water of resistivity not less than 18 M Ω cm and were thoroughly degassed with nitrogen before analysis. All measurements were performed with a Palmsens EMSTAT (Palm Instruments BV, The Netherlands) potentiostat.

The pencil drawn electrodes (PDEs) were fabricated by hand-drawing a 4 mm diameter circle onto a flexible polyester substrate (Autotex AM 150 μ m (F157L)) using a bespoke stainless steel stencil (see Figure 1) and a range of pencil grades 6B, 5B, 4B, 3B, 2B, B, HB, H, 2H from a commercially available box of STAEDTLER tradition[®] 110 pencils.

Upon referring to 'one draw' within this paper, this stipulates that we have moved the pencil whilst in contact with the substrate such that the complete area within the 4 mm diameter circle/disc (to be defined as the working area) is drawn as shown in Figure 1. After defining the surface area, a connecting strip from the top of the circle allows for a crocodile clip connection to be employed to the potentiostat.²⁷⁸ Sellotape[®] was applied to each individual electrode to cover the conductive carbon connections. In all experiments utilising the PDEs, a platinum wire electrode and saturated calomel electrode (SCE) were used as the counter and reference respectively for comparative purposes.

Scanning electron microscope (SEM) images were obtained with a JEOL JSM-5600LV (JEOL, Tokyo, Japan) model. For the high-resolution transmission electron microscope (TEM) images a JEOL JEM 2100F was used. Raman analysis was carried out using the Thermo Scientific[™] DXR Raman (Thermo Scientific[™], Waltham, MA, USA). XPS chemical analysis were performed with a VG-Microtech Multilab electron spectrometer, by using the Mg K⁻¹ (1253.6 eV) radiation of a twin anode in constant analyser energy mode with a pass energy of 50 eV.

7.1.3 Results and Discussion

As exhibited in Table 4 (within the Appendices), the majority of the current literature concerning PDEs either do not identify or optimise the layers/draws of the pencil required for the construction of the PDE nor explore the range of pencils that can be used to fabricate the PDEs. In many cases reported within Table 4 (within the Appendices), the PDEs are fabricated from carbon paste electrodes, which consist of the bulk pencil “lead” as the source of graphite, they are then used to draw the PDE. In this paper, ‘one draw’ stipulates that the pencil has moved whilst in contact with the substrate such that the complete area within the 4 mm diameter circle/disk (to be defined as the working area) is “pencilled in” as shown in Figure 7.1.

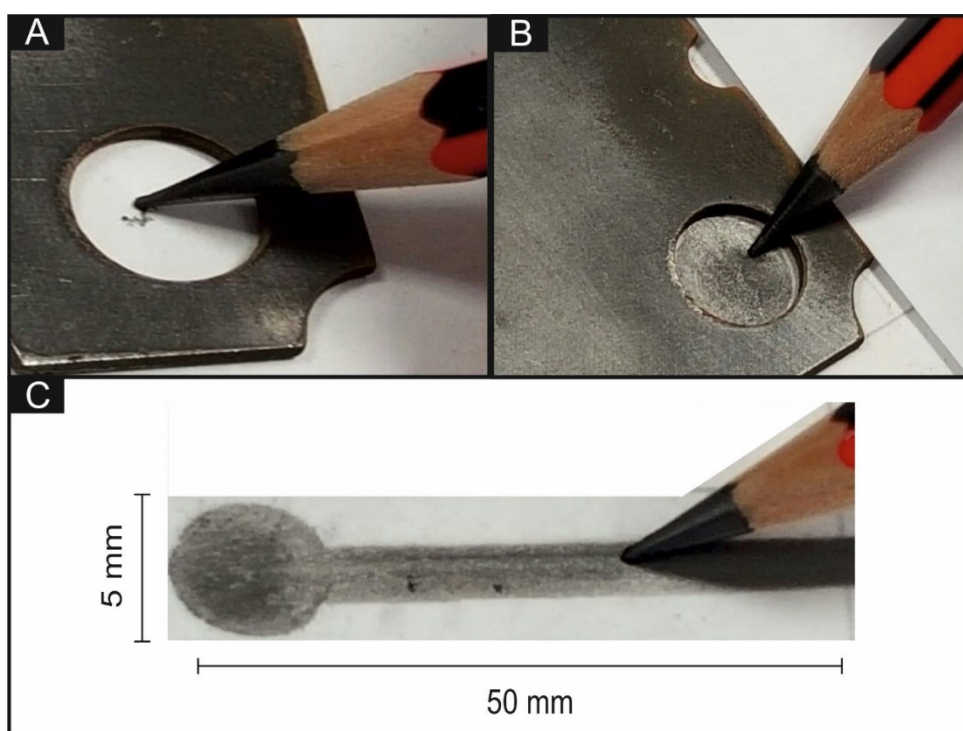


Figure 7.1: Optical image of the bespoke metallic stencil used throughout this work (A) to fabricate the PDEs. Shown in (B) is the PDE after one draw and the completed PDE with a connecting strip (C). Sellotape® was applied to each individual electrode to cover the conductive carbon connections and define the 4 mm working area.

Electrochemical Characterisation of the Pencil Drawn Electrode (PDEs)

Figure 7.2A shows cyclic voltammograms recorded using the redox probe hexaammineruthenium (III) chloride with PDEs which have been drawn just once. Generally, the observed responses are typical of that expected for graphitic-based electrochemical sensors where useful voltammetric signatures are observed, with the 6B found to exhibit the relatively largest peak current; however, the 5B shows the best electrochemical reversibility. To further explore this, Figure 7.2B, C, D show the PDEs drawn three, five and ten times respectively, where it is clear that as the number of layers are increased, the magnitude of the electrochemical response/peak current also increases. Note the 6B PDE drawn ten times gives rise to a clear decrease in the peak-to-peak separation and an increase of the voltammetric peak current over that of the other PDEs, indicating a more beneficial electrode surface with relatively improved/faster electrochemical reversibility and larger effective area, making this PDE the most suited for further electrochemical analysis .

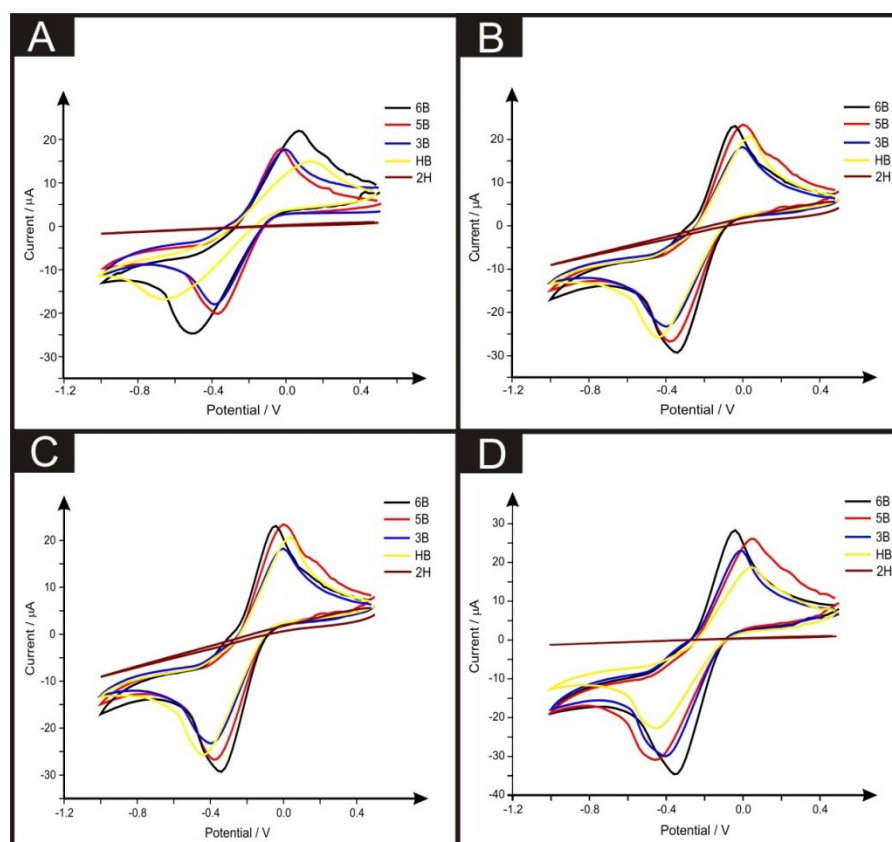


Figure 7.2: Typical cyclic voltammograms utilising different pencil grades drawn once (A), three (B), five (C) and ten (D) times recorded in 1 mM hexaammineruthenium (III) chloride / 0.1 M KCl. Scan rate: 50 mV s^{-1} (vs. SCE).

The effect of pencil type and number of draws is presented in Figure 7.3, where plots of peak height vs. pencil type are summarised; it is clear that the 6B in all cases exhibits the optimal electrochemical response as evaluated using this redox probe, in particular for the PDE drawn ten times. Thus, herein the PDEs for all further studies are drawn with a 6B PDE drawn ten times in order to ensure maximum electrochemical performance.

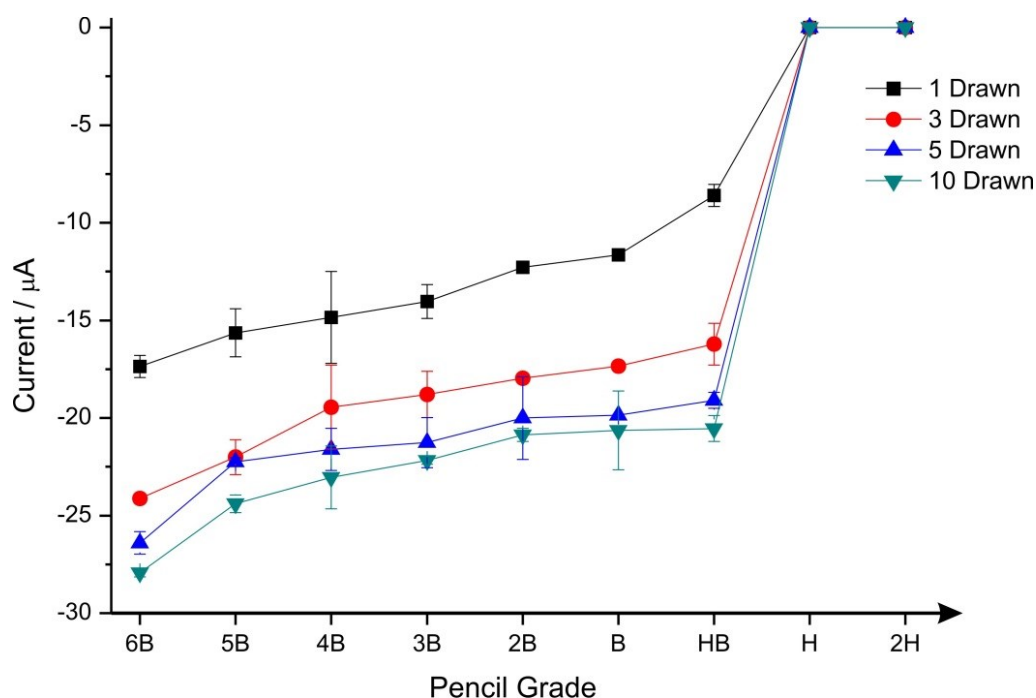


Figure 7.3: Plots of pencil composition/grade vs. peak height (cathodic current) recorded in 1 mM hexaammineruthenium (III) chloride / 0.1 M KCl as a result of increasing the number of draws. Scan rate: 50 mV s^{-1} (vs. SCE). Data shown is an average and corresponding standard deviation $N = 3$

The electrochemical profiles of the PDEs using the redox couple hexaammineruthenium (III) chloride were explored over a range of voltammetric scan rates (as presented within Figure 7.4A) where a plot of peak height vs. the square root of scan rate was constructed and found to be linear indicating that the electrochemical process at PDEs is diffusionally controlled. Electrochemical characterisation was next explored using the potassium ferricyanide redox probe (Figure 7.4B). It is clear, that an unexpected response is observed for this redox couple, implying that there is a contamination present within the clay (which is a component of the pencil used to draw the PDE) giving rise to an oxidation peak at $\sim +0.20 \text{ V}$. Further analysis of this redox

probe was carried out over a range of scan rates; with a plot of peak height vs. the square root of scan rate found to be linear indicating a diffusional controlled electrochemical process.

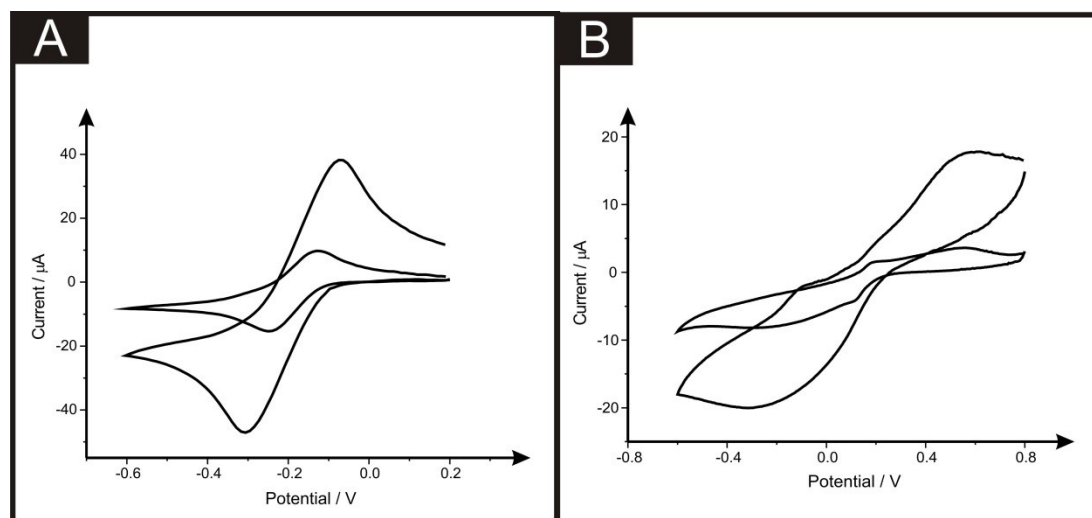


Figure 7.4: Typical cyclic voltammetric responses recorded in 1 mM hexaammineruthenium (III) chloride / 0.1 M KCl (A) and in 1 mM potassium ferricyanide / 0.1 M KCl (B) at 5 mV s^{-1} (dotted line) and 100 mV s^{-1} (solid line) (vs. SCE) using the 6B PDE drawn ten times.

It is important to note, that within preliminary experiments the electrochemical oxidation of an electroactive species is only successful if an electrochemical reduction step occurs first, severely hindering the overall application of these electrodes. This is exemplified within Figure 7.5, where an attempt to electrochemically oxidise potassium ferrocyanide (in 0.1 M KCl) is unsuccessful, and a featureless voltammetric signature is observed, even after carrying out extensive electrochemical pretreatment/cycling of the electrode. Such responses are unlike those seen within the literature by Dossi *et al.*,²⁷⁴,²⁷⁵ casting doubt over the reproducibility of different batches of pencils used to fabricated PDEs.

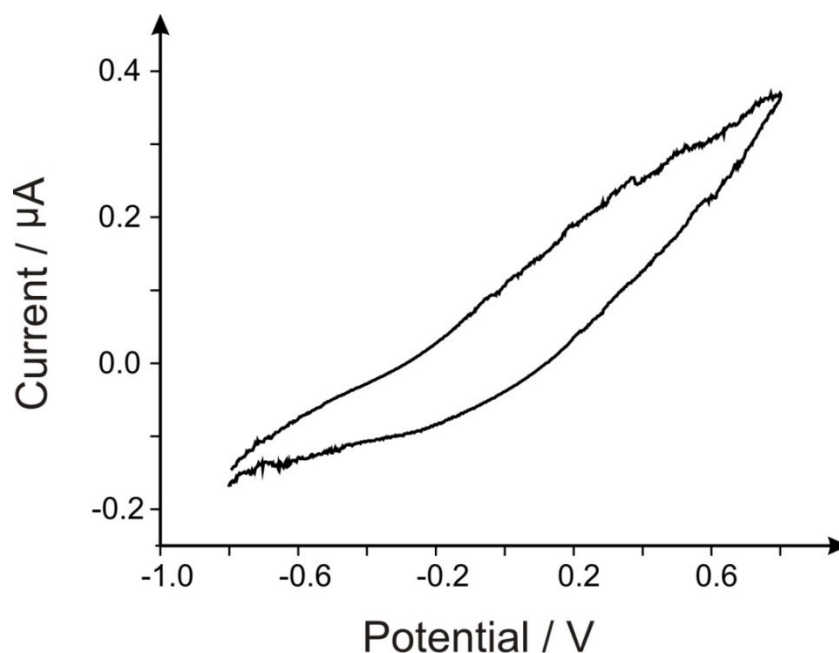


Figure 7.5: Typical cyclic voltammetric response using the 6B PDE drawn ten times recorded in 1 mM potassium ferrocyanide / 0.1 M KCl. Scan rate: 100 mV s^{-1} (vs. SCE). Note that this figure reiterates that electrochemical processes which require an electrochemical oxidation step first give rise to featureless voltammetric profiles.

Physiochemical Characterisation: Bulk Pencil “lead” and Pencil Drawn Electrode (PDEs)

First, characterisation of the bulk 6B pencil “lead” (later used for the fabrication of the PDEs) utilising TEM imaging is shown in Figure 7.6. It is clear that the sheets of graphite within the pencil are folded and contain many defects, which could potentially provide useful electrochemical properties. Figure XB also shows some areas of potential contamination from the clay utilised within the manufacture process of these pencils. Additionally, indicated within Figure 7.6D are areas of few-layer graphene, which may indicate that multi-layer graphene could be potentially fabricated upon drawing of these electrode systems. Depicted within Figure 7.7 are typical SEM images of the hand drawn graphitic surfaces of 6B PDEs drawn once and ten times where it is clear that upon the ten layers of pencil, the amount of graphite transferred is increased, and upon further magnification the flakes of graphite are visible.

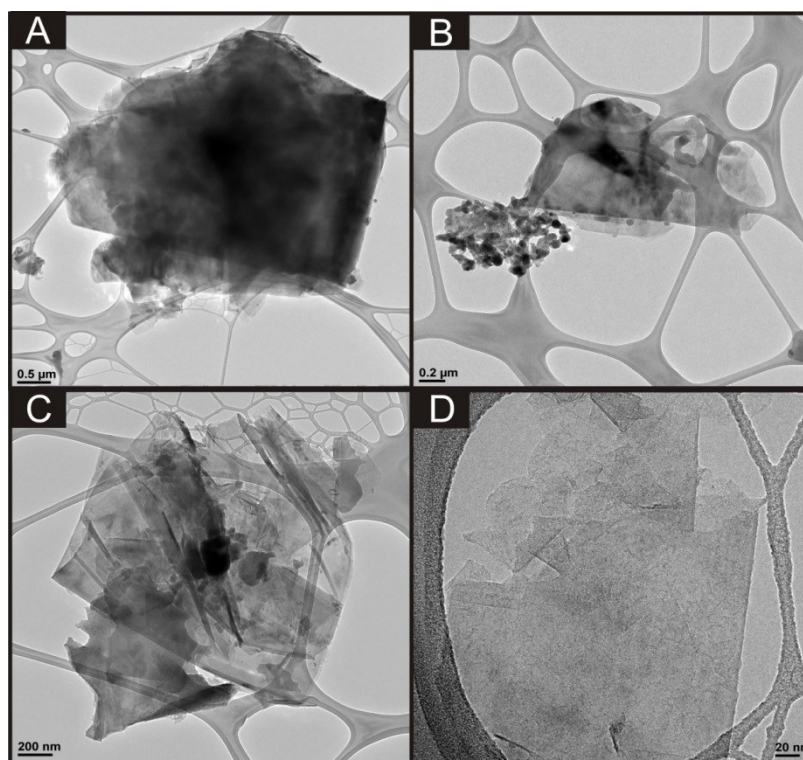


Figure 7.6 (above): TEM images of the bulk 6B pencil 'lead' (used for the fabrication of the PDEs) at increasing magnifications.

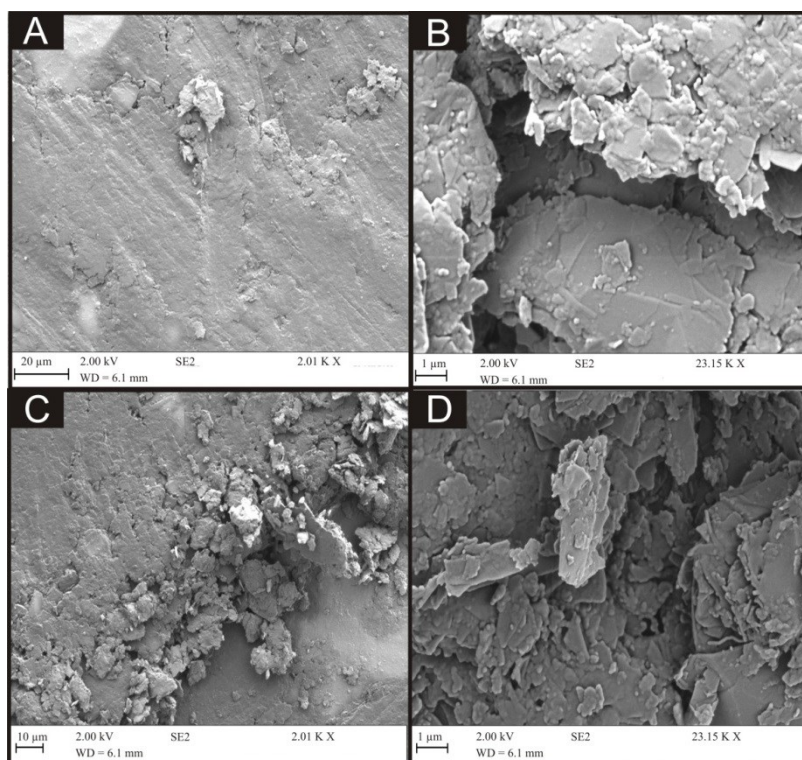


Figure 7.7 (above): SEM images of 6B PDEs drawn once (A and B) and ten times (C and D).

Raman analysis was next performed and depicted within Figure 7.8 where comparative Raman spectra for the bulk 6B pencil "lead" (used to fabricate the PDEs

but analysed “as is”) and PDEs drawn once and ten times are presented. Clearly, the transfer of graphite from the pencil to the substrate successfully occurs as electrodes are pencilled in/drawn which is indicated by the Raman spectrum showing high quality graphite, with characteristic D, G and 2D peaks at 1340, 1580 and 2700 cm^{-1} respectively. In the case of the bulk 6B pencil “lead”, there is a shift within the Raman spectra to 2980 cm^{-1} , which could be associated with compounds present within the clay/binder support within the pencil. To understand further the transfer of graphite onto the supporting substrate, Raman maps were obtained over a large area of two different 6B PDEs. Figures 7.9A and D represent variations within the intensity of the 2D peak at 2750 cm^{-1} over the area of interest, where it is clear that upon the 6B PDE being drawn ten times the amount of ‘black spots’ are reduced, as the increase of clay/binder from the pencil lead is deposited upon the substrate surface. This is also evident within Figures 7.9B and E, where the response from the intensity of the Raman peak has created a three dimensional reconstruction of the 6B PDE surface, representing a relatively smoother surface when the 6B PDE has been drawn ten times, likely from an increase of the binder/clay which is also transferred.

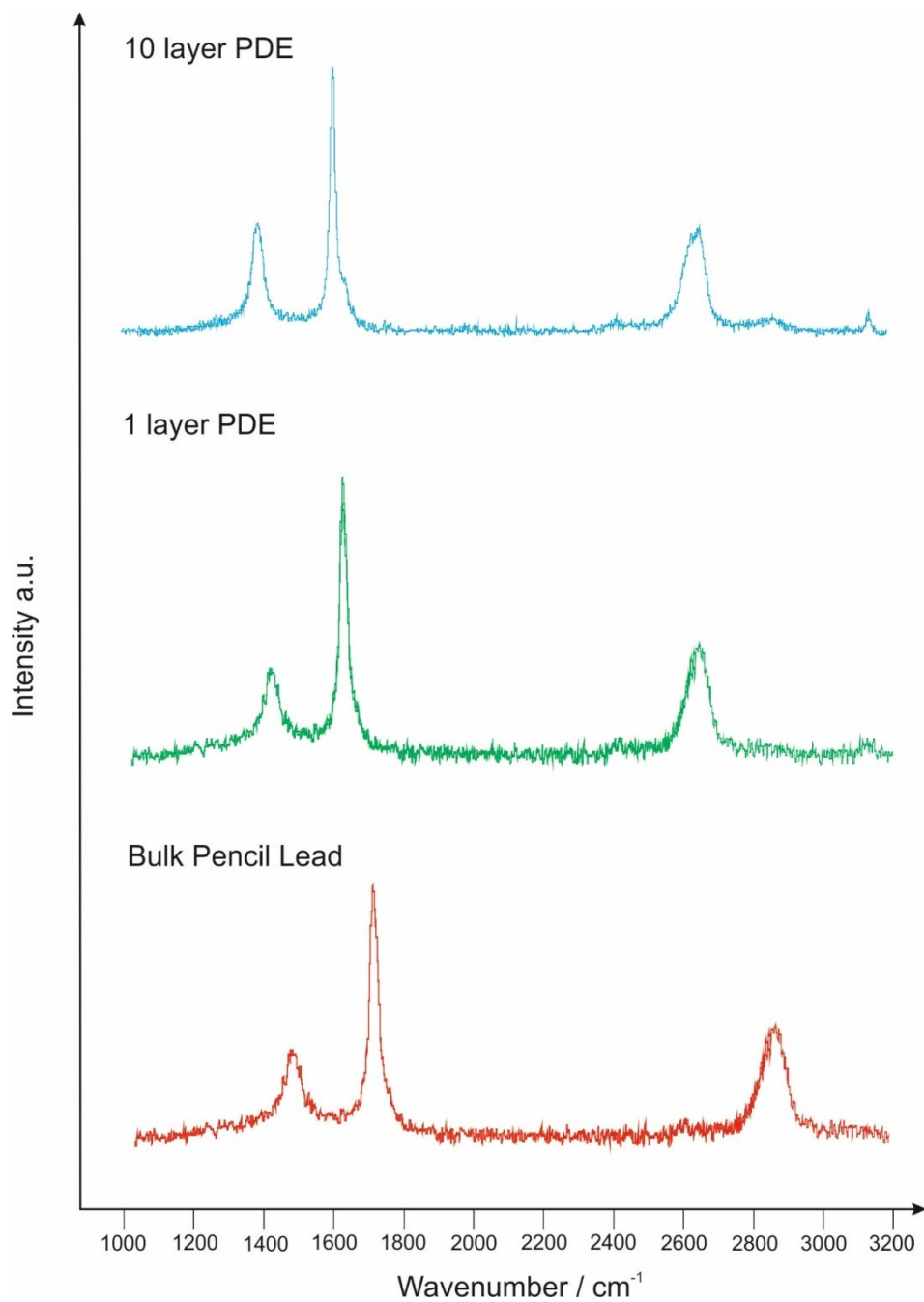


Figure 7.8: Raman spectra for the bulk 6B pencil lead (red line; pencil lead analysis as received), 6B PDE drawn once (green line) and ten times (blue line).

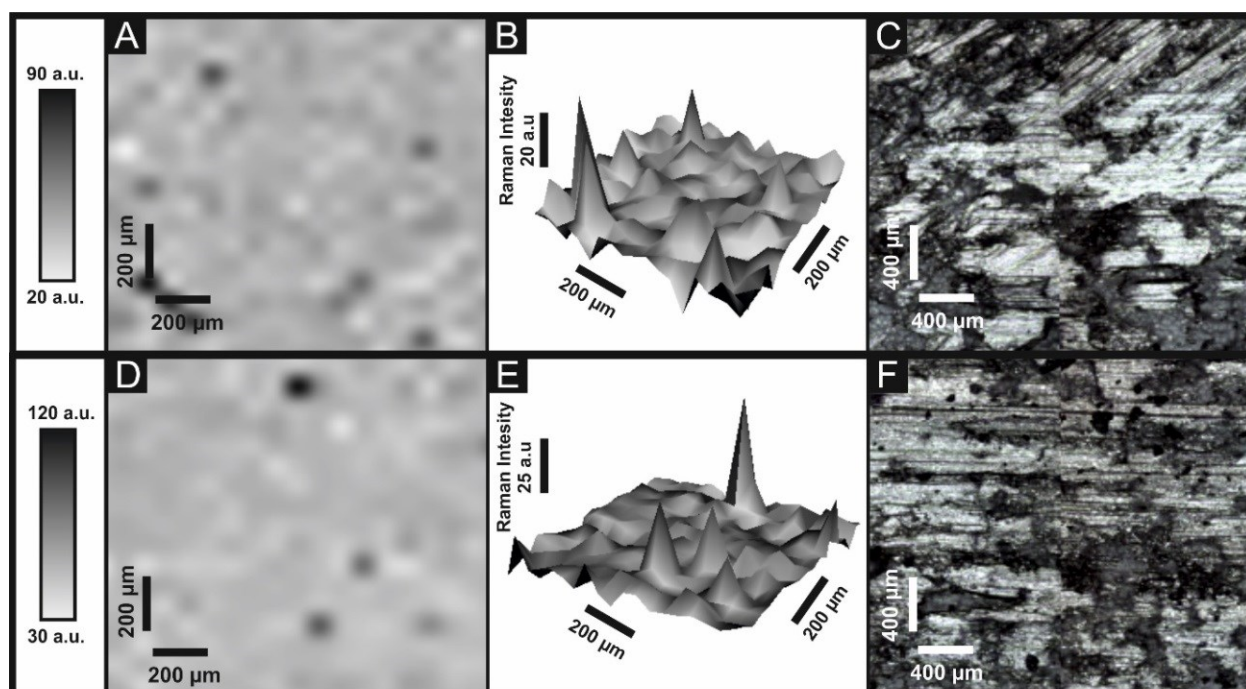


Figure 7.9: 2D (A and D) and 3D (B and E) schematic Raman maps generated from analysis of 6B PDEs drawn once (A, B and C) and ten (D, E and F) times respectively and their corresponding optical images (C and F). Raman intensities were recorded at the characteristic 2D peak occurring ca. 2750 cm^{-1} .

XPS was performed on the bulk 6B pencil lead that is used to fabricate the PDEs, the analysis is reported in ESI Table 1. Deconvolution of the XPS reveals 91.92 % carbon and 7.90% oxygen. Analysis of the spectra, as presented in ESI Table 1 reveals that the PDEs are dominated by the presence of C-O / C-OH and, to a lesser extent, carboxylic groups. As a benchmark, if one considers the XPS analysis of graphitic screen-printed electrodes, as reported by Gomis-Berenguer *et al.*²⁷⁹ who examined the surface of an edge-plane 'like' graphitic screen-printed electrode, revealed the presence of graphitic, C-O and carbonyl functional groups at 284.5 (65.3%), 285.7 (10.5%) and 286.6 (10.1%) eV.²⁷⁹ In comparison to our PDEs there is a clear difference in the composition and the atom percentages. It is also noted that there are other elements present on the PDEs that possibly originate from within the clay (not identified by XPS). These factors are likely to be the underlying reason that these PDEs can only be explored to electrochemical reduced probes (see above) and additionally these observations agree with the voltammetric profiles presented in ESI Figure 1B.

Element	Element atom %	Assignment	Atom %	BE / eV
C 1s	91.92	Graphite	37.17	284.5
		C-C	39.98	285.2
		C-O / C-O-C / C-OH	11.40	286.2
		-O / C=O	3.37	289.5
O 1s	7.90	C-O / C-OH	6.07	532.4
		-O / C=O	1.83	534.0

Table 7.1: De-convoluted data from XPS spectra for the bulk 6B pencil lead (prior to fabricating PDEs) and assignments based on binding energies (BE).

Electroanalytical capabilities of the 6B PDE towards *p*-benzoquinone

Attention was next turned towards utilising the electroactive analyte *p*-benzoquinone, which is a toxic metabolite of benzene.^{280, 281} It is also important to note that due to its role within biological redox processes, it is a common redox mediator within electrochemistry.²⁸² Figure 7.10A exhibits a typical cyclic voltammogram utilising the 6B PDE drawn 10 times, where it is apparent that there are oxidation and reduction peaks present at +0.40 V and -0.30 V respectively, that are characteristic of the electrochemical redox process of *p*-benzoquinone to hydroquinone.²⁸² A plot of peak height vs. the concentration of *p*-benzoquinone is depicted in Figure 7.10B, where the response is found to be linear over the range of 100 to 1000 μM ($I_p / \mu\text{A} = 1.50 \times 10^{-2} \mu\text{A}/\mu\text{M} + 1.13 \mu\text{A}$; $R^2 = 0.99$; $N = 10$). The limit of detection (3σ) is found to correspond to 0.31 μM , which is extremely low for this type of electrode system, as to our knowledge this is the first study utilising PDEs for the analytical detection of *p*-benzoquinone.

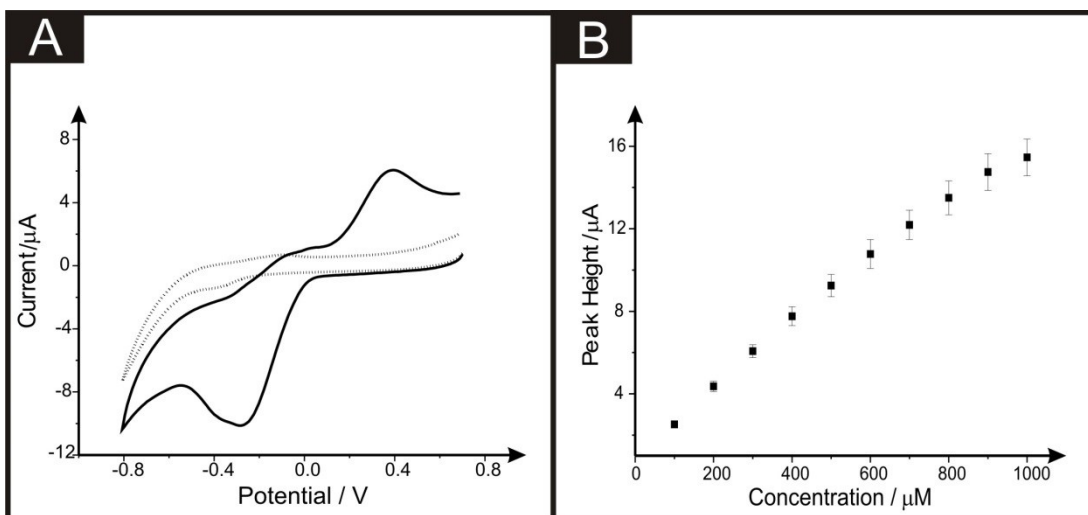


Figure 7.10: Typical cyclic voltammograms (A) recorded in the absence (dotted line) and presence of 500 μM *p*-benzoquinone (solid line) within a pH 7.4 phosphate buffer solution. Typical calibration plot (B) corresponding to additions of *p*-benzoquinone over the range of 100 to 1000 μM into a pH 7.4 phosphate buffer solution recorded using a 6B PDE drawn ten times. Error bars indicate the average response and standard deviation $N = 3$. Scan rate: 50 mV s^{-1} (vs. SCE).

Application of 6B PDE towards the simultaneous sensing of Pb (II) and Cd (II)

The 6B PDE systems are next considered towards the simultaneous sensing of lead (II) and cadmium (II). The reproducibility of the 6B PDEs (drawn 10 ten times) are first explored towards the simultaneous detection of lead (II) and cadmium (II) at concentrations of $150 \mu\text{gL}^{-1}$ and $250 \mu\text{gL}^{-1}$ respectively, within a model 0.1 M HCl solution. It is clear from Table 7.2, that the 6B PDE drawn ten times offers a larger peak current for the electrochemical detection of both analytes when contrasted to the lesser-drawn 6B PDEs. It is also apparent, that such electrodes are extremely reproducible, offering values as low as 4.8 % deviation within the peak current.

To improve the electrochemical performance of these sensors, inspiration from a recent publication, where the utilisation of a back-to-back design (within model 0.1 M HCl solutions) was undertaken, thus increasing the effective electrode area available for the electrodeposition of lead (II).²⁸³ Figure 7.11 depicts the utilisation of a back-to-back 6B PDE (drawn ten times) towards the simultaneous detection of lead (II) and cadmium (II) over the linear ranges of $10 - 150 \mu\text{gL}^{-1}$ and $98 - 375 \mu\text{gL}^{-1}$ respectively. Calibration plots are linear for both of the chosen analytes: (Pb (II)): $I_p / \mu\text{A} = 0.042 \mu\text{A} / \mu\text{gL}^{-1} - 0.275$

μA ; $R^2 = 0.99$; $N = 11$; $\text{Cd (II)} I_p / \mu\text{A} = 0.006 \mu\text{A} / \mu\text{gL}^{-1} - 0.694 \mu\text{A}$; $R^2 = 0.90$; $N = 6$). Interpretation of these plots indicate that the detection of cadmium (II) is not as sensitive as in the case of the lead (II) however, an improvement within the sensing capabilities is offered, as a response is found at a concentration of $98 \mu\text{gL}^{-1}$. This proof-of-concept also shows an improvement within the detection of lead (II), allowing for a detection limit within the range set by the world health organisation ²³⁹ ($10 \mu\text{gL}^{-1}$ in model aqueous samples), expressing that this PDE setup has merit for further examination as an electrochemical sensing platform in the future.

Times Drawn	Lead (II)		Cadmium (II)	
	Average Peak Height (μA)	RSD/ %	Average Peak Height (μA)	RSD/ %
1	4.8	0.08	5.2	4.8
3	4.6	0.30	5.0	4.6
5	4.9	0.57	5.0	4.9
10	4.8	0.60	4.8	4.8

Table 7.2: Anodic stripping voltammetry of lead (II) and cadmium (II) utilising a 6B PDE as a function of different times drawn. Deposition time and potential of 120 seconds and -1.5 V (vs. SCE) respectively; $N = 3$.

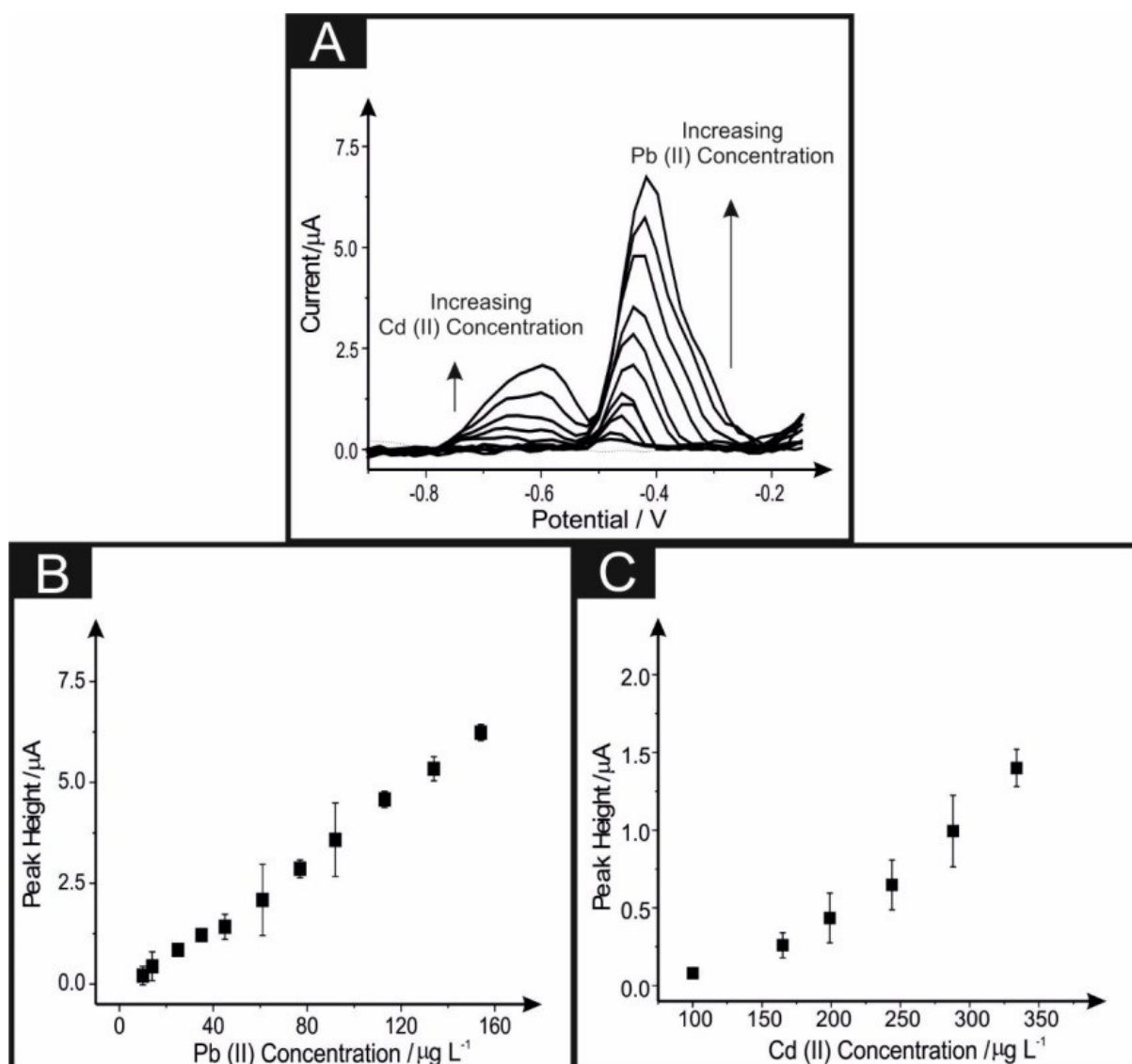


Figure 7.11: Simultaneous determination of Pb (II) and Cd (II) recorded in 0.1 M HCl (dotted line) utilising a back-to-back 6B PDE drawn ten times. Shown in (A) are the corresponding linear sweep voltammograms with corresponding calibration plots (B) and (C) respectively. Error bars indicate the standard deviation of $N = 3$. Deposition potential and time: -1.2 V (vs. SCE) and 120 seconds respectively.

7.1.4 Conclusions

In this Chapter, the fabrication, characterisation and implementation of hand-drawn PDE sensors are considered. This proof-of-concept exhibits that the bulk pencil 'lead' can be utilised to create an electrochemical surface, which adheres to a flexible polyester substrate. For the first time, characterisation of the number of drawn pencil layers and the grade of pencil are examined; this is something that is not routinely explored within the literature. It was found that there was no quantifiable electrochemical response upon utilising these PDEs with an analyte that required an oxidation step first. With such limitations, consideration of analytes that require reduction as the first process were solely analysed, with beneficial electroanalytical capabilities demonstrated towards *p*-benzoquinone and the simultaneous detection of heavy metals, namely, lead (II) and cadmium (II). Inspired by a recent publication, which utilised a novel back-to-back screen-printed sensor for the enhanced electroanalytical detection of heavy metals (within a model aqueous 0.1 M HCl solution), the exploration of this electrode configuration allowed for these PDE systems to simultaneously detect both lead (II) and cadmium (II), at concentrations of 10 μgL^{-1} and 98 μgL^{-1} respectively in model aqueous buffer solutions. In reflection of the above-mentioned limitations, these bulk pencil "leads" are not manufactured for the purpose of electrochemical studies and may contain contaminants, which can contribute/hinder the electrochemical signatures available at these PDEs. However, in this report these PDEs provide relatively good electrochemical properties, in a low cost and simplistic fashion, giving them promise as a competitor to similar electrode platforms in the future.

Chapter 8 - *Conclusions and Future Work*

8.1 Overall Conclusions

Demonstrated within Chapter 3.1 was the fabrication and utilisation of ultra-flexible sensors upon paper and polyester substrates, the latter provides the most robust sensors upon mechanical contortion and stress. Such experiments and results were the first of their kind with a thorough examination of stress and potential waterproofing alternatives for flexible electrode systems. Upon determination of the ultra-flexible substrate, implementation of the electrocatalyst (CoPC) was incorporated within the working electrode *via* the screen-printing process. Extension of the modifications were next analysed within Chapter 4, again for the first time, with a critical comparison of drop-cast and bulk modified screen-printed electrodes. With each modification encountering strict control measures, where it has been reported that no catalytic effect is demonstrated towards L-Ascorbic acid, over the underlying electrode. Further chemical modifications were next explored within Chapter 5 with the *in-situ* metallic modification upon these sensors for the critical analysis of bismuth electrodes. Throughout literature there is a common theme of utilising a GCE or BDDE, in these studies these electrode materials are compared and contrasted to electrode systems with faster electrode kinetics. Work within this thesis is the first to compare these three electrodes, towards their metallic modified counterparts.

Consideration has also been focused towards the application of a novel back-to-back printed design (within Chapter 6), allowing for improved electrochemical analysis due to the doubled working area with each having a separate electrochemical diffusional zone. Such electrode systems were analysed towards lead (II) ions, and upon the improvement of this analytical procedure the incorporation of a range of different modified screen-printing inks were utilised, towards target analytes. In search of low cost, reproducible and ease-of-use sensors the exploration of pencil drawn electrode systems has also been demonstrated, with such sensors offering a possible alternative to screen-printed electrodes, however in the case shown in Chapter 7 these electrode systems are only beneficial if the target analyte undergoes reduction first.

This thesis has extended the knowledge of the fabrication and modification of screen-printed configurations and their electroanalytical competencies. The aims and objectives expressed at the start of this thesis have been met and exceeded, by the critical comparison of modified and unmodified electrodes systems.

8.2 Suggestions for Future Work

The recommendations of research that could be continued from this thesis are as follows:

1. The screen-printing technology allows for the creation of mass produced sensors, the ability to incorporate *new* 2D electrocatalysts within the electrode system would provide a major benefit to the future progression of electrochemistry. Upon incorporation of these electrocatalysts, not only could the analytical perspective be improved, but applications that require powerful capacitors and the progression of fuel cell technology.
2. The fabrication of arrays is also another factor that could be studied, to see if the distance between each of the working electrodes to their auxiliary counterparts has an effect upon the electron transfer and overall electroanalytical capabilities.
3. The movement towards other printing techniques such as 3D printing would be a natural evolutionary step for the creation of novel electrode designs, as this technology can provide an easily manufactured three dimensional electrode support.
4. In terms of the pencil drawn electrodes, in this thesis the proof-of-concept has been shown. It would be ideal if physiochemical and electrochemical characterisation of a range of pencils is studied, to explore the overall reproducibility of each pencil type and manufacturer.

Publications arising from this Thesis

1) Metallic modified (Bismuth, Antimony, tin and combinations thereof) film electrodes. *Analyst*, 2015, Accepted.

Contributions: Fabrication of screen-printed electrodes, electrochemical measurements, data analysis and writing of the peer-reviewed article.

2) Back-to-Back Screen-Printed Electroanalytical Sensors: Extending the Potential Applications of the Simplistic Design, *Electroanalysis*, 2015, *In Press*.

Contributions: Fabrication of screen-printed electrodes, electrochemical measurements, data analysis and writing of the peer-reviewed article.

3) Screen-printed back-to-back electroanalytical sensors: heavy metal ion sensing, *Analyst*, 2015, 140, 4130.

Contributions: Fabrication of screen-printed electrodes, electrochemical measurements, data analysis and writing of the peer-reviewed article.

4) Exploring the electrical wiring of screen-printed configurations utilised in electroanalysis, *Analytical Methods*, 2015, 7, 1208.

Contributions: Fabrication of screen-printed electrodes, electrochemical measurements, data analysis and writing of the peer-reviewed article.

5) Cobalt Phthalocyanine Modified Electrodes Utilised in Electroanalysis: Nano-Structured Modified Electrodes vs. Bulk Modified Screen-Printed Electrodes, *Sensors*, 2014, 14, 21905.

Contributions: Fabrication of screen-printed electrodes, electrochemical measurements, data analysis and writing of the peer-reviewed article.

6) Ultra Flexible Screen-Printed Graphitic Electroanalytical Sensing Platforms. *Electroanalysis*, 2014, 26, 262.

Contributions: Fabrication of screen-printed electrodes, electrochemical measurements, data analysis and writing of the peer-reviewed article.

7) Ultra Flexible Paper Based Electrochemical Sensors: Effect of Mechanical Contortion upon Electrochemical Performance. *Electroanalysis*, 2013, 25, 2275.

Contributions: Electrochemical measurements, data analysis and writing of the peer-reviewed article.

References

1. A. K. Shukla and T. Prem Kumar, *Electrochem. Soc. Interface*, 2008, **17**, 31.
2. A. J. Bard and L. R. Faulkner, *Electrochemical Methods*, Wiley-VCH, New York, Second edn., 2001.
3. J. Wang, *Analytical Electrochemistry*, Wiley-VCH, New York, Second edn., 2000.
4. R. G. Compton and C. E. Banks, *Understanding Voltammetry*, Imperial College Press, London, Second edn., 2011.
5. C. G. Zoski, *Handbook of Electrochemistry*, Elsevier, Oxford, First edn., 2007.
6. A. C. Fisher, *Electrode Dynamics*, Oxford University Press, Oxford, First edn., 1996.
7. F. Scholz, *Electroanalytical Methods*, Springer-Verlag Berlin Heidelberg, Second edn., 2010.
8. A. Kaifer and M. Gómez-Kaifer, *Fundamentals of Electrochemical Theory*, Wiley-VCH Verlag GmbH, Germany, 2007.
9. Z. Galus, *Fundamentals of Electrochemical Analysis*, Polish Scientific Publishers PWN, Warsaw, Second edn., 1994.
10. R. S. Nicholson, *Anal. Chem.*, 1965, **37**, 1351-1355.
11. J. P. Metters, S. M. Houssein, D. K. Kampouris, C. E. Banks, *Anal. Methods*, 2013, **5**, 103.
12. I. Lavagnini, R. Antiochia, F. Magno, *Electroanalysis*, 2004, **16**, 505.
13. R. J. Klingler and J. K. Kochi, *J. Phys. Chem.*, 1981, **85**, 1731-1741.
14. H. Matsuda, Y. Ayabe, *Z. Electrochem*, 1955, **59**, 494.
15. D. A. C. Brownson and C. E. Banks, *Handbook of Graphene Electrochemistry*, Springer, 2014.
16. K. K. Cline, M. T. McDermott and R. L. McCreery, *The Journal of Physical Chemistry*, 1994, **98**, 5314-5319.
17. R. L. McCreery, *Chem. Rev.*, 2008, **108**, 2646-2687.
18. P. Chen and R. L. McCreery, *Anal. Chem.*, 1996, **68**, 3958-3965.
19. H. O. Pierson, *Handbook of Carbon, Graphite, Diamonds and Fullerenes* Noyes Publications, USA, 1994.
20. K. Ravichandran and R. P. Baldwin, *Journal of Electroanalytical Chemistry and Interfacial Electrochemistry*, 1981, **126**, 293-300.
21. L. Mooring, N. G. Karousos, C. Livingstone, J. Davis, G. G. Wildgoose, S. J. Wilkins and R. G. Compton, *Sensors and Actuators B: Chemical*, 2005, **107**, 491-496.
22. S. Bae, H. Kim, Y. Lee, X. Xu, J.-S. Park, Y. Zheng, J. Balakrishnan, T. Lei, H. Ri Kim, Y. I. Song, Y.-J. Kim, K. S. Kim, B. Ozyilmaz, J.-H. Ahn, B. H. Hong and S. Iijima, *Nat Nano*, 2010, **5**, 574-578.
23. J. Liu, B. Su, G. Lager, P. Tacchini and H. H. Girault, *Analytical Chemistry*, 2006, **78**, 6879-6884.
24. J. P. Metters, R. O. Kadara and C. E. Banks, *Analyst*, 2011, **136**, 1067-1076.
25. K.C. Honeychurch, J.P. Hart, *Trends Analytical Chemistry*, 2003, **22**, 456.
26. A. Heller, B. Feldman, *Chemical Reviews*, 2008, **108**, 2482.
27. M. Schlesinger, *Modern Aspects of Electrochemistry: Applications of Electrochemistry in Medicine*, 2013, **56**, 83.
28. J. P. Metters, R. O. Kadara and C. E. Banks, *Analyst*, 2011, **136**, 1067.

29. E. P. Randviir, D. A. C. Brownson, J. P. Metters, R. O. Kadara and C. E. Banks, *Physical Chemistry Chemical Physics*, 2014, **16**, 4598-4611.
30. A. V. Kolliopoulos, J. P. Metters and C. E. Banks, *Analytical Methods*, 2013, **5**, 3490-3496.
31. K. C. Honeychurch, A. Crew, H. Northall, S. Radbourne, O. Davies, S. Newman and J. P. Hart, *Talanta*, 2013, **116**, 300-307.
32. Y. Shih, J. M. Zen and H. H. Yang, *Journal of Pharmaceutical and Biomedical Analysis*, 2002, **29**, 827-833.
33. Y. Wang, H. Xu, J. Zhang and G. Li, *Sensors (Basel, Switzerland)*, 2008, **8**, 2043-2081.
34. S. Carrara, V. V. Shumyantseva, A. I. Archakov and B. Samorì, *Biosensors and Bioelectronics*, 2008, **24**, 148-150.
35. J. Wang, G. Rivas, M. Ozsoz, D. H. Grant, X. Cai and C. Parrado, *Analytical Chemistry*, 1997, **69**, 1457-1460.
36. R. Ren, C. Leng and S. Zhang, *Biosensors and Bioelectronics*, 2010, **25**, 2089-2094.
37. Z. Taleat, A. Khoshroo and M. Mazloum-Ardakani, *Microchim Acta*, 2014, **181**, 865-891.
38. R. A. S. Couto, J. L. F. C. Lima and M. B. Quinaz, *Talanta*, DOI: <http://dx.doi.org/10.1016/j.talanta.2015.06.011>.
39. Y. Li, L. Zhang, M. Li, Z. Pan and D. Li, *Chemistry Central Journal*, 2012, **6**, 103-103.
40. E. P. Randviir, J. P. Metters, J. Stainton and C. E. Banks, *Analyst*, 2013, **138**, 2970-2981.
41. A. P. Ruas de Souza, M. Bertotti, C. W. Foster and C. E. Banks, *Electroanalysis*, 2015, DOI: 10.1002/elan.201500155, n/a-n/a.
42. C. W. Foster, J. P. Metters, D. K. Kampouris and C. E. Banks, *Electroanalysis*, 2014, **26**, 262-274.
43. J. Wang and L. Chen, *Analytical Chemistry*, 1995, **67**, 3824-3827.
44. A. Amine, H. Mohammadi, I. Bourais and G. Palleschi, *Biosensors and Bioelectronics*, 2006, **21**, 1405-1423.
45. Z. Nie, C. A. Nijhuis, J. Gong, X. Chen, A. Kumachev, A. W. Martinez, M. Narovlyansky and G. M. Whitesides, *Lab on a Chip*, 2010, **10**, 477-483.
46. A. P. Ruas de Souza, C. W. Foster, A. V. Kolliopoulos, M. Bertotti and C. E. Banks, *Analyst*, 2015, **140**, 4130-4136.
47. J. P. Smith, J. P. Metters, C. Irving, O. B. Sutcliffe and C. E. Banks, *Analyst*, 2014, **139**, 389-400.
48. E. P. Randviir and C. E. Banks, *ELECTROPHORESIS*, 2015, DOI: 10.1002/elps.201500153, n/a-n/a.
49. M. Jalali, R. Siavash Moakhar, A. Kushwaha, G. K. L. Goh, N. Riahi-Noori and S. K. Sadrnezhaad, *Electrochimica Acta*, 2015, **169**, 395-401.
50. S. Ito, P. Chen, P. Comte, M. K. Nazeeruddin, P. Liska, P. Péchy and M. Grätzel, *Progress in Photovoltaics: Research and Applications*, 2007, **15**, 603-612.
51. V. Yurkiv, G. Constantin, A. Hornes, A. Gondolini, E. Mercadelli, A. Sanson, L. Dessemond and R. Costa, *Journal of Power Sources*, 2015, **287**, 58-67.
52. X. Ge, X. Huang, Y. Zhang, Z. Lu, J. Xu, K. Chen, D. Dong, Z. Liu, J. Miao and W. Su, *Journal of Power Sources*, 2006, **159**, 1048-1050.

53. R. Kluczowski, M. Krauz, M. Kawalec and J. P. Ouweltjes, *Journal of Power Sources*, 2014, **268**, 752-757.
54. Micro-co Ltd, http://www.e-microtec.co.jp/topics/ev_pvexpo09E.html, (accessed 09/08/2015).
55. K. Bullis, Efficient Cheap Solar Cells, <http://www.technologyreview.com/news/410862/efficient-cheap-solar-cells/>, (accessed 09/08/2015).
56. Y. Xu, M. G. Schwab, A. J. Strudwick, I. Hennig, X. Feng, Z. Wu and K. Müllen, *Advanced Energy Materials*, 2013, **3**, 1035-1040.
57. X. Ji, P. M. Hallam, S. M. Houssein, R. Kadara, L. Lang and C. E. Banks, *RSC Advances*, 2012, **2**, 1508-1515.
58. P. M. Hallam, M. Gomez-Mingot, D. K. Kampouris and C. E. Banks, *RSC Advances*, 2012, **2**, 6672-6679.
59. N. Thiagarajan, J.-L. Chang, K. Senthilkumar and J.-M. Zen, *Electrochemistry Communications*, 2014, **38**, 86-90.
60. J. P. Hart and S. A. Wring, *TrAC Trends in Analytical Chemistry*, 1997, **16**, 89-103.
61. J.-L. Chang and J.-M. Zen, *Electroanalysis*, 2006, **18**, 941-946.
62. L. Authier, C. Grossiord, P. Brossier and B. Limoges, *Analytical Chemistry*, 2001, **73**, 4450-4456.
63. D. H. Craston, C. P. Jones, D. E. Williams and N. El Murr, *Talanta*, 1991, **38**, 17-26.
64. K. S. Prasad, J. C. Chen, C. Ay and J. M. Zen, *Sensors and Actuators B: Chemical*, 2007, **123**, 715-719.
65. K. C. Honeychurch, S. Al-Berezanchi and J. P. Hart, *Talanta*, 2011, **84**, 717-723.
66. K. C. Honeychurch, J. P. Hart, *Adv. Anal. Chem.*, 2012, **2**, 46-52.
67. J. P. Metters, R. O. Kadara and C. E. Banks, *Analyst*, 2013, **138**, 2516-2521.
68. J.-L. Chang and J.-M. Zen, *Electrochemistry Communications*, 2006, **8**, 571-576.
69. T. J. Davies, S. Ward-Jones, C. E. Banks, J. del Campo, R. Mas, F. X. Muñoz and R. G. Compton, *Journal of Electroanalytical Chemistry*, 2005, **585**, 51-62.
70. J. F. Rusling, G. W. Bishop, N. Doan and F. Papadimitrakopoulos, *Journal of materials chemistry. B, Materials for biology and medicine*, 2014, **2**, 10.1039/C1033TB21323D.
71. B. A. Otieno, C. E. Krause, A. Latus, B. V. Chikkaveeraiah, R. C. Faria and J. F. Rusling, *Biosensors and Bioelectronics*, 2014, **53**, 268-274.
72. J. F. Rusling, C. V. Kumar, J. S. Gutkind and V. Patel, *The Analyst*, 2010, **135**, 2496-2511.
73. R. O. Kadara, N. Jenkinson and C. E. Banks, *Sensors and Actuators B: Chemical*, 2009, **142**, 342-346.
74. J. Wang, B. Tian, V. B. Nascimento and L. Angnes, *Electrochimica Acta*, 1998, **43**, 3459-3465.
75. J. P. Metters, F. Tan, R. O. Kadara, C. E. Banks, *Analytical Methods*, 2012, **4**, 721.
76. J. P. Metters, R. O. Kadara, C. E. Banks, *Analyst*, 2012, **137**, 896.
77. C. Foster, J. Pillay, J. Metters and C. Banks, *Sensors*, 2014, **14**, 21905-21922.
78. I. Tiwari, M. Singh, M. Gupta, J. P. Metters and C. E. Banks, *Analytical Methods*, 2015, **7**, 2020-2027.
79. N. A. Choudhry, R. O. Kadara, N. Jenkinson and C. E. Banks, *Electrochemistry Communications*, 2010, **12**, 406-409.

80. P. Salazara, M. Martín, R.D. O'Neill, R. Roche, J.L. González-Mora, *Electroanalytical Chemistry*, 2012, **674**, 48.
81. F. Matemadombo, C. Apetrei, T. Nyokong, M. L. Rodríguez-Méndez, J. Antonio de Saja, *Sensors and Actuators B: Chemical*, 2012, **457**, 166.
82. O. Ramdani, J. P. Metters, L. C. S. Figueiredo-Filho, O. Fatibello-Filho, C. E. Banks, *Analyst*, 2013, **153**, 1053.
83. J. Cai, K. Cizak, B. Long, K. McAferty, C. G. Campbell, D. R. Allee, B. D. Vogt, J. La Belle, J. Wang, *Sensors and Actuators B: Chemical*, 2009, **137**, 379.
84. E. P. Randviir, J. P. Metters, J. Stainton, C. E. Banks, *Analyst*, 2013, **138**, 2970.
85. Y. Yang, M. Chuang, S. Lou, J. Wang, *Analyst*, 2010, **135**, 1230.
86. K. Malzahn, J. R. Windmiller, G. Valdes-Ramirez, M. J. Shoning, J. Wang, *Analyst*, 2011, **136**, 2912.
87. J. R. Windmiller, A. J. Bandodkar, G. Valdes-Ramirez, S. Parkhomovsky, A. G. Martinez and J. Wang, *Chemical Communications*, 2012, **48**, 6794-6796.
88. A. J. Bandodkar, D. Molinnus, O. Mirza, T. Guinovart, J. R. Windmiller, G. Valdés-Ramírez, F. J. Andrade, M. J. Schöning and J. Wang, *Biosensors and Bioelectronics*, 2014, **54**, 603-609.
89. TQC USA, <https://www.tqc-usa.com/en/products/article/grindometers-fineness-of-grind-gauges>, (accessed 11/08/2015).
90. A. V. Koliopoulos, J. P. Metters, C. E. Banks, *Analytical Methods*, 2013, **5**, 851.
91. R.O. Kadara, N. Jenkinson, C.E. Banks, *Electrochemistry Communications*, 2009, **11**, 1377.
92. A. Cranny, N. R. Harris, M. Nie, J. A. Wharton, R. J. K. Wood and K. R. Stokes, *Sensors and Actuators A: Physical*, 2011, **169**, 288-294.
93. C. W. Foster, J. P. Metters, C. E. Banks, *Electroanalysis*, 2013, **25**, 2275.
94. J. P. Metters, S. M. Houssein, D. K. Kampouris, C. E. Banks, *Analytical Methods*, 2013, **5**, 103.
95. J. P. Metters, S. M. Houssein, D. K. Kampouris and C. E. Banks, *Analytical Methods*, 2013, **5**, 103.
96. R. O. Kadara, N. Jenkinson, C. E. Banks, *Sensors and Actuators B: Chemical*, 2009, **138**, 556.
97. L. Gorton, *Encyclopedia of Electrochemistry*, 2002, Wiley-VCH, Weinheim, p. 67.
98. H. K. Chenault, G. M. Whitesides, *Appl. Biochem. Biotechnol.*, 1987, **14**, 147.
99. W. M. Clark, *Oxidation-Reduction Potentials of Organic Systems*, R. E. Krieger Publishing, Huntington, New York, 1972.
100. F. L. Rodkey, *J. Biol. Chem.*, 1955, **213**, 777.
101. J. Wang, *Electroanalysis*, 2005, **17**, 7.
102. J. P. Metters, F. Tan, R. O. Kadara and C. E. Banks, *Analytical Methods*, 2012, **4**, 721.
103. Apac Chemical, Citric Acid, <http://www.apacchemical.com/CitricAcid.htm>.
104. K. C. Honeychurch, L. Gilbert & J. P. Hart, *Anal. Bioanal. Chem*, 2010, **396**, 3103.
105. K. R. Sankaran, K. Gnanasekaran, *Asian Journal of Chemistry*, 1999, **11**, 75.
106. B. Mohammed Nawaz, K. Subramani, K. Anandaratchagan, *Journal of Current Chemical and Pharmaceutical Sciences*, 2011, **1**, 19.
107. R. F. do Nascimento, T. M. G Selva, W. F. Ribeiro, M. F. Belian, L. Angnes, V. B. do Nascimento, *Talanta*, 2013, **105**, 354.

108. H. Ahmar, S. Keshipour, H. Hosseini, A.R Fakhari, A. Shaabani, Akbar Bagheri, *Electroanalytical Chemistry*, 2013, **690**, 96.
109. N. Nasirizadeh, H. R. Zare, A. R. Fakhari, H. Ahmar, M. R Ahmadzadeh, A. Naeimi, *Solid State Electrochemistry*, 2011, **15**, 2683.
110. United States Environmental Protection Agency, Hydrazine Information, <http://www.epa.gov/ttnatw01/hlthef/hydrazin.html>.
111. J. Wang, Z. Lu, *Electroanalysis*, 1989, **1**, 517.
112. M. A. Kamyabi, O. Narimani, H. H. Monfared, *Electroanalytical Chemistry*, 2010, **644**, 67.
113. J. H. Zagal, S. Lira, S. Ureta-Zanartu, *Journal of Electroanalytical Chemistry*, 1985, **210**, 95.
114. M. Isaacs, M. J. Aguirre, A. Toro-Labbe, J. Costamagna, M. Paez, J. H. Zagal, *Electrochimica Acta*, 1998, **43**, 1821.
115. J. H. Zagal, S. Griveau, J. F. Silva, T. Nyokong, F. Bedoui *Coordination Chemistry Reviews*, 2010, **254**, 2755.
116. D. Geraldo, C. Linares, Y. Y. Chen, S. Ureta-Zanartu, J. H. Zagal, *Electrochemistry Communications*, 2002, **2**, 182.
117. M. M. Ardakani, M. A. Karimi, M. M. Zare, S. M. Mirdehghan, *Electrochemical Science*, 2008, **3**, 246.
118. Z. H Li, H. Guedri, B. Viguier, S. G Sun, J. L Marty, *Sensors*, 2013, **13**, 5028.
119. K. I. Ozoemena, *Sensors*, 2006, **6**, 874.
120. C. F. Zinola, M. E. Martins, E. P. Tejera and N. P. Neves Jr., *International Journal of Electrochemistry*, 2012, **2012**, 1.
121. W. Preidel, S. Saegar, I. von Lucadou, W. Lager, *Biomedical instrumentation & technology* 1991, **25**, 215.
122. A. Morozan, B. Jousset, S. Palacin, *Energy and Environmental Science*, 2011, **4**, 1238.
123. X. Zuo, H. Zhang, N. Li, *Sensors and Actuators B: Chemical*, 2012, **161**, 1074.
124. B. R. Kozub, R. G. Compton *Sensors and Actuators B: Chemical*, 2010, **147**, 350.
125. M. A. T. Gilmartin, J. P. Hart, D. T. Patton, *Analyst*, 1995, **120**, 1973.
126. L. M. Santos, R. P. Baldwin *Analytical Chemistry*, 1987, **59**, 1766.
127. P. N. Mashazi, K. I. Ozoemena, T. Nyokong, *Electrochimica Acta*, 2006, **52**, 177.
128. K. I. Ozoemena, T. Nyokong, *Electrochimica Acta*, 2006, **51**, 5131.
129. T. Kondo, M. Horitani, M. Yuasa, *International Journal of Electrochemistry*, 2012, **2012**, 6.
130. S. A. Wring, L. Bracey, B. J. Birch, J. P. Hart, *Analytica Chimica Acta*, 1990, **231**, 203.
131. K. M. Korfhage, K. Ravichandran, R. P. Balwin, *Analytical Chemistry*, 1984, **56**, 1514.
132. M. Issacs, M. J. Aguirre, A. Toro-Labbe, J. Costamanga, M. Paez, J. H. Zagal, *Electrochimica Acta*, 1998, **43**, 1821.
133. Q-Y. Peng, T. F. Guarr *Electrochimica Acta*, 1994, **39**, 2629.
134. D. A. Geraldo, C. A. Tongo, J. Limson, T. Nyokong, *Electrochimica Acta*, 2008, **53**, 8051.
135. M. Chicharro, A. Zapardiel, E. Bermejo, E. Madrid, C. Rodriguez, *Electroanalysis*, 2002, **14**, 892.

136. C. A Caro, F. Bedioui, J. H. Zagal, *Electrochimica Acta*, 2002, **47**, 1489.
137. F. Matemadombo, C. Apetrei, T. Nyokong, M. L. R.-Méndez, J. A. de Saja, *Sensors and Actuators B: Chemical*, 2012, **166**, 457.
138. K. Wang, Ji. Xu, K. Tang, H. Chen, *Talanta*, 2005, **67**, 798.
139. B. O. Agboola, A. Mocheke, J. Pillay, K. I. Ozoemena, *Journal of Porphyrins and Phthalocyanines*, 2008, **12**, 1289.
140. J. Pillay, S. Vilakazi, *Journal of Porphyrins and Phthalocyanines*, 2012, **16**, 785.
141. C. M. Welch, R. G. Compton, *Analytical and Bioanalytical Chemistry*, 2006, **384**, 601.
142. T. Patoisa, J-B. Sanchez, F. Berger, P. Fievet, O. Segut, V. Moutarlier, M. Bouvet, B. Lakard, *Talanta*, 2013, **117**, 45.
143. X. Sun, F. Li, G. Shen, J. Huang, X. Wang, *Analyst*, 2014, **139**, 299.
144. H. Hosseini, M. Mahyari, A. Bagheri, A. Shaabani, *Biosensors and Bioelectronics*, 2014, **52**, 136.
145. C. W. Foster, J. P. Metters, D. K. Kampouris, C. E. Banks, *Electroanalysis*, 2014, **26**, 262.
146. K. C. Honeychurch, L. Gilbert, J. P. Hart, *Analytical and Bioanalytical Chemistry*, 2010, **396**, 3103.
147. G-J. Yang, K. Wang, J-J. Xu, H-Y. Chen, *Analytical Letters*, 2005, **37**, 629.
148. N. Pereira-Rodrigues, R. Cofr, J. H. Zagal, F. Bedioui, *Bioelectrochemistry*, 2007, **70**, 147.
149. M. G. Traber, J. F. Stevens, *Free Radical Biology and Medicine*, 2011, **51**, 1000.
150. M. W. Davey, M. V. Montagu, D. Inzé, M. Sanmartin, A. Kanellis, N. Smirnoff, I. J. J. Benzie, J. J. Strain, D. Favell, J. Fletcher, *Science of Food and Agriculture*, 2002, **80**, 825.
151. Z. Zhuang, J. Li, R. Xu, D. Xiao, *International Journal of Electrochemical Science*, 2011, **6**, 2149.
152. X. Ma, M. Chao, Z. Wang, *Analytical Methods*, 2012, **4**, 1687.
153. S. A. Wring, J. P. Hart, *Analytica Chimica Acta*, 1990, **229**, 63.
154. J. Li, M. Hu, R. Yu, *Sensors and Actuators B: Chemical*, 1996, **30**, 65.
155. P. Y. Chen, C. H. Luo, M. C. Chen, F. J. Tsai, N. F. Chang, Y. Shih, *International Journal of Molecular Sciences*, 2011, **12**, 3810.
156. A. Elzing, A. van der Putten, W. Visscher, E. Barendrecht, *Journal of Electroanalytical Chemistry and Interfacial Electrochemistry*, 1986, **200**, 313.
157. S. D. Zelnick, D. R. Mattie, P. C. Stepaniak, *Aviat., Space Environ. Med*, 2003, **74**, 1285.
158. P. J. N. Kobayashi, A. B. P. Lever, *Inorganic Chemistry*, 1992, **31**, 5172.
159. I. Kruusenberg, L. Matisen, K. Tammeveski, *International Journal of Electrochemical Science*, 2013, **8**, 1057.
160. J. Zagal, M. Páez, *Journal of Electroanalytical Chemistry*, 1992, **339**, 13.
161. A. El Hourch, S. Belcadi, 1992, **339**, 1.
162. K. I. Ozoemena, *Sensors and Actuators B: Chemical*, 2006, **6**, 874.
163. A. J. Bard, L. R. Faulkner, *Electrochemical Methods: Fundamentals and Applications*, Wiley, 2001.
164. A. Economou, P. R. Fielden, *Analyst*, 2003, **128**, 205.

165. World Health Organisation, Exposure to mercury: A major public health concern, Preventing disease through healthy environments, WHO Document Production Services, Geneva, 2010. .
166. S. B. Hocevar, I. Scancara, K. Vytras, B. Ogorevc, *Electrochim. Acta*, 2005, **51**, 706.
167. R. O. Kadara, N. Jenkinson, C.E. Banks, *Electroanalysis*, 2009, **21**, 2410.
168. United Nations Environment Program, 2013, Minimata Convention Agreed by Nations, January 19.
169. J. Wang, *Electroanalysis*, 2005, **17**, 1341.
170. A. M. Ashrafi, K.Vytrās, *Electrochemical Science*, 2013, **8**, 2095.
171. G.H. Hwang, W.K. Han, S.J. Hong, J.S. Park, S.G. Kang, *Talanta*, 2009, **77** 1432.
172. K. E. Toghil, G.G.Wildgoose, A. Moshar, C. Mulcahy, R.G. Compton, *Electroanalysis*, 2008, **20**, 1731.
173. R.T. Kachoosangi, C.E. Banks, X. Ji, R.G. Compton, *Anal. Sci.*, 2007, **23**, 283.
174. S. Legeai, O. Vittori, *Anal. Chim. Acta*, 2006, **560**, 148.
175. A. Economou, *Trends Anal. Chem.*, 2005, **24**, 334.
176. V. Guzsvany, *J. Flow Inject. Anal.*, 2007, **24**, 126.
177. I. Scancara, C. Prior, S. B. Hocevar, J. Wang, *Electroanalysis*, 2010, **22**, 1405.
178. B. L. Li, Z. L. Wu, C. H. Xiong, H. Q. Luo, N. B. Li, *Talanta*, 2012, **88**, 707.
179. N.B.Li, W.W.Zhu, J.H.Luo, H.Q.Luo, *Analyst*, 2012, **137**, 614.
180. A. Bobrowski, M. Putek, J.Zarebski, *Electroanalysis*, 2012, **24**, 1071.
181. E. Kinoshita, F. Ingman, G. Edwall, S. Thulin, S. Glab, *Talanta*, 1986, **33**, 125.
182. M. Wang, Y. Ha, *Biosens. Bioelectron.*, 2007, **22**, 2718.
183. R. Pauliukaite, R. Metelka, I. Svancara, A. Krolicka, A. Bobrowski, E. Norkus, K. Kalcher, K. Vytras, *Sci. Pap. Univ. Pardubice Ser. A*, 2004, **10**, 47.
184. S. B. Hocevar, I. Scancara, B. Ogorevc, K. Vytras, *Anal. Chem.*, 2007, **79**, 8639.
185. I. Svancara, S. B. Hocevar, L. Baldrianova, E. Tesarova, K. Vytras, *Sci. Pap. Univ. Pardubice Ser. A*, 2007, **13**, 5.
186. E. Tesarova, L. Baldrianova, S. B. Hocevar, I. Scancara, K. Vytras, B. Ogorevc, *Electrochim. Acta*, 2009, **54**, 1506.
187. BMJ Group, <http://www.bmj.com/content/310/6989/1216>; Accessed January 2015.
188. National Environment Protection Council, <http://www.npi.gov.au/publications/tap/pubs/npi-tap-report.pdf>; Accessed January 2015.
189. C. Kokkinos, A. Economou, I. Raptis, T. Speliotis, *Electrochem. Commun.*, 2009, **11**, 250.
190. M. Slavec, S. B. Hocevar, L. Baldrianova, E. Tesarova, I. Svancara, B. Ogorevec, K. Vytras, *Electroanalysis*, 2010, **33**, 1617.
191. E. Czop, A. Economou, A. Bobrowski, *Electrochim. Acta*, 2011, **56**, 2206.
192. W.W Zhu, N. B. Li, H. Q. Luo, *Talanta* 2007, **72**, 1733.
193. Y. Q. Tian, N. B. Li, H. Q. Luo, *Electroanalysis*, 2009, **21**, 2584.
194. U. S. Department of Health and Human Services, *Toxicological Profile for Tin and Tin Compounds*, 2005, Public Health Service, Agency for Toxic Substances and Disease Registry, August
195. The Food Standards Agency UK, http://www.food.gov.uk/multimedia/pdfs/evm_tin.pdf; Accessed January 2015.

196. World Health Organisation, *FAO Nutrition Meetings, Report Series No. 48A, WHO/FOOD* ADD/70.39, <http://www.inchem.org/documents/jecfa/jecmono/v48aje12.htm>; Accessed January 2015.
197. R. O. Kadara, I. E. Tothill, *Anal. Chim. Acta*, 2008, **623**, 76.
198. U. A. Kurgoz, S. Marin, M. Pumera, A. Merkoci, S. Alegret, *Electroanalysis*, 2005, **17**, 881.
199. G. Kefala, A. Economou, A. Voulgaropoulos, M. Sofoniou, *Talanta*, 2003, **61**, 603.
200. G. Kefala, A. Economou, A. Voulgaropoulos, *Analyst*, 2004, **129**, 1082.
201. H. Xu, L. Zeng, S. Xing, Y. Xian, G. Shi, L. Jin, *Electroanalysis*, 2008, **20**, 2655.
202. E.O. Jorge, M. M. M. Neto, M. M. Rocha, *Talanta*, 2007, **72**, 1392.
203. C. E. Banks, J. Kruusma, M. E. Hyde, A. Salimi, R. G. Compton, *Anal. Bioanal. Chem.*, 2004, **379**, 277.
204. G. Kefala, A. Economou, *Anal. Chim. Acta*, 2006, **576**, 283.
205. M. Khairy, R. O. Kadara, D. K. Kampouris, C. E. Banks, *Electroanalysis*, 2010, **22**, 1455.
206. K.C. Honeychurch, J.P. Hart, D.C. Cowell, D.W.M. Arrigan, *Electroanalysis*, 2002, **14**, 177.
207. L.C.S Figueiredo, B.C. Janegitz, O. Fatibello, L.H. Marcolino, C.E. Banks, *Analytical Methods*, 2013, **5**, 202.
208. D.A.C Brownson, C.E.Banks, *Electrochemistry Communications*, 2011, **13**, 111.
209. M. Lu, K. E. Toghill, R.G. Compton, *Electroanalysis*, 2011, **23**, 1089.
210. C. Babyak, R.R. Smart, *Electroanalysis*, 2004, **16**, 175.
211. J. Wang, J. Lu, S. B. Hocevar, P. A. M. Farias and B. Ogorevc, *Analytical Chemistry*, 2000, **72**, 3218-3222.
212. Z. Wang, G. Liu, L. Zhang, H. Wang, *Int. J. Electrochem. Sci.*, 2012, **7**, 12326 - 12339.
213. A. Economou, *TrAC Trends in Analytical Chemistry*, 2005, **24**, 334-340.
214. C. W. Foster, J. P. Metters, D. K. Kampouris, C. E. Banks, *Electroanalysis*, 2013, **26**, 262.
215. R. W. Murray, A. G. Ewing, R. A. Durst, *Anal. Chem.*, 1987, **59**, 379A.
216. S. A. Wring, J. P. Hart, *Analyst*, 1992, **117**, 1215.
217. D. W. M. Arrigan, *Analyst*, 1994, **119**, 1953.
218. K. E. Toghill, L. Xiao, G. G. Wildgoose, R. G. Compton, *Electroanalysis*, 2009, **21**, 1113.
219. E. Svobodova-Tesarova, L. Baldrianova, M. Stoces, I. Scancara, K. Vytras, S. B. Hovecar, B. Ogorevc, *Electrochim. Acta*, 2011, **56**, 6673.
220. E. Svobodova, L. Baldrianova, S. B. Hocevar, I. Svancara, *Int. J. Electrochem. Sci.*, 2012, **7**, 197.
221. T. Bassie, K. Siraj, T. E. Tesema, *Adv. Sci. Eng.*, 2013, **5**, 275.
222. W. J. Yi, Y. Li, G. Ran, H. Q. Luo, N. B. Li, *Microchim. Acta*, 2012, **179**, 171.
223. M. Khairy, R. O. Kadara, D. K. Kampouris, C. E. Banks, *Analytical Methods*, 2010, **2**, 645.
224. J. Wang, *Electroanalysis*, 2005, **17**, 1341-1346.
225. Ø. Mikkelsen, K. H. Schrøder, *Electroanalysis*, 2003, **15**, 679.
226. F. E. Beamish, *Anal. Chim. Acta*, 1969, **44**, 253.

227. J. Kruusma, C. E. Banks, R. G. Compton, *Anal. Bioanal. Chem.*, 2004, **379**, 700.
228. E. A. McGaw, G. M. Swain, *Analytica Chimica Acta*, 2006, **575**, 180.
229. C. Kokkinos, A. Economou, *Curr. Anal. Chem.*, 2008, **4**, 183.
230. J. P. Metters, E. P. Randviir and C. E. Banks, *Analyst*, 2014, **139**, 5339-5349.
231. E. Ghali and M. Girgis, *Metallurgical Transactions B-Process Metallurgy*, 1985, **16**, 489-496.
232. R. G. Compton and C. E. Banks, *Understanding Voltammetry*, Imperial College Press, 2007.
233. Y. Wang, H. L. Ge, Y. C. Wu, G. Q. Ye, H. H. Chen and X. Y. Hu, *Talanta*, 2014, **129**, 100-105.
234. D. Yang, L. Wang, Z. L. Chen, M. Megharaj and R. Naidu, *Microchimica Acta*, 2014, **181**, 1199-1206.
235. V. B. dos Santos, E. L. Fava, N. S. de Miranda Curi, R. C. Faria and O. Fatibello-Filho, *Talanta*, 2014, **126**, 82-90.
236. N. Wang and X. D. Dong, *Analytical Letters*, 2008, **41**, 1267-1278.
237. Y. Wu, N. B. Li and H. Q. Luo, *Sensors and Actuators B-Chemical*, 2008, **133**, 677-681.
238. D. Li, J. Jia and J. Wang, *Talanta*, **83**, 332-336.
239. World Health Organisation, Exposure to Lead: A major public health concern, Public Health and Environment, WHO Document Production Services, Geneva, 2010.
240. S. J. Hood, R. O. Kadara, D. K. Kampouris and C. E. Banks, *Analyst*, 2010, **135**, 76-79.
241. S. J. Hood, D. K. Kampouris, R. O. Kadara, N. Jenkinson, F. J. del Campo, F. X. Munoz and C. E. Banks, *Analyst*, 2009, **134**, 2301-2305.
242. O. Ordeig, J. del Campo, F. X. Muñoz, C. E. Banks and R. G. Compton, *Electroanalysis*, 2007, **19**, 1973-1986.
243. J. F. van Staden and M. C. Matoetoe, *Analytica Chimica Acta*, 2000, **411**, 201-207.
244. J. Gardiner and M. J. Stiff, *Water Research*, 1975, **9**, 517-523.
245. I. Rutyna and M. Korolczuk, *Sensors and Actuators B: Chemical*, 2014, **204**, 136-141.
246. M. Á. G. Rico, M. Olivares-Marín and E. P. Gil, *Talanta*, 2009, **80**, 631-635.
247. R. de Cássia Silva Luz, F. S. Damos, A. Bof de Oliveira, J. Beck and Lauro T. Kubota, *Electrochimica Acta*, 2005, **50**, 2675-2683.
248. Y. Wang, Y. Li, L. Tang, J. Lu and J. Li, *Electrochemistry Communications*, 2009, **11**, 889-892.
249. Z. Y. Xun, C. X. Cai, W. Xing and T. H. Lu, *Journal of Electroanalytical Chemistry*, 2003, **545**, 19-27.
250. F. P. Zhang, L. Yang, S. P. Bi, J. Liu, F. Liu, X. L. Wang, X. D. Yang, N. Gan, T. Yu, J. Hu, H. Z. Li and T. M. Yang, *Journal of Inorganic Biochemistry*, 2001, **87**, 105-113.
251. F. Valentini, D. Romanazzo, M. Carbone and G. Palleschi, *Electroanalysis*, 2012, **24**, 872-881.
252. M. Moreno, A. S. Arribas, E. Bermejo, M. Chicharro, A. Zapardiel, M. C. Rodríguez, Y. Jalit and G. A. Rivas, *Talanta*, 2010, **80**, 2149-2156.
253. B. B. Y. Lau, J. Panchompoo and L. Aldous, *New Journal of Chemistry*, 2014, DOI: 10.1039/c4nj01416b.

254. R. T. Kachoosangi, G. G. Wildgoose and R. G. Compton, *Analyst*, 2008, **133**, 888-895.
255. P. Anand and K. Bley, *British Journal of Anaesthesia*, 2011, **107**, 490-502.
256. J. P. Metters, F. Tan, R. O. Kadara and C. E. Banks, *Analytical Methods*, 2012, **4**, 1272-1277.
257. J. P. Metters, R. O. Kadara and C. E. Banks, *Analyst*, 2012, **137**, 896-902.
258. L. C. S. Figueiredo-Filho, D. A. C. Brownson, O. Fatibello-Filho and C. E. Banks, *Analyst*, 2013, **138**, 4436-4442.
259. R. J. Bowling, R. T. Packard and R. L. McCreery, *Journal of the American Chemical Society*, 1989, **111**, 1217-1223.
260. D. A. C. Brownson, S. A. Varey, F. Hussain, S. J. Haigh and C. E. Banks, *Nanoscale*, 2014, **6**, 1607-1621.
261. D. A. C. Brownson and C. E. Banks, *Electrochemistry Communications*, 2011, **13**, 111-113.
262. W. Li, C. Tan, M. A. Lowe, H. D. Abruña and D. C. Ralph, *ACS Nano*, 2011, **5**, 2264-2270.
263. I. Dumitrescu, P. R. Unwin and J. V. Macpherson, *Chemical Communications*, 2009, DOI: 10.1039/b909734a, 6886-6901.
264. M. Pumera, *Chemistry – A European Journal*, 2009, **15**, 4970-4978.
265. D. A. C. Brownson, D. K. Kampouris and C. E. Banks, *Chemical Society Reviews*, 2012, **41**, 6944-6976.
266. K. C. Honeychurch, *Analytical Methods*, 2015, **7**, 2437-2443.
267. A. M. Bond, P. J. Mahon, J. Schiewe and V. Vicente-Beckett, *Analytica Chimica Acta*, 1997, **345**, 67-74.
268. J. Wang and A.-N. Kawde, *Analytica Chimica Acta*, 2001, **431**, 219-224.
269. D. King, J. Friend and J. Kariuki, *Journal of Chemical Education*, 2010, **87**, 507-509.
270. J. K. Kariuki, *Journal of The Electrochemical Society*, 2012, **159**, H747-H751.
271. M. d. Vestergaard, K. Kerman and E. Tamiya, *Analytica Chimica Acta*, 2005, **538**, 273-281.
272. E. Alipour and S. Gasemlou, *Analytical Methods*, 2012, **4**, 2962-2969.
273. N. Dossi, R. Toniolo, F. Impellizzieri and G. Bontempelli, *Journal of Electroanalytical Chemistry*, 2014, **722–723**, 90-94.
274. N. Dossi, R. Toniolo, A. Pizzariello, F. Impellizzieri, E. Piccin and G. Bontempelli, *Electrophoresis*, 2013, **34**, 2085-2091.
275. N. Dossi, R. Toniolo, F. Terzi, F. Impellizzieri and G. Bontempelli, *Electrochimica Acta*, 2014, **146**, 518-524.
276. N. Dossi, R. Toniolo, E. Piccin, S. Susmel, A. Pizzariello and G. Bontempelli, *Electroanalysis*, 2013, **25**, 2515-2522.
277. L. C. S. Figueiredo-Filho, D. A. C. Brownson, M. Gomez-Mingot, J. Iniesta, O. Fatibello-Filho and C. E. Banks, *Analyst*, 2013, **138**, 6354-6364.
278. F. E. Galdino, C. W. Foster, J. A. Bonacin and C. E. Banks, *Analytical Methods*, 2015, **7**, 1208-1214.
279. A. Gomis-Berenguer, M. Gomez-Mingot, V. Montiel, A. Canals, T. Thiemann, R. O. Kadara, C. E. Banks and J. Iniesta, *RSC Advances*, 2012, **2**, 7735-7742.
280. E. S. Johnson, S. Langård and Y.-S. Lin, *Science of The Total Environment*, 2007, **374**, 183-198.

281. Y. S. Lin, W. McKelvey, S. Waidyanatha and S. M. Rappaport, *Biomarkers*, 2006, **11**, 14-27.
282. D. A. C. Brownson, C. W. Foster and C. E. Banks, *Analyst*, 2012, **137**, 1815-1823.
283. A. P. Ruas de Souza, C. W. Foster, A. V. Kolliopoulos, M. Bertotti and C. E. Banks, *Analyst*, 2015, DOI: 10.1039/c5an00381d.
284. C. Kokkinos, A. Economou, I. Raptis, C. E. Efstathiou, *Electrochim. Acta*, 2008, **53**, 5294.
285. R. Pauliukaite, C. M. A. Brett, *Electroanalysis*, 2005, **17**, 1354.
286. G. H. Hwang, W. K. Han, J. S. Park, S. G. Kang, *Talanta*, 2008, **76**, 301.
287. S. Daniele, D. Battistel, S. Bergamin, C. Bragato, *Electroanalysis*, 2010, **22**, 1511.
288. J. Wang, J. M. Lu, S. B. Hocevar, P. A. M. Farias, B. Ogorevc, *Anal. Chem.*, 2000, **72**, 3218.
289. K. Vytras, I. Svancara, R. Metelka, *Electroanalysis*, 2002, **14**, 1359.
290. E. A. Hutton, S. B. Hocevar, B. Ogorevc, M. R. Smyth, *Electrochem. Commun.*, 2003, **5**, 765.
291. A. Krolicka, A. Bobrowski, *Electrochem. Commun.*, 2004, **6**, 99.
292. A. Charalambouse, A. Economou, *Anal. Chim. Acta*, 2005, **547**, 53.
293. E. A. Hutton, B. Ogorevc, M. R. Smyth, *Electroanalysis*, 2004, **16**, 1616.
294. V. Guzsvany, M. Kadar, F. Gaal, L. Bjelica, K. Toth, *Electroanalysis*, 2006, **18**, 1363.
295. B. Claux, O. Vittori, *Electroanalysis*, 2007, **19**, 2243.
296. A. Economou, A. Voulgaropoulos, *Talanta*, 2007, **71**, 758.
297. C. Kyrisoglou, A. Economou, C. E. Efstathiou, *Electroanalysis*, 2012, **24**, 1825.
298. A. Economou, A. Voulgaropoulos, *Electroanalysis*, 2010, **22**, 1468.
299. L. Zhu, L. Xu, B. Huang, N. Jia, L. Tan and S. Yao, *Electrochimica Acta*, 2014, **115**, 471.
300. D. Yang, L. Wang, Z. Chen, M. Mallavarapu and R. Naidu, *Electrochim. Acta*, 2014, **132**, 223.
301. Z. Li, L. Chen, F. He, L. Bu, X. Qin, Q. Xie, S. Yao, X. Tu, X. Luo and S. Luo, *Talanta*, 2014, **122**, 285-292.
302. J. Ping, Y. Wang, J. Wu and Y. Ying, *Food Chem.*, 2014, **151**, 65.
303. R. Iwona, K. Mieczyslaw, *Sensors and Actuators B: Chemical*, 2014, **204**, 136-141.
304. V. Jovanovski, S. B. Hocevar, B. Ogorevc, *Electroanalysis*, 2009, **21**, 2321.
305. V. Guzsvany, H. Nakajima, N. Soh, K. Nakano, T. Imato, *Anal. Chim. Acta*, 2010, **658**, 12.
306. V. Urbonova, K. Vytras, A. Kuhn, *Electrochem. Commun.*, 2010, **12**, 114.
307. H. Sopha, L. Baldrianova, E. Tesarova, S. B. Hocevar, I. Svancara, B. Ogorevc, K. Vytras, *Electrochim. Acta*, 2010, **55**, 7929.
308. S. B. Hocevar, I. Švancara, B. Ogorevc and K. Vytřas, *Analytical Chemistry*, 2007, **79**, 8639-8643.
309. H. Xu, P. Yang, Q. Zheng, J. Liu and L. Jin, *Chinese Journal of Chemistry*, 2010, **28**, 2287-2292.
310. WHO, *Journal*, 1993, **1**.
311. J. Saturno, D. Valera, H. Carrero and L. Fernandez, *Sensors and Actuators B-Chemical*, 2011, **159**, 92-96.
312. G.-H. Hwang, W.-K. Han, J.-S. Park and S.-G. Kang, *Sensors and Actuators B-Chemical*, 2008, **135**, 309-316.

313. H. Lin, M. Li and D. Mihailovič, *Electrochimica Acta*, 2015, **154**, 184-189.
314. H. Devnani, D. S. Rajawat and S. P. Satsangee, *Proceedings of the National Academy of Sciences India Section a-Physical Sciences*, 2014, **84**, 361-370.
315. C. Chen, X. Niu, Y. Chai, H. Zhao and M. Lan, *Sensors and Actuators B: Chemical*, 2013, **178**, 339-342.
316. V. Sosa, C. Barceló, N. Serrano, C. Ariño, J. M. Díaz-Cruz and M. Esteban, *Analytica Chimica Acta*, 2015, **855**, 34-40.
317. H.-L. Fang, H.-X. Zheng, M.-Y. Ou, Q. Meng, D.-H. Fan and W. Wang, *Sensors and Actuators B: Chemical*, 2011, **153**, 369-372.
318. W. Yantasee, L. A. Deibler, G. E. Fryxell, C. Timchalk and Y. Lin, *Electrochemistry Communications*, 2005, **7**, 1170-1176.
319. M. Santhiago, C. S. Henry and L. T. Kubota, *Electrochimica Acta*, 2014, **130**, 771-777.
320. H. Yang, Q. Kong, S. Wang, J. Xu, Z. Bian, X. Zheng, C. Ma, S. Ge and J. Yu, *Biosensors and Bioelectronics*, 2014, **61**, 21-27.
321. C.-W. Lin, Z. Zhao, J. Kim and J. Huang, *Scientific Reports*, 2014, **4**, 3812.

Appendices

Table 1: Troubleshooting guide for the screen-printing process

Issue	Equipment Causing the Problem	Cause of the Problem	How to Resolve Issue
Screen-Print Incomplete	Squeegee	Not parallel with the screen.	Turn blade round or renew blade.
		Gap is too large between the squeegee and the screen.	Decrease the gap between the squeegee and screen.
		The squeegee is not wide enough for full coverage.	Minimum squeegee must have a width that is 10 mm larger on each side of screen image.
	Printing Medium	Viscosity of printing medium too thick for successfully filling of screen-design.	Use a recommended screen; with a less viscous ink or emulsion.
		Dried ink within the screen-design	Remove the screen and clean with appropriate solvent

	Screen	Incorrect positioning of the print area.	Correct so that the print design is in the middle of substrate.
		Print gap too large or small.	Change to the appropriate screen-substrate gap.
		Screen mesh too fine.	Change to screen recommended for work.
Erroneous and Undesirable Screen-Print	Squeegee	Areas of un-printed ink, could be caused by dusty/dirty components	Raise printhead and clean the underside removing any dirty or dust.
		Image may contain streaks check squeegee edge for worn/damaged behaviour.	Fit new squeegee blade.
		Printing medium not cleared from the screen mesh due to the squeegee pressure being too low.	Increase pressure in small steps until a clear track is obtained and then increase slightly
		Print smudging from the squeegee to screen gap being too small.	Increase the gap until the screen peels away from substrate in a controlled manner.

		Squeegee pressure too heavy causing poor definition of the edge of the design.	Reduce squeegee pressure in small steps until good print is obtained, then increase pressure slightly
	Printing Medium	Stringing and serrating of the image edges due to the ink being too thin.	Use thicker or more viscous inks.
		Thin deposit of ink upon the print.	Use less viscous ink.
	Screen	Mesh damaged and affecting the print area.	Fit a new screen.
		Print image serrated at edge, and has poor definition as the screen-mesh is too coarse or the screen open area is too small.	Change to screen to one with a recommended finer mesh/ use recommended screen with thicker emulsion.
		Deposit too thin, from the screen mesh being too fine.	Use a coarser mesh.
Substrate Issues	Substrate	Contaminated printing surfaces or excessively bowed	Clean substrates thoroughly before printing. Increase vacuum, mechanical gripping, reduce squeegee pressure or reject substrate

		Vacuum is insufficient to hold substrates when very viscous pastes are used	Check whether: i) Vacuum pipe not fully secured to unions ii) Holes at registered printing position are blocked iii) Filter of pump is blocked iv) Pump exhaust pipe is restricted v) Other leaks exist
		Print gap too small	Set print gap correctly

Table 2: An overview of current literature reports on the use of metallic-film modified electrodes for the sensing of key metal ion species.

Electrode Modification	Underlying Electrode	In-/Ex-situ	Target Analyte(s)	Limit of Detection	Technique	Notes / Comments	Reference
Bismuth							
Bismuth film	GCE	In-situ	Lead (II)	1.1 µg/L (5.30 nM)	ASV	One of the first reports into Bismuth Modified Electrodes, explaining that Acetate buffer solution is used to recreate identical conditions to the mercury electrode system.	211
Bismuth powder mixed	CPE	Ex-situ	Cadmium (II)	1.2 µg/L (10.67 nM) 0.9 µg/L (4.34 nM)	SW-ASV	Proof of concept demonstrated in a real sample (tap water). Model solution: pH 4.5 0.2 M Acetate Buffer.	166

within carbon paste			Lead (II)				
Bismuth film	Edge-plane pyrolytic graphite	<i>In-situ</i>	Cadmium (II) Lead (II)	0.062 µg/L (0.55 nM) 0.084 µg/L (0.40 nM)	SW-ASV	Excellent recovery in spiked river water (100.5 % Cd (II) and 98 % Pb (II)). Model solution: pH 4.5 0.2 M Acetate Buffer.	173
Bismuth oxide	SPE	<i>Ex-situ</i>	Cadmium (II) Lead (II)	16 µg/L (142.35 nM) 8 µg/L (38.61 nM)	CCSCP	Proof of concept demonstrated through detection of lead (II) in soil extracts and waste water. Model solution: 0.5 M ammonium acetate containing 0.1 M HCl (pH 4.6)	197
Bismuth film	Graphite-epoxy composite	<i>In-situ</i>	Cadmium (II) Lead (II)	2.2 µg/L (19.57 nM) 23.1 µg/L (111.49 nM)	SW-ASV	Exhibits well-defined, undistorted, reproducible and sharp stripping signals with RSD of 2.99%, 1.56% and 2.19% for Pb (II), Cd (II) and Zn (II) respectively.	198

			Zinc (II)	600 µg/L (9230.76 nM)		Application of this electrode towards tap water and soil samples showed promise for the future. Model solution: pH 4.5 0.1 M Acetate Buffer.	
Bismuth film	GCE	<i>In-situ</i>	Cadmium (II) Lead (II) Zinc (II)	0.2 µg/L (1.77nM) 0.2 µg/L (0.96 nM) 0.7 µg/L (10.77 nM)	SW-ASV	Successfully applied to the determination of Pb (II) and Zn (II) in tapwater and human hairwith the results in agreement with atomic absorptions spectroscopy. Model solution: pH 4.5 1.0 M Acetate Buffer.	199
Bismuth film	Silicon dioxide produced via photolithography	<i>Ex-situ</i>	Cadmium (II) Lead (II)	1 µg/L (8.89 nM) 0.5 µg/L (2.41 nM)	SW-ASV	Interference caused by Cu (II) was alleviated by the addition of ferrocyanide in the sample solution. Successful determination of Cd (II) and Pb (II) in a phosphate fertilizer and a river water sample. Model solution: pH 4.5 1.0 M Acetate Buffer.	284

Nafion coated bismuth film	GCE rotating disk	<i>In-situ</i>	Cadmium (II) Lead (II) Zinc (II)	0.1 µg/L (0.88 nM) 0.1 µg/L (0.48 nM) 0.4 µg/L (6.15 nM)	ASV	Applied towards detection in tap-water, urine and wine. Model solution: pH 4.5 0.1 M Acetate Buffer.	200
Bismuth oxide	SPE	<i>Ex-situ</i>	Zinc (II)	33 µg/L (507.69 nM)	SW-ASV	Bismuth oxide present within sensor removing requirement of electrode preparation. Applied towards detection in sea water samples allowing for a limit of detection of 50 µg/L. Model solution: pH 4.5 0.1 M Acetate Buffer.	205
Multiwalled carbon nanotubes dispersed in	GCE	<i>In-situ</i>	Cadmium (II) Lead (II)	0.04 µg/L (0.03 nM) 0.03 µg/L (0.14 nM)	DP-ASV	Proof of concept demonstrated in tap water of which the findings were in excellent agreement with atomic absorption spectroscopy. Model solution: pH 4.5 0.1 M Acetate Buffer.	201

Nafion mixed with bismuth							
Bismuth film	Carbon film resistor	<i>In-situ</i>	Cadmium (II) Lead (II) Zinc (II)	0.11 µg/L (1.05 nM) 0.16 µg/L (0.79 nM) 0.008 µg/L (1.30 nM)	SW-ASV	Electrodes were characterised voltammetrically and using electrochemical impedance spectroscopy. Bismuth films deposited galvanostatically and via potential cycling studied for the first time,. Model solution: pH 4.5 0.1 M Acetate Buffer.	285
Bismuth film	GCE Rotating disc	<i>In-situ</i>	Thallium (I)	0.21 µg/L (10.8 nM)	ASV	Cadmium interference determined interference from cadmium (II) ions. Model solution: pH 4.5 0.1 M Acetate Buffer.	202
Bismuth film	Multi-Walled	<i>In-situ</i>	Cadmium (II)	0.7 µg/L (6.22 nM)	SW-ASV	Zn (II) could not be determined in the presence of Cu, xylene and PDPA even at	286

	Carbon Nanotubes		Lead (II) Zinc (II)	1.3 µg/L (6.22 nM) 12 µg/L (184.61 nM)		low concentration. Model solution: pH 4.5 0.1 M Acetate Buffer.	
A mono- or submonolayer of adsorbed bismuth	Mesoporous platinum microelectrode	<i>In-situ</i>	Glucose	2775.37 µg/L (5 x10 ⁵ nM) ^m	CV	The performance displayed by the non-enzymatic BiMPtEs proposed here suggests wider potential applications with respect to those for classical enzymatic glucose sensors. Examples include glucose detection in media at very low or high pH values, at temperature higher than room values, and for continuous monitoring of glucose in a bioreactor or foods. Model solution : 0.2 M NaOH solution.	287
Bismuth film	GCE	<i>Ex-situ</i>	Cadmium (II) Zinc (II)	0.67 µg/L (6.0 nM) 13.00 µg/L (200 nM)	SW-ASV	The stability of the bismuth film under ultrasound was assessed using voltammetric and AFM measurements: after the initial loss, the bismuth film	203

						remains intact. Model solution: pH 5.2 0.1 M Acetate Buffer.	
Polymer coated- bismuth film	GCE	<i>In-situ</i>	Cadmium (II) Lead (II) Zinc (II)	2 µg/L (17.79 nM) 2 µg/L (9.65 nM) 6 µg/L (92.30 nM)	SIA-ASV	Polymer coating improves tolerance to surfactants and long-term stability of the electrode whilst increasing potentially time consuming preparatory steps. Model solution: pH 4.5 0.1 M Acetate Buffer.	204
Bismuth film	GCE	<i>In-situ</i>	Cadmium (II) Lead (II) Zinc (II) Thallium (I)	γ 1.1 µg/L (5.31 nM) γ γ	ASV	Bismuth presence overcomes problem of overlapping peaks for simultaneous measurement of the three analytes. pH 4.5 0.1 M Acetate Buffer.	288

Bismuth film	CPE	<i>In-situ</i>	Lead (II)	0.41 µg/L (2.00 nM)	PSA	Simultaneous detection of Pb (II) and Cd (II) using Bismuth film electrode. Model Solution: pH 4.5 0.1 M Acetate Buffer.	289
Bismuth film	GCE	<i>Ex-situ</i>	Cobalt (II) Nickel (II)	0.08 µg/L (1.36 nM) 0.26 µg/L (4.43 nM)	ASV	Robust sensor not susceptible to dissolved oxygen when attempting simultaneous sensing of the analytes. Model Solution: pH 9.2 0.01 M Ammonium Buffer.	290
Bismuth film	GCE	<i>Ex-situ</i>	Cobalt (II)	γ	DP-AdSV	Composition of the plating solution, the influence of accumulation potential, and the stability of bismuth coating as well as the memory effect is studied. Model Solution: pH 9.2 0.01 M Ammonium Buffer.	291
Bismuth film	GCE	<i>In-situ</i>	Indium	10 µg/L (87.09 nM) ^m	SW-ASV	Studies in the presence of Cd (II) and Pb (II). Determined that simultaneous	292

						determination of indium, cadmium and lead is possible. Model Solution 0.1 M Acetate Buffer with 0.1 M KBr.	
Bismuth film	GCE	<i>Ex-situ</i>	2-nitrophenol 4-nitrophenol 2,4-dinitrophenol	0.4 µg/L (2.88 nM) 1.4 µg/L (10.06 nM) 3.3 µg/L (23.72 nM)	CV	Suitable for both batch voltammetric and flow amperometric detection of the environmentally significant nitrophenols. Model Solution: Britton-Robinson buffer	293
Bismuth film	GCE	<i>Ex-situ</i>	Thiamethoxam	380 µg/L (1302.66 nM)	DPV	Results were justified by the comparative HPLC/DAD measurements. Model Solution: Britton-Robinson buffer.	294
Bismuth film	GCE	<i>Ex-situ</i>	Azorubine Ponceau 4R	300 µg/L (594.71 nM) 100 µg/L (165.43 nM)	DPV	Simultaneous detection of the	295

						two azo dyes cannot be done, as their potentials are in the same range. Such detection is only possible using mercury electrodes. Model Solution: 0.5 M HNO ₃ .	
Bismuth film	GCE	<i>In-situ</i>	Cadmium (II) Lead (II) Cobalt (II) Nickel (II)	2 µg/L (17.79 nM) 1 µg/L (4.82 nM) 1 µg/L (16.96 nM) 1 µg/L (17.03 nM)	ASV (Cd, Pb) AdSV (Co, Ni)	Simultaneous detection of Pb (II), Cd (II) and Zn (II) using the bismuth film electrode, within a fertiliser sample. Model Solution: 1.0 M Acetate Buffer.	296
Bismuth film	Iridium microwire	<i>In-situ</i>	Cadmium (II) Lead (II)	1.5µg/L (13.35 nM) 1 µg/L (4.82 nM)	SW-ASV	Applied to determination in wastewater and tapwater samples. Model Solution: pH 4.5 0.1 M Acetate Buffer	297

Bismuth film	GCE	<i>Ex-situ</i>	Cadmium (II) Lead (II) Zinc (II) Indium (III)	10 µg/L (88.97 nM) 10 µg/L (48.26 nM) 10 µg/L (153.85 nM) 10 µg/L (8.71 nM)	ASV	Zn (II) detection hindered through the presence of aluminium. Model Solution: PIPES buffer solution.	298
Bismuth film	BDDE	<i>In-situ</i>	Cadmium (II) Lead (II)	2.3 µg/L (20.46 nM) 1.9 µg/L (9.17 nM)	SW-ASV	Pb (II) and Cd (II) could not be detected simultaneously at a bare BDDE, whilst on a bulk Bismuth macro electrode the limits of detection for the simultaneous determination were ~ ten times higher. Model Solution: pH 1 0.1 M HClO ₄ .	172
Gold nanoparticle-graphene-cysteine composite	GCE	<i>In-situ</i>	Cadmium (II) Lead (II)	0.1 µg/L (0.88 nM) 0.05 µg/L (0.24 nM)	SW-ASV	The developed electrode displayed a good repeatability and reproducibility. These studies imply that the gold nanoparticle-graphene-cysteine composites might be an alternative candidate for practical applications in	299

modified bismuth film						electrochemical detection of metal ions. Model solution: pH 4.5 0.1 M Acetate Buffer.	
Bismuth film electrode modified with mesoporous silica nanoparticles	GCE	<i>In-situ</i>	Cadmium (II) Lead (II)	0.6 µg/L (5.39 nM) 0.2 µg/L (0.97 nM)	SW-ASV	The modified electrodes admirable stripping performance for Pb (II) and Cd (II) detection was attributed to the increased surface area and mass transfer on the electrode surface due to the incorporation mesoporous nano-silica. Model Solution: pH 4.5 0.2 M acetate buffer.	300
Bismuth film electrode modified with electroreduced graphene oxide-supported	GCE	<i>In-situ</i>	Cadmium (II) Lead (II)	0.1 µg/L (0.90 nM) 0.05 µg/L (0.24 nM)	SW-ASV	The study concluded that functional nanocomposites based on the thiol-ene chemistry may offer high application potential to treatment and analysis of environmental heavy metals. Model solution: pH 4.5 0.1 M Acetate Buffer.	301

thiolated thionine							
Bismuth film	SPE	<i>In-situ</i>	Cadmium (II) Lead (II)	0.5 µg/L (4.45 nM) 0.8 µg/L (3.86 nM)	SW-ASV	The disposable electrode demonstrated high selectivity for the target metal ions determination and was applied to quantitatively analyze Cd (II) and Pb (II) levels in milk sample extracts with satisfactory results. Model solution: pH 4.5 0.1 M Acetate Buffer.	302
Bismuth Film	GCE	<i>In-situ</i>	Cadmium (II) Lead (II)	0.005 µg/L (0.045 nM) 0.04 µg/L (0.19 nM)	ASV	This study utilises a 12 mm GCE and uses double deposition, gaining exceptional limits of detection, due to the large size of the working electrode. Model solution: pH 4.5 0.1 M Acetate Buffer.	303

Antimony							
Antimony film	GCE	<i>In-situ</i>	Cadmium (II) Lead (II)	0.7 µg/L (6.23 nM) 0.9 µg/L (4.34 nM)	ASV	Convenient operation in acidic solutions of pH 2 or lower (which is superior to that reported for Bismuth films) in the presence of dissolved oxygen. Model solution: pH 2 0.01 M HCl.	184
Antimony film	CPE	<i>In-situ</i>	Cadmium (II) Lead (II)	0.8 µg/L (7.12 nM) 0.2 µg/L (0.97 nM)	ASV	The practical applicability of the proposed electrode was successfully ascertained via measurement of cadmium and lead ions in the real sample of lake water. Model solution: pH 2 0.01 M HCl.	186
Antimony film	GCE	<i>Ex-situ</i>	Cadmium (II) Lead (II)	1.1 µg/L (9.79 nM) 0.3 µg/L (1.45 nM) 6 µg/L (102.23 nM) ^m	ASV (Cd, Pb) AdSV (Ni)	The antimony-film revealed favourable electroanalytical performance similar to that of the in-situ prepared antimony-film and comparable to bismuth- and	304

			Ni (II)			mercury-based electrodes. Model solution: pH 1 0.1 M HCl.	
Antimony film	GCE	<i>In-situ</i>	Cadmium (II) Lead (II)	1.4 µg/L (12.46 nM) 1.2 µg/L (5.79 nM)	SIA-ASV	The presence of KSCN in the sample solution offers the possibility of detecting ions with more negative oxidation potentials like Zn(II), Mn(II) or Cr(III). Model solution: pH 1 0.1 M HCl.	305
Macroporous antimony film	Gold	<i>Ex-situ</i>	Cadmium (II) Lead (II)	0.7 µg/L (6.23 nM) 0.5 µg/L (2.41 nM)	ASV	Further studies would optimise the pore structure and study the limits of this enhancement effect. Model solution: pH 1 0.1 M HCl.	306

Antimony film	CPE	<i>In-situ</i>	Indium (III) Thallium (I)	2.4 µg/L (20.91 nM) 1.4 µg/L (6.85 nM)	Stripping Chronopotentiometry	Potential selective determination of Tl (I) in the presence of Ir (III) and Zn (II) is discussed. Model solution: pH 1 0.1 M HCl.	307
Antimony film	Titanium	<i>Ex-situ</i>	Nickel (II)	0.2 µg/L (3.39 nM)	SW-AdSV	Novel antimony-sputtered electrodes, fabricated by standard microelectronics thin-film technology. Model Solution: pH 9.2 0.01 M Ammonium Buffer.	189
Antimony film	CPE	<i>In-situ</i>	Cadmium (II) Lead (II)	10 µg/L (88.97 nM) 10 µg/L (48.26 nM)	PSA	Simultaneous detection of Pb (II) and Cd (II), using SbF-CPE and BiF-CPE. Model solution: pH 2 0.01 M HCl.	186
Antimony film	Carbon fiber	<i>In-situ</i>		1.9 µg/L (16.90 nM) 3.1 µg/L (14.96 nM)	ASV	Practical application of the SbFME was demonstrated <i>via</i> measuring Cu (II) in the standard reference solution of	190

	microelectrode		Cadmium (II) Lead (II)			natural water. Model solution: pH 2 0.01 M HCl.	
Antimony film	GCE	<i>Ex-situ</i>	Sulfasalazine	310.75 µg/L (780 nM)	SW-ASV	The first application of the antimony film electrode in pharmaceutical analysis. The antimony film electrode revealed favourable electroanalytical characteristics and when compared to its bismuth and bare GCE counterparts. Model solution: pH 2 0.01 M HCl.	308
Nafion-coated antimony film electrode	Δ	<i>In-situ</i>	Cadmium (II) Lead (II)	0.3 µg/L (2.67 nM) 0.15 µg/L (0.72 nM)	DP-ASV	The electrode was successfully applied to determining Pb (II) and Cd (II) in vegetable and water samples with satisfactory results. Model solution: pH 2 0.01 M HCl.	309

<i>Tin</i>							
Tin-film	GCE	<i>In-situ</i>	Cadmium (II) Zinc (II)	0.7 µg/L (6.23 nM) 0.9 µg/L (13.85 nM)	SW-ASV	Extended by exploring the possibility to detect other metals normally determined by ASV Tl (I), Pb (II), Cu (II)). Model solution: pH 2 0.01 M HCl.	191

^m= Lowest concentration addition recorded

^v = Limit of detection not provided

Δ = Information not accessible

ASV = Anodic Stripping Voltammetry, SW-ASV = Square-Wave Anodic Stripping Voltammetry, DP-ASV = Differential Pulse Anodic Stripping Voltammetry, DPV – Differential Pulse Voltammetry, CCSCP = Constant Current Stripping Chronopotentiometric Measurement, CV = Cyclic Voltammetry, SIA-ASV = Sequential-Injection Analysis Anodic Stripping Voltammetry, PSA = Potentiometric Stripping Analysis, DP-AdSV = Differential Pulse Adsorptive Stripping Voltammetry, SW-AdSV = Square Wave Adsorptive Stripping Voltammetry

Table 3: Comparison of the current state-of-the-art electrochemical techniques for the electroanalytical detection of lead (II) ions

Electrode of Choice	Limit of Detection (3σ) / (μgL^{-1})	Linear Range/ (μgL^{-1})	Deposition time / s	Comments	Reference
WHO level in Drinking Water	N/A	10	N/A	WHO recommended level of lead in drinking water	310
GC	18.0 11.0	100-400	120	Simultaneous detection of lead (II) and cadmium (II) in a 0.1 M acetate buffer solution using a bismuth film electrode.	311
	2.30 1.50	20-100	300	Simultaneous detection of lead (II) and cadmium (II) with an introduction of $\text{K}_4[\text{FeCN}_6]$ within a 0.1 M acetate buffer solution, using bismuth film electrode. Limits of detection revealed to be below that stated by WHO.	312
	0.80	5-60	600	Simultaneous detection of lead (II) and cadmium (II) using bismuth	234

				nanoparticles upon the working electrode, within a tap water solution, results were validated with ICP-MS.	
	2.30	1.5-450	240	Simultaneous detection of lead (II), cadmium (II) and copper (II) with analytical applications within tap water. Results validated by AAS.	313
CPE	0.45	50-200	180	Simultaneous detection of lead (II), cadmium (II) and copper (II) and zinc (II) in HCl.	314
Amino-functionalized metal-organic frameworks	1.04	2-70	300	Lead (II) detection using a NH ₂ -Cu ₃ (BTC) ₂ modified GCE, in a 0.1 M acetate buffer solution.	233
SPE	0.03	0.05 -30	300	Modified porous bismuth SPE demonstrates simultaneous detection of lead (II) and cadmium (II), in real water samples, with the porous electrode offering higher sensitivity due to the increased surface area.	315

	5.00	16.8–62.6	120	<i>In-situ</i> modified antimony SPE showing detection of lead (II) in a 0.1 M acetate buffer solution.	316
	2.00	10-100	120	Detection of lead (II) within surface waters and validated with ICP-AES using a bismuth film SPE.	317
	0.91	2.5-100	120	Detection of lead (II) within a solution of HCl using acetamide phosphonic acid self-assembled monolayer on a mesoporous silica modified SPE.	318
b²SPE	1.10	5-110	30	Detection of lead (II) within drinking water samples validated against ICP-OES, using an intelligent design which allows for a shorter deposition time compared to current literature.	This work

GC: glassy carbon; CPE: carbon paste electrode; SPE: screen-printed electrode; AAS: Atomic Absorption Spectroscopy

Table 4: An overview of current literature reports on the use of pencil-drawn electrode systems.

Electrode Fabrication	Pencil and Substrate Utilised	Number of Layers Drawn	Target Analytes	Analytical Method	Ref.
Pencil-drawn counter electrode only	Bulk pencil "lead" working electrode with the counter electrode drawn using Pentel (grade 'H' only) pencil upon paper substrates	Not Stated	<i>p</i> -nitrophenol	Differential pulse voltammetry	319
Pencil-drawn working macroelectrode	Staedtler Mars (grade '3B' only) upon paper substrates	Not Stated	Potassium ferrocyanide and 1,2-hydroxybenzene	Cyclic voltammetry	275
Pencil-drawn immune device	6B-type Black Pencil only upon a paper substrate	Not Stated	Carbohydrate antigen 199	Electro-chemiluminescence	320
Pencil-drawn working macroelectrode	Derwent (grade '6B' only) upon polyvinyl chloride substrate	Not Stated	Lead (II)	Anodic stripping voltammetry	266
Pencil-drawn macroelectrodes	Derwent, Staedtler Mars Lumograph, FILA and Koh-i-Noor Hardtmuth (HB, B, 2B, 3B, 4B, 6B, 8B explored) upon paper substrates	Not Stated	Potassium ferrocyanide, ascorbic acid and sunset yellow	Cyclic voltammetry and hydrodynamic voltammetry	274
Pencil-drawn strain electrode and Chemresistor	Blick pencils (9H, 2H, HB, 2B, 6B, 9B explored) upon paper substrates	Not Stated	Toluene, THF, ethyl acetate, methanol, hexane to acetone	Solvent vapour measured	321

Pencil-drawn dual electrode with pseudo reference electrode	Staedtler Mars (grade '3B' only) upon paper substrates	Not Stated	Ascorbic acid, dopamine and paracetamol	Thin-layer chromatography and cyclic voltammetry	276
Pencil-drawn working macroelectrode with pseudo reference and counter electrode	Working electrode was manufactured within laboratory utilising mixture of graphite, sodium bentonite and potassium silicate, then doped with decamethylferrocene or cobalt(II) phthalocyanine upon paper substrates. Additional counter and reference electrodes are also drawn onto the substrate.	4 draws	Cysteine and hydrogen peroxide	Linear sweep voltammetry and cyclic voltammetry	273
Pencil-drawn working macroelectrode	Commercially Available Staedtler Mars Tradition Pencils upon an ultra-flexible polyester substrate (6B, 5B, 4B, 3B, 2B, B, HB, H, 2H explored)	1-10 draws	Hexaammineruthenium(III) chloride, potassium ferricyanide, <i>p</i>-benzoquinone and simultaneous detection of lead (II) and cadmium (II) ions	Cyclic voltammetry and anodic stripping voltammetry	This Work